OPTIMISATION OF XENON-RICH STOPPED-FLOW SPIN-EXCHANGE OPTICAL PUMPING FOR FUNCTIONAL LUNG IMAGING

Jason Graham Skinner

MPhys (Hons)

Thesis submitted to the

University of Nottingham

for the degree of Doctor of Philosophy

School of Medicine

October 2016

Abstract

Spin-exchange optical pumping (SEOP) is a hyperpolarisation method used in the hyperpolarisation of noble gases and can enhance nuclear spin polarisation by five orders of magnitude. Hyperpolarised (HP) ^{129}Xe has many properties that make it ideally suited to clinical lung imaging, but since its first demonstration in animals in 1994 and humans in 1996, translation to the clinic has been hampered by challenges associated with scaling up production.

Within this thesis, construction and demonstration of a clinical-scale stopped-flow hyperpolariser is described, the design of which is based on the record-holding XeUS and XeNA polarisers developed previously by our consortium, which had aimed to address the issue of production scale-up. Modifications enhancing the ease of operation and utility in-clinic are presented, as are modifications that reduce the capital cost of such a system. These include a re-design of the gas manifold and the development of a low-cost low-field NMR spectrometer which achieved an SNR of 125 at a cost of ∼$300, a 13-fold improvement in cost/SNR compared with the existing spectrometer at a saving of ∼$19,000.

In continuous-flow ^{129}Xe polarisers there has long been a discrepancy in the polarisation achieved and that predicted by the standard model of SEOP which was shown recently to be due to the presence of rubidium clusters. Here, the standard model is applied to- and validated for the first time against the stopped-flow regime. The validated model is used to explore parameter space to identify the most effective ways to increase production yield in future stopped-flow polarisers.

Stopped-flow SEOP in the xenon-rich regime presents unique thermal management problems due to the absence of gas flow and abundance of poorly thermally conductive, Rb spin destroying Xe. Raman spectroscopy is used to spatially examine in-cell thermal behaviour under steady-state and turbulent 'rubidium runaway' conditions as a function of temperature and Xe density and the beneficial impact of adding thermally conductive helium to the standard N_2-Xe gas mix is demonstrated.

Hybrid Rb-Cs-Xe SEOP is demonstrated for the first time and examined using in-situ NMR and Raman spectroscopies. High polarisations of ∼50% were obtained. (Collaborative work, previously reported in [1])

Finally, progress on the HP-Xe clinical trial is presented to illustrate the impact of the 4-fold increase in SNR that will come with the installation of the new N-XeUS stopped-flow polariser.

Publications

1. B.M. Goodson, N. Whiting, H. Newton, **J.G. Skinner**, K. Ranta, P. Nikolaou, M.J. Barlow and E.Y. Chekmenev, 2015, "Spin-exchange Optical Pumping at High Xenon Densities and Laser Fluxes: Principles and Practice," in T. Meersmann (ed.) & E. Brunner (ed.), *Hyperpolarized Xenon-129 Magnetic Resonance: Concepts, Production, Techniques and Applications*, pp. 96-121, Royal Society of Chemistry, Cambridge, UK.

2. B.M. Goodson, N. Whiting, J. Birchall, **J.G. Skinner**, K. Ranta, M. Gemeinhardt, B. Gust, P. Nikolaou, A. Coffee, M.J. Barlow, E.Y. Chekmenev, 2016, "Hyperpolarization Methods for MRS," in J. Griffiths (ed.) & P. Bottomley (ed.), *Handbook of in-vivo Magnetic Resonance Spectroscopy*, pp. 557-574, John Wiley & Sons.

3. B.M. Goodson, K. Ranta, **J.G. Skinner**, A.M. Coffee, P. Nikolaou, M. Gemeinhardt, D. Anthony, S. Stevenson, S. Hardy, J. Owers-Bradley, M.J. Barlow and E.Y. Chekmenev, 2017, "The Physics of Hyperpolarised Gas MRI," in F. Hane (ed.) & M. Albert (ed.), *Hyperpolarized and Inert Gas MRI: From Technology to Application in Research and Medicine*, pp. 23-46, Elsevier.

4. J. Birchall, N. Whiting, **J.G. Skinner**, M.J. Barlow, B.M. Goodson, 2017, "Using Raman Spectroscopy to Improve Hyperpolarized Noble Gas Production for Clinical Lung Imaging Techniques," in *Raman Spectroscopy and Applications*, pp. 247-268, InTechOpen.

5. A.B. Schmidt, S. Berner, W. Schimpf, C. Müller, T. Lickert, N. Schwaderlapp, S. Knecht, **J.G. Skinner**, A. Dost, P. Rovedo, J. Hennig, D. von Elverfeldt, J.-B. Hövener, "Liquid-state carbon-13 hyperpolarization generated in an MRI system for fast imaging," *Nature Communications*, vol. 8, p. 14535, Mar 2017.

6. **J.G Skinner**, K. Ranta, N. Whiting, P. Nikolaou, A.M. Coffee, E.Y. Chekmenev, M.J. Barlow, B.M Goodson, P.G Morris, manuscript in preparation, "Simulations of Xenon Rich Stopped-Flow Spin-Exchange Optical Pumping at High Laser Fluxes."

Acknowledgements

Studying towards this PhD has been the most incredible period of personal, professional and scientific growth and there have been many people who have contributed to this and helped me along the way and I'd like to take this opportunity to give my thanks. First and foremost, thank you to my supervisors Peter Morris, Ian Hall, and Mike Barlow for your support, insight, and wisdom, and for giving me the opportunity to work in such a stimulating and promising field of research.

Since the start of the project I've had the privilege of working with a number of fantastic scientists in the USA; Boyd Goodson, Ed Chekmenev, Peter Nikolaou, Aaron Coffee, Kaili Ranta, Brogan Gust, Nick Whiting and Laura Walkup, thank you for all the insights you gave me, for loving SEOP, for making me feel at home when I visited, and for introducing me to Quattros.

Back in Nottingham I'd like to thank the teams I've worked with. Thanks to Hayley Chung who showed me the ropes and provided me with valuable guidance and friendship throughout. James Thorpe, Steven Hardy, Brett Haywood, Jonathan Birchall and Thomas Bailey, thank you for being such a great team to work with and for being there to share the odd Carlsberg. Thanks to John Owers-Bradley for guidance and for giving me and N-XeUS a place to live for the last two years. Thanks also to Pete, Alan, Stuart and all in the mechanical and electrical workshops in Physics and the MR centre for bringing many parts of the project to life.

Thanks to my family, for always loving and supporting me. Particularly my parents Julie and Wayne, who instilled in me a strong work ethic and a passion for learning. Thanks to my in-laws Alex and Jane for keeping me sane and well fed during my final weeks of writing up. And thank you to my incredible wife Elizabeth, who has lived every part of this journey with me and supported and believed in me from the moment we met.

Finally, I'd like to express my gratitude for having had the privilege to embark on a PhD program in the first place and to acknowledge all those who set me on this path or helped me along the way. These include the teachers that shaped my early education and fuelled my curiosity - particularly Mr Garbutt, Mr Watkinson and Dr. Harron; the labour ministers who proposed the (now defunct) Education Maintenance Allowance in 1999, that no doubt made all the difference to my obtaining A-levels; the foundation and widening participation programs at Wyggeston & Queen Elizabeth I College and the University of Leicester; and all those at the University of Leicester's Department of Physics and Astronomy (particularly Stan Cowley), without whom I would not have attained my degree.

Contents

List of Figures

List of Abbreviations

Abbreviation	Meaning
AM	Alkali Metal
AR	Anti-Reflective [coating]
bbFGRE	broadband Fast Gradient Echo sequence
COPD	Chronic Obstructive Pulmonary Disease
Cs	Caesium
CT	Computed Tomography
DNP	Dynamic Nuclear Polarisation
FID	Free Induction Decay
FWHM	Full Width at Half Maximum
γ_{SE}	Rate of Rb-Xe spin-exchange
γ_{SEOP}	Rate constant for P_{Xe} accumulation ($= \gamma_{SE} + \Gamma$)
γ_{OP}	Optical Pumping rate
Γ	Rate of Xe spin destruction
Γ_{SD}	Rate of Rb spin destruction
GE	General Electric
He	Helium
HP	Hyperpolarised
HPNG	Hyperpolarised Noble Gas
HXTC	Hyperpolarised Xenon Technology Consortium
IPF	Idiopathic Pulmonary Fibrosis
K	Potassium
LDA	Laser Diode Array
MHRA	Medicines and Healthcare products Regulatory Agency
MIU	Medical Imaging Unit at the Queen's Medical Centre

Continued on Next Page...

Abbreviation	**Meaning**
N_2	Nitrogen
N-XeUS	XeUS polariser at Nottingham
NG	Noble Gas
ppm	parts per million
ppb	parts per billion
$\langle P_{\mathrm{Rb}} \rangle$	Cell averaged rubidium polarisation
P_{Rb}	Rubidium polarisation
P_{Xe}	^{129}Xe polarisation
Rb	Rubidium
rf	radio frequency
SDK	Software Development Kit
SE	Spin-Exchange
SEOP	Spin-Exchange Optical Pumping
SNR	Signal to Noise Ratio
S/V	Surface to Volume ratio
T_1	Longitudinal relaxation time
T_2	Transverse relaxation time
TE	Echo Time
TEC	Thermo-Electric Cooler
TR	Repetition Time
$T_{\mathrm{N_2}}$	Nitrogen rotational temperature
T_{opt}	Temperature at which maximum P_{Xe} occurs
T_{LDA}	Laser Diode Array temperature
T_{cell}	Cell thermocouple temperature
VHG	Volume Holographic Grating
Xe	Xenon
XeNA	Xenon polarizatioN Automated
XeUS	Xenon Ultimate Spin-exchange
YO	Year Old

Chapter 1

Introduction

The work presented within this thesis aims to aid progress in the development of hyperpolarised (HP) xenon based MRI measurements of lung disease. The case for such an endeavour is easy to make. Chronic Obstructive Pulmonary Disease (COPD) - a degenerative lung disease characterised by airflow obstruction that is not fully reversible - affects approximately 3 million people in the UK of which 2 million are undiagnosed [4]. The American Thoracic Society (ATS) and European Respiratory Society (ERS) state COPD is a leading cause of morbidity and mortality worldwide, and the fourth leading cause of death in the USA and Europe [5]. The total annual cost of COPD to the NHS is estimated to be over £800 million, which equates to £1.3 million per 100,000 people [4]. Idiopathic Pulmonary Fibrosis (IPF) is a chronic, progressive fibrotic interstitial lung disease of unknown origin which is difficult to diagnose and often requires the collaborative expertise of a consultant respiratory physician, a radiologist and a histopathologist to reach a consensus [6]. Over time, IPF causes a decline in lung function, reduced quality of life and ultimately death. The median survival period for people with idiopathic pulmonary fibrosis in the UK is approximately 3 years from the time of diagnosis [6]. As will be shown, HP-Xe has the potential to provide information which is unavailable using current methods of spirometry and CT, and may allow the

development of targeted metrics that are sensitive to the progression of the diseases. Moreover, unlike CT which relies on ionising radiation, MRI scans of HP xenon are completely harmless which means that repeat measurements - a crucial aspect in any longitudinal therapeutic drug trial - are not limited by cumulative exposure to ionising radiation. HP xenon then may provide a pathway to drug studies to identify much needed drug therapies for COPD and IPF, among others.

Conventional MRI, one of the most powerful diagnostic tools in modern medicine, derives signal from protons found in human tissue and is therefore useful in almost all human organs except the lungs. Diagnosis of lung disease therefore relies on spirometric pulmonary function tests or CT. One can imagine that the ideal manner to image the lung for diagnostic purposes using MRI would involve the patient inhaling an MR visible exogenous gas that was completely harmless. Such a gas would fill the airways and acquiring an image at the point of maximal inhalation would result in an image that reveals the shape and structure of the container - the lungs. This is the principle of HP xenon pulmonary MRI.

^{129}Xe is endowed with a number of properties that, when combined with existing MRI methods, make it almost ideal for the purposes of diagnostic lung imaging. It is naturally abundant (87 ppb in the Earth's atmosphere) and produced as a by-product of commercial air separation [7], making it affordable. It has a nuclear spin = 1/2 and is therefore NMR active and, as a noble gas, it is non-toxic making it safe for human inhalation. By virtue of these properties *macroscopic* MR images of lung structure can be produced. Complementary information on the lung *microstructure* can also be obtained by exploiting that fact that xenon is a gas with a known coefficient of diffusion: the extent to which the gas is or is not restricted results in an apparent

diffusion coefficient that can be determined regionally, making it ideal in the diagnosis or study of emphysema where alveolar structure is compromised and heterogeneity of the disease is common. These capabilities alone would make xenon an interesting prospect for development as a lung imaging agent. Xenon however also has the capacity to offer *functional* information due to its ability to diffuse into the blood and because of its exquisite chemical shift sensitivity. Spectroscopically, xenon signals originating in the gas phase are easily distinguished from those which originate from both xenon dissolved in the blood, and those which originate in the lung tissue [8]. With the appropriate imaging sequence these properties can be exploited to provide surrogate measures of oxygen and carbon-dioxide gas exchange within the lung, and with enough signal this information can be encoded in a regional manner [9] i.e. maps of lung function can be produced. It is anticipated that these properties will not only yield new metrics that can be used for clinical diagnosis and monitoring, but also provide new insights into the physiology of the lung and the pathology of various pulmonary diseases.

Already, hyperpolarised noble gases - and hyperpolarised xenon in particular - are showing great promise as a class of contrast agents for clinical pulmonary imaging. Hyperpolarised gases can be generated by spin-exchange optical pumping (SEOP) and have nuclear spin polarisations that are approximately 10^5 times greater than their non-hyperpolarised equivalents [10, 11]. This level of signal enhancement more than compensates for the signal density reduction due to them being in the gas phase. To date, the biggest barrier to in-clinic realisation of HP xenon MRI methods has been scaling up the production. Other challenges are associated with the development of bespoke coils and imaging sequences, and the fact that, at present, none of the vendors offer clinically approved polarisers.

The first xenon polariser built for the purposes of producing HP-Xe for clinical use was a prototype developed by MITI in the 1990's [12]. It was a continuous-flow device and produced 1 litre of hyperpolarised xenon gas polarised to 5% which was sufficient for the initial proof-of-concept work but insufficient for routine clinical usage. A number of continuous-flow devices were developed over subsequent years and significant gains in output were achieved [13, 14, 15] but all had one thing in common: the polarisation predicted by theory was not realised by the devices, and often by a significant margin. This was the case until recently when Freeman *et al.* hypothesised that the theoretical model for a continuous-flow system was incomplete [16]. Inclusion of a deleterious rubidium cluster term brought the theoretical level in line with the data for a range of experimental conditions and compelling evidence of these clusters was presented. Polarisation levels in continuous-flow systems are likely to increase as the model is harnessed to identify design optimisations, and work has already begun towards this end [17].

Hyperpolarised xenon can also be produced by stopped-flow SEOP, and this is the regime that has been researched and developed by the consortium to which my group belongs [18, 19, 20, 19, 21, 22]. Various advances, mainly in the field of high-powered laser diode arrays [23, 24, 25], have enabled the group to discover a regime in which high concentrations of xenon can be polarised to high levels - something that was not anticipated due to xenon's capacity to depolarise the rubidium spins that are required to hyperpolarise it. Within this regime, xenon polarisation drops as the xenon concentration is increased, but the drop in polarisation is less than would be expected, and thus, when combined with the higher concentrations, it means that the magnetisation, or observable signal, actually increases with increased xenon density. This discovery was harnessed in the consortium's clinical-scale stopped-flow polarisers,

XeNA and XeUS. XeNA, the first of the two systems, generated record levels of polarisation at the time it was published and, aside from the second generation device, has yet to be matched. In-cell polarisations were measured as 90%, 57%, 50% and 30% for loadings of 300, 500, 760 and 1545 torr respectively in a volume of 0.5 litres [18].

The work presented within this thesis aims to aid progress in the development of HP-Xe based MRI measurements of lung disease by focusing on issues relating to production and is structured as follows: **Chapter 2** introduces the relevant underlying theory. The fundamentals of thermal- and hyperpolarisation are laid out, and a brief review is given to emerging methods of hyperpolarisation relevant to biomedical research. SEOP - the key method of xenon hyperpolarisation in this thesis - is discussed in greater detail. Considerations for handling and imaging hyperpolarised spin systems are also discussed and a brief review is given to progress of hyperpolarised noble gases (HPNGs) in and towards the clinic.

Chapter 3 details the construction of the N-XeUS polariser, the generation '2.5' xenon polariser developed by the HXTC consortium that is to be used in the hyperpolarised xenon lung imaging study at the University of Nottingham. It will replace the currently installed GE polariser and provide 4-fold gain in apparent polarisation with a corresponding gain in image SNR. This chapter opens with a discussion of the record-holding first and second generation polarisers on which N-XeUS is based - XeNA and XeUS - and the new xenon rich SEOP regime these polarisers were designed to exploit. The construction and workings of the N-XeUS polariser are discussed and results which demonstrate the operational state of the polariser are presented. Modifications enhancing the ease of operation and utility in-clinic relative to XeNA and XeUS are presented, as are modifications that aimed to reduce that capital cost of such a

system. These include a re-design of the gas manifold and the development of a low-cost low-field NMR spectrometer (1-100 kHz) which achieved an SNR of 125 at a cost of ∼$300, a 13-fold improvement in cost/SNR compared with the existing spectrometer and a saving of ∼$19,000. The anticipated impact of the N-XeUS polariser on the imaging study is also discussed.

Chapter 4 contains simulations of xenon-rich stopped-flow SEOP using the standard model. These simulations are validated against two datasets; the initial dataset where the xenon-rich regime was first discovered, and a much larger dataset generated using the XeUS polariser. The validated model is then used to propose design modifications that may be exploited to bring about further gain in magnetisation output on the existing and subsequent consortium polarisers.

Chapter 5 contains the results of Raman investigations of stopped-flow SEOP conducted at Nottingham. Xenon-rich stopped-flow SEOP is a regime in which thermal effects can become strongly manifest due to 1) the high concentrations of xenon, which conducts heat poorly relative to commonly used buffer gases and causes high rates of rubidium spin destruction, 2) because there is no flow of gas to remove excess heat in the system (as is the case in continuous-flow SEOP), and 3) because high-flux lasers are commonly employed for optical pumping. Due to its ability to probe the temperature of the gas directly, Raman spectroscopy provides a unique insight into these thermal effects.

Chapter 6 covers work on the development of rubidium-caesium (Rb-Cs-Xe) 'hybrid' SEOP, a compelling regime which may enhance existing SEOP methods by including a spin 'catalyst' into the conventional Rb-Xe system: The spin-exchange cross-sections for Rb-Cs and Cs-Xe interactions are greater than that of Rb-Xe, and therefore spin order can theoretically transfer more

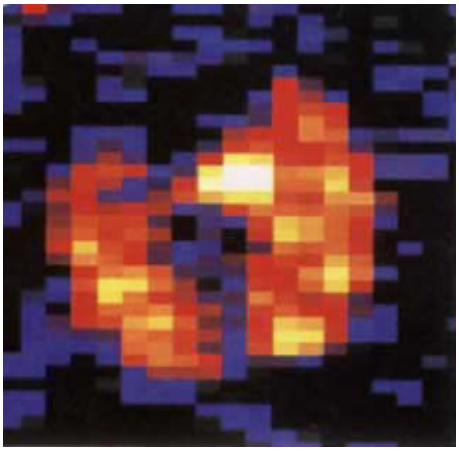

Figure 1.1: The first hyperpolarised ^{129}Xe lung image, reported in the journal *Nature* in 1994. Excised mouse lungs at 9.4 T. Reprinted from [2] with permission.

rapidly if caesium is present within the system. When developed further, it may enhance polariser performance while mitigating the need for any major hardware modifications because the system can still be optically pumped using the 795 nm rubidium laser. (This was collaborative work, previously reported in [1]).

Finally **chapter 7** summarises progress to date at Nottingham on our hyperpolarised xenon clinical pilot study and the impact of the new N-XeUS polariser on the study is discussed. Namely - an approximate 4-fold gain in image SNR. More, if modifications detailed in chapter 4 are implemented.

The conclusions are brought together and summarised in **chapter 8**.

Chapter 2

Theory: NMR, Hyperpolarisation and HP Noble Gas MRI

2.1 Thermal Polarisation

Central to the nuclear magnetic resonance (NMR) phenomenon is the magnetic moment of the nucleus μ, which is a function of the nuclear spin quantum number I and the gyromagnetic ratio γ:

$$\mu = \gamma I. \tag{2.1}$$

The orientation of the magnetic moment is random unless it is subjected to an external magnetic field B_0, which breaks the degeneracy of the magnetic quantum states. Given an ensemble of nuclei, individual nuclei therein will align relative to the external field, taking one of a number of possible discrete orientations, where the number of possible orientations N for the given nucleus depends on the value of the nuclear spin:

$$N = 2I + 1. \tag{2.2}$$

In the case of a spin = 1/2 system (such as ^{1}H or ^{129}Xe), N = 2, and the nuclear spin polarisation P - the difference in population of the spin states -

can be described as:

$$P = \frac{N_\uparrow - N_\downarrow}{N_\uparrow + N_\downarrow}. \tag{2.3}$$

Here, $N_\uparrow$ and $N_\downarrow$ represent the $m+$ and m- magnetic quantum numbers where $m = +\frac{1}{2}$ is the lower energy state and $m = -\frac{1}{2}$ is the upper energy state and $\Delta E = -\hbar\gamma B_0$ is the energy difference between the two. $m+$ and m- assume the nuclear spin values I, i.e. $m = 1/2$ or -1/2 for a spin = 1/2 nucleus, or for a spin = 3/2 nucleus, m = -3/2, -1/2, 1/2 or 3/2. Figure 2.1 illustrates energy level splitting in systems of varying quantum number.

In a conventional NMR or MRI experiment where the spin system is at thermal equilibrium, the amount of observable signal - or magnetisation, M_0 - is governed by the thermal polarisation P of the spin system:

$$M_0 = \frac{1}{2} N_s \gamma \hbar P, \tag{2.4}$$

where N_s is the number of spins, γ is the gyromagnetic ratio of the species of interest and $\hbar$ is the reduced Planck's constant. In the case where I=1/2, the value of the nuclear spin polarisation P can be calculated with the following equation:

$$P = \tanh\left(\frac{\gamma\hbar B_0}{2kT}\right), \tag{2.5}$$

where k is the Boltzmann constant and T is the temperature. This is the Boltzmann thermal equilibrium polarisation. Due to the relative weakness of the magnetic moment (i.e. $\gamma\hbar B_0/kT \ll 1$), this expression can often be simplified to:

$$P \approx \frac{\gamma\hbar B_0}{2kT} \left(= \frac{N_\uparrow - N_\downarrow}{N_\uparrow + N_\downarrow}\right). \tag{2.6}$$

It can be seen here (from equation 2.6) that the sensitivity of conventional NMR is inherently poor due to the small population difference between the nuclear spin levels, even at the highest fields currently available. For example,

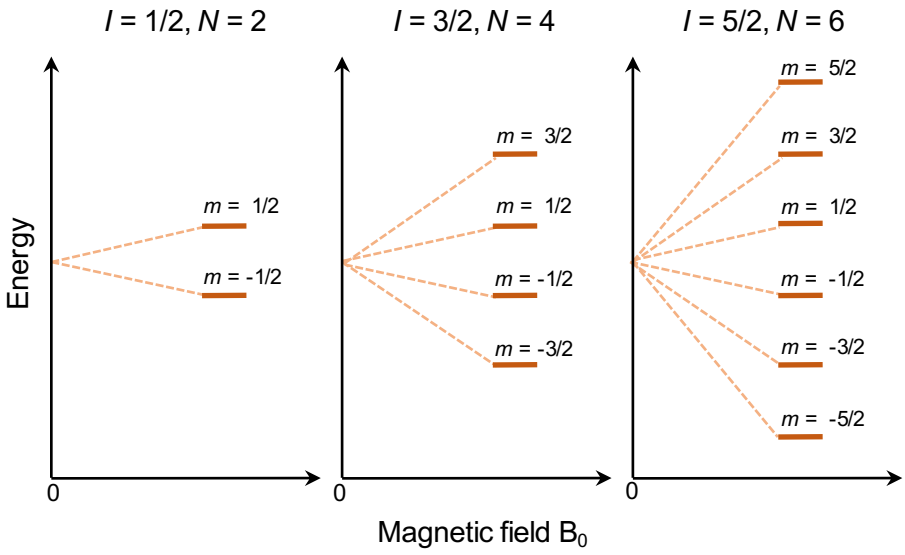

Figure 2.1: Energy level splitting as a function of field strength for atoms with nuclear spin $I = 1/2$, $3/2$ and $5/2$.

in a field of 9.4 T at room temperature, the polarisation of protons is less than 4 x 10^{-5} [10], and to enhance the signal by equilibrium means would require either significantly increasing the magnetic field strength B_0 - which is impractical and becomes increasingly expensive beyond a certain point - or reducing the temperature to close to absolute zero - which is not possible where a living sample is the target. Fortunately, non-equilibrium means can be used to manipulate the polarisation of the system. Figure 2.2 shows a thermally polarised sample in panels (A) and (C). In panel (A) the small population difference between the energy states can be observed. (C) shows the resulting NMR signal after 2048 signal averages. Panels (B) and (D) show the population difference induced via hyperpolarisation and the resulting signal enhancement in the spectrum, which has a 10,000-fold amplitude and was acquired in a single acquisition.

2.2 Hyperpolarisation

In order to significantly enhance the nuclear spin polarisation non-equilibrium methods must be used. These so-called hyperpolarisation methods drive the spin system out of thermal equilibrium, typically delivering orders-of-magnitude gains in nuclear spin polarisation. Indeed, numerous strategies for the manipulation of nuclear spin states have emerged with recent progress driven primarily by the biomedical fields. These methods can be grouped into the following categories: Metastability Exchange Optical Pumping (MEOP), Spin-Exchange Optical Pumping (SEOP); Brute Force Polarisation (BFP), Dynamic Nuclear Polarisation (DNP), ParaHydrogen Induced Polarisation (PHIP) and Signal Amplification By Reversible Exchange (SABRE). SEOP and MEOP are most commonly used for the polarisation of noble gases; BFP, DNP and PHIP are most commonly used in the polarisation of ^{13}C based substrates. SABRE has been most successful to date with ^{15}N. A brief summary of each follows, with a standalone section given over to SEOP - the hyperpolarisation method used throughout this work.

The simplest in terms of conceptual description is BFP method of hyperpolarisation. Here, the sample is cooled at high field. While the sample is held in these conditions nuclear spin polarisation accumulates in accordance with the Boltzmann thermal equilibrium for those conditions (as per equation 2.5) and the hyperpolarised state is manifest when the sample is quickly returned to standard temperature and pressure (STP) conditions. The polarisation process can take many tens of hours but can be achieved more quickly with the addition of a nanoparticle catalyst [26]. This method has great flexibility in that it is not restricted to a single or small selection of nuclear species: many nuclei can in principle be hyperpolarised in this way although [^{13}C]pyruvate

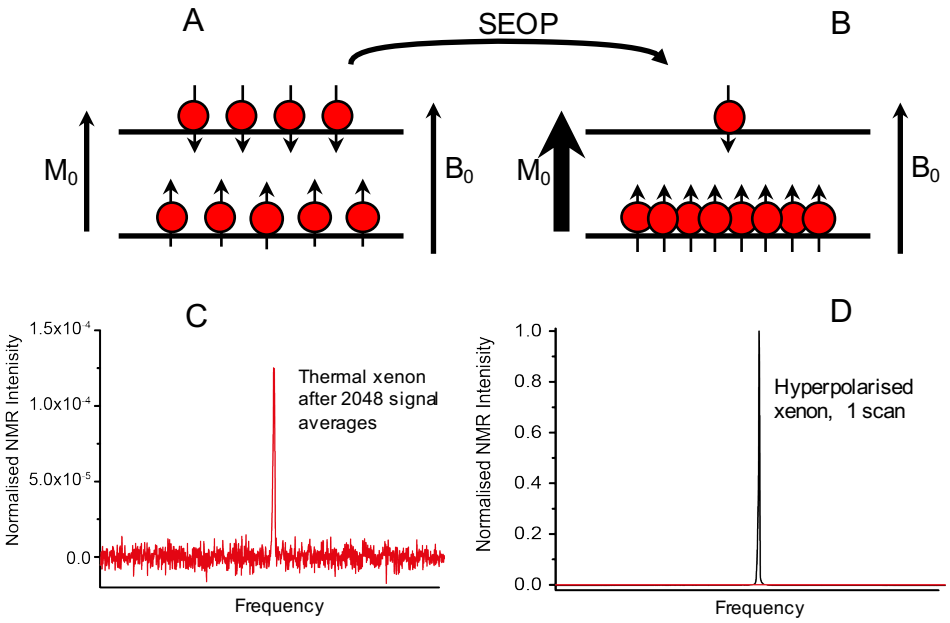

Figure 2.2: Nuclear spin distributions in a spin 1/2 system at thermal equillibrum (A,C) and when hyperpolarised (B,D). A small population difference between the energy states can be observed in (A). (C) shows the resulting NMR signal after 2048 signal averages. Panels (B) and (D) show the population difference induced via hyperpolarisation (B) and the resulting signal enhancement in the spectrum (D), which has a 10,000-fold amplitude and was acquired in a single acquisition.

has been the molecule of greatest interest due to its utility in metabolic cancer imaging [27, 28]. Current BFP polarisation levels in [^{13}C]pyruvate fall in the region of 0.01% [26], though recent breakthroughs with nanoparticle catalysts promise orders-of-magnitude gains [26].

DNP is based on the Nuclear Overhauser Effect: spin order is transferred from highly polarised electrons onto the target nucleus via an excess of free-radicals that are added to the sample during preparation. The electrons are initially polarised by exposure to low temperatures and high magnetic fields, and microwave irradiation effects transfer of additional spin-order to the sample. Once polarised the sample is rapidly ejected from the polariser and thawed, at which point it can be transported to the scanner and injected in its now-

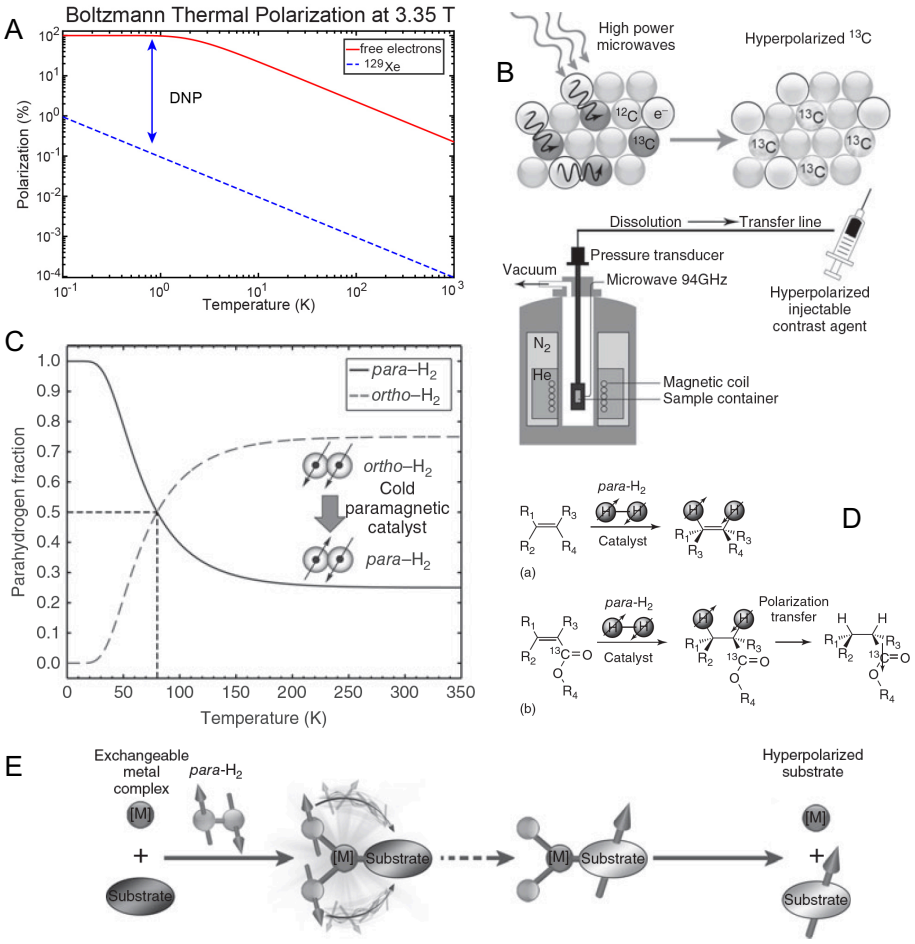

Figure 2.3: Methods of hyperpolarisation. A) The high gyromagnetic ratio of elections can be harnessed through DNP to enhance nuclear polarisation, here imparted on ^{129}Xe. The potential gain in polarisation offered by DNP is indicated by the blue arrow. B) High powered microwaves induce polarisation transfer from free radicals in the sample onto the target ^{13}C nuclei via the cross effect within the polariser. Once polarised, the sample is typically ejected rapidly from the polariser into a syringe via a sterile transfer line ((B), lower). C) Para- and ortho- hydrogen fraction as a function of temperature. Close to 80% can be obtained at liquid nitrogen temperatures. D) Schematic representation of para-H_2 pariwise addition in PHIP. E) Schematic representation of the SABRE process. Para-hydrogen can induce a polarisation in substrates in the presence of a metal complex catalyst. Compositite compiled and reprinted from [29] (A), [30] (B, C, D) and [31] (E) with permission.

liquid state. The process exploits the fact that the gyromagnetic ratio of the electrons is ∼660 greater than that of the ^{13}C nucleus [29]. Dissolution DNP, the most succesful variant of DNP to date, was introduced in 2003 [32] and has made excellent progress in development as biomedical hyperpolarisation method; it was the polarisation method used in the first-into-man clinical trial of [^{13}C]pyruvate metabolic imaging of prostate cancer [27]. [^{13}C]pyruvate polarisations of 15-20 % are possible [29]. A drawback of the method is that it is highly technical, instrumentation intensive and exhibits poor scalability [29]. Part (A) of figure 2.3 shows nuclear and electronic polarisations as a function of temperature at 3.35 T, in this case for ^{129}Xe. Part (B) illustrates incident microwaves inducing spin order in the ^{13}C nuclei and the process of ejecting the polarised substrate from the magnetic bore to the syringe via a transfer line.

In contrast, para-hydrogen induced polarisation is a cheap and simple method of hyperpolarisation which can most simply be conducted via hydrogenation reactions with para-hydrogen. In order to be compatible with the PHIP method, target molecules must have an unsaturated carbon-carbon bond that can be occupied by para-hydrogen in a hydrogenation reaction. Reactions are typically conducted in the presence of a rhodium catalyst to increase the reaction rate. ^{1}H nuclei are fermions and therefore the overall wave function for the H_2 molecule must be antisymmetric with respect to exchange. That is, all H_2 molecules in the ground state J=0 (which is symmetric) must be in the singlet spin state (which is antisymmetric), i.e. $[\propto (|\uparrow\downarrow\rangle - |\downarrow\uparrow\rangle)]$, otherwise known as para-hydrogen, and all the molecules in the J=1 antisymmetric state must be in the triplet nuclear spin state, i.e. $[\propto (|\uparrow\downarrow\rangle + |\downarrow\uparrow\rangle), |\uparrow\uparrow\rangle, |\downarrow\downarrow\rangle]$, otherwise known as ortho-hydrogen. At room temperature the Boltzmann distribution dictates that the four states are roughly evenly populated, which means ortho-

and para-hydrogen exist in a proportion of 3:1 [30], (figure 2.3(C)). Reducing the temperature to liquid helium temperature causes a redistribution of the state populations which favours the lower energy 'para' state [30, 33]. The generation of a high para-hydrogen fraction can be accelerated with a metal catalyst and once a high para-hydrogen fraction is generated it can be stored for long durations due to the fact that the transitions back to the ortho state are forbidden quantum mechanical selection rules. Relative to other hyperpolarisation methods, para-hydrogen has the potential to remain a low cost technique. Panel (C) of figure 2.3 shows the how the para-fraction of hydrogen is enhanced as a function of decreasing temperature. Panel (D) shows two forms of pairwise addition PHIP.

The most recent method of hyperpolarisation, demonstrated in 2009, is signal amplification by reversible exchange (SABRE) [34]. SABRE is a variant of PHIP which increases the utility of the technique by enabling the transfer of spin-order from the para-hydrogen in a manner that does not deplete the spin bath. ^{15}N is most commonly polarised with this technique in nicotinamide or pyridine [35, 36]. Due to the fact that development of this technique is at an earlier stage, few clinical targets are clearly defined though it has been used to polarise biologically relevent molecules such as pyrazinamide and isoniazid [37] - tuberculosis drugs. A major barrier to widespread biomedical application for both PHIP and SABRE is the fact that so far only toxic catalysts have been found to work with substrates of biological relevance. Efforts are ongoing to find safe catalysts or polarisation preserving methods to remove toxic catalysts. A schematic representation of the SABRE process can be seen in panel (E) of figure 2.3.

Metastability-exchange optical pumping is primarily used in the hyperpolarisation of ^{3}He, but has also been demonstrated in ^{21}Ne [38], ^{83}Kr [39], ^{131}Xe

[40]. In MEOP a small portion of the gas must be excited via RF discharge into a metastable state to enable the C8 and C9 depletion optical pumping which leads to the highly polarised ground state. The method must be conducted at low pressures to permit RF discharge so a major challenge in the field has been re-compression of the gas without loss of polarisation [41].

2.3 Spin-Exchange Optical Pumping (SEOP)

Spin-exchange optical pumping is the method of hyperpolarisation used throughout this work. The key elements of the theory and method are described here. More detail is provided in chapter 4, 'Simulations of Xenon-Rich Stopped-Flow SEOP'. SEOP has a long history, starting with Kastler's work in 1950 [42] which demonstrated circularly polarised light can be used to optically pump the electronic spins of alkali metal vapours. The spin-exchange aspect was later shown in ^{3}He experiments by Bouchiat, Carver and Varnum [43] in 1960 and demonstrated later still in ^{129}Xe by Grover [44] in 1978. In SEOP, the spin populations of noble gas nuclei are driven far from equilibrium via spin-exchange collision with alkali metal vapours that have been polarised using circularly polarised light [45, 46].

In the first step of the process, linear polarised laser light at the resonant frequency of the D_1 transition of the alkali metal is passed through a quarter wave-plate, which imparts angular momentum of $\pm\hbar$ onto the photons, and these photons transfer this angular momentum onto intermediate alkali metal (AM) electrons. The AM is typically rubidium and this will be assumed case henceforth. The Rb electrons can populate two otherwise degenerate Zeeman states which are separated during SEOP by the presence of an external magnetic B_0 field.

At thermal equilibrium, the $m_J = -\frac{1}{2}$ and $m_J = +\frac{1}{2}$ sub-levels of the $^2S_{\frac{1}{2}}$

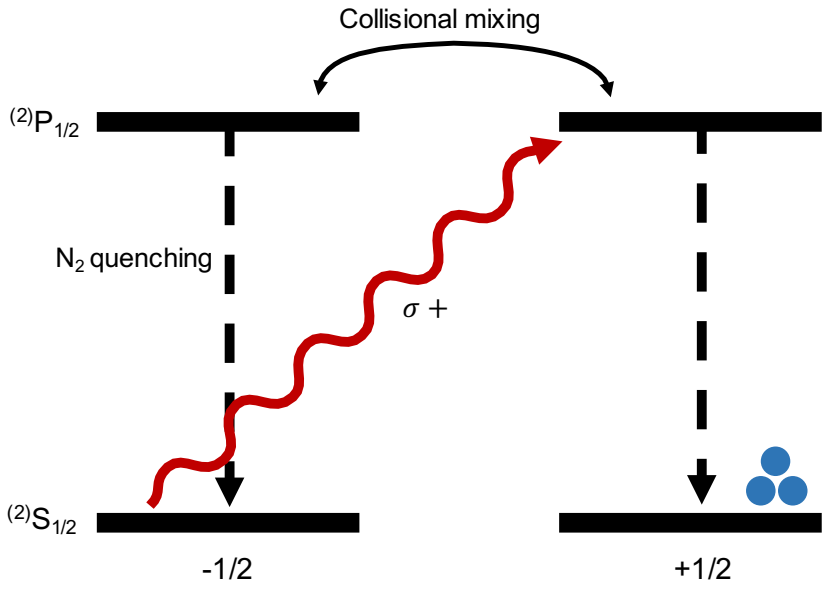

Figure 2.4: Grotrian diagram of the sub-levels of Rb during the optical pumping process. Collisional mixing of the upper state causes equal rates of relaxation to the ground state but polarisation accumulates as only one ground state is optically pumped. Figure inspired by [45].

electronic ground state of Rb are close to equal in population. The difference in population between the two states is increased by optically pumping atoms into the $m_J = +\frac{1}{2}$ sub-level of the $2P_{\frac{1}{2}}$ first excited state using σ^+ circularly polarised light (figure 2.4), which imposes the selection rule of $\Delta m_J = +1$ on the alkali metal ground state. Once atoms are in the excited state, collisional mixing occurs, equalising the probability of decay down to the $m_J = -\frac{1}{2}$ and $m_J = +\frac{1}{2}$ ground state sub-levels. Over time, a population difference grows as the $m_J = -\frac{1}{2}$ ground state sub-level becomes depleted by constant optical pumping, resulting in a bath of highly polarised Rb atoms. The process is often termed 'de-population optical pumping'.

The steady state rubidium polarisation [$P_{\mathrm{Rb}} = (N_+ - N_-)/N_{Total}$, where N_+ and N_- indicate the populations of the $m_J = +\frac{1}{2}$ and $m_J = -\frac{1}{2}$ states]

will be a function of position within the cell:

$$P_{\mathrm{Rb}}(z,r) = \frac{\gamma_{\mathrm{OP}}(z,r)}{\gamma_{\mathrm{OP}}(z,r) + \Gamma_{\mathrm{SD}}}, \tag{2.7}$$

where z and r respectively refer to the depth into the optical cell along the central axis and the radial distance from the central axis. $\gamma_{\mathrm{OP}}(z,r)$ is the optical pumping rate per atom and is defined as:

$$\gamma_{\mathrm{OP}}(z,r) = \int \Phi(z,r,\nu)\sigma_0(\nu)d\nu, \tag{2.8}$$

where $\Phi(z,r,\nu)$ is the laser flux per unit frequency and $\sigma_0(\nu)$ is the absorption cross section. Γ_{SD} is the electron spin destruction rate which is dominated by collisions with the gases in the cell:

$$\Gamma_{\mathrm{SD}}^{\mathrm{BC}} = \sum_{\mathrm{i}} [\mathrm{G_i}]\kappa_{\mathrm{SD}}^{\mathrm{Rb\text{-}i}}. \tag{2.9}$$

Here, $\kappa_{\mathrm{SD}}^{\mathrm{Rb\text{-}i}}$ is the Rb spin-destruction cross-section for Rb binary collisions with each of the gas atoms present in the cell and $[\mathrm{G_i}]$ is the atomic number density of each gas. Values of the cross-sections can be found in table (4.1). In the case of HP xenon, spin destruction can occur by a van der Waal's mechanism which dominates at lower pressures:

$$\Gamma_{\mathrm{SD}}^{\mathrm{vdW}} = \left(\frac{66183}{1 + 0.92\frac{[\mathrm{N_2}]}{[\mathrm{Xe}]} + 0.31\frac{[\mathrm{He}]}{[\mathrm{Xe}]}}\right)\left(\frac{T}{423}\right)^{-2.5} \tag{2.10}$$

where square brackets indicate gas number density in m^{-3}. Gathering expressions 2.10 and 2.9, the total spin destruction is thus:

$$\Gamma_{\mathrm{SD}} = \Gamma_{\mathrm{SD}}^{\mathrm{BC}} + \Gamma_{\mathrm{SD}}^{\mathrm{vdW}}. \tag{2.11}$$

Next, the polarised electrons of the rubidium collide with the nuclei of xenon atoms. During such collisions there is a chance that spin-exchange will occur.

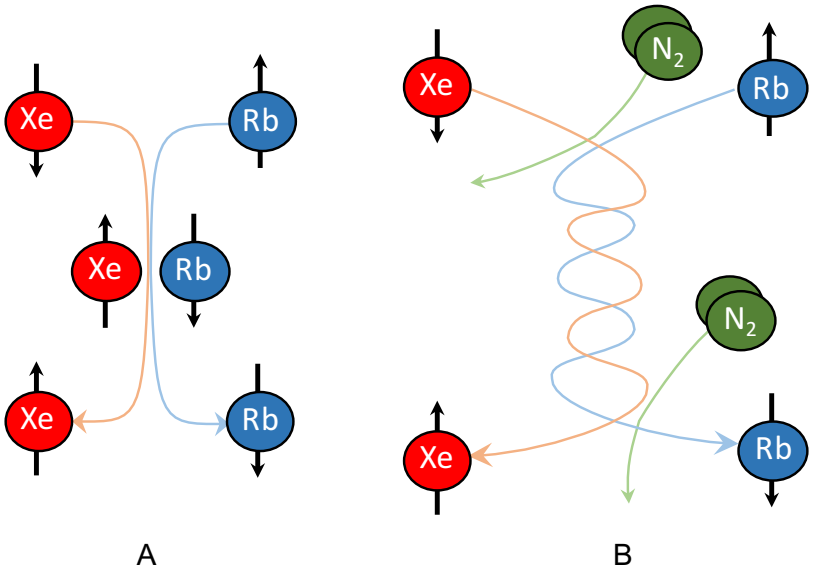

Figure 2.5: Polarization transfer processes. (a) Binary collision between an alkali-metal atom and a noble gas atom. (b) Formation and breakup of an alkali-metal/noble-gas van der Waals molecule. Figure inspired by [45].

Spin-exchange is mediated by Fermi-contact hyperfine interactions [47]:

$$\alpha \mathbf{SI} = \frac{\alpha}{2}[S^+I^- + S^-I^+] + \alpha S_z I_z \tag{2.12}$$

where S and I are the electronic and noble gas nuclear spins respectively. The so-called 'flip-flop' term in brackets expresses the spin-exchange between the alkali metal and the noble gas, and the coupling constant α is proportional to the probability of finding the un-paired electron of the alkali metal at the nucleus of the noble gas atom and is given by $\mid \eta\Phi_0 \mid$. Φ_0 denotes the un-perturbed ground state function of the AM electron in the absence of the noble gas atom. The so-called enhancement factor η results from the perturbation of the ground state wavefunction by the noble gas atom and of all the noble gases, xenon has the highest value of $\mid \eta \mid$ (-50) besides radon (63) [47, 45].

The spin-exchange process can occur by two mechanisms, a two-body collision between the the alkali metal atom and the noble gas atom, or as a

three-body interaction, in which the alkali metal and xenon atoms combine with a nitrogen molecule to form a van der Waal's complex (figure 2.5). The chance of spin-exchange during any given collision is low but, given enough laser flux, polarisation can accumulate over time because the T_1 of xenon can be relatively long (minutes to hours). The accumulation of xenon polarisation over time is given by:

$$P_{\mathrm{Xe}}^{\mathrm{cell}}(t) = \frac{\gamma_{\mathrm{SE}}}{\gamma_{\mathrm{SE}} + \Gamma}\langle P_{\mathrm{Rb}}\rangle(1 - \exp^{-(\gamma_{\mathrm{SE}}+\Gamma)t}), \tag{2.13}$$

where $\langle P_{\mathrm{Rb}}\rangle$ is the spatially averaged electronic spin polarisation of the rubidium. The overall relaxation rate is partitioned into a sum of the Xe-AM spin exchange rate, γ_{SE}, and Γ, the xenon spin destruction rate which comprises all deleterious relaxation terms and is equivalent to $\frac{1}{T_1}$. Finally, the Rb-Xe spin-exchange rate, γ_{SE}, which is the sum of a binary and vdW's terms, is given by the following expression:

$$\gamma_{\mathrm{SE}} = \gamma_{\mathrm{SE}}^{\mathrm{vdW}} + \gamma_{\mathrm{SE}}^{\mathrm{BC}} = \left(\frac{1}{\sum_{\mathrm{i}}\left(\frac{[\mathrm{G_i}]}{\xi_{\mathrm{i}}}\right)} + \kappa_{\mathrm{SE}}^{\mathrm{Rb\text{-}Xe}}\right)[\mathrm{Rb}], \tag{2.14}$$

where ξ_{i} is the vdW rate for each gas atom, with number density given by $[\mathrm{G_i}]$. The vdW rates are given later in table (4.2). In the case that relaxation is low the xenon nuclear spin polarisation will accumulate according to equation (2.13) and the polarisation will reach steady state as t tends infinity. Under this condition the terminal polarisation can be calculated as:

$$\lim_{t\to\infty} P_{\mathrm{Xe}} = \frac{\gamma_{\mathrm{SE}}}{\gamma_{\mathrm{SE}} + \Gamma}\langle P_{\mathrm{Rb}}(z, r)\rangle. \tag{2.15}$$

Alkali metals have a number of physical attributes that make them well suited to SEOP. Firstly, they have a single, weakly bound electron in their valence shells, which have spin $S = \frac{1}{2}$. Secondly, they have low melting points. In the case of rubidium, its melting point is 39.39 °C, which means it exists

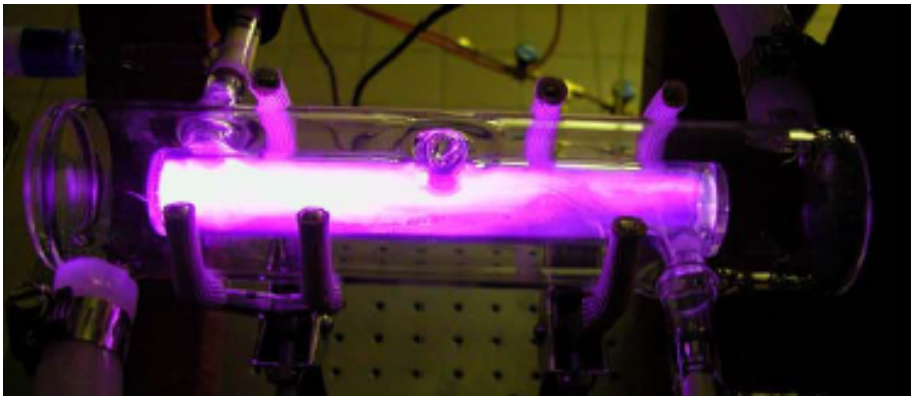

Figure 2.6: An unfiltered photograph of an optical pumping cell exhibiting bright violet emission which is characteristic of SEOP in the absence of nitrogen. Experimental parameters: 300 Torr Xe, 140 °C, 33 W incident laser. Reprinted from [48] with permission.

in the vapour phase at typical SEOP temperatures of 60-150 °C, facilitating photon absorption and spin-exchange. Finally, the wavelengths at which alkali metal electronic transitions occur are covered by commercially available high flux lasers [49]. For example, the rubidium D_1 transition, $5^2S_{\frac{1}{2}}$ occurs at 794.77 nm.

Nitrogen and helium are often added as buffer gases to the spin-exchange gas mixture. Nitrogen is diatomic and is therefore primarily added to facilitate the collisional mixing of the $m_J = +\frac{1}{2}$ and $m_J = -\frac{1}{2}$ sub-levels of the $2P_{\frac{1}{2}}$ excited Rb atoms. Without nitrogen present in the cell there is a high chance that the excited states will relax to the ground states via optical emission. Violet emission of the 421 nm 6P to 5S transition is shown as an example in figure 2.6 [48]. If fluorescence occurs it depolarises Rb atoms due to its omnidirectional and unpolarised nature. Helium was added to the gas mix in the original continuous-flow polarisers to pressure broaden the D_1 line of Rb, to increase the couple of the then broad and poorly matched pump laser lines. As laser technology has improved this role has become less important. It may be, however, that helium becomes significant in *stopped*-flow SEOP as ever

higher laser fluxes and xenon densities - which cause thermal issues - are used. Helium is 25 times more thermally conductive than xenon and arguments for its use in stopped-flow SEOP are presented throughout this thesis.

As well as I=1/2 ^{129}Xe, SEOP can be used for the hyperpolarisation of ^{3}He, ^{131}Xe, ^{83}Kr, and ^{21}Ne (with I=1/2, 3/2, 9/2 and 3/2 respectively). Each gas has differing properties which determine its utility and application. ^{3}He and ^{129}Xe, as spin $\frac{1}{2}$ nuclei, have enjoyed the most widespread and continued usage as the spin $\frac{1}{2}$ property results in reduced relaxation facilitating a long T_1. ^{3}He has long been used primarily as a neutron spin filter in nuclear physics neutron experiments [50, 51, 52, 53, 54], in studies of fundamental symmetries [55, 56], and later found application in lung imaging where it is well suited to structural imaging [57, 58, 59, 60] and ADC diffusion studies [61, 62] due to its high gyromagnetic ratio. ^{3}He was instrumental in the development of the hyperpolarised lung imaging field. Its use has become less common due to its limited availability and high cost [63].

In contrast to ^{3}He, ^{129}Xe is mildly soluble in blood and organic solvents and has a broad chemical shift range that makes it attractive for a number of applications including the study of porous materials [64], surface interactions [65], and in a variety of chemical, biophysical, and biomedical applications, including those involving cryptophane-based host systems and void-space imaging [10, 66, 67, 68, 69, 70]. There has been much progress in ^{129}Xe lung methods which are breifly reviewed at the end of this chapter, and also in the brain [71, 72], and blood [73].

The other noble gases ^{131}Xe, ^{83}Kr, and ^{21}Ne have been studied and utilised less extensively due either to low natural abundance and high cost, or due to their quadrupole nature which increases relaxation and results in an often prohibitively short T_1. For example, ^{21}Ne may have use as a navigational

gyroscope [74], and has been used in tests of CPT and Lorentz symmetries [75]. For ^{131}Xe, ^{83}Kr, the short relaxation has been harnessed as a form of contrast in the study of void spaces [76, 77, 78, 79, 80], including the lungs [81, 82].

2.4 Handling and Imaging of HPNGs: Relaxation and Imaging

Hyperpolarisation offers many advantages over thermal MRI. However, after a hyperpolarised signal is generated it must firstly be maintained long enough to perform the desired experiment. Further, for maximum efficiency consideration should be given to the use of the HP signal due to the non-renewable nature of the signal and the fact that each rf excitation uses a finite amount of the magnetisation.

Relaxation of HP xenon can be broken down into the intrinsic (Γ_i) and extrinsic (Γ_i) components [83]:

$$\mathrm{T}_1^{-1} = \Gamma_{\mathrm{it}} + \Gamma_{\mathrm{ip}} + \Gamma_{\mathrm{eo}} + \Gamma_{\mathrm{eg}} + \Gamma_{\mathrm{ew}} \tag{2.16}$$

where contributions to the intrinsic rate are due to (t)ransient Xe_2 dimers and (p)ersistent Xe_2 dimers, and extrinsic contributions are due to interactions with (o)xygen, diffusion through magnetic field (g)radients and (w)all collisions. The first three terms can be quantified by [84]:

$$\frac{1}{\mathrm{T}_1} = \frac{[\mathrm{Xe}]}{56.1\mathrm{h}} + \frac{1 + (3.65 \times 10^{-3})}{4.59\mathrm{h}(1 + r_{\mathrm{B}}\frac{[B]}{[\mathrm{Xe}]})} + 0.4\mathrm{s}^{-1}\mathrm{amg}^{-1} \times n_{\mathrm{O}_2} \tag{2.17}$$

where $\mathrm{r_B}$ is the persistent dimer breakup efficiency of a secondary gas B in the mixture relative to that of xenon, and n_{O_2} is the oxygen concentration in amagats. Wall coating methods - typically Surfacil - have been developed to counter these the effects of wall relaxation [11, 85, 22]. Relaxation can also

be brought about by diffusion through magnetic field gradients, and therefore care should be taken to ensure that fields used to produce or store the hyperpolarised gas are kept homogeneous [83]. As this term scales with γ, this point is most crucial for HP ^{3}He. HP gases should also be kept away from zero-field crossings due to the risk of rapid depolarisation [86].

Due to the non-Boltzmann nature of the polarisation enhancement, great care must be taken to preserve the available magnetisation of the hyperpolarised agent during measurements. Before excitation, the longitudinal magnetisation is in an enhanced, non-equilibrium state of polarisation. After excitation, the individual spins are unable to return to this enhanced state; they must return to thermal equilibrium, as governed by the Boltzmann distribution. In this 'post-excitation' state the magnetisation, and hence obtainable signal, is many orders of magnitude diminished when compared with the hyperpolarised state.

2.5 Clinical Progress in HPNG Lung MRI

Hyperpolarised noble gas MRI of the lungs has been in development for approximately 20 years. It began with the first HPNG image of excised mouse lungs by Albert *et al.* in 1994 using ^{129}Xe [2]. In 1995 Middleton *et al.* demonstrated ^{3}He MRI, publishing images of the lungs of dead guinea pigs [87]. The first HPNG human lung images were produced in 1996 by Macfall *et al.*, Bachert *et al.* and Ebert *et al.* using ^{3}He [88, 89, 57]. The first ^{129}Xe human lung image was produced one year later by Mugler *et al.* in 1997 [90]. Using ^{129}Xe gas polarised to approximately 2% they were able to obtain images and spectra originating from the lungs of 3 healthy volunteers using a Fast Low Angle SHot (FLASH) sequence. In the spectroscopy experiments, signal was sufficient to resolve the 3 dissolved phase peaks; one at 0 and two at $\sim$200 ppm.

The diagnostic potential of HPNGs was demonstrated when Kauczor *et al.* imaged the lungs of 5 healthy subjects and 5 patients with pulmonary disease, revealing ventilation defects [91]. Later in 1997 Kauzor *et al.* imaged the lungs of 12 COPD patients with laser polarised ^{3}He [92]. Recently, a comparison of ventillation imaging was performed in smokers with COPD with both ^{129}Xe and ^{3}He [93] and HPNG lung imaging has been demonstrated with 3 nuclei: HP helium and xenon with simultaneous co-registration with proton imaging [60].

In 2006 Woods *et al.* validated measurements of ADC values against histology in patents with emphysema [94]. Histological data from the paper can be seen in figure 2.7. In 2013, Ouriadov *et al.* used the ADC method to investigate lung morphological changes associated with COPD [95]. They used three different non-zero diffusion sensitisations (b-value = 12, 20 and 30 s/cm^2) in the lungs of four COPD patients and four healthy volunteers. The image data were fitted to a morphological model allowing extraction of the length scales associated with the terminal airways. These lengths were external radius R, internal radius r, mean airspace chord length L_m and depth of alveolar sleeve h. They found that longitudinal and transverse anisotropic diffusion coefficients, D_L and D_T, were both significantly increased (P=0.004) in the COPD subjects relative to the healthy subjects. There were significant differences in lung morphology between the COPD and healthy subjects, manifest in both L_m and h.

In 2002, Patz *et al.* demonstrated the ability to measure surface area per unit gas voulme in porous polyethene phantoms using Chemical Shift Saturation Recovery (CSSR) by comparison of MR results to confocal microscopy results of the mean chord length [96]. CSSR involves the selective saturation of the xenon magnetisation in the dissolved phase (i.e in the septal tissue) fol-

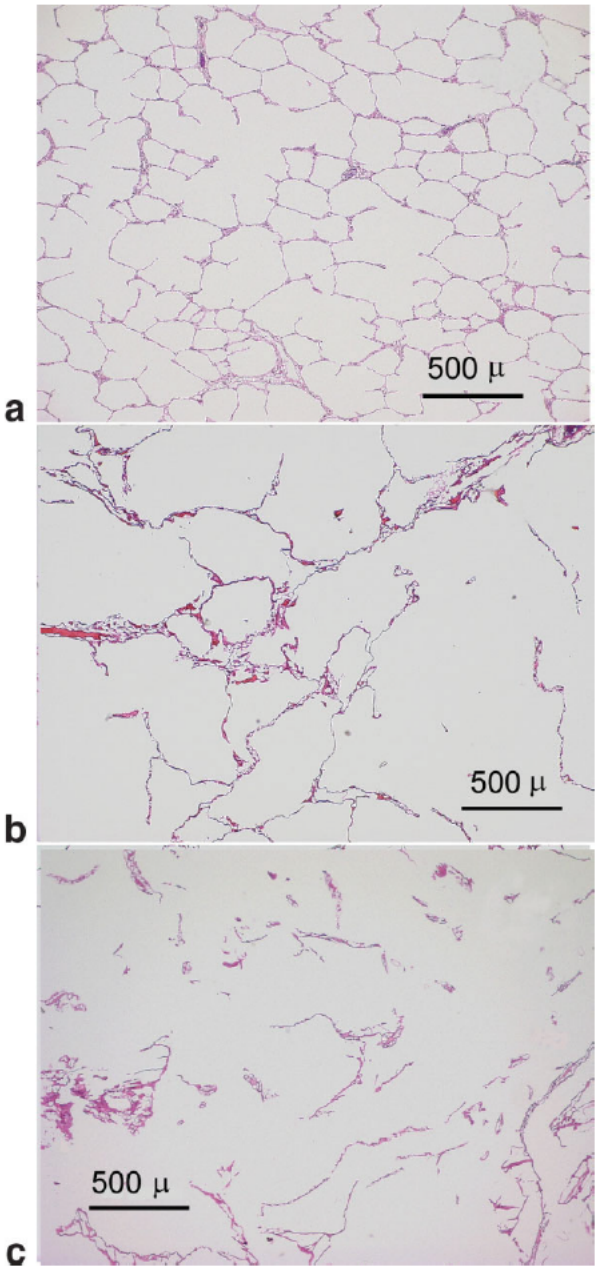

Figure 2.7: Histological slides for various degrees of emphysema. **a)** A nominally healthy lung, L_m = 0.027 cm, SA/V = 204 cm^{-1}, and ADC = 0.23 cm^2/s. **b)** A moderately diseased lung, L_m = 0.041 cm, SA/V = 134 cm^{-1}, and ADC = 0.42 cm^2/s. **c)** A severely diseased lung, L_m = 0.062 cm, SA/V = 89.5 cm^{-1}, and ADC = 0.63 cm^2/s. Reprinted from [94] with permission.

lowed by the measurement of its recovery by diffusion of hyperpolarised xenon from the alveolar spaces into the septal tissue. The method has been demonstrated by multiple groups in animals [97, 98, 99, 100]. Mansson *et al.* used CSSR to show that by solving the 1D diffusion equation and fitting their data to this model, one can obtain quantitive information about the thickness of both the parenchymal and blood compartments as well as information about perfusion [99]. Driehuys *et al.* showed that by observing the time delays in the appearance of the spectral peak associated with the blood, one can determine the thickness of the parenchymal layer separating the blood and gas components, providing a means of identifying thickening due to interstitial disease [100].

^{129}Xe can also provide a means by which to image the pulmonary vasculature. The approach that is typically adopted is to ventilate the lungs with ^{129}Xe and detect the growing blood signal as the xenon dissolves through the septal tissue, such as in CSSR or SBXTC [101]. Another approach would be to inject the contrast agent directly into the vasculature. This would circumvent the slow uptake of ^{129}Xe into the capillaries thus providing a greater reservoir of magnetisation in the blood pool which could be combined with further magnetization in the gas phase, introduced by ventilation, or imaged in the gas phase as it emerges from the pulmonary capillaries. This intravenous method has been demonstrated by Driehuys *et al.* in 2009 [102]. They refined the method further in 2012, demonstrating continuous extracorporeal (EC) infusion of ^{129}Xe [103]. The EC circuit allows for the continuous delivery of ^{129}Xe to the vasculature, and overcomes temporal and spatial constraints imposed by injection. They obtained diffusive gas exchange and pulmonary diffusion dependent 3D MR images with a nominal resolution of 2 x 2 x 2 mm^3, and presented and validated an analytical mass transport model of the ^{129}Xe signal

dynamics that incorporates both mass transport into the blood and longitudinal relaxation. The EC method should allow ^{129}Xe to be delivered to other parts of the body and make possible functional and molecular imaging that are not currently feasible with inhaled HP ^{129}Xe .

In 2010 Mugler *et al.* described a method by which to image ventilation and gas uptake within one imaging sequence, using an increased flip angle for the dissolved phase to account for the smaller amount of xenon in that phase. The experiment was conducted in 11 human subjects, 6 healthy, 3 with asthma, 2 with smoking induced COPD. They found that subjects with lung disease showed variations in gas uptake that differed from variations in ventilation suggesting that the method is sensitive to underlying pathological alterations of lung tissue or of local blood flow [104].

A number of models that describe gas-exchange and the uptake of xenon through the septal tissues have been presented by Mansson *et al.* in 2003 [99], Patz *et al.* in 2011 [105], and Chang (MOXE) in 2012 [106, 107]. The most recent model, MOXE, consists of two expressions and characterises the uptake of dissolved ^{129}Xe in the lung at two different resonant frequencies. Five pulmonary parameters critical to lung structure and function are incorporated into the model: the surface-area-to-volume ratio, the barrier-to-septum- ratio (ratio between the air-blood barrier thickness and the septal thickness), haematocrit (the extent to which red blood cells are oxygenated), gas-exchange time constant and pulmonary capillary transit time. Chang concluded that MOXE is sensitive to various functional and structural changes of the lung and that it will allow for screening for a variety of pulmonary diseases. Patz *et al.* measured surface-area-per-unit-gas-volume, S_A/V_{gas}, alveolar spetal thickness, h, and capillary transit time, T, in four healthy subjects, two subjects with mild interstitial lung disease (ILD) and two subjects with mild COPD. They found

that in the healthy subjects S_A/V_{gas} decreased with increasing lung volume while h and T remained relatively constant. For the ILD subjects, h was 36% and 97% larger than normal, signifying an increased gas/blood tissue barrier; S_A/V_{gas} and T were normal. In the COPD patients, S_A/V_{gas} values were elevated by 25%, signifying emphysematous septal surface loss, h and T were normal. The measurements were the first non-invasive, non-radiation based, quantitative measurements of h and T in patients with pulmonary disease.

Chapter 3

The N-XeUS Polariser

This chapter describes the N-XeUS polariser and its subsystems. The start of the chapter provides historical background by reviewing previous relevant polariser technology, including the first major research polariser, which was continuous-flow, and the two record-holding stopped-flow polarisers that preceded the N-XeUS polariser - XeUS and XeNA. This is followed by a description of each of the subsystems of the N-XeUS polariser including design, construction and calibration (where applicable). A prototype low-field NMR spectrometer which may later be installed on the polariser is also presented in this section. Next, all experimental methods associated with conducting SEOP on the polariser are described. Finally, three groups of results are presented 1) in-cell optimisations including a) ^{129}Xe magnetization and b) P_{Rb}, both as a function of gas mix and temperature and c) in-cell T_1 measurements 2) demonstration of imaging, including bag images created using HP-Xe generated with the N-XeUS polariser and measurements of the associated absolute polarisation values; 3) results of the prototype NMR spectrometer that was designed specifically for the N-XeUS polariser.

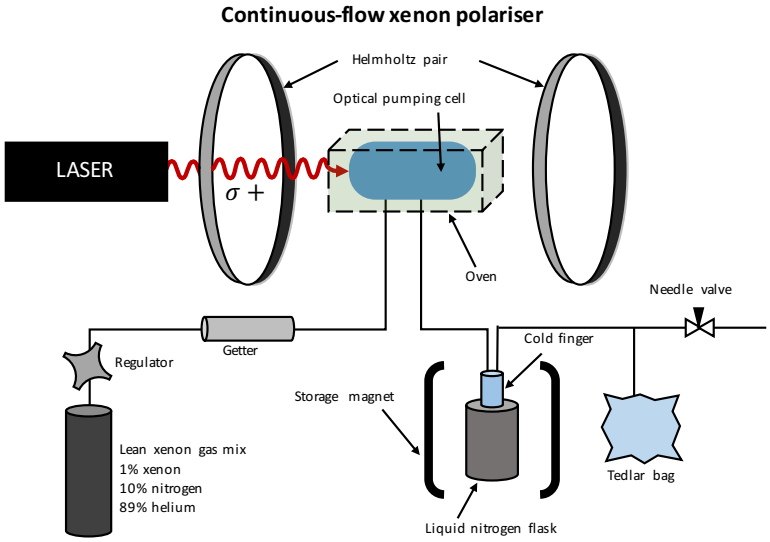

(a)

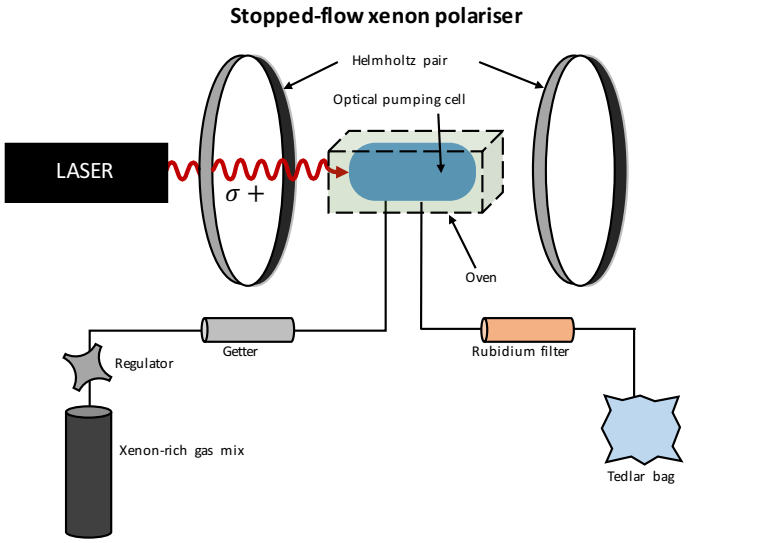

(b)

Figure 3.1: Schematic representations of a continuous-flow polariser (a) and a stopped-flow polariser (b). Both polarisers typically feature a laser, a magnetic field, and an optical cell enclosed within an oven. The most significant engineering differences are in gas handling (input to and from the cells) and in the separation of the xenon from the SEOP gas mixture.

3.1 Emergence of the Xenon-Rich Stopped-Flow Method

As covered in the previous chapter, the amount of signal that can be obtained in an MR experiment is proportional to the total magnetisation within the sample, which is in turn governed by the polarisation and volume of the sample. Historically, the major barrier to the widespread adoption of HP xenon imaging methods in the clinic has been the amount of highly polarised xenon that can be produced. The first published polariser design, by Driehuys *et al.* in 1996 [12], was capable of producing 1 litre quantities of 5% polarised xenon. This polariser was a continuous-flow style polariser, which means that xenon is exposed to polarised rubidium vapour for a short time as it transits through the optical cell and is separated from the gas mixture using a cryogenic cold finger (as shown in figure 3.1). Since 1996, further polariser designs have emerged with the advent of new technology, and a recent version of this polariser, which has since been developed into an advanced research prototype and deployed to a number of clinical research environments including the MIU here at Nottingham, typically produces 10% polarised xenon at a rate of 1 litre per hour (as shown later in figure 7.3(b)). It has been hypothesised by Freeman *et al.* [16] that with various design modifications, particularly to the optical cell design, the polariser should be capable of generating a polarisation of over$\sim$50% [17]. These modifications will be designed to suppress the formation of rubidium clusters within the SEOP cell that limit the maximum polarisation in a number of ways [16] and are discussed in greater detail in the next chapter. Some of these modifications have been incorporated by Polarean in their most recent release of their continuous-flow polariser the 9820. Polarization levels range over 35-45% depending on the volume and throughput

of produced xenon, typically at 1-3 L/h [108]. Figure 3.1 shows key design differences between continuous-flow and stopped-flow polarisers.

3.1.1 XeNA

The XeNA polariser [18, 19], developed by Nikolaou *et al.*, primarily aimed to address the issues of low polarisation and low production rate, while also striving to achieve a number of other design aims including ease of use (through automation), and ease of duplication (by being open source and constructed of primarily of 'off the shelf' components) but instead utilised the stopped-flow method. In stopped-flow SEOP, the gas mixture is held within the optical cell for the full duration of the SEOP process before being ejected into a bag for use in an experiment (3.1(b)). The reason for this shift in approach to polariser design, and indeed what enabled the shift, was the discovery of an unexpected inverse relationship between the temperature at which the peak xenon polarisations occurred for a given xenon density and the xenon density within the cell, where higher temperatures favoured lower xenon densities [23]. This relationship can be seen in panel (a) and its inset in figure 3.2.

It was a discovery made while conducting stopped-flow SEOP with newly developed volume holographic grating narrowed laser diode arrays (VHG LDAs) [23, 24, 25]. These VHG LDAs exhibit increased tunability due to the on-chip nature of the VHG and reduced the spectral width of the light by an order of magnitude compared with the previous generation of lasers ($\sim$3 nm to $\sim$0.3 nm). This is shown in figure 3.3. This provided a much greater coupling of the laser light to the D_1 transition of the rubidium, negating the need for high total pressure to pressure broaden the D_1 line to the width of the laser light. That is, an entirely unexplored SEOP regime at a reduced total pressure became accessible (2.5 ATM, as compared with the 10 ATM of the original

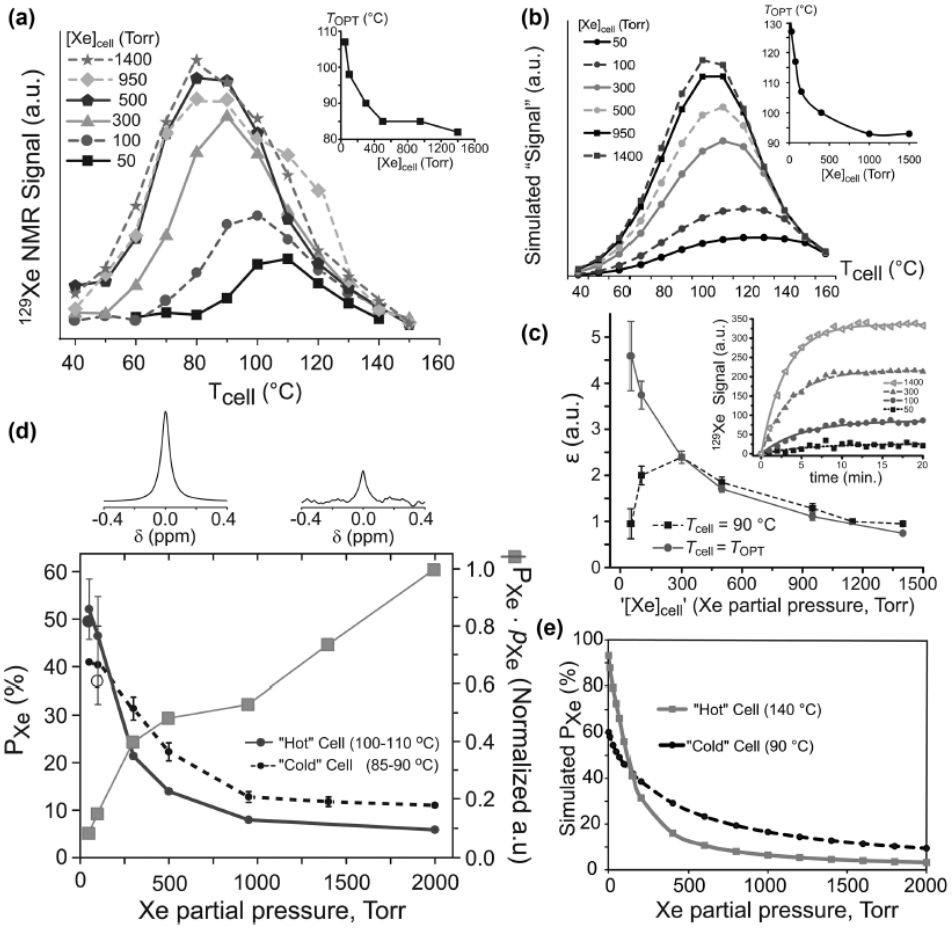

Figure 3.2: (a) NMR signal intensity (or magnetisation) of hyperpolarised ^{129}Xe as a function oven temperature and gas mix. (b) 2D simulation of the data in (a). The sub-plots in (a) and (b) show the inverse relationship between T_{opt} and the [Xe]. (c) efficiency factor as a function of [Xe] and temperature. Sub-plot shows the time-course build-up data from which the data in (c) was derived. (d) Further illustration of the optimal temperature as a function of [Xe] trend; polarisation per gas mix plotted at two temperatures (one high T, one low T, favouring low and high [Xe] mixes respectively). It also can be seen from this plot that although P_{Xe} decreases with increasing [Xe], magnetisation increases. (e) Simulation of (d). Figure reprinted from [46] with permission.

continuous-flow system). These experiments may have taken inspiration from Ruset *et al.* who employed a 5-fold broader laser (1.5 nm) and low pressures (500 torr, total) on their large scale continuous flow polariser to obtain, at the time, record levels of polarisation [13].

A particularly striking aspect of the results was the fact that the optimal polarisation at the higher xenon densities was significantly greater than expected; polarisation levelled off at a non-zero value with increasing density as opposed to falling to zero, in a manner that was inversely proportional to temperature (apparent in figures 3.2(c,d,e), reprinted from [46]). This was an important finding because it meant that although higher polarisations could be achieved at lower xenon densities, greater *magnetisation* could be achieved at higher xenon densities - where magnetisation is the product of polarisation and density (and the key quantity in increasing SNR in NMR and MRI experiments). This is illustrated in figure 3.2(d). Clearly the regime had excellent potential for application to bio-medical lung imaging and these findings formed the basis of the design concept for XeNA. Ongoing efforts of the group, particularly with the second polariser XeUS discussed next, have focused on further increasing polarisation at higher and higher densities.

It is possible that the inverse temperature dependence of the xenon trend described above was due to the increased rate of Rb spin destruction, Γ_{SD}, at higher xenon densities. The elevated Γ_{SD}- mediated by the Rb-Xe spin-rotation interaction - causes the AM to be more opaque, reducing the Rb polarisation, P_{Rb}, within the cell. By reducing the temperature of the cell as the xenon density increases, the density of the Rb reduces, increasing transmission of the light, which increases P_{Rb} again and thus the xenon polarisation P_{Xe}. The fact that the polarisation did not drop so steeply at higher xenon densities was shown to be linked to the fact that narrowed lasers were used: simulations

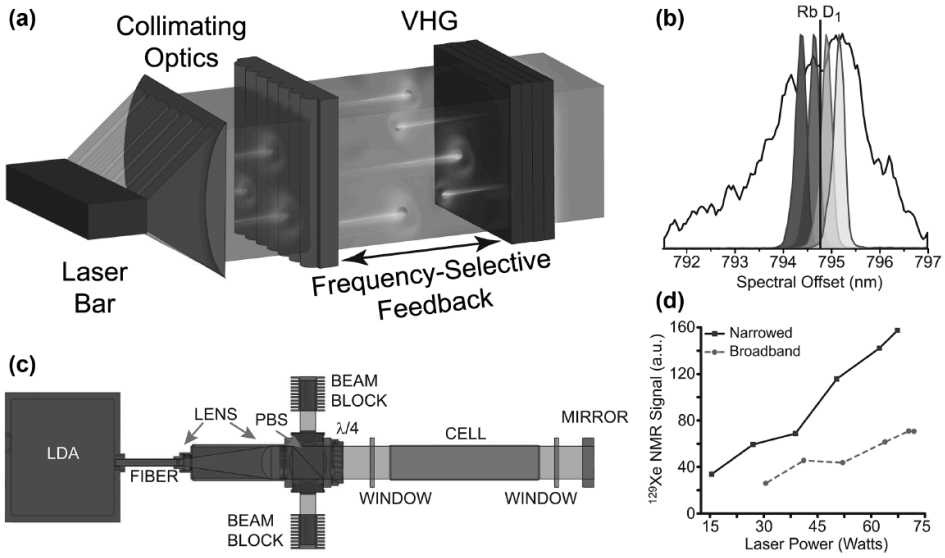

Figure 3.3: Overview of frequency-narrowed volume holographic grating (VHG) technology. (a) VHGs enable frequency-selective feedback to high precision. (b) spectral width and frequency tunability of a VHG laser plotted against the output of a non-VHG, broadband laser. (c) Optical arrangement in the XeNA stopped-flow polariser. The beam is collimated and circulary polarised before entering the optical cell. Beam blocks collect the beam after retro-reflection through the cell. (d) Resulting NMR signal intensity when pumping with otherwise equivalent VHG-narrowed and non-narrowed lasers. Reprinted from [46] with permission.

performed after the fact showed that narrowed lasers appear to be differentially beneficial at higher xenon densities [109]. These are discussed in greater detail in the next chapter.

The fact that higher polarisations at higher densities could be achieved allowed for major changes to be made to the continuous-flow design. The most significant of these being that gas mixtures with high xenon densities could be used, and this negated the need to cryogenically separate the xenon from the buffer gases. In a continuous-flow system, cryogenic separation of the xenon from the gas mix can be thought of as a simple distillation of the mixture and it is necessary because a typical gas mixture for a continuous-

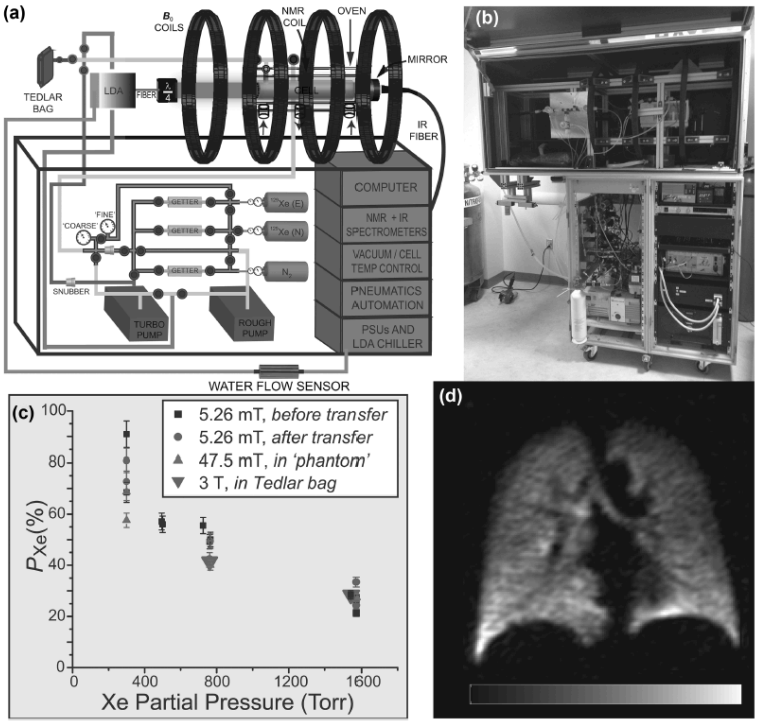

Figure 3.4: The XeNA polariser. (a) Schematic representation of key systems within the polariser. (b) Corresponding photograph. (c) XeNA polarisation as a function of gas mix and measured field both before and after transfer. A record of polarisation of 90% at 300 torr was obtained on XeNA. (d) HP-Xe lung image using gas produced with XeNA. The polariser is now installed at Women and Brighams Hospital, Boston, MA, where it is used to supply HP-Xe for such ventilation studies. Figure reproduced from [46] with permission.

flow system contains 1% Xe and 2% to 10% N_2, with the remainder as He. If the xenon were not separated the resulting concentration would be low. The cryogenic separation method takes advantage of the high melting point of xenon relative to the other gases in the mixture ($T^{\mathrm{Xe}}_{\mathrm{Boil}}$ = -111.8 °C, $T^{\mathrm{N_2}}_{\mathrm{Boil}}$ = -210 °C, $T^{\mathrm{He}}_{\mathrm{Boil}}$ = -272.2 °C). The result is such that when the gas mixture is flowed through a section of the outlet manifold that is submerged in liquid nitrogen (-195 °C, 77K), the xenon gas condenses to form xenon ice while the nitrogen and helium gases continue to flow through the outlet manifold and are released to atmosphere via the exhaust line. Figure 3.1 shows the cold-finger

on the continuous-flow polariser.

The cryo-collection method is an effective way of 'distilling' the xenon from initial gas mixture, but has some drawbacks. Polarisation is lost during the storage period as the xenon gas is accumulated, and further losses occur during the phase transition from solid to gas [12]. The xenon-rich stopped-flow method is a compelling alternative method because it negates the need for a coldfinger because the xenon is already present in a high concentration. A further benefit of removing the cryogenic collection process is that the entire polarisation process becomes simpler and hence easier to automate, the benefits of which should not be understated.

In a continuous-flow polariser, a trade-off exists between gas flow rate and storage time for a given volume of polarised gas. A greater flow rate means the gas spends less time being in contact with optically pumped rubidium vapours but Xe ice will be quickly accumulated. A slow flow rate means that the xenon has a greater residence time within the optical cell and will be more highly polarised but it will take longer to accumulate the same volume of Xe ice. In this time the T_1 of the xenon ice becomes a factor [110, 12, 111]. Further loses occur in the phase transition from ice to gas where the T_1 can be as short as 6 seconds [111].

The XeNA polariser, the first stopped-flow polariser developed by the consortium (figure 3.4), operates at a pressure of ∼2000 torr and is capable of producing polarisations of ∼90%, ∼57%, ∼50% and ∼30% for xenon densities of ∼300, ∼500, ∼760 and ∼1570 torr at the rate of 1 litre per hour. These results are illustrated in figure 3.4(c). XeNA is currently housed at Brigham and Women's hospital, producing HP xenon for an ongoing COPD study.

XeNA featured a (i) 200 W frequency-narrowed LDA, (ii) a vacuum pump system, (iii) NMR and IR spectrometers reporting on xenon polarisation and

laser light transmittance, (iv) a gas-handling manifold for optical cell loading and ejection (v) a B_0 field provided by four 24 inch (inner diameter) coils, (vi) a controller box, and (vii) an oven containing the optical cell with a ∼0.5 L volume. The oven temperature was maintained by heaters and a cold gas supply from a self-pressurised liquid nitrogen dewar. Although XeNA has the ability to cryo-collect HP xenon, the combinations of such high Xe fractions and polarisations made cryo-collection unnecessary. While XeNA was controlled primarily via a GUI, some operations were not automated, including those involving the liquid N_2 dewar, measurement of the xenon polarisation, and LDA adjustment, and general operation of the polariser was divided into several steps instead of a single 'push-button' operation. The engineering aspects of the polarsier are detailed extensively in [19] and the accompanying supplementary information.

3.1.2 XeUS

The second generation polariser produced by the consortium, XeUS (shown in figure 3.5), refined a number of the design features developed on XeNA, and took the idea of automation, high performance and ease of user maintenance further. The gas manifold is simpler and uses a lesser number of pneumatic valves which 1) increases the simplicity of both the design and the gas handling manoeuvres (e.g. cell loading and ejection of the hyperpolarised gas into a bag) and 2) reduces the risk of leaks (as most leaks occur at the joints). It uses only one cylinder of premixed xenon and nitrogen (and only one gas purifier). This modification increases simplicity at the cost of reducing flexibility when compared with the XeNA polariser. However, this gain simplicity and constraint to use only one gas mixture is well suited to the needs of a clinical study, where bag-to-bag changes in gas mix are unlikely to be needed and

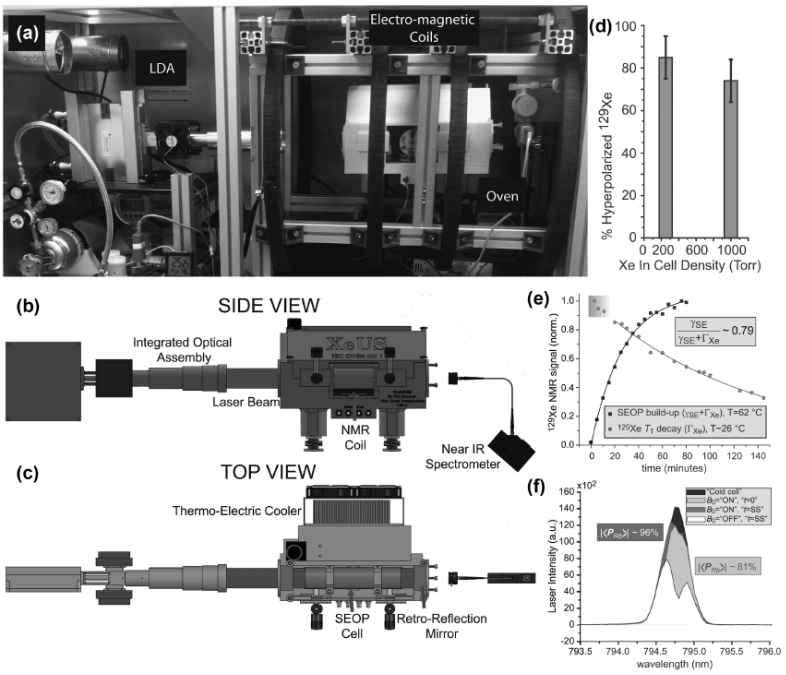

Figure 3.5: The XeUS polariser. (a) Photograph of subsystems within the upper chassis including the laser, B_0 field and oven. (b,c) Schematic of the optical assembly on the XeUS polariser from the side and above respectively. (d) Polarisation performance as a function of [Xe]. (e) Time course build-up and T_1 decay data. (f) Absorption spectra used here to calculate P_{Rb}=81% using a method described later in section 3.3.10. Reproduced from [46] with permission.

reproducibility will be a high priority. The dead volume in the gas lines was also reduced in XeUS and a flow snubber was required for XeNA to prevent catastrophic shock within the optical cell during gas loading (caused by rapid exposure of the cell to high pressure). This was not required on XeUS because the 1/8 inch lines sufficiently impede the gas flow from the gas cylinder to the optical cell.

XeUS has a 3D printed oven (shown later in figure 3.11) much like XeNA, but the unique opportunities offered by 3D printing are better harnessed in XeUS [21]. For example, the optical cell is inherently optically aligned with the windows and the retro reflector, eliminating troublesome alignment and greatly simplifying the fabrication process; an identical duplicate of the oven

can be produced within hours by simply re-printing the CAD image of the oven. Moreover, the oven is designed to fit the thermoelectric cooler precisely (responsible for the heating and cooling of the optical cell), and the mass of material and leg positions are distributed such that the entire assembly balances unaided. Where possible, the polycarbonate plastic walls of the oven were made thick to increase insulation. Where the walls were thin, additional insulation was added to the system. Effective thermal management of the optical cell is important for a number of reasons 1) control of the initial Rb density 2) prevention of rubidium runaway, and 3) to permit efficient thermal manoeuvres (heating and cooling of the cell) which have the potential to be a limiting factor in the duty cycle of the production process.

A thermo-electric cooler (TEC) is used on XeUS - the first time this method has been employed in a xenon polariser for the purpose of oven temperature management. This makes the system far more portable - a further design aim of the polariser - as a hefty nitrogen dewar containing nitrogen vapour is no longer needed to cool the oven (as was the case with XeNA), and a compressed air line is not required for a force-air oven to heat the optical cell (as was the case with XeNA). These thermal management issues - particularly with respect to increasing the operational duty cycle - are unique to stopped-flow polarisers, as continuous-flow polarisers require that only the optical pumping cell is heated and maintained at temperature; cooling of the hyperpolarised gas in preparation for patient administration happens as a by-product of cryogenically storing the gas and therefore there are no lags in production due to thermal manoeuvres of the SEOP oven.

The cooling action of the cold finger in a continuous-flow system also aids the removal of Rb vapour in the gas phase. On both XeNA and XeUS (and N-XeUS, discussed next), a paediatric filter is used to remove any residual rubid-

ium vapour from the hyperpolarised gas, the number density of which is orders of magnitude lower than what would be found in a continuous-flow polariser due to the lower operating temperatures favoured in xenon-rich stopped-flow SEOP.

Realisation of a fully automated system was a key design aim for XeUS. Building on the progress made with XeNA which was partially automated, software was developed for XeUS that consists of a Graphical User Interface (GUI), and the main code that triggers changes in the hardware. Arduino micro-controllers were chosen as the processor for the polariser and the interface was developed in Processing. The GUI allows the user to communicate with and control the various subsystems of the polariser, such as the TEC oven, the laser, and B_0-field power supplies, as well as the valves of the gas manifold. The automation allows the user to initiate the entire SEOP experiment at the press of a button. The software will then begin the process, take measurements from the various sensors to determine the state of the system and modify the experimental parameters accordingly and repeatedly until the terminal equilibrium is reached, or the specified polarisation level is obtained.

In 2014 the consortium published results of a systematic, multiparameter study of Rb/Xe SEOP on XeUS. In-cell P_{Xe} values of 95±9%, 73±4%, 60±2%, 41±1% and 31±1% at 275, 515, 1000, 1500 and 2000 torr Xe were achieved and subsequently validated with low-field MRI at 47.5 mT after ejection [20]. The results of this study are shown in chapter 4 (in figure 4.9) where they are used in the validation of the standard model of SEOP in the xenon-rich stopped-flow regime.

3.2 N-XeUS: The XeUS Polariser at Nottingham

In the same spirit that improvements were made on XeUS relative to XeNA, development of the N-XeUS polariser (the XeUS polariser at Nottingham) was used as an opportunity to make changes and improvements to the XeUS polariser design. These modifications aimed to improve 1) the clinical readiness of the design, 2) the ease of use, and 3) affordability. The modifications that were implemented include:

1. Introduction of nitrogen fill/purge capability
2. Introduction of a check valve on the inlet manifold
3. Change in vacuum protocol (that enabled the removal of the turbomolecular vacuum pump)
4. Change from a 4 coil B_0 field to a 3 coil configuration
5. Development of a low-cost, low-field (1-100 kHz) NMR spectrometer

The addition of a second gas cylinder containing dry N_2 gas means that it is possible to clean and prepare the gas lines of both the inlet and outlet manifolds without wasting Xe gas. This is especially important when isotopically enriched Xe gas mixtures are employed, which can cost up to £150 per litre at STP, as would be the case when the polariser is in full clinical operation. Moreover, where a fill/purge approach to preparing gas lines is adopted it also opens the possibility that only a rotary pump is required to adequately dilute the contamination within the gas lines (to sub 10 ppm O_2 levels) - as opposed to a combination of rotary rough pump with a backed turbomolecular pump. Elimination of the turbomolecular pump from the polariser constitutes a significant saving in cost, space, heat and power load, but also time, as it would no longer be necessary to reach 'hard' a vacuum using the turbo pump

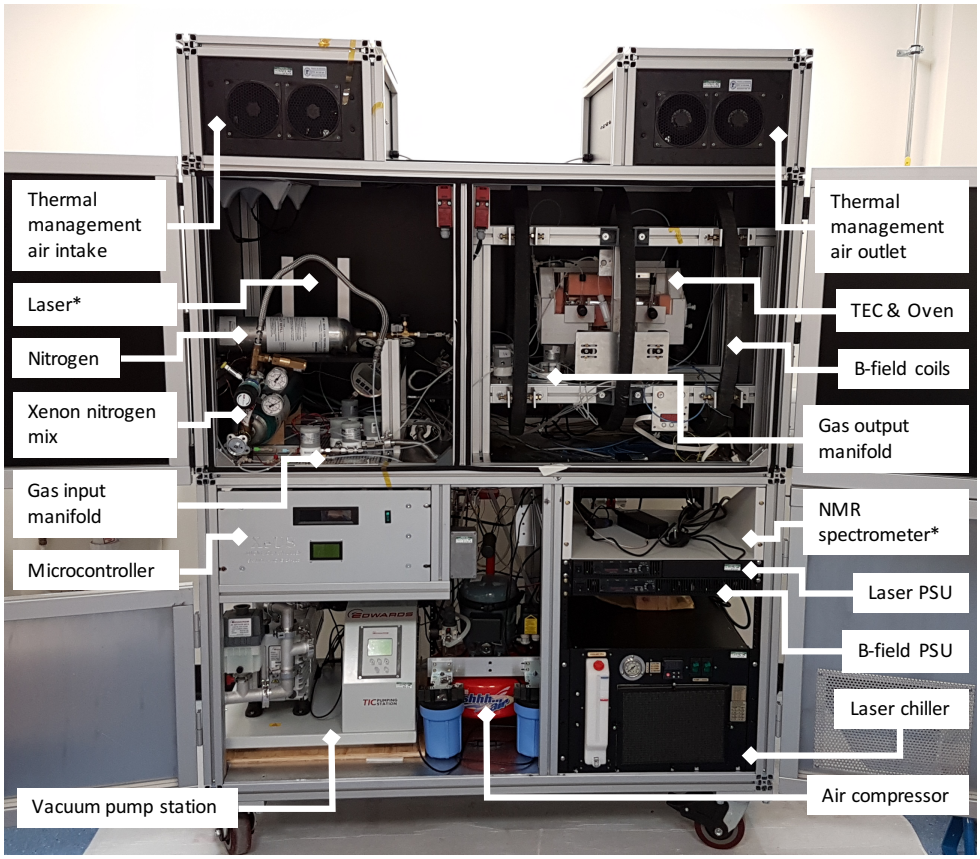

Figure 3.6: The N-XeUS polariser. Labels indicate key polariser subsystems including: (1) the chassis, (2) the B_0 field, (3) the oven and thermo-electric cooler, (4) the pump laser and associated optics, (5) the gas manifold, optical cells and Tedlar bags, (6) the NMR spectrometer, (7) the micro-controller and (8) thermal management system. '*' markers indicate items not present at the time the photograph was taken.

(which can take several minutes); the roughing vacuum would suffice before filling with nitrogen.

The inclusion of the check valve was made possible by the addition of the nitrogen cylinder. The check valve has two purposes. Firstly, when the Xe pre-mix cylinder is changed, it prevents in-flow of atmospheric oxygen into the inlet manifold by flowing nitrogen gas out of the xenon inlet, reducing the incidence of contamination within the polariser. Secondly, it is a fail-safe feature. In a severe failure mode where a significant leak occurs on the inlet manifold (which is normally held at ∼2000 torr pressure by the regulator of the

Xe pre-mix cylinder) the contents of the Xe cylinder will leak to atmosphere. If this occurs the check valve will open as the pressure drops, maintaining a positive pressure within the system until it too runs out, thus providing more time to resolve the issue. It is essential to avoid inward leaks, because the atmospheric oxygen will react exothermically with the zeolite material of the gas purifier, destroying the purifier.

The change from a 4 coil B_0 field to a 3 coil design has two major benefits. Firstly, driving one less coil reduces the power load and subsequent heat load. This is a benefit because effective thermal management is crucial in xenon-rich stopped-flow SEOP. Second, from a practical standpoint, having one less coil permits greater access to the optical cell and oven assembly during cell loading and un-loading, improving ease-of-use. The 3 coil design was implemented with little loss to homogeneity relative to the 4 coil design as implemented on XeUS.

The NMR spectrometer was developed because it was identified as an aspect of the polariser where the cost could be readily reduced: The spectrometer currently employed by XeUS is a Magritek Kea. While it serves its intended purpose of in-situ polimetry, it was expensive and contains many redundant features. Development of a purpose made spectrometer has the benefit of reducing cost while tailoring functionality. In the case of the XeUS series of polarisers where there are a number of subsystems operating in parallel, ease of integration is valuable and a custom system has more potential to better meet those needs.

3.2.1 Subsystem Overview

The N-XeUS polariser is comprised of many parts which can be broken down and grouped into a number of categories or subsystems. These include (1) the chassis, (2) the B_0 field, (3) the oven and thermo-electric cooler, (4) the

pump laser and associated optics, (5) the gas manifold, optical cells and Tedlar bags, (6) the NMR spectrometer, (7) the micro-controller and (8) thermal management system. The subsequent sections give an overview of the purpose, operation and installation of these subsystems. The prototype low-field NMR spectrometer is also presented in this section.

3.2.2 Chassis

The chassis is of (non-magnetic) aluminium construction and supplied by Minitek. It was designed by the Vanderbilt team using SolidWorks design software. The dimensions are such that it can easily be manoeuvred through doors: 54 inches long x 32 inches wide x 69 inches high. It provides a housing and mounting points for all of the other components and optically encloses the system such that the polariser can be operated as a class 1 laser device i.e. with no need for laser goggles.

3.2.3 B_0-field

The B_0 field is needed to break the degeneracy of the rotational quantum states to enable selective optical pumping of the Rb sub-levels. It is also required for NMR measurements of the Xe magnetisation. In order to minimise T_1 to improve the maximum possible polarisation and lifetime of the hyperpolarised state, and to minimise T_2^* decay to maximise the SNR of NMR measurements, the B_0 field must optimised for homogeneity. In order to do this the copper coils were carefully designed and adjusted.

The B_0 field of XeUS is produced by 4 wound coils of equal inner diameter positioned in a barker configuration (visible in figure 3.5(a)). This configuration was chosen because it allowed for an adequately homogeneous field to be produced while keeping the overall dimensions of the polariser small enough

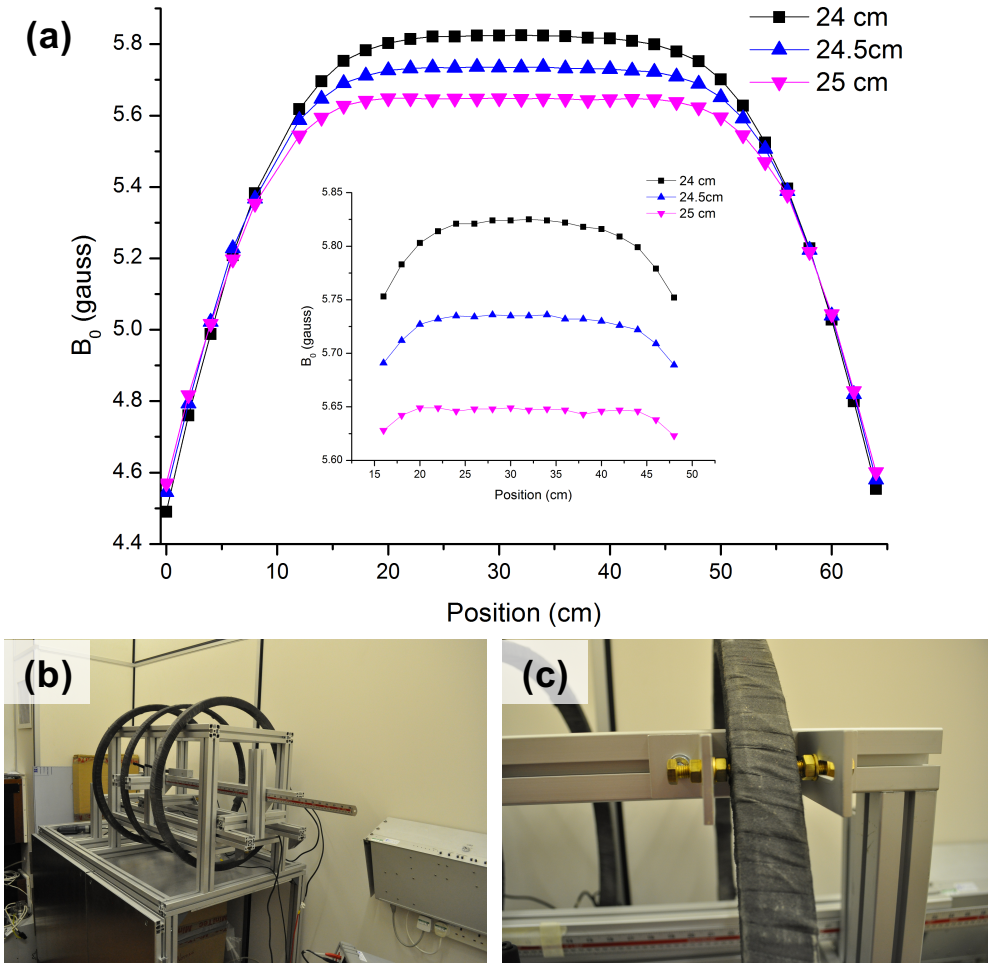

Figure 3.7: Installation and initial alignment of B_0 coils on N-XeUS. (a) B_0 as a function of coil spacing. B_0 was measured at spacings of 24, 24.5 and 25 cm. (b) Photograph of the B_0 coils mounted on the N-XeUS chassis also showing frame used for B_0 measurements. (c) Nuts that enable fine adjustment of the coil positions.

such that it can be manoeuvred with relative ease through doorways and corridors with no need for disassembly.

On the N-XeUS polariser a 3 coil design was adopted (visible in figures 3.7(b,c)). This had the benefit of allowing more space between the coils for the operator to place the optical cell within the oven during cell loading while not losing significant homogeneity across the length of the optical cell. The coil dimensions can be seen in table 3.1.

The chassis was partially disassembled in order to mount the 3 coils. Spacing was determined by a calculation in Matlab which minimised the standard deviation of the field over the length of the optical cell (25 cm) and yielded an optimal coil spacing of 24.5 cm. A frame was constructed to enable discrete measurements of the z axis B_0 were made at 1 cm intervals using a 3-plane Bartington fluxgate magnetometer. Figures 3.7(a) and (b) show the frame and the B_0 field z-axis measurements as a function of coil spacing.

After a first-order positioning of the coils the homogeneity of the B_0 field was further optimised by maximising the length of FID from a HP ^{129}Xe signal. A HP signal was used as it can be acquired in a single scan. The positions of the outer coils were adjusted relative to the centre coil to sub-mm accuracy using the adjustment nuts in figure 3.7(c), finely changing the B_0 field. As the homogeneity increased, the T_2^* decay of the Xe reduced, increasing the length of the FID. Using this method the FWHM of the NMR magnitude spectrum was reduced from $\sim$50Hz to $\sim$10Hz as shown in figure 3.8(a).

A Hall probe, with a 10-fold greater dynamic range than the Bartington fluxgate magnetometer, was used to determine the B_0 field amplitude as a function of current. Measurements of the field were recorded in both directions along the z-axis of the polariser. The B_0 field is powered with a Sorensen XG 80-10.5 PSU. COM ports on the rear enable the PSU to be interfaced with and

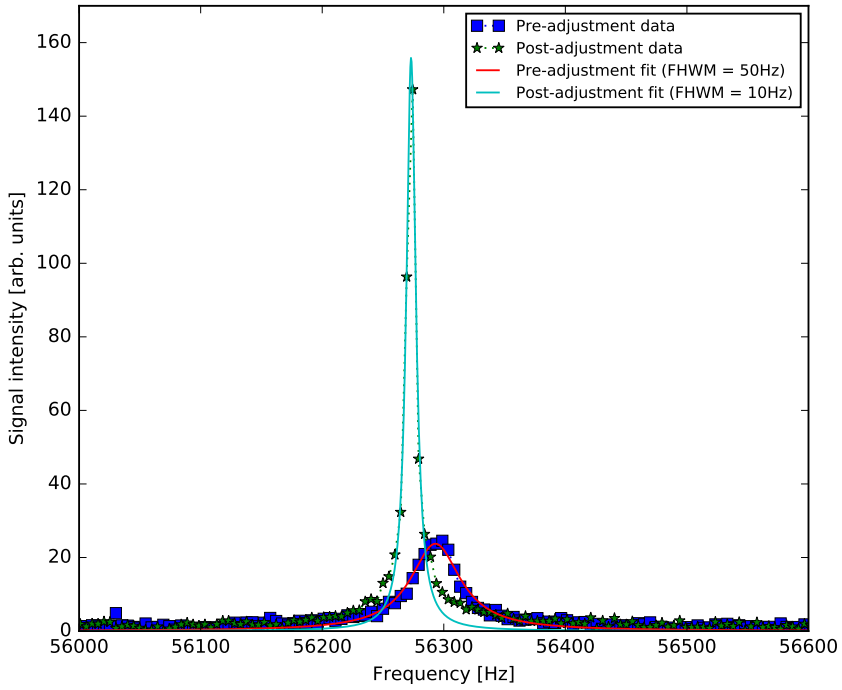

(a)

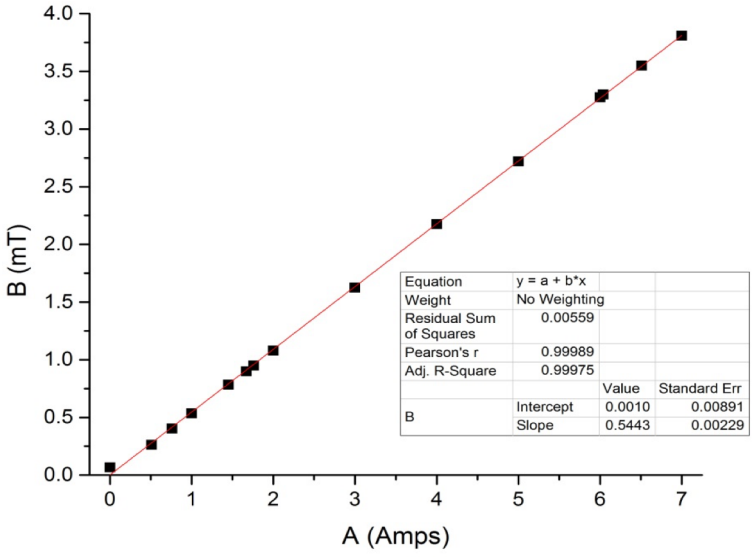

(b)

Figure 3.8: a) Lorentzian fits to HP-Xe NMR spectra pre- and post- B_0 coil adjustment using the FID lengthening method. b) N-XeUS B_0 as a function of driving current.

Coil	Coil 1	Coil 2	Coil 3
Number of turns N	179	95	179
Inductance L [mH]	35	18	34
Resistance R [Ω]	1.6	1	1.7

Table 3.1: Parameters of the 3-coil N-XeUS B_0 field.

thus manipulated by the GUI. Specifications of the N-XeUS 3 coil arrangement can be seen in table 3.1. The field strength at the centre of the coils as a function of PSU driving current can be seen in figure 3.8(b).

3.2.4 Laser and Optics

The N-XeUS polariser employs a 6 bar ∼150 W LDA supplied by QPC Lasers. The spectral width is ∼0.3 nm which is narrowed by an on-chip VHG. During the development of XeUS an optical train was developed in collaboration with QPC Lasers that can be mounted directly onto the front of the laser. After light emerges from the LDA via a short polarisation preserving optical fibre, the optical train broadens the beam to 2 inches and performs collimation. This is followed by circular polarisation using a polarisation beam splitting cube (PBS) that rejects the s-polarised light (∼10% of the light) by reflecting it 90 ° into a beam dump. The main p-polarised beam is then directed at the optical cell. The combination of the on-chip grating and the single-piece optical train means that alignment and adjustment of the optics is much simpler relative to older littrow based configurations [112] and the system is more robust against knocks to the polariser.

The beam path is such that it emerges from the optical train, enters the oven first through an AR coated window, enters the front of the optical cell, exits the back of the optical cell and is then retro-reflected back again via a retro-reflecting mirror (Thorlabs) which is ∼99% efficient. The reflected beam is directed to a beam dump via the PBS within the optical train. The beam

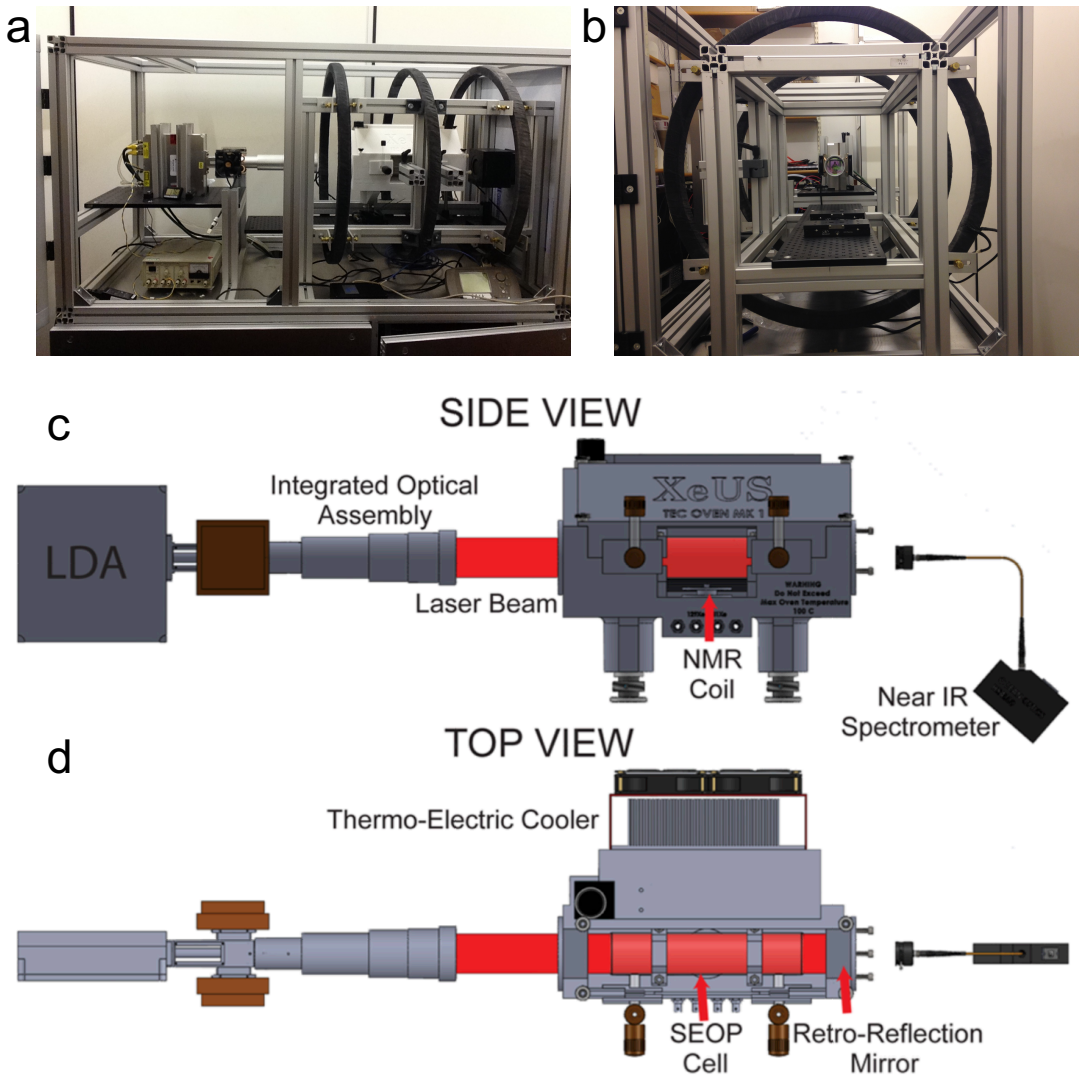

Figure 3.9: The Ultra 500 laser mounted on the N-XeUS polariser (a,b) Photos of the laser taken along the z-axis after alignment with the B_0 field. (c, d) schematic impression of the co-aligned laser, optical assembly, oven, optical cell and retro-reflector from the side and above respectively. Both show the placement of the IR spectrometer relative to the optical cell and laser. (c) and (d) reproduced from [20] with permission.

dumps are cooled with mounted heat sinks and fans. A fibre optic coupled to an Ocean Optics HR4000 IR spectrometer is situated on the far side of the retro-reflector and used to monitor the laser output and profile. The optical pathway and placement of the IR spectrometer can be seen in figure 3.9, as can photographs of the laser co-aligned to the oven (a) and the z-axis of the B_0 field before the oven was installed (b).

The laser module is powered by a Sorensen XG 20-84 PSU and chilled by a KO concepts 600 W water chiller. A thermistor within the laser module allows for direct monitoring of the LDA temperature. Throughout SEOP experiments the laser was driven at 52 amps. The output of the laser as a function of driving current and the spectral tunability as a function of temperature are shown in figures 3.10(a) and (b) respectively.

For optimal SEOP, the laser must be aligned to the centre of the field. This was done by adjusting the position of the laser such that the aiming beam co-aligned with the spatial centres of the B_0 coils. The oven was then adjusted to the beam using the stems and Newport lateral fine adjusters, visible in 3.9(c), such that the cell, when loaded into the oven, would fall perfectly co-aligned to the z-axis of the B_0 field.

Due to differences in the construction of the laser diode arrays on XeUS and N-XeUS the range of laser powers that can be explored N-XeUS is more limited (i.e. to the maximum available power only). Briefly, the laser on the original XeUS system contains 8 stacked diodes and the N-XeUS laser contains 6 stacked diodes. The output of the N-XeUS laser is therefore slightly less than that of the XeUS laser (in spite being slightly more efficient) but crucially, it can not be run at less than full power without overheating the diodes. i.e. using less than 52 A of driving current results in an elevated LDA temperature which quickly exceeds the safe temperature for the LDA. (T_{LDA}=32.5 °C at 52 A

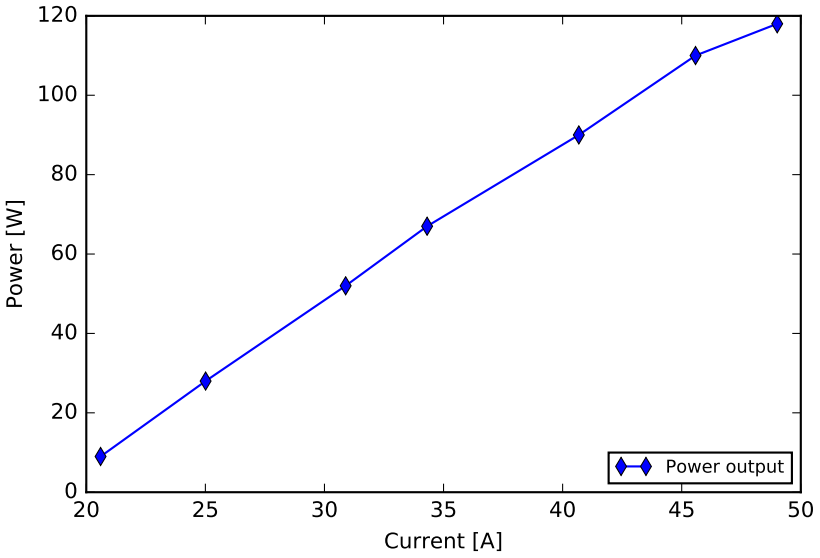

(a)

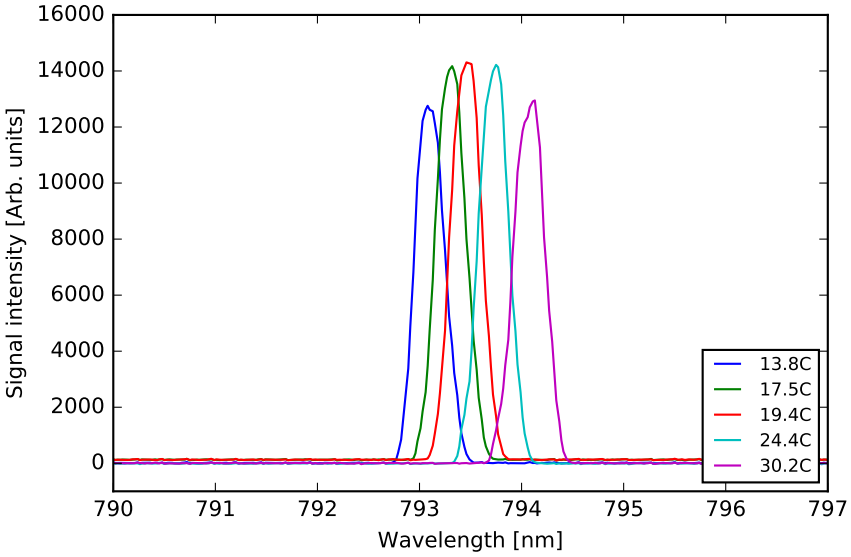

(b)

Figure 3.10: a) Ultra 500 laser power output as a function of current. b) Spectral tunability of the Ultra 500 laser as a function of temperature.

driving current. T_{LDA} should not exceed 35.0 °C). This has the implication that SEOP as a function of incident power is not possible on N-XeUS as was the case with XeUS.

3.2.5 Oven

The oven of the polariser is a key subsystem. Its role is to maintain thermal control of the optical cell during experiments, and to bring the cell up to and down from operational temperature at the commencement and conclusion of SEOP experiments. There are two major components in the oven subsystem: 1) the 3D printed polycarbonate body, and 2) the thermo electric cooler (TEC). The fact that the body of the oven is 3D printed has a number of benefits: it is easy to develop during the prototyping stage, requires minimal work to finalise and install, and minimal alignment of optics/cells is required as the cell mounts and optical windows are inherently co-aligned from the point of manufacture (best visualised in figures 3.11(a,b,c,d)). It also facilites the incorporation of the many instruments necessary to conduct and monitor SEOP experiments; the NMR circuit, the ∼0.3 nm narrowed 150 W laser source, in-situ high resolution IR spectrometry, the TEC, the rotary blower (which thermally couples the TEC to the optical cell), the retroreflecting optics, and the opto-mechanical alignment system [21]. The material used to make the XeUS oven is polycarbonate, and has high heat deflection and glass transition temperatures at 138 °C and 161 °C respectively, both of which are adequate for stopped-flow SEOP [21].

The oven is heated and cooled by a thermoelectric cooler (TEC) unit. This method negates the need for liquid nitrogen or permanent plumbing for a forced air oven and facilitates usability by enabling the system to be operated using purely mains power. The heating power is distributed within the oven by a

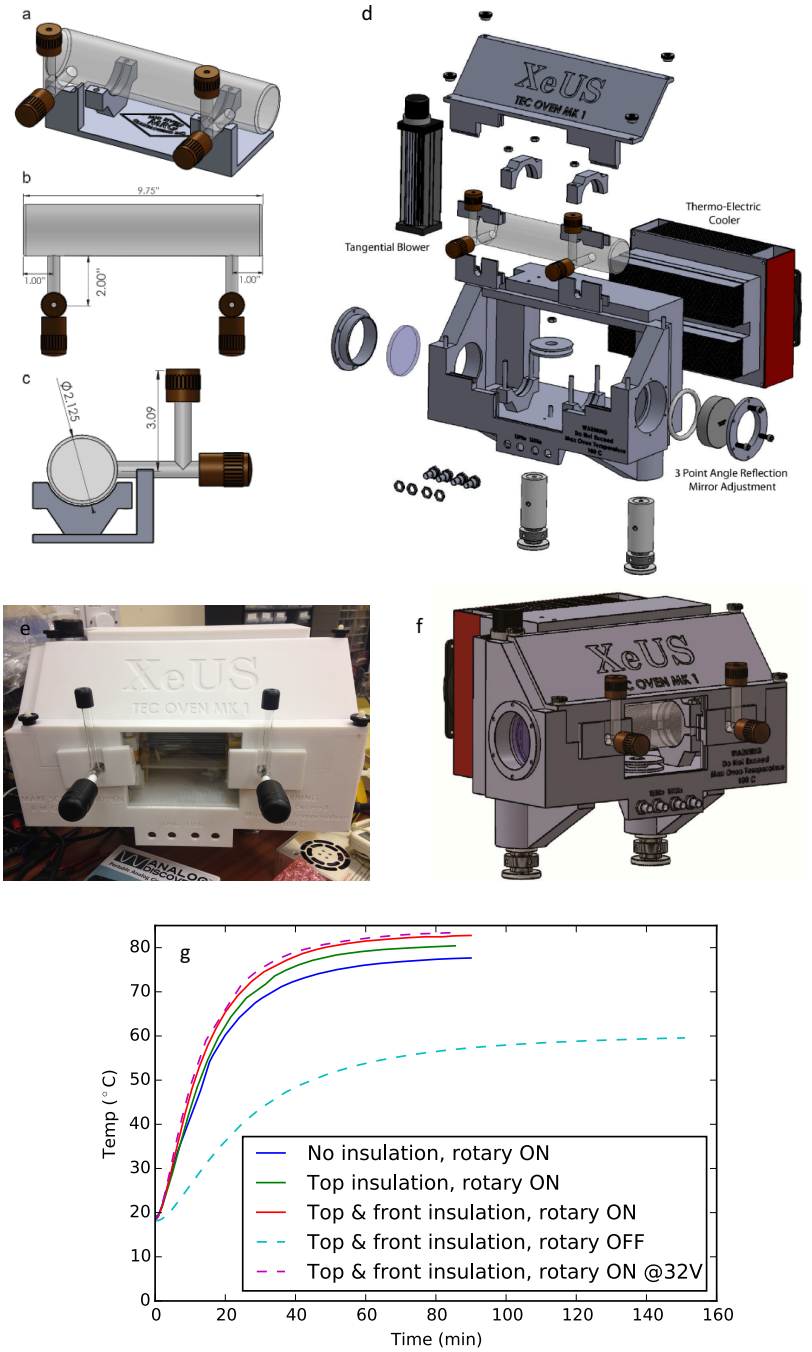

Figure 3.11: Summary figure of the XeUS and N-XeUS optical cells and oven. (a,b,c) Geometry of the the XeUS and N-XeUS optical cells. (c) Shows how the cells sit within a custom 3D printed saddle. (d) Exploded schematic of the 3D printed oven and TEC unit. (e) Photograph of the assembled 3D oven with optical cell in place. (f) Corresponding CAD drawing. (g) Performance of the TEC unit with increasing amounts of insulation added (blue, green, red lines) and in the presence and absence of the rotary blower (dashed lines). The temperature set point was 80 °C in all cases. (a),(b),(c) and (d) reproduced from the SI of [21] with permission. (f) Reproduced from the main text with permission.

rotary blower placed at the corner of the oven. The rotary blower circulates the air within the oven, moving actively heated (or cooled) air from the immediate vicinity of the TEC to the optical cell and back again. In order to improve the thermal properties of the oven, i.e. to increase the rate of active heating or cooling by the TEC, insulation was added. Figure 3.11(g) shows the cumulative affect of adding insulation (red, blue, green solid lines). Also illustrated is the impact of the rotary blower. The light blue dashed line shows the TEC heater operating with no power supplied to the rotary blower. When the rotary blower is not engaged, a substantial lag in heating can be observed, furthermore, the terminal temperature is significantly lower than the setpoint. The target temperature was the same in all experiments: 80 °C, and the thermocouple was attached in all experiments to the middle of the optical cell.

Power must be cut to the oven when NMR acquisitions are made due to spurious noise caused by the TEC heating elements and the motor of the rotary blower which are located close to the NMR coil. Blanking is performed by the micro-controller when acquisitions are triggered using the GUI.

3.2.6 Gas Manifold

The gas manifold is used to load Xe gas into the optical cell from the gas cylinder, and to eject polarised gas from the optical cell into the Tedlar bags for patient administration. It has an upstream (of the optical cell) section, a down stream section, and sections used for the preparation and cleaning of the gas lines: the N_2 line and the vacuum pump systems.

The manifold comprises a mixture of Swagelok, VCR, teflon and KF plumbing standards. Diameters are kept large in the lower manifold immediately above the rotary pump to facilitate a fast pump-down time, and small diameter 1/8 inch lines are used on the Xe path to minimise waste. Pneumatic values

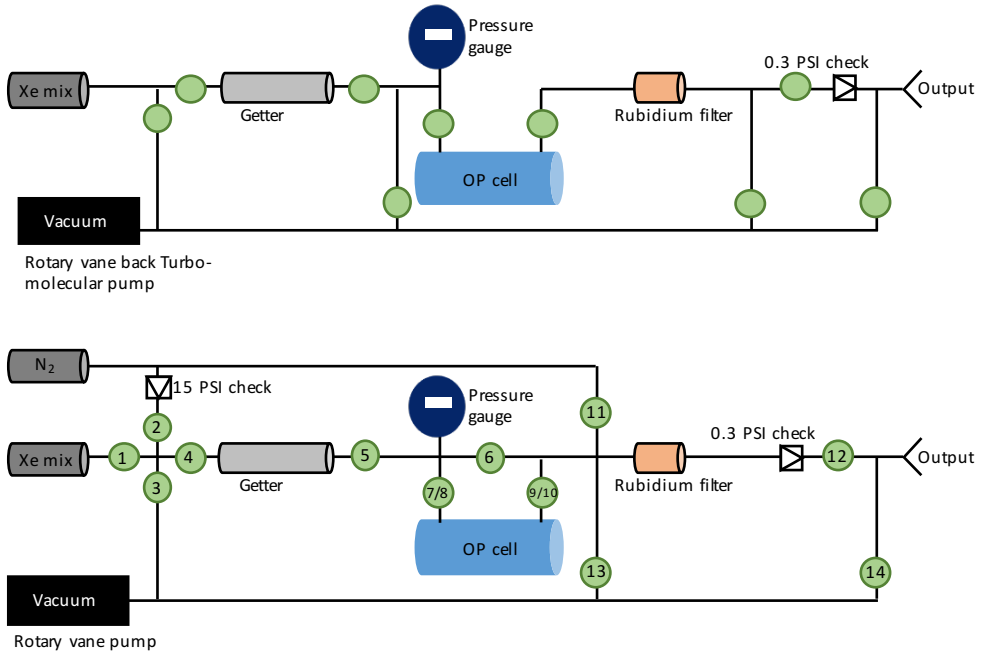

Figure 3.12: Schematics of the gas manifolds of the XeUS (top) and N-XeUS (bottom) polarisers. Note the addition of the N_2 line which can fill before and after the cell, the check valve near the N_2 cylinder, and the removal of the turbo-molecular pump. A cell by-pass line was also added.

are used to avoid depolarising the gas with solenoid valves. An Edwards rotary pump was selected due to its capacity to interface with the micro-controller (via an Edwards TIC controller). Teflon tubing is used for the HP Xe paths due to its compatibility with the HP state: it contains no paramagnetic impurities that would depolarise the gas. The gas purifier is an inert gas purifier by Entegris. The specified outlet purity is <1 ppb H_2, CO and CO_2; <100 ppt H_2O, O_2. The purifier cannot be regenerated and was installed under nitrogen gas flow. The purifier does not remove N_2 and is therefore compatible with the Xe/N_2 pre-mix gas cylinders employed by XeUS and N-XeUS (XeNA creates the desired gas mix using separate cylinders and employs 3 different gas purifiers).

Figure 3.12 shows a schematic representation of the gas manifolds of XeUS and N-XeUS. New features introduced on N-XeUS include the N_2 cylinder

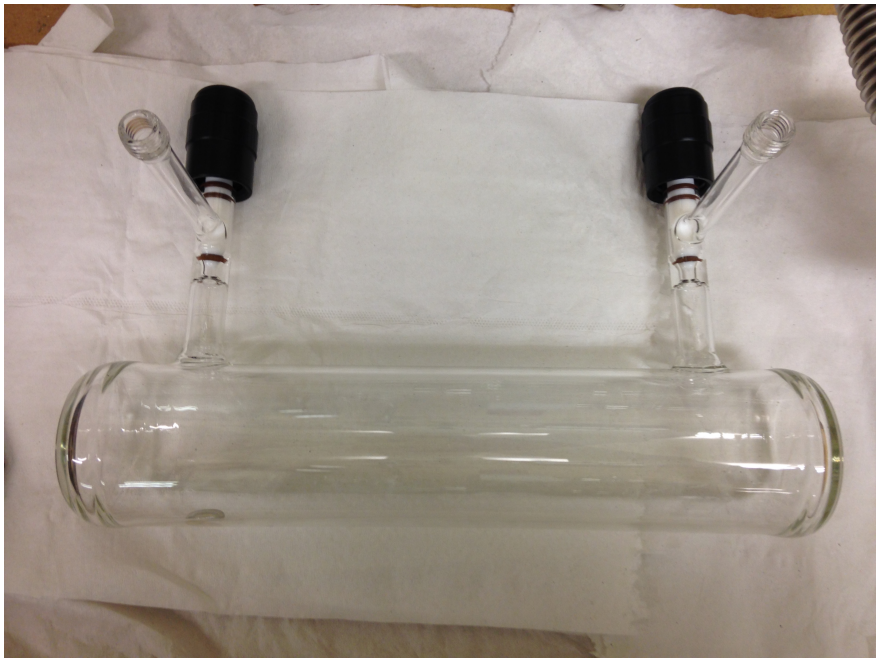

Figure 3.13: The optical cell design of the XeUS and N-XeUS polarisers used in the SEOP experiments. The cells are 25 cm in length an 2.54 cm in diameter providing a volume of ∼0.5 litres.

that can be injected into the upstream part of the manifold via valve 2, and into the downstream section at valve 11. Note that the introduction of N_2 for preparation and cleaning of the gas lines means the turbo pump is no longer required and a safety check value on the inlet can be introduced.

Figure 3.13 shows an example of the XeUS and N-XeUS optical cells. They measure ∼25 cm in length and ∼2.54 cm in radius giving an internal volume of ∼0.5 litres. The cells are opened and closed by the black stopcocks which are actuated by 'helicals' when the cells are installed on the polariser. The helicals are pneumatically actuated stopcock turning devices.

3.2.7 NMR Spectrometer

A crucial aspect of any Xe polariser is the ability to monitor polarisation levels. This is done on XeUS and N-XeUS using a Magritek Kea NMR spectrometer and a small surface coil that is situated directly beneath - but not touching -

the optical pumping cell (contact can strongly effect the thermal behaviour of the cell and oven with detrimental results on P_{Rb}).

In NMR experiments, the resonant frequency of the target nucleus is proportional to the magnetic field according to the fundamental Larmor relation:

$$\omega = B\gamma. \tag{3.1}$$

The B_1 frequency was selected such that it coincided with as little external noise as possible. A low current was desirable to minimise resistive heating from the B_0 coils, but a moderate field is required to boost the polarisation of the water signal when in-situ calibration is performed. A further constraint to consider is that whichever frequency is selected for the water signal, the PSU must be able to reach four times that current in order to bring the xenon resonance up to the same frequency for calibration. For the majority of SEOP experiments, the B_0 PSU was set to 5.832 A which corresponded to a Xe B_1 frequency of 37.5 kHz

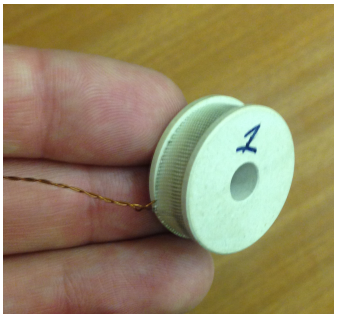

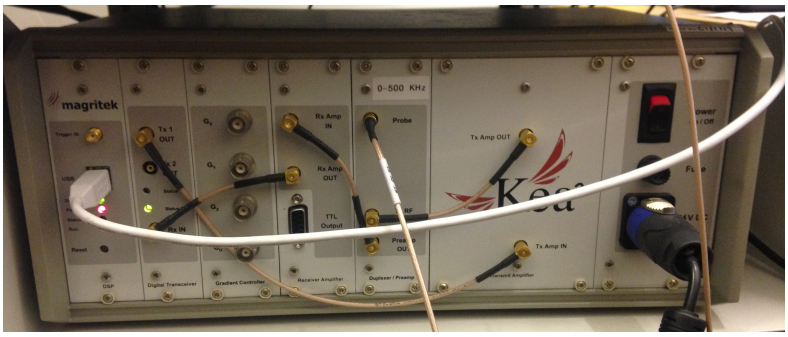

Figure 3.14: The Kea NMR spectrometer and surface NMR coil. The coil has ∼350 turns and a Q of ∼20.

3.2.8 Microcontroller and Automation

A primary design goal of the XeUS polariser was to allow it to be operated from beginning to end by a non-specialist. For example, so that a nurse, hospital technician or radiographer would be able produce bags of HP ^{129}Xe for medical scans in an MRI suite. To meet this aim, many aspects of the polariser functionality were automated, complete with safety checks and safeguards.

Aspects of the polariser that are automated include gas handling; a program guides the user through steps to install the optical cell. Once in place and secure the program actuates the necessary values using a manifold housed within the microcontroller box to clean the gas lines on the upstream end of the manifold with N_2, before filling the upstream line with Xe, which is the polariser's default mode. The Edwards pump can be turned on automatically via the software through the TIC controller. When ejecting gas for an imaging

experiment an eject sequence can be initiated. In this case the evacuation/fill cycle with the rotary pump and nitrogen is applied to the Tedlar bag to clear it of oxygen that would otherwise depolarise the gas. Opening and closing of the optical cell is also handled by the software: 'helicals' which unscrew the cell's stopcocks can be actuated in the same way as the pneumatic values. The duration for which the xenon is allowed to expand from the optical cell into the Tedlar bag must be set by the user in the GUI. Setting too low will result in too small a dose being dispensed. Too high will rupture the Tedlar bag. Figure 3.15(a) shows the inside of the microcontroller. 3.15(b) is a guide to the connections on the back of the box. A screenshot of the GUI can be seen in figure 3.16(a).

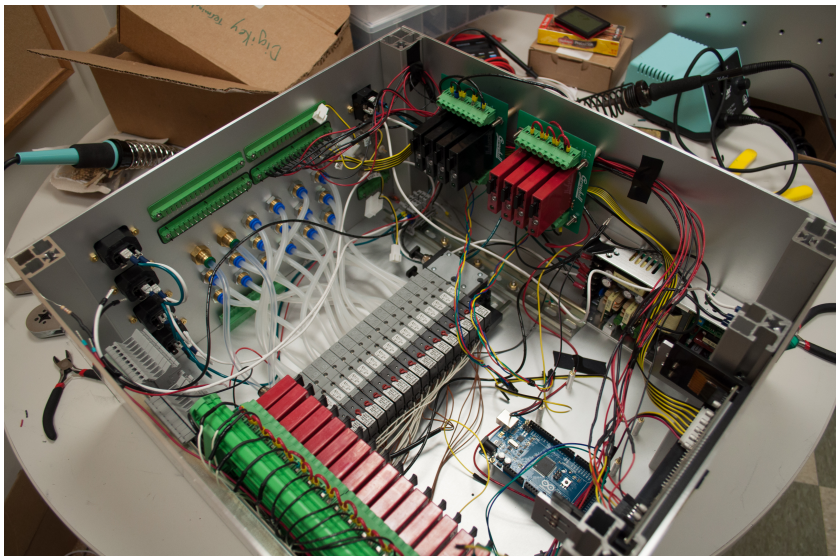

(a)

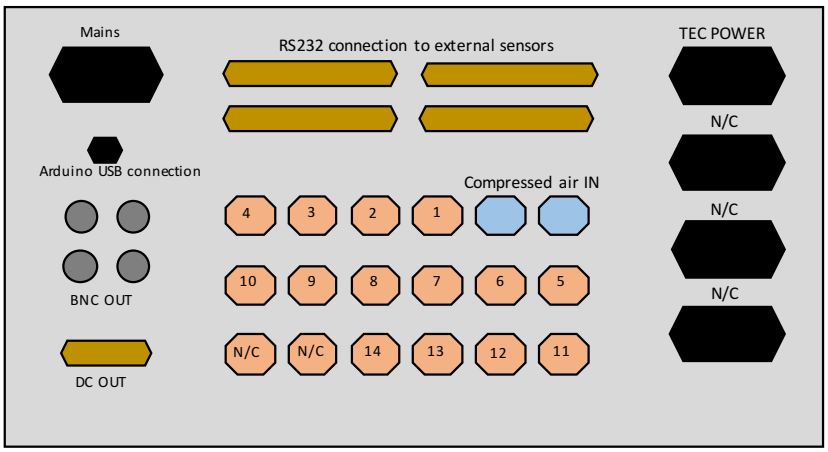

(b)

Figure 3.15: (a) Photograph of the inner microcontroller box. Visible within is the Arduino microcontroller, PSUs, DC and AC solid state relays and a burket manifold for the manipulation of the pneumatic valves. (b) Schematic of the rear of the microcontroller box illustrating the connection points.

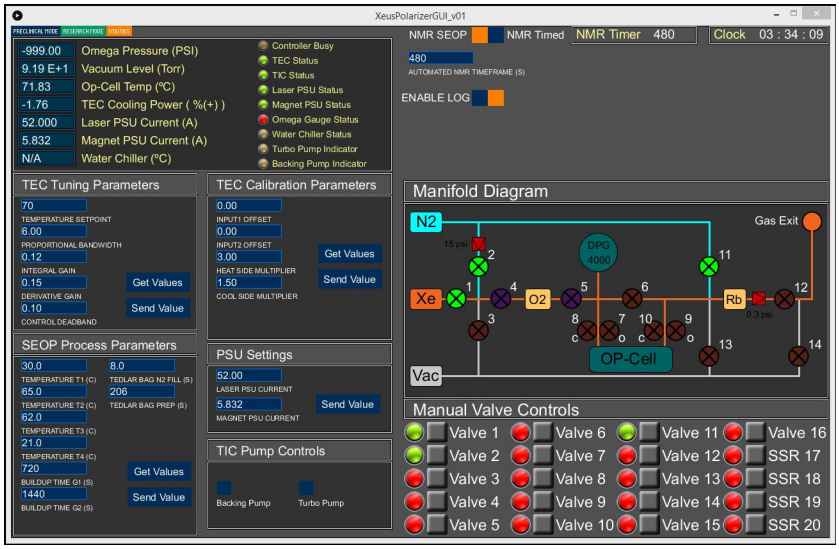

(a)

(b)

Figure 3.16: (a) Graphical user interface of the N-XeUS microcontroller. (b) Photographs of the thermal management system.

3.2.9 Thermal Management System

A thermal management system was later retrofitted to the chassis in order to mitigate thermal issues caused primarily by the laser but also by other components including the oven and B_0 coils. This comprised two towers added to the top of the polariser each fitted with 20 fans. The inlet was located above the laser and draws air inside. Warm air is ejected via the tower above the TEC and oven. The primary purpose of the thermal management system was to ensure the TEC had access to an adequate source of cool air throughout SEOP experiments so it could effectively cool the optical cell during optical pumping. A design constraint was that it could not compromise the optical seal. The chassis at the early stages of construction can be seen in figure 3.7. The thermal management solution is shown in figure 3.16(b).

3.2.10 Prototype Low-Field NMR Spectrometer

In parallel to the construction of the N-XeUS polariser, a low-cost, low-field NMR spectrometer for the N-XeUS polariser was developed. There were a number of motivations for this. Firstly to reduce cost; the two most expensive components on a xenon polariser are the laser and NMR spectrometer ($\sim$\$50,000 and $\sim$\$20,000 respectively for N-XeUS). This presents a significant cost barrier to any group hoping to build or install a new xenon polariser.

The design aims for the homebuilt NMR spectrometer were that it should be low-cost, have a compact profile, be easy to use in terms of both hardware and software, be easy to duplicate, have high performance (resolution, sensitivity), be universal such that it can be powered in the UK or elsewhere (240 V and 120 V compatible), and amenable to automation. These aims have been achieved with a combination of carefully selected analogue and digital components.

Analog Discovery

The component which forms the core of the NMR spectrometer, the Analog Discovery, is a recent device (2013) which was developed as a collaboration between Digilent, Analog Devices and Xilinx. It was intended as a versatile teaching tool for university electrical engineering courses and a represents excellent value for money because both Analog Devices and Xilinx subsidised its development by providing many components at cost. To this end, extensive documentation exists for the hardware within the Analog Discovery, including schematics of every circuit and the details of every IC chip.

The Analog Discovery contains a number of digital 'instruments' that can be used in place of a several of desktop bench instruments including: a function generator (2 channels), an oscilloscope (2 channels), a power supply, a voltmeter, a network analyser, a pattern generator and a logic analyser, all which are controlled via the 'Waveforms' software provided freely by Digilent. In a recent update Digilent released a software development kit (SDK) for the Analog Discovery which contains all the information necessary to allow the user to develop custom software, opening the possibility that any of its onboard instruments can manipulated to meet the needs of a custom hardware application. This feature was exploited to fashion the function generator and oscilloscope channels into the T_x and R_x channels of an NMR spectrometer, while using the digital pins of the pattern generator to control the timing of an active duplexer.

The Analog Discovery was therefore well suited to form the basis of the homebuilt NMR spectrometer. It is cheap as it is aimed at an academic and student market; it is well specified and excellent value for money due to the commercial investment in the device; it contains the necessary hardware to

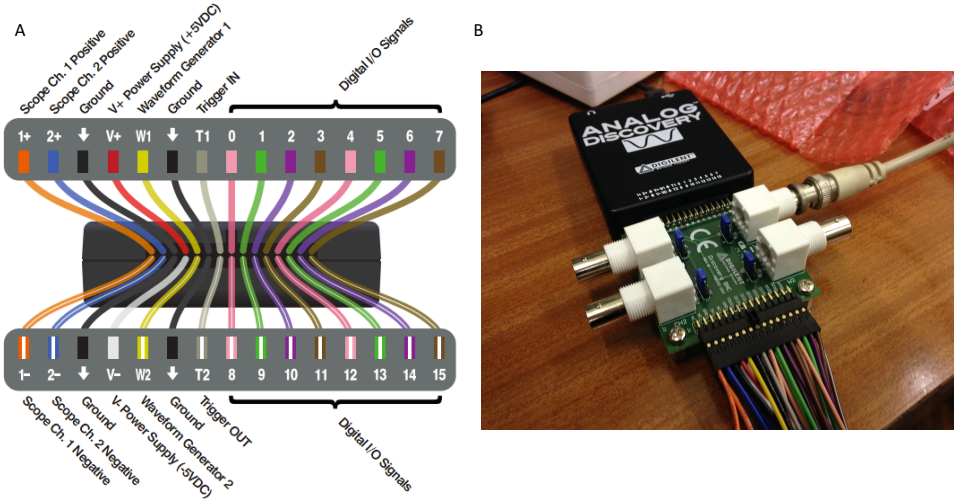

(a)

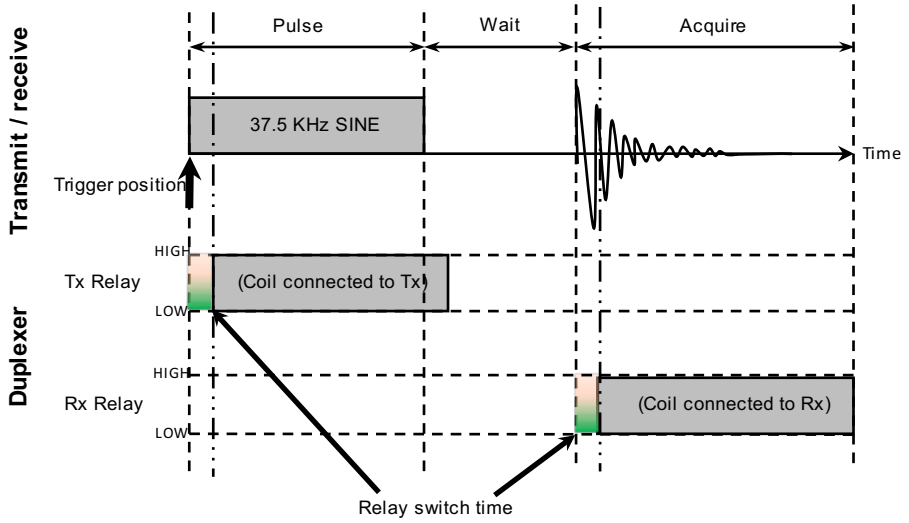

(b)

Figure 3.17: a) The Analog Discovery by Digilent. (A) Analog Discovery pin-out diagram. Reprinted from [113] with permission. (B) The Analog Discovery connected to the BNC breakout board. b) Timing diagram for the prototype NMR spectrometer.

generate pulses and to receive FIDs (or echoes) via the function generator and oscilloscope channels; and the availability of the SDK means that all of these features can be harnessed and controlled using a custom program.

The specification of the two-channel function generator is formidable for the cost of the system (∼$100): 22 MΩ, ± 5 V, 14 bit resolution, 100 Msample/sec and 5 MHz bandwidth. As is the specification of the two channel oscilloscope: 1MΩ, ± 25 V, differential, 14 bit resolution, 100 Msample/sec and 5 MHz bandwidth, each with a buffer of 8192 data points. A photo and pin-out diagram for the Analog Discovery can be seen in figure 3.17. The photo shows the BNC breakout board with for BNC connections; two for the function generator channels, two for the oscilloscope.

The open-source Python programming language was used to write the code responsible for interfacing with the Analog Discovery due to its free availability and capabilities; extensive scientific, mathematical and signal processing libraries exist that may be used for on-line (or post-)processing of the FIDs, and it is possible to create stand alone executable programs that can be run without the need for a python compiler. The latter is a considerable advantage for a system where low cost and a small foot print is important, such as on board a polariser, as it means that a low-powered and compact computing solution - such as the newly released Raspberry Pi Zero (which costs merely £4) - can be used to run the program in place of a physically larger and more expensive laptop or PC solution. It should be noted that the SDK is compatible with other languages such as Matlab, but these were not considered due to the licence fees that may be restrictive to future users.

Pulse Sequence

The only sequence required for noble gas polimetry is a basic pulse-acquire sequence. There are three portions to this sequence. 1) An excitation pulse, which has a given amplitude and duration; 2) an acquisition delay period, during which time the ring down of the tuned coil plays out; and 3) an acquisition period, in which the FID of the sample is digitised and recorded. In the prototype NMR spectrometer the Analog Discovery coordinates all of this. The excitation pulse is generated by the function generation instrument and the FID is digitised and recorded using the oscilloscope instrument. Further to this, the Analog Discovery also controls the (active) duplexer using digital 3.3 V signals generated by its pattern generator instrument. The timing of these pulses coincide with the relevant portion of the sequence (i.e. there is a 'pulse signal', an 'acquisition delay signal' and an 'acquire' signal) via the internal clock of the Analog Discovery. The duration of each period and various experimental parameters can be prescribed by the user. The timing diagram can be seen in figure 3.17.

Active Duplexer

The prototype NMR spectrometer uses an active duplexer design based on fast-switching mercury wetted Hamlin relays. As a pulse-acquire NMR sequence plays out, the transmit relay closes to couple the sinusoidal excitation pulse from the transmit amplifier to the NMR coil for the duration of the excitation pulse. The receive relay then closes to couple the NMR coil receiver of the Analog Discovery via the pre-amplifier. An acquisition delay period, which allows for the ring down of the coil to play out (discussed below), separates the opening of the transmit relay and closing of the receive relay. Thus, the receiver is always actively shielded from the excitation pulse. As described

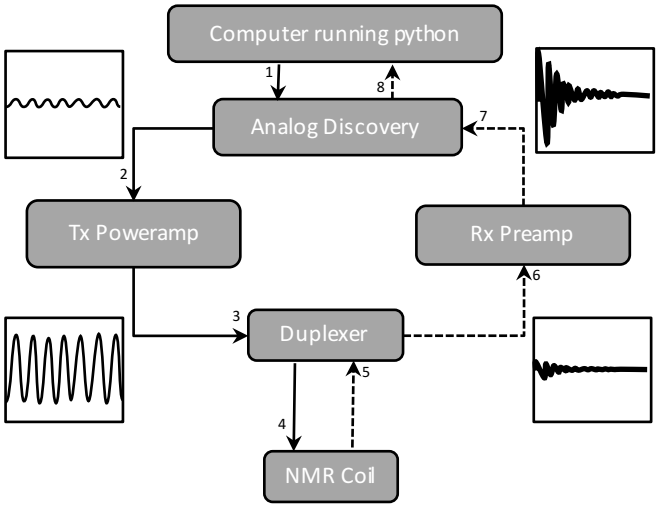

(a)

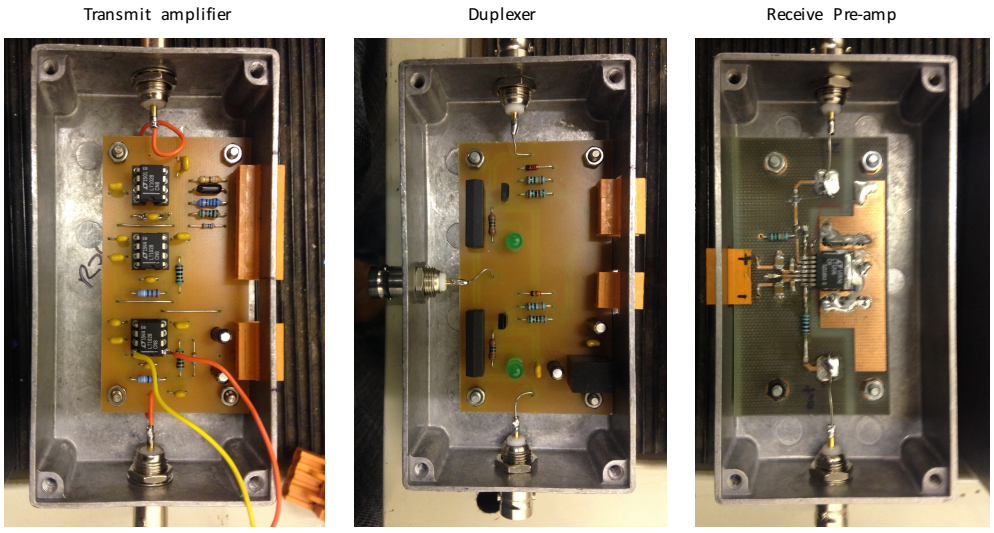

(b)

Figure 3.18: a) Workflow of the prototype spectrometer. b) Prototype spectrometer hardware modules. Shown here from left to right are the transmit amplifier, active duplexer, and the receive amplifier.

above, the signals that trigger the actuation of the relays are generated by the pattern generator instrument on board the Analog discovery.

During testing it was found that the mercury wetted Hamlin relays 'bounce' when closing for a period of 200 μs (see figure 3.19). This was accounted for in the relative timings of 1) the duplexer actuations and 2) the timings of the excitation pulse and ADC. The timings can be seen in figure 3.17(b).

Transmit Amplifier

The function generator instrument of the Analog Discovery is capable of producing a 5 V_{pp} sinusoidal excitation pulse which is insufficient to conduct an NMR experiment. This signal must therefore be amplified and is done so using a LT2106 OP AMP with a gain of 20 which is driven by a 15 V split-rail supply.

NMR Coil and the Tuned LCR Circuit

The NMR coil is a surface coil design with ∼350 turns and a Q factor of ∼20. In the development stages the coil was tuned to the B_1 frequency (56.3 kHz) using a capacitive decade box. With a Q of 20 the ring-down of the coil can be calculated to last approximately 2 ms. This was verified by experiment. For the purposes an NMR experiment ring-down can be a difficult issue, as it is an undesired by-product of an otherwise well-executed NMR experiment; it is a resonance phenomenon in which the NMR coil continues to resonate at the B_1 frequency beyond the duration of the excitation pulse. A coil with a high Q will be more sensitive to the NMR sample of interest, but will also ring-down for a greater period of time once the excitation pulse has ended. Therefore a trade-off must be made because if the Q is too high, it will be sensitive to the sample but will ring-down for too long, usually at an amplitude that is significantly larger than the FID, if the Q is too low there will be a short

ring-down relative to the envelope of the FID but the coil may not have the sensitivity to detect it. The situation becomes more challenging when the T_2^* of the sample is very short, and in this case it would be wise to lessen the Q of the coil and optimise the homogeneity of the B_0 field to increase the T_2^*.

Further strategies exist to avoid this issue and can be employed where appropriate. One such solution would be to use two coils positioned at right-angles to each other where one is used to transmit and the other to receive. Another approach, relevant to hyperpolarised gas NMR, is to implement a Q-damping circuit. In this approach, the Q of the coil is 'spoiled' immediately after the excitation pulse and 'unspoiled' again to receive. In other words, it is spoiled during the acquisition delay period, greatly suppressing the ring-down and hence shortening he required acquisition delay period. This is done by placing a resistor in series with the coil. The first Q-damping circuit for use with HP noble gases was developed by Conradi [114]. A version of this circuit is used within the current NMR spectrometer of the polarisation measurement station supplied by Polarean with their xenon polarisers.

Receive Pre-Amplifier

FIDs are typically on the order of microvolts. Therefore a low noise pre-amplifier is required to amplify the signal to a detectable level. The LT1028 is a low-cost, low-noise pre-amplifier and was selected for use as the pre-amplifer in the NMR spectrometer. Adjustable gain was implemented (20, 200, or 400), and to optimise the noise performance the bandwidth of the pre-amp was limited with a simple bandpass filter which eliminates the DC and very low frequency components, gives a maximum response at the frequency of interest, with a roll off from 90 kHz and up. The response of the bandpass filter can be seen in figure 3.20. The gain value should be chosen such that

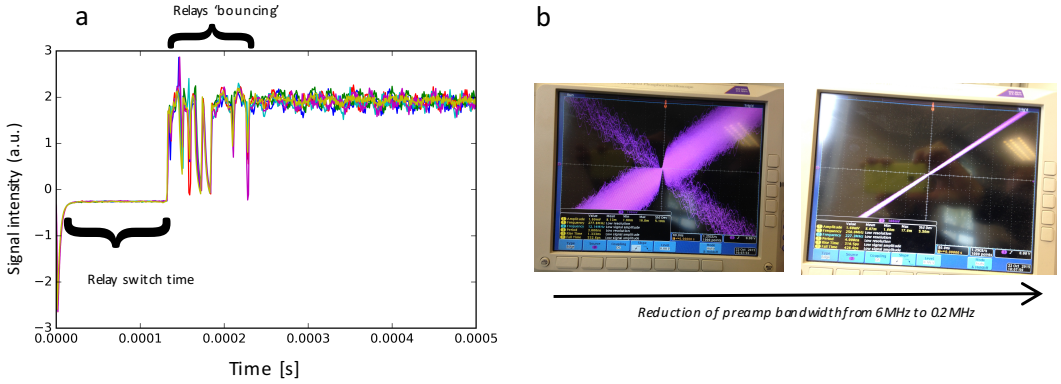

Figure 3.19: a) Prototype NMR spectrometer relay bouncing artefacts. The relays were found to bounce for a period of 200 μs and this was accounted for in the relative timings of 1) the duplexer actuations and 2) the timings of the excitation pulse and ADC. Visible in figure 3.17. b) Noise reduction that resulted in the reducing the pre-amp bandwidth from 6 MHz to 0.2 MHz.

the FID is amplified to match to range of the Analog Discovery's oscilloscope instrument ($\pm$25 V). This ensures that the FID is digitised at the maximum available resolution by the 14 bit analogue-digital converter.

Spectrometer Construction

The spectrometer has been constructed in a modular fashion to increase the amount of shielding enjoyed by the components (reducing noise) and to increase the ease with which repairs, replacements or upgrades can be made. The modules can be enclosed within a 1 U rack mount unit for installation on the polariser. The power amp, duplexer and preamp can be seen in figure 3.18

The performance of the prototype spectrometer was compared to the commercial Kea system in a xenon SEOP experiment. The results are shown later in figure 3.32.

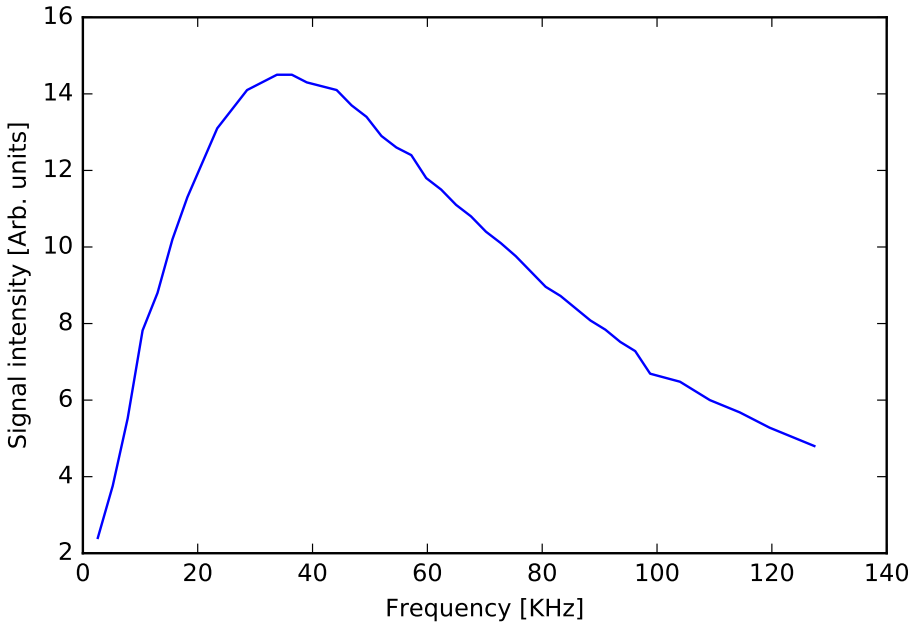

Figure 3.20: The bandpass response of the pre-amplifer

3.3 Methods

3.3.1 Cell Cleaning and Preparation

The optical cells were prepared for SEOP experiments according to the following protocol:

1. The cell is first placed in a KOH/methanol base-bath for a 24 hour period to remove any impurities attached to the glass surface.
2. Next, the cell is removed from the base bath and rinsed with distilled water, followed by methanol, and this is repeated at least three times.
3. The cell is then submerged in 50:50 water/methanol solution and ultrasonically cleaned for $\sim$1 hour.
4. After the sonic bath, the cell is rinsed again with distilled water and methanol.
5. The cell is then heated to evaporate any residual methanol.

6. Once the cell has dried and cooled, the next step is to coat the interior surface with Surfasil siliconizing agent which is prepared by diluting 1 mL of Surfasil with 9 mL of hexane.
7. The prepared solution is then pipetted into the cell via a side stem and swirled for several minutes to coat all internal surfaces.
8. Next, the siliconizing solution is removed and the cell is rinsed with hexane. These two steps are repeated 2 more times for a total of 3 coatings/washings with Surfacil/hexane.
9. The cell is then connected to vacuum to remove any residual hexane.

This Surfasil coating prevents direct contact of HP ^{129}Xe with the glass surface and any paramagnetic centres that may exist in the glass, reducing depolarization and increasing the in-cell ^{129}Xe T_1 relaxation time. Achieving long in-cell ^{129}Xe T_1 times is key in building up high levels of polarisation in stopped-flow SEOP.

Once the cell is cleaned and coated with Surfasil it can be loaded with Rb. This is a delicate procedure that must be done in an inert atmosphere as caution must be taken not to 'poison' the reactive alkali metal. A controlled environment glove-box is used, in which the atmosphere is catalytically purified. Water and oxygen levels are monitored and maintained at low ppm concentrations. Before the procedure begins, all of the necessary items are loaded into the glove-box transfer chamber which is purged multiple times with nitrogen. Among the items is a hair-dryer, which is used to heat the rubidium above its melting point of 37 °C so that it can be loaded into the cell using a pipette. Once loaded, it is crucial to allow the alkali metal time to cool, as it must not touch the optical windows of the optical cell. If this occurs the optical cell will be at risk of hairline fractures due to localised heating of

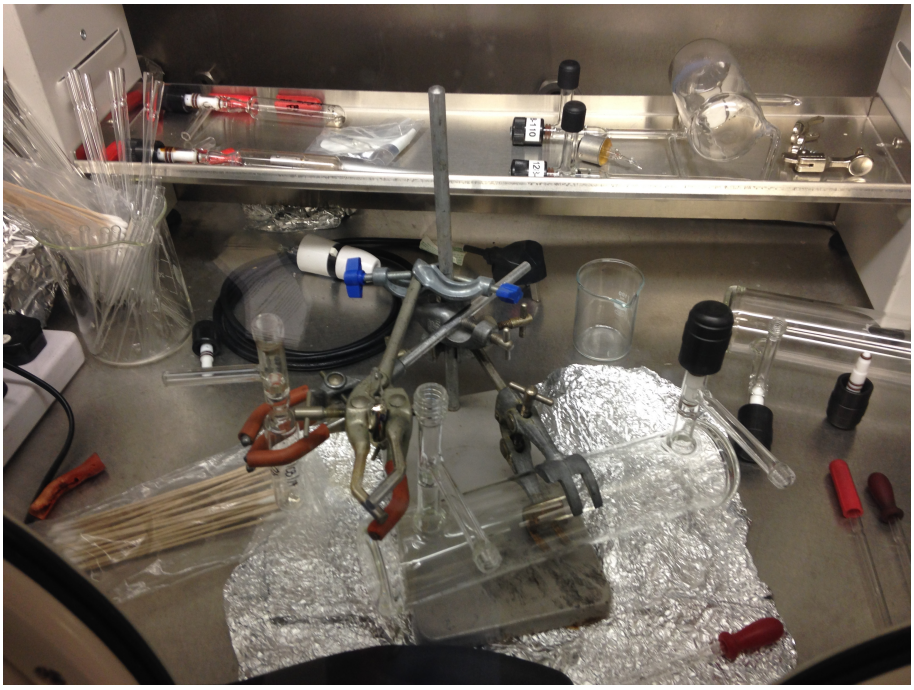

Figure 3.21: Photograph of the inert-environment glove box prior to loading an optical cell with Rb. A sealed 1 g ampoule of Rb is visible in the central clamp. Loading would commence when H_2O and O_2 levels fell beneath 2 ppm and 10 ppm, respectively.

the metal on the window. Figure 3.21 shows the optical cell in the glove box prior to an Rb loading.

3.3.2 Spreading of Rb

A method for distributing Rb across the inner surface of the optical cell using temperature gradients induced by the presence of dry ice was developed, inspired by a similar method employed by our collaborators in which the Rb is distributed using liquid N_2 vapours. A hot air gun boils the droplet of rubidium which forms a vapour. The vapour then condenses wherever the surface of the cell is cold. A holder was therefore designed which covers the optical cell everywhere except at the ends of the cell where optical access if required for the pump laser. The holder can be seen in figure 3.22(A) along with indicators which show how the thermal gradient is applied. Panel (B) shows two

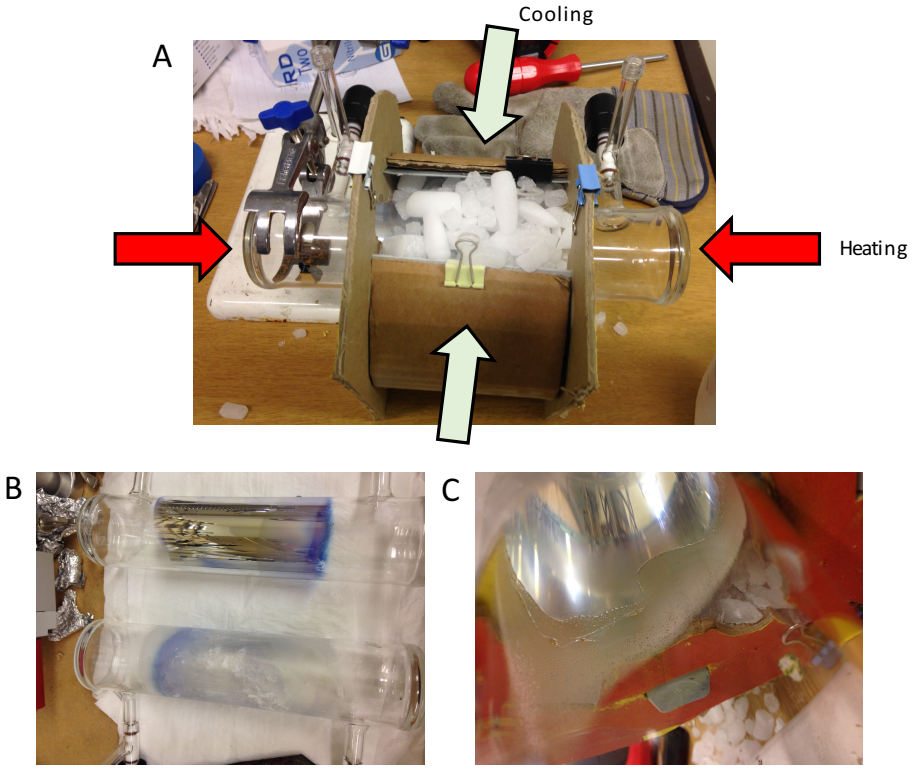

Figure 3.22: Method for distributing rubidium. (A) Heat is applied at the ends of the optical cell and dry ice is suspended around the middle to create a temperature gradient in which the vapour phase Rb atoms condense on inner walls of the cell where the dry ice is located. (B) Results of temperature gradient Rb spreading in two N-XeUS cells. (C) Close-up of the Rb on the inner surface of the glass.

cells after the spreading process. The bottom cell appears frosty due to water vapour that has frozen on the outside of the cell. Panel (C) shows a close up of the inside of the cell. A fine, highly mirrored Rb coating can be seen within. Spreading the Rb improves the performance of the cells by increasing the surface area from which the Rb can vaporise, and enables it to equilibrate more quickly throughout the optical cell.

The optical cell can be loaded with the SEOP gas mixture of choice once it has been heated and evacuated to release any gases that may have been trapped within the Rb as it solidified. For the N-XeUS experiments, gas was loaded

using the manifold of the polariser. For the Raman experiments, described in chapters 5 and 6, all gases were loaded using a stand-alone manifold where each gas is passed through its own respective oxi-clear filter to minimise impurities. For all of the experiments - N-XeUS and Raman - the optical cell was loaded to a total pressure of 2000 Torr. For Raman experiments, gases were loaded in ascending order of partial pressure in order to minimise gas loading errors. On N-XeUS, one reading accounts for all of the gases (as the cylinders are pre-mixed).

3.3.3 Installing an Optical Cell

When a new optical cell is installed on the polariser it is attached to the inlet and outlet portions of the gas manifold. It is then necessary to clean these gas lines as oxygen will now be present in the lines due to exposure to atmosphere. On the inlet side of the manifold on N-XeUS, the inlet line is purged with the vacuum pump and filled with dry nitrogen gas a total of three times to ensure the lines are clear. The final nitrogen load is then evacuated and the line is filled with an over pressure of xenon pre-mixture (e.g. 20% xenon and 80% nitrogen). At this point the optical cell can be opened to the inlet gas line and filled to the desired total pressure (typically 2000 torr), which is set using the gas regulator on the Xe/N_2 premix cylinder and monitored using the positive pressure OMEGA pressure gauge just upstream of the optical cell. This positive pressure of 2000 torr is then maintained on the inlet manifold until the optical cell is changed. This ensures high duty cycle between SEOP runs and also means that any leaks will flow out of the manifold and prevent atmospheric O_2 from flowing into the manifold. All actuations of the valves for this procedure are controlled by the microcontroller and GUI.

3.3.4 Preparing a Tedlar Bag

A similar procedure is used to prepare the Tedlar bags and the outlet side of the gas manifold; the gas lines are first purged with the vacuum pumps and then filled with dry nitrogen. Again this ensure that no oxygen is present in the lines or the Tedlar bag when the polarised gas mixture is ejected into the bag which may rapidly depolarise the Xe or, in the worst case, flow back into the optical cell and immediately oxidise the rubidium. A one-way check valve is employed upstream of the bag and downstream of the cell to prevent the later from occurring.

3.3.5 Flip Angle Calibration

A flip angle calibration was conducted using HP ^{129}Xe which was polarised to steady state. The excitation pulse length of the Kea was set to 0.2 ms, 0.6 ms and 1 ms, and the gain was varied between -3 and -28 dB. A 90 degree flip angle can be achieved at -10 dB with a pulse length of 1 ms, and -8 dB at 600 us. The results of the flip angle calibration can be seen in figure 3.23.

3.3.6 SEOP Protocol and Hardware Settings

The following protocol was adopted when preparing for a SEOP experiment on the N-XeUS polariser:

1. Confirm NMR coil connection.
2. Install bottom oven sliders which locate under the cell stems.
3. Insert optical cell.
4. Add the cell clamps which secure the optical cell in place.
5. Tighten the 4 nuts holding clamps.
6. Secure the thermocouple to the middle of the cell and fix in place with Kapton tape.

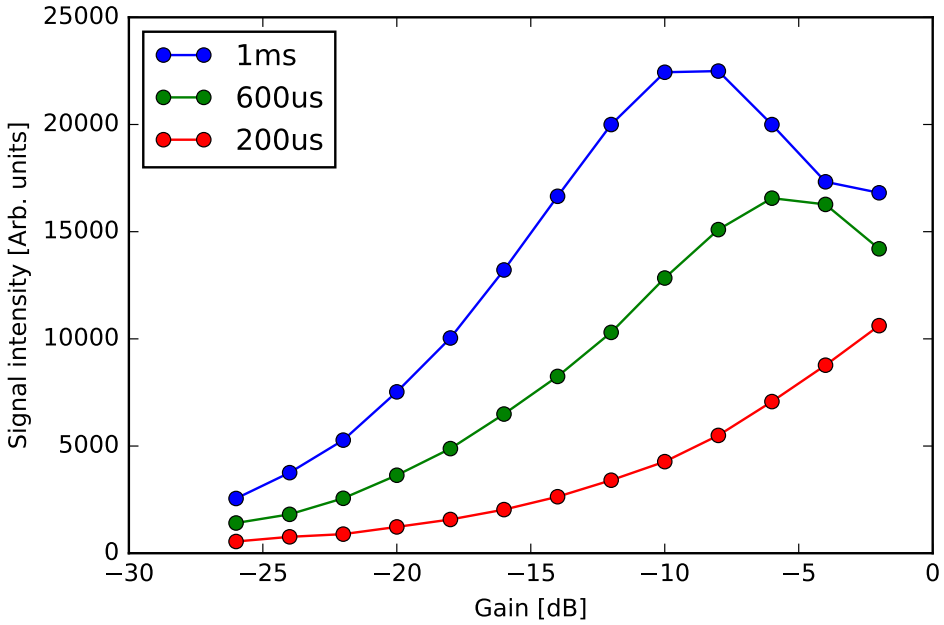

Figure 3.23: Kea flip angle calibration. The excitation pulse length of the Kea was set to 0.2 ms, 0.6 ms and 1 ms (red, green and blue respectively), and the gain was varied between -3 and -28 dB. 90 ° pulses can be achieved with pulse lengths of 0.6 ms and 1 ms.

7. Add the top slider parts over the cell stems.
8. Add the glass window to the front of the oven.
9. Adjust the helical mounting plate and attach them to the stopcocks.
10. Place the lid on the oven and tighten the 4 black nuts.
11. Confirm IR fibre is aligned.
12. Close and seal outer doors.

The following protocol was adopted when initiating and conducting a SEOP experiment on the N-XeUS polariser:

1. Turn the chassis fans on.
2. Open the GUI.
3. Confirm TEC operational by checking the LCD display is ON.
4. Lock the enclosure doors, switch on the laser interlock.

5. Open Ocean View software to monitor output from the IR spectrometer.
6. Turn on the pump laser PSU, B_0 PSU and the laser chiller.
7. Simultaneously set the chiller to 26.5 °C and set laser PSU to 52 A.
8. Confirm an LDA rest temperature of 32.5 °C.
9. Set the TEC temperature to the SEOP target temperature.
10. Set B_0 PSU to 5.832 A (37.5 kHz).
11. Set up Kea acquisition settings using the parameter files.
12. Open '1pulse killer' and crush any signal that accumulate during initiation
13. When the HP signal is crushed and the target temperature is reached, begin the experiment by pressing 'NMR SEOP' in the GUI. (Can be seen in figure 3.16(a).)

3.3.7 Gas Mixtures

Two gas mixtures were studied on the N-XeUS polariser: 1) a 50:50 mix of 1000 torr xenon, 1000 torr nitrogen, and 2) an 80:20 mix of 1600 torr xenon, 400 torr nitrogen. Both were loaded into the optical cell using the manifold of the N-XeUS polariser and drawn from pre-mixed gas cylinders.

3.3.8 Temperature Ramped SEOP

An innovation introduced by the XeUS polariser is the concept of temperature ramped SEOP [22]. The aim of the concept is to reduce the duty cycle of the polaristion process, while also optimising the yield of HP xenon. During the build-up process, two temperatures are used. An initial higher temperature at which the initial build up rate is high but for which the terminal polarisation would be low, and a lower temperature at which the terminal polarisation is optimal but the initial build up rate would be low. Combining these two tem-

peratures - a higher temperature to increase the initial rate of polarisation and a lower temperature to maximise the terminal polarisation - a higher polarisation can be obtained in a shorter time as compared with a SEOP experiment where only one temperature is used. The method further increases the duty cycle by maintaining illumination of the optical cell during all stages of the SEOP process. During a TR-accelerated SEOP, the cell remains illuminated during build-up, but also during cool-down, extraction and reloading of the optical cell. This has further gains in duty cycle because after ejection of the first batch from the OP cell, some of the gas remains (roughly half a litre at atmospheric pressure). Because this gas is already highly polarised, it therefore takes less time to polarise the second batch as it already has a 'head start' relative to the first bag, or relative to a more linear work flow wherein the entire process is run from start to conclusion and then repeated (as was the case on XeNA).

3.3.9 T_1 Measurements

T_1 values were determined with fits to the following equation:

$$S(t) = S_0 \exp\{[-t/T_1]\} \tag{3.2}$$

where $S(t)$ is the signal at time t and S_0 is the signal strength of the first measurement. NMR measurements were typically made at intervals of 12 minutes. T_1's were measured in three optical cells (results in figure 3.30(a)) and in two Tedlar bags. One Tedlar bag measurement was while located on the polarisation measurement station, and one measurement was made while the bag was located in the transporter (results in figure 3.30(b)). The transporter was used to move the bags from the N-XeUS polariser - located in the physics department - to the MRI scanner and polarisation measurement station located

in the medical imaging unit (MIU) at the Queen's medical centre (QMC). The transporter and measurement station are shown in figure 3.25 and described in section 3.3.11. Where in-cell measurements were conducted, the optical cell was cooled to room temperature prevent Rb vapour induced spin-destruction of the xenon polarisation.

3.3.10 In-Cell Rb Polarisation Measurements

During SEOP experiments, measurements of the global rubdium polarisation, $\langle P_{\mathrm{Rb}} \rangle$, were made using a field cycling method in which the integrated absorption spectra of the laser light transmitted through the cell are compared when the magnetic field is cycled. The technique utilizes Beers law and the bleaching of the IR absorption spectrum that results from the depletion pumping of the ground state magnetic sub-levels. The first step of the OP process, in which the Rb electrons become spin-polarized, leaves a smaller concentration of Rb atoms in the laser-absorbing state. In turn, this population reduction allows more laser light to be transmitted through the cell, allowing the alkali metal polarisation to be estimated from the difference [18, 24]. More precisely, the Beer-Lambert law, with absorption A, is defined as:

$$A = -\ln \frac{I_{\mathrm{hot}}}{I_{\mathrm{cold}}} \tag{3.3}$$

where I_{hot} is the intensity of light after travelling through a 'hot' cell and I_{cold} is the intensity of the pump laser light after a 'cold' cell. Here, a 'cold' cell is defined as room temperature - $\sim 25\,^{\circ}\mathrm{C}$, and a 'hot' cell is defined as 70-140 °C, i.e. typical SEOP conditions. For A_0, below, the same applies but the magnetic field must be off and the global rubidium polarisation $\langle P_{\mathrm{Rb}} \rangle$ can be determined from:

$$\langle P_{\mathrm{Rb}} \rangle = \frac{A}{A_0} - 1 \tag{3.4}$$

A conceptual schematic of the phenomenon can bee seen in figure 3.24(a). In part (b) of the figure an example measurement is shown in which the rubidium polarisation is computed to be 44.4% ± 6.65%.

3.3.11 Measurement of Xenon Polarisation at the MIU

As indicated above, during collection of demonstration data (i.e. bag images) the N-XeUS polariser was located in a different building to the MRI scanner. Therefore a low-field battery-powered transporter was used to move the Tedlar bags containing HP xenon polarised by N-XeUS to the scanner. It was close to the scanner that the polarisation was measured using the polarisation measurement station. This is a piece of hardware provided by Polarean which is essentially a pre-calibrated low-field NMR system. It can be seen in figure 3.25(b). The transporter was driven with a 12.95 V battery, and had a resistance and current of 4.3 Ω and 3 A, respectively. Its magnetic field was measured as 1.58 mT.

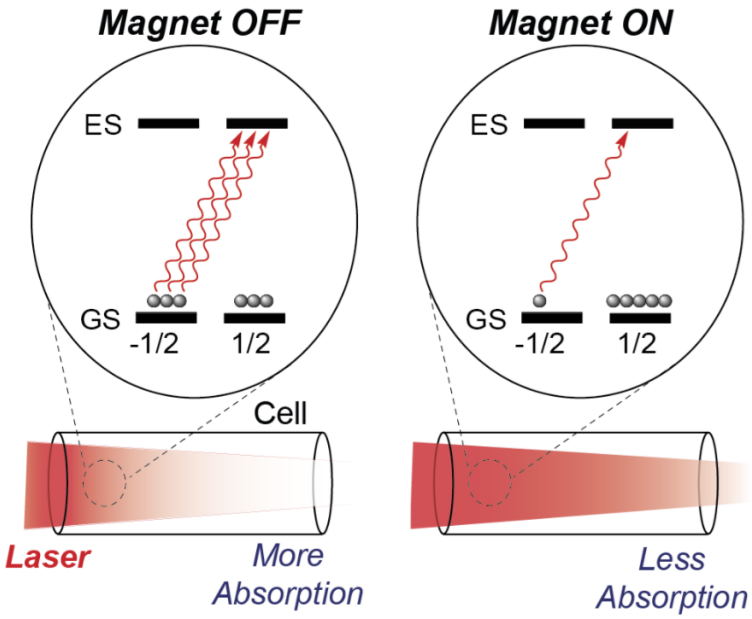

(a)

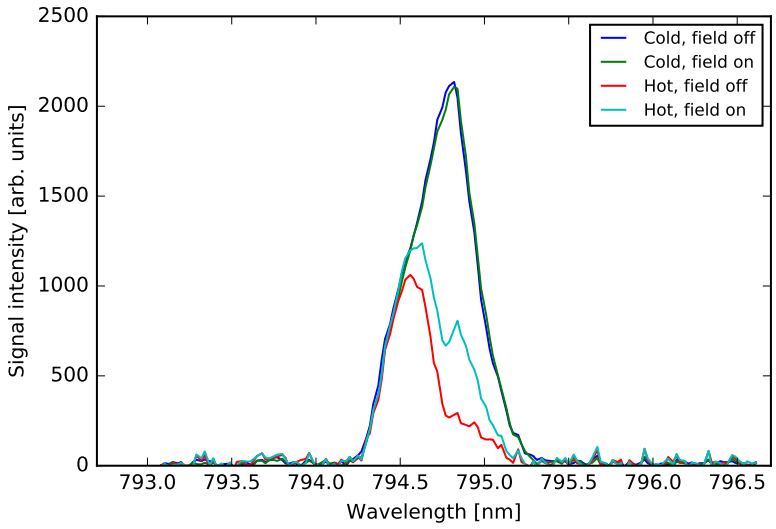

(b)

Figure 3.24: (a) Conceptualisation of the measurement method for global Rb polarisation, adapted from [18] and reproduced with permission. (b) Measurement of the Rb polarisation in Cell A at 85 °C. Measured polarisation = 44.4% ± 6.65%.

a b

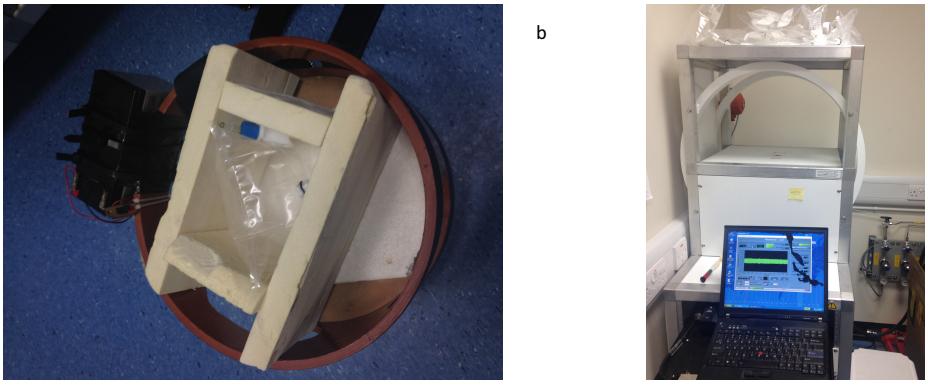

Figure 3.25: a) Low-field Tedlar bag transporter and b) the polarisation measurement station at the MIU

3.4 Results and Discussion

3.4.1 In-Cell Xenon Polarisation as a Function of Temperature and Gas Mix

The results of the SEOP experiments are shown in figures 3.26, 3.27 and 3.28. Figures 3.26 and 3.27 show the results for the two 1000 torr Xe 1000 torr N_2 cells and figure 3.28 shows the 1600 torr Xe 400 torr N_2 mix cell. In all three figures panel (a) shows the data with an accompanying fit to $P_{\mathrm{Xe}}(t) = 1 - \exp\{[-\gamma_{\mathrm{SEOP}}t]\}$. (b) panels show, for clarity, the results of the fits alone.

The primary purpose of the experiments was to determine the optimal temperature T_{opt} for a given gas mixture, but also to identify 'fast build-up' temperatures and 'optimal build-up' temperatures for the purposes of temperature ramped SEOP (described in section 3.3.8). In the first cell (figure 3.26), P_{Xe} continues to rise with temperature through the 65 °C to 85 °C range. The highest P_{Xe} is observed at 85 °C with little gain observed relative to the 80 °C run, suggesting that T_{opt} for this mixture is ∼85 °C. The second cell, shown in figure 3.27, was loaded with the same gas mixture and the experiment was repeated between temperatures of 70 °C and 90 °C. Polarisation characteris-

tics as a function of temperature were very similar and in this dataset T_{opt} was confirmed as ∼85 °C, as at 90 °C P_{Xe} folded over, plateauing at a lower level.

The third cell contained a 1600 torr Xe gas mix. Here, in keeping with the group's previous results [23, 20], T_{opt} was lower for the higher [Xe] mix. The temperature range examined was 60 °C to 80 °C and the optimal P_{Xe} occurred at a temperature of 70 °C.

The fits were used to generate the plot in figure 3.29(a) which shows terminal xenon polarisation as a function of temperature for each set of results. That is, the equation $P_{\text{Xe}}(t) = 1 - \exp\{-\gamma_{\text{SEOP}}t\}$ was evaluated for each experiment at $t = \infty$. The figure allows inter-cell comparison of the T_{opt} trends. It can be seen clearly here that cells A and B, which were both loaded with the same 1000 torr gas mixture, both peaked at 85 °C, and that the higher density xenon mix peaks at the lower temperature of 70 °C.

These cells provided the HP xenon gas for the demonstration images and absolute polarisation measurements. Three bags were produced: two bags from cell C (80:20 Xe:N_2) and one bag from cell B (50:50 Xe:N_2). For one of the 80:20 bags the polarisation was measured and imaging was performed. In the second 80:20 bag a T_1 measurement was preformed on the measurement station. In the final bag - 50:50 Xe:N_2 - the polarisation was measured, an imaged acquired, and a T_1 measurement performed on the bag transporter.

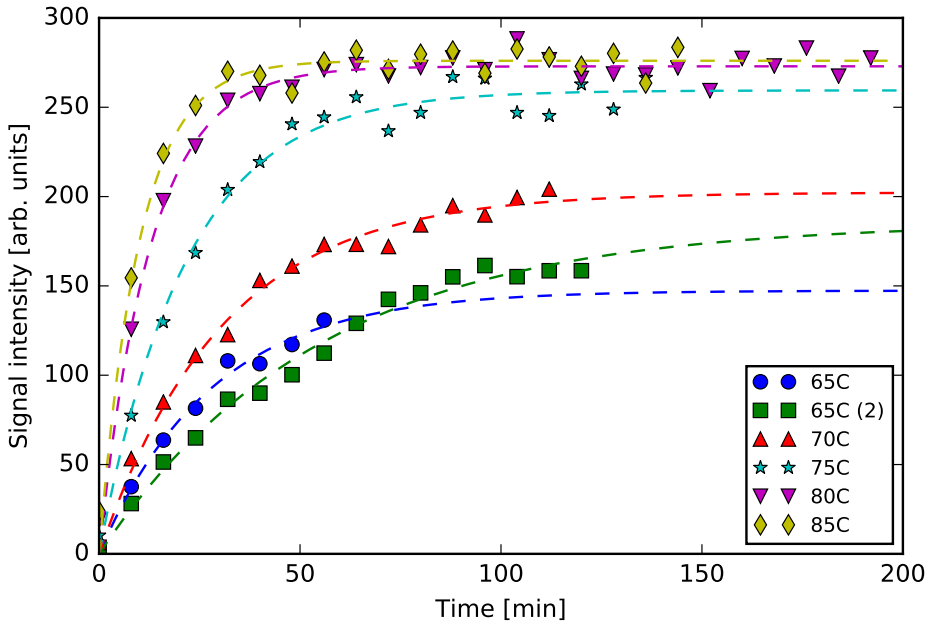

(a)

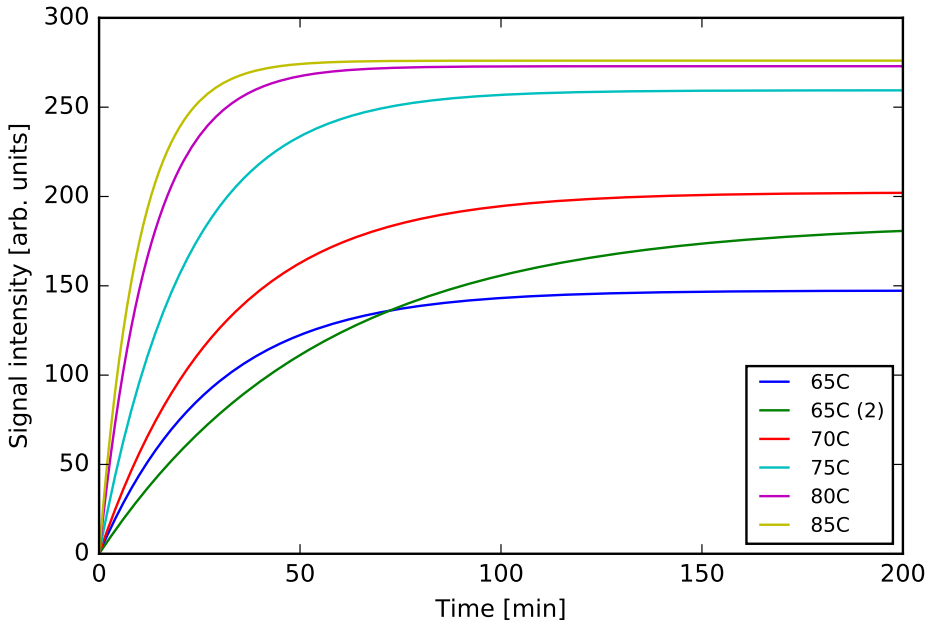

(b)

Figure 3.26: NMR signal intensity as a function of temperature in cell A containing an 50:50 mix of Xe:N_2 at 2000 torr total pressure. a) shows the observed experimental data with fits to $P_{\mathrm{Xe}}(t) = 1 - \exp\{-\gamma_{\mathrm{SEOP}} t\}$. For clarity, b) shows the only the fit lines. $T_{\mathrm{opt}} = 85\,^{\circ}\mathrm{C}$.

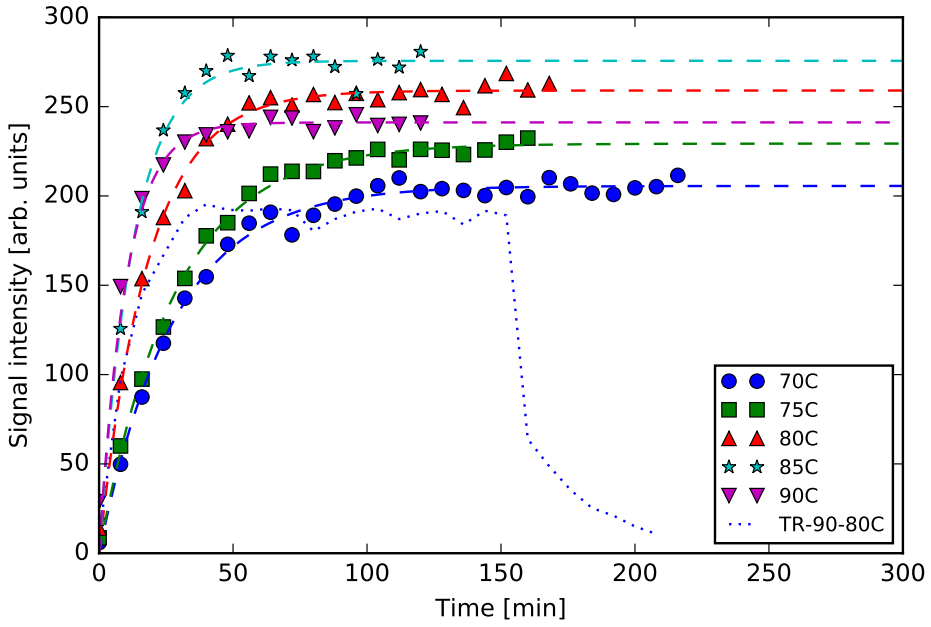

(a)

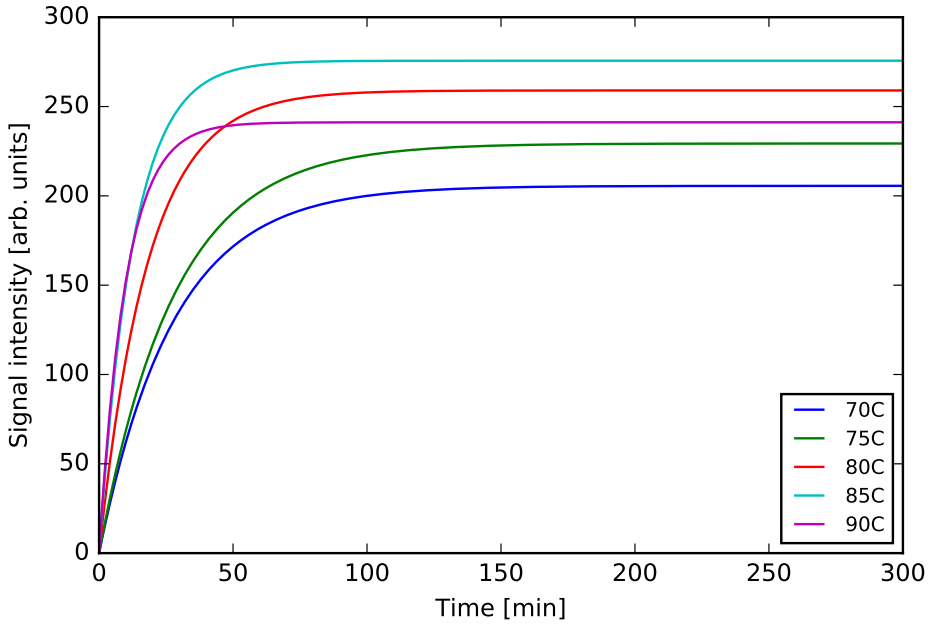

(b)

Figure 3.27: NMR signal intensity as a function of temperature in cell B containing an 50:50 mix of Xe:N_2 at 2000 torr total pressure. a) shows the observed experimental data with fits to $P_{\mathrm{Xe}}(t) = 1 - \exp\{-\gamma_{\mathrm{SEOP}} t\}$. For clarity, b) shows the only the fit lines. $T_{\mathrm{opt}} = 85\,^{\circ}\mathrm{C}$. The dashed line in panel a) at 160 min shows residual in-cell polarisation after ejection is still at 25% after 12 min. This 'head-start' can be used to increase the production rate.

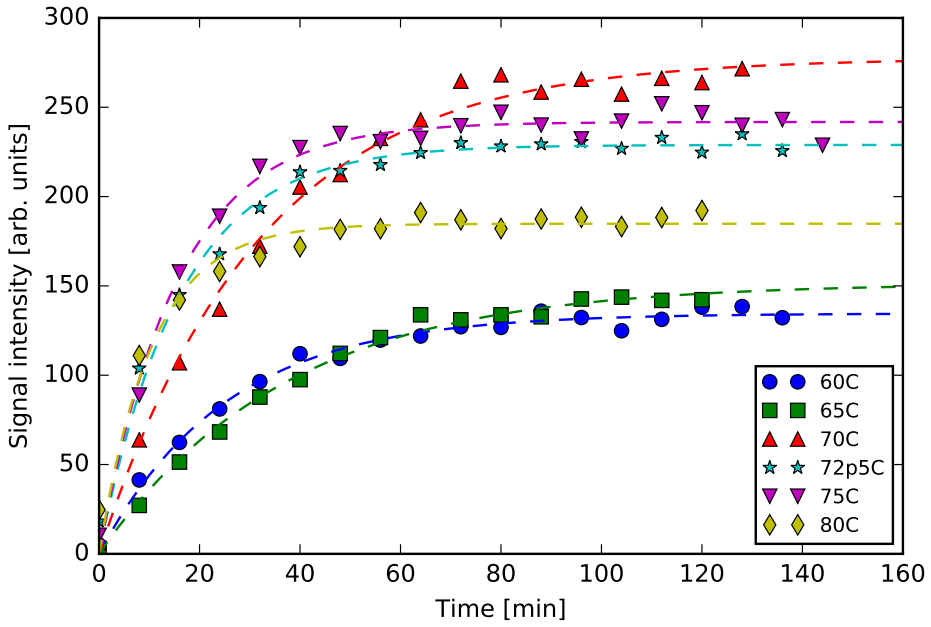

(a)

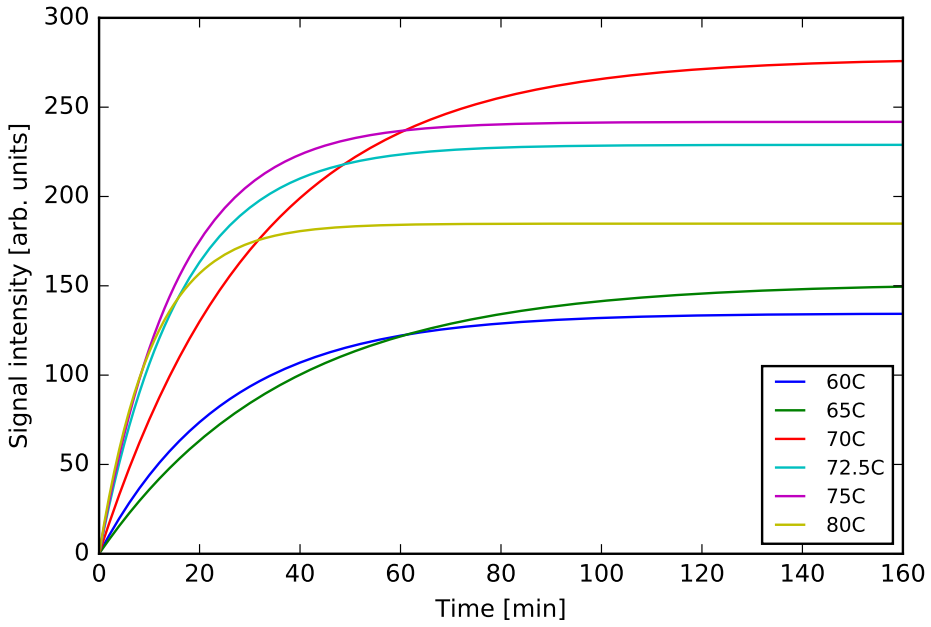

(b)

Figure 3.28: NMR signal intensity as a function of temperature in cell C containing an 80:20 mix of Xe:N_2 at 2000 torr total pressure. a) shows the observed experimental data with fits to $P_{\mathrm{Xe}}(t) = 1 - \exp\{-\gamma_{\mathrm{SEOP}} t\}$. For clarity, b) shows the only the fit lines. $T_{\mathrm{opt}} = 70\,^{\circ}\mathrm{C}$.

3.4.2 In-Cell Rb Polarisations

Figure 3.29(b) shows the measured $\langle P_{\mathrm{Rb}} \rangle$ values for the three cells. Cells A and B (blue and green) are the two 50:50 cells, cell C is the 80:20 mix (red). Polarisation measurements were not obtained for all SEOP experiments, but where data is available the trends behave as expected. That is, $\langle P_{\mathrm{Rb}} \rangle$ values for cell A and cell B, which contain the same gas mix, correlate well. On the whole, $\langle P_{\mathrm{Rb}} \rangle$ decreases with increasing temperature. This is to be expected due to the exponential increase in absorbers which have the effect of blocking laser transmission and reducing the global Rb polarisation. Additionally, cell C has lower $\langle P_{\mathrm{Rb}} \rangle$ values which is in keeping with the fact that more spin-destructive Xe is present in the cell. These values represent the maximum possible xenon polarisations that could have been achieved in the cells as P_{Xe} can never exceed P_{Rb}.

3.4.3 T_1 Measurements: In-Cell, Transporter and Measurement Station

Figure 3.30(a) shows the measured in-cell T_1 values for the three cells. Fits to equation 3.3.9 yielded values of 31.2, 39.2 and 41.4 minutes respectively. These values are reasonable but provide room for improvement. For instance, in the recent publications our collaborators reported in-cell T_1 values of 3.78 hrs $\pm$ 0.07 [22], although in the record breaking XeNA publication, in-cell T_1 values of 38 minutes were reported [18]. Two aspects to focus on to improve the T_1 values would be to 1) confirm that there are no flaws with the cell preparation process i.e. during the surfacil coating and rubidium loading stage, 2) confirm that is no contamination in the gas manifold. Oxidised rubidium in the cell is known to increase relaxation.

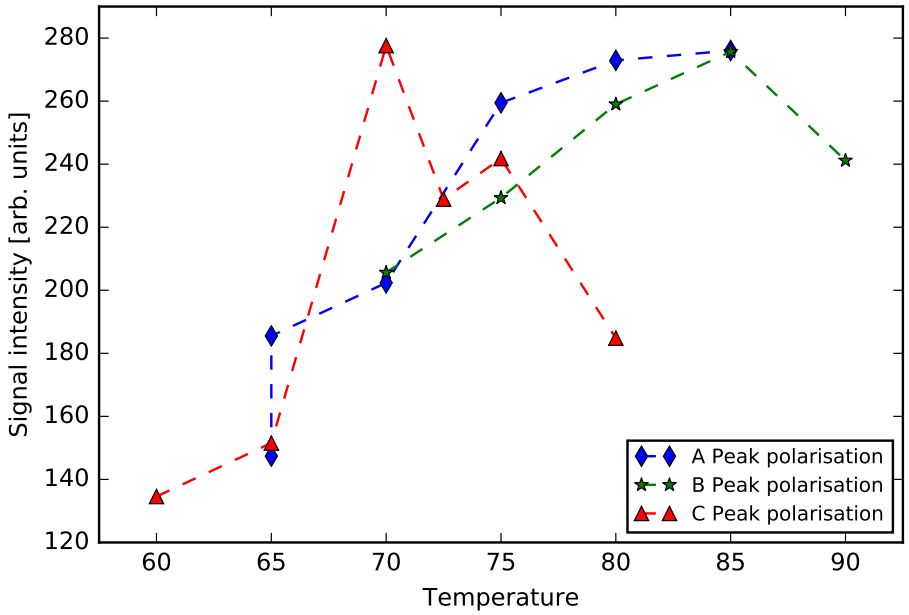

(a)

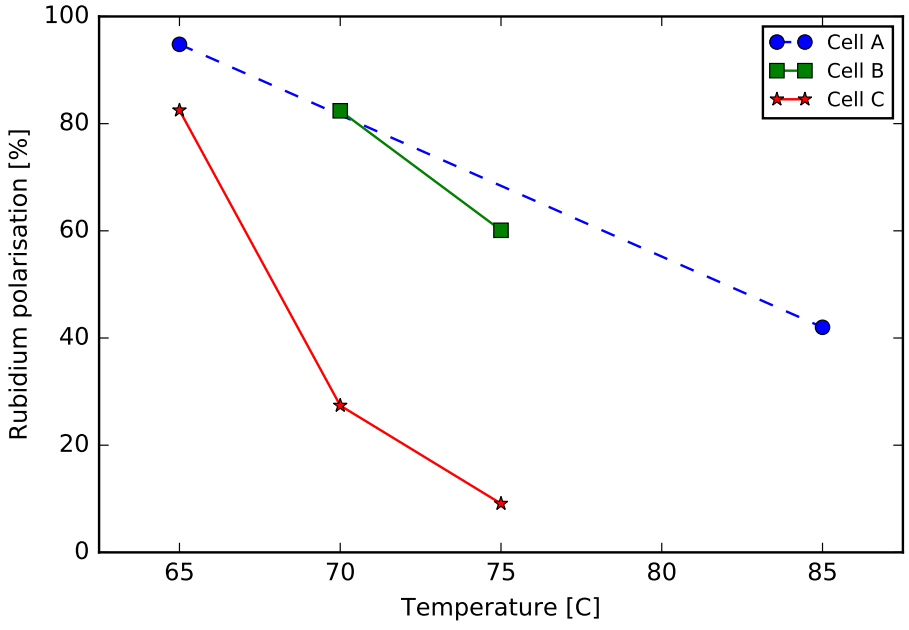

(b)

Figure 3.29: a) Summary of HP-Xe NMR signal intensities in cells A, B and C. This plot shows projected polarisations by evaluating fits of the data to the equation $P_{\mathrm{Xe}}(t) = 1 - \exp\{-\gamma_{\mathrm{SEOP}} t\}$ at $t = \infty$ b) In-cell global Rb polarisations determined using the method described in section 3.3.10.

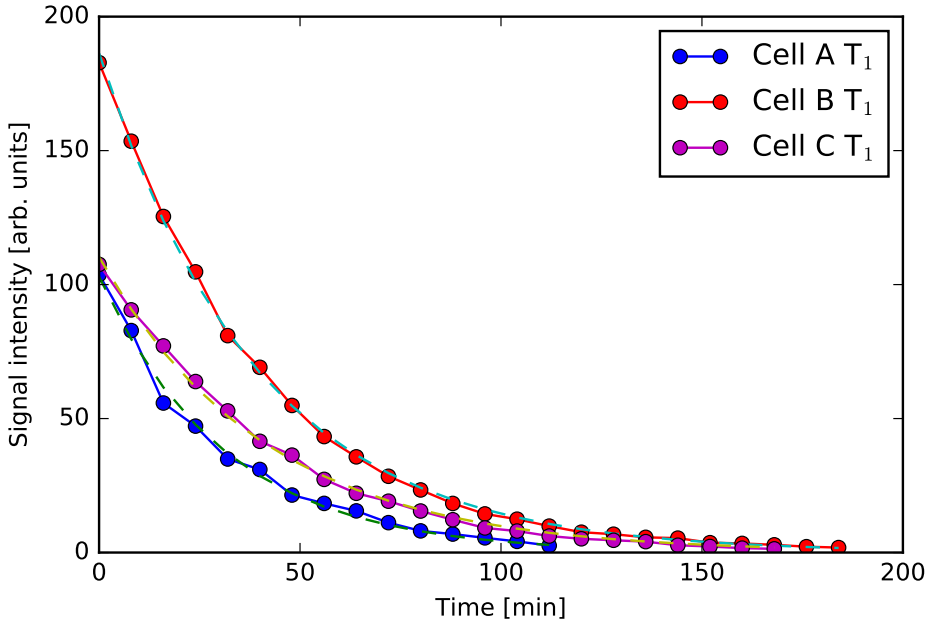

(a)

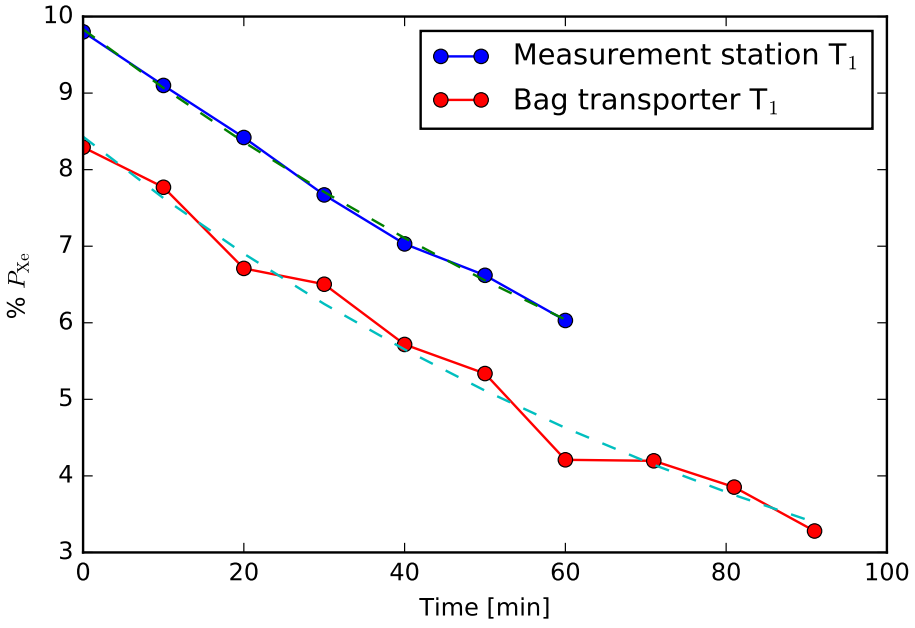

(b)

Figure 3.30: a) In-cell T_1 measurements of 31.2, 39.2, 41.4 minutes respectively for cells A, B and C. b) Transporter and measurement station T_1 measurements. T_1 = 123.2 mins and 100.0 mins, respectively.

3.4.4 Bag Images and Absolute P_{Xe} Measurements

The bag images are displayed in figure 3.31. The bag in image (a) contains 80% Xe and 20% N_2 with a polarisation value of 8.52±0.17% as measured by the measurement station. Scaling for the N_2 within the bag gives an absolute polarisation of 10.22±0.21%. The bag in image (b) contains 50% Xe and 50% N_2 and gave a polarisation value of 7.32±0.12% when measured on the polarisation measurement station. Scaling for the nitrogen present in the bag gives an absolute polarisation of 14.62±0.24%. Transit from the physics department to the MIU was timed as 13 minutes, and scaling for this using the measured T_1 of the low-field transporter gives a polariser ejection value of 16.65±0.27% for the 50:50 mix and 11.64±0.23% for the 80% mix.

These values were low relative to what was expected based on the results from the record holding XeUS and XeNA polarisers on which N-XeUS is heavily based (as stated earlier, in-cell P_{Xe} values of 95±9%, 73±4%, 60±2%, 41±1% and 31±1% at 275, 515, 1000, 1500 and 2000 torr Xe have previously been achieved on XeUS [20]), so checks were performed to determine what caused the shortfall in polarisation. It was found by power measurements that the output of the laser had in fact dropped by over 50%, and at the time of the imaging experiments output was 50 W for a driving current of 52 A, where previously it had been ∼130 W. While disappointing in one respect, it is interesting to consider that even with a compromised laser the N-XeUS polariser was not only successfully demonstrated, but capable of matching the performance of the currently installed GE polariser, the performance of which is close to but has not exceeded 10% in a 1 litre bag 7.3(b).

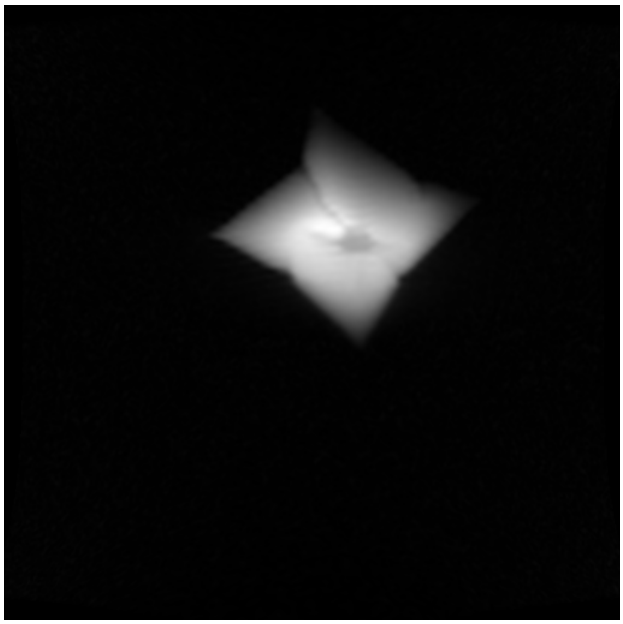

(a)

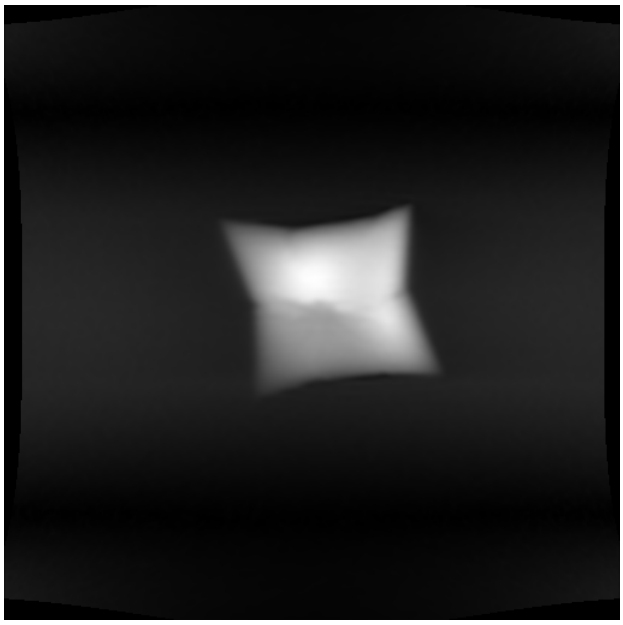

(b)

Figure 3.31: a) Bag 1, 80% xenon and 20% N_2. Polarisation measurement station measured a value of 8.52±0.17% . Scaling for N_2 content and transporter T_1 gives a post-ejection polarisation of 11.64±0.23% b) Bag 2, 50% xenon and 50% N_2. Polarisation measurement station measured a value of 7.32±0.12%. Scaling for N_2 content and transporter T_1 gives a post-ejection polarisation of 16.65±0.27%.

3.4.5 Prototype Low-Field NMR Spectrometer

The prototype NMR spectrometer was compared directly to the commercial Kea spectrometer at the conclusion of a build-up experiment 3.32(a,b), the result of which can be seen in figure 3.32(c,d). Acquisition parameters were matched as closely as possible, for instance: the B_1 pulse amplitude and duration of the Kea were measured directly by oscilloscope and matched on the prototype spectrometer to ensure identical excitations. SEOP was conducted for a period of 35 minutes and the build-up of HP-Xe signal was measured every 5 minutes using the prototype spectrometer, this build-up can be seen in the top half of figure 3.32(a,b). At the 35 minute mark, immediately after the acquisition with the prototype spectrometer, the NMR coil was detached and connected to the commercial Kea spectrometer and an acquisition was made. Spectra from both spectrometers at $t = 35$ minutes can be seen in figure 3.32(c,d). The commercial system provides superior SNR - a factor of $\sim$707, while the prototype spectrometer yields a lower SNR of $\sim$125. It is interesting to note however the level of SNR provided by the prototype spectrometer is clearly enough to monitor xenon dynamics within the cell, as demonstrated by the build-up data in figure 3.32, and this fact becomes more interesting still when cost/SNR is considered. The commercial system, costing approximately \$20,000 has a \$ per SNR of 28. The prototype spectrometer on the other hand, comes in at 2.4 \$ per SNR and costs over $\sim$\$19,000 less ($\sim$\$300): the Kea is 66 times more expensive while performing with only 5 times greater SNR. SNR was determined by dividing the maximum value by the standard deviation of a noise region (in this case 42.8 kHz to 43 kHz).

Promisingly, there is scope for further optimisation of the prototype spectrometer. As no mixer is used in the current configuration, the bandwidth

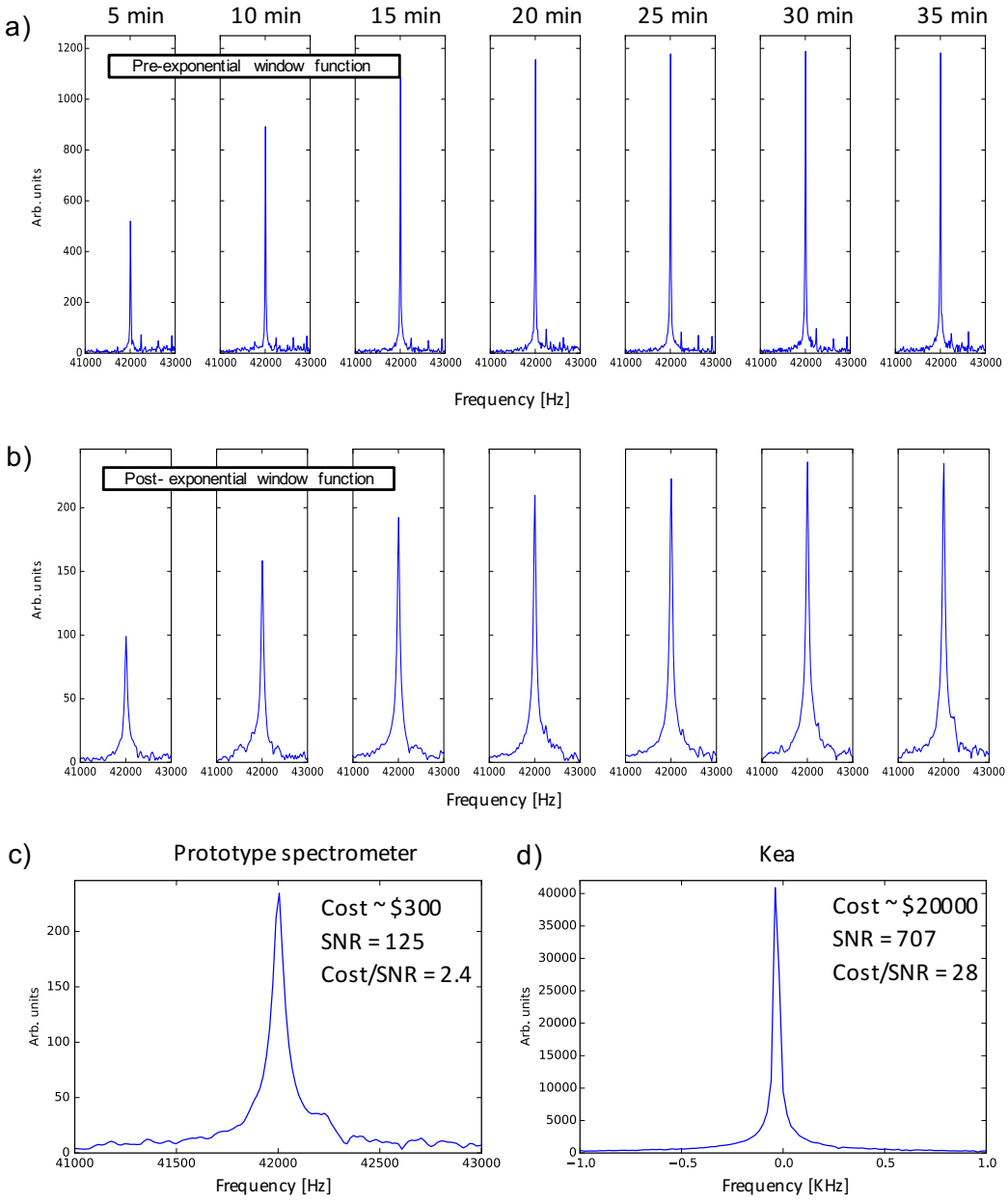

Figure 3.32: a) Time-course magnitude spectra from a HP-Xe build-up experiment measured with the prototype NMR spectrometer at intervals of 5 minutes. b) same as a) but with exponential window function ($e^{(-130t)}$) applied. (c,d) NMR spectra acquired in quick succession using the prototype and Kea NMR spectrometers.

of the acquisition is constrained to be at least twice the B_1 frequency by the Nyquist theory: a lower frequency would result in under-sampling. Also, the buffer of the Analog Discovery is fixed at 8192 data points. In the data presented, the B_1 frequency was 42 kHz, and the bandwidth (BW) was set to 130 kHz (figure 3.33(a,c)), giving a dwell time (DT) of 7.69×10^{-6} s. With the fixed buffer, the acquisition period was constrained to be 60 ms (= DT $\times$ buffer), as can be seen in figure 3.33(b,d). If a mixer were incorporated - which can be based on cheap OP AMP ICs - the bandwidth could be reduced. This would result in less noise by sampling a narrower frequency range, and boost the signal because the acquisition period can be longer (and the FIDs detected here have not fully decayed by the end of the 60 ms acquisition). Besides addition of a mixer, the quality of the data could be further improved by better matching the amplitude of the FID to the ADC (by further increasing the pre-amp gain) - the current voltage range is roughly 1 V_{pp} in a 25 V window (figure 3.33(b,d)).

An exponential window function was applied ($e^{(-130t)}$) to the raw FID data for two reasons. Firstly, without the function applied, the curtailed FID can be considered to be convoluted with a box function: there is a immediate drop to 0 at the end of the acquisition period because the FID has not yet fully decayed (figure 3.33(b)). When fourier transformed, this step causes a 'ringing' artefact that diminishes the quality of the spectrum by producing a non-flat baseline (figure 3.33(a)). With the function applied, this step can be smoothly tapered to 0 3.33(d)). Secondly, to increase SNR. The exponential window function is commonly used to increase the SNR of NMR spectra, because a) it gives greater weight to the FID at small time values where it has the greatest amplitude, and lesser weight to the large time values where its amplitude decreases into the noise and b) in the frequency domain it has a Lorentzian form and this is

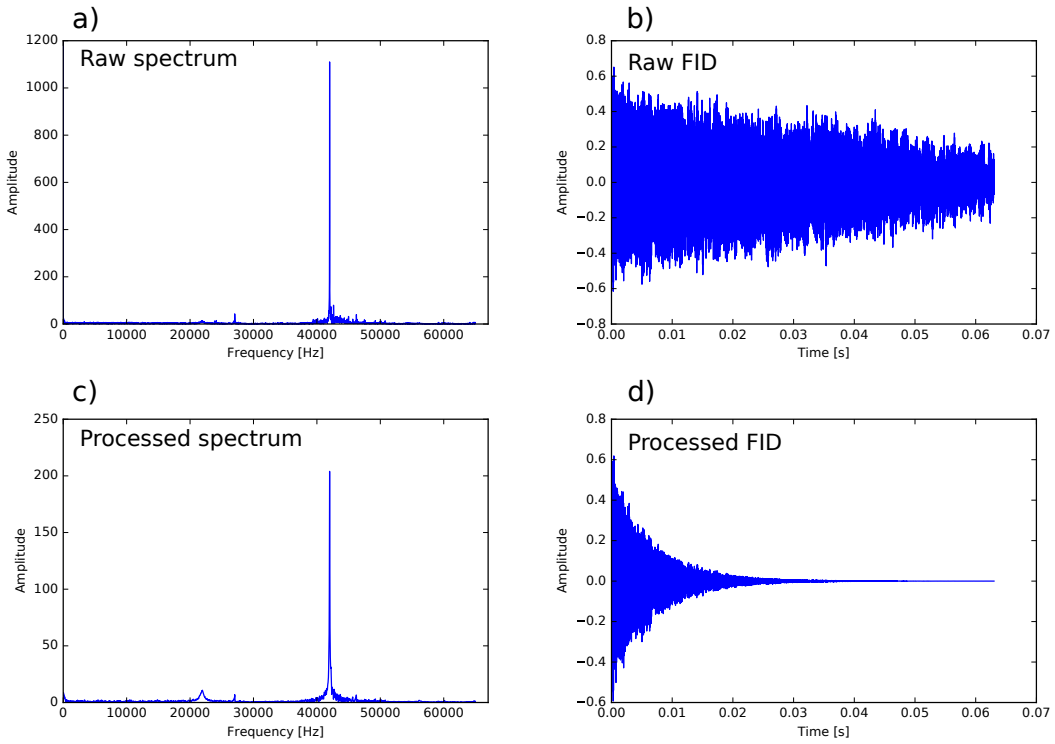

Figure 3.33: Raw and processed FIDs and magnitude spectra from the prototype low-field NMR spectrometer. a) Magnitude spectrum resulting from the fourier transform of b) which is the raw Xe FID data. c) is the magnitude spectrum of d) which is the exponentially filtered version of the raw data in b). It can be seen that the filter tapers the FID smoothly to zero, and results in a smoother spectrum with greater SNR.

the natural shape of NMR lines, therefore no colouring of the data occurs.

3.5 Conclusion

In this chapter the construction and demonstration of a clinical scale hyperpolariser was described. Although performance of the polariser was compromised due to a faulty laser, the achieved polarisation levels (16.65±0.27% for the 50:50 mix and 11.64±0.23% for the 80% mix, corresponding to apparent polarisations of 8.33±0.14% and 9.312±0.18% respectively) were still comparable to that of the existing continuous-flow system installed at the MIU (the performance of which has not exceeded 10% polarisation in 1 litre bags during

the course of the study (see 7.3(b))). In the coming months, the laser of the N-XeUS polariser will be replaced with an improved model that has a 2-fold narrower linewidth (FWHM = 0.15 nm) with a further 30 W of output power (P = 180 W). The gain in SNR of the MR images when the N-XeUS polariser is ultimately operational in the clinic should therefore improve firstly by approximately the factor the current laser fell short (a factor of more than 2), plus a substantial additional factor, due to both the narrower linewidth and increased power of the new laser. As will be demonstrated in the next chapter, xenon-rich SEOP gains differentially at narrower linewidths. For instance, the simulation in figure 4.19 shows that P_{Xe} of a 2000 torr Xe mix increases from 46.9% to 57.1% when the linewidth of the pump laser is halved from 0.3 nm to 0.15 nm at 170 W - a gain of over 10% polarisation, and that is without a boost in additional power (note how close this example is to the current and incoming lasers). Once the new laser is installed and optical cell preparation is brought in line with that of our collaborators (who have obtained longer than 3 hr T_1's [22]) the polarisation performance of the N-XeUS polariser stands a very strong chance of setting new records, particularly if further modifications laid out in the next chapter are implemented.

The N-XeUS polariser is now installed at the medical imaging unit (MIU) at the Queens Medical Centre and, pending MHRA approval and installation of the new laser, will provide HP-xenon in the ongoing Xe lung imaging study. The N-XeUS polariser introduced new clinically-oriented features to the XeUS line of polarisers, including modifications to the gas manifold enabling a nitrogen fill/purge capability, and permitting the removal of the costly turbomolecular vacuum pump system. Simulations in the next chapter show how this polariser and the existing XeNA and XeUS polarisers can be modified for enhanced performance.

Additionally, a low-cost low-field prototype NMR spectrometer was developed and demonstrated, which will further reduce the capital cost of such a polariser and further facilitate automation of the system. The prototype reached a high level of maturity, achieving an SNR of 125 at a cost of ∼$300. This is 66 times cheaper than the commercial alternative currently in use on N-XeUS (costing ∼$20000) while only being outperformed by a factor of 5. Encouragingly, there is still room to affordably improve the design by 1) including a mixer to reduce the bandwidth (and increase acquisition periods), and 2) further increasing the amplification of the FID.

At such a low cost and with such potential for customisation and integration (in terms of both hardware and software), the prototype NMR spectrometer is well placed to be incorporated into the N-XeUS polariser and has the potential to be an attractive prospect to any hyperpolarisation lab engaged in the development of HP methods or instrumentation.

Chapter 4

Simulations of Xenon-Rich Stopped-Flow SEOP

Spin-exchange optical pumping of Xe can be described with the so-called standard model of SEOP. Originally presented by Chupp and Wagshul for simulations of helium SEOP [115], the model has since been adapted for Xe SEOP and was recently updated by Norquay *et al.* in 2013, when they used the model to optimise their continuous-flow polariser for lung imaging applications [15]. A long existing issue with the model, which to date has only been applied to continuous-flow polarisers, is that it predicted polarisation levels that could not be realised in experiment or by large scale polarisers that were built, including the polariser presented by Norquay *et al.* which yielded 12% polarisation against a predicted 24%. Worse still, it was not understood why.

In 2015 this issue was addressed by Freeman *et al.* [16]. Their version of the model reconciled the long existing gap between the predicted performance and experimental reality for continuous-flow systems by postulating the presence of rubidium electronic spin-destroying, xenon relaxing, laser-attenuating rubidium clusters in continuous-flow polarisers, and these effects were incorporated in the model accordingly. This model was validated under a variety of continuous-flow conditions and it succeeded in describing data generated using

a range of optical cell sizes and a range of laser linewidths [16].

Xenon-rich stopped-flow SEOP is now well established in the literature [19, 20, 19, 21, 22] and holds the record for P_{Xe} performance [18], but very little has been shown in terms of modelling the regime, bar [109]. For instance, there has been no validation against the widely accepted model of SEOP described above. In this chapter, the standard model is used for the first time to simulate stopped-flow SEOP under conditions of high laser fluxes and high xenon densities; i.e. the a-typical regimes of the XeUS, XeNA and N-XeUS polarisers. The simulations validate the result that, contrary to expectation, high xenon polarisations can be obtained at high xenon densities (i.e. in-spite of high levels of Rb-Xe spin-destruction that scale with xenon density), and therefore show that the 'surprising' performance of the XeNA and XeUS polarisers is in fact in keeping with existing theory.

This chapter has the following structure: firstly, the model is described, as are modifications that enable simulation of stopped-flow SEOP which include: (1) the omission of flow optimisation terms which are specific to continuous-flow polarisers, (2) the inclusion of retro-reflection into the optical pumping model, and (3) the omission of the rubidium cluster terms, which are not relevant to the stopped-flow regime. The model is then used to simulate for the early experimental results obtained by the group when the benefits of going to higher xenon densities and lower temperatures became first evident during the first use of VHG narrowed LDAs [23]. This allows for validation of the model against experimental data under 'low-power' conditions (conditions are tabulated in table 4.3), and also for comparison against early simulations based on similar theoretical framework that were conducted by the group. Next, the model is validated against an extensive data set that was generated using the XeUS polariser during a multi-parameter optimisation study [20]. This is a

rich dataset containing P_{Xe} as a function of five xenon-rich gas mixtures (∼275, ∼515, ∼1000, ∼1500 and ∼2000 torr), four laser powers (∼100, ∼125, ∼140 and ∼170 W at 0.3 nm FWHM) and a broad range of 'low' temperatures (45-95 C).

Following validation against the two datasets, the model is used to explore regimes and experimental scenarios which may yield further gains in magnetisation output. For instance, what happens to the magnetisation output when the total pressure of the system is doubled? or if the diameter of the optical cell is increased? or if further other buffer gases are added to the system (such as helium)? or what if the linewidth of the laser is further reduced? Results of these simulations are presented and will inform the design of subsequent stopped-flow polarisers.

Finally, an unexpected trend in the optimal polarisation against power absorbed is presented and explored. It may provide, in situations where full thermal control can be maintained, a way to quickly optimise operating conditions in stopped-flow polarisers.

4.1 The Standard Model of SEOP

The standard model can be conceptually divided into three key steps. Firstly the model begins with the determination of the optical pumping rate, γ_{OP}. Second, the optical pumping rate is used to determine the rubidium polarisation, P_{Rb}. Finally, P_{Rb} is used to determine an estimate for the xenon polarisation, P_{Xe}.

4.1.1 Optical Pumping

The optical pumping rate, γ_{OP}, is dependent on the absorption cross-section of the rubidium, σ_0, and the photon flux of the laser, Φ, as it traverses the

length of the optical pumping cell, z:

$$\gamma_{\mathrm{OP}}(z,\nu) = \int \Phi(z,\nu)\sigma_s(\nu)d\nu. \tag{4.1}$$

The Rb absorption cross-section has a Lorentzian line-shape that varies as a function of frequency, ν, in the following way:

$$\sigma_{\mathrm{s}}(\nu) = \sigma_0 \frac{\Gamma_{\mathrm{Rb}}^2}{4(\nu-\nu_{D_1})^2 + \Gamma_{\mathrm{Rb}}^2} \tag{4.2}$$

where Γ_{Rb} is the FWHM of the pressure broadened Rb cross-section which has a central frequency ν_{D_1} of 794.77 nm. The peak amplitude σ_0 is given by:

$$\sigma_0 = \frac{2r_{\mathrm{e}}cf}{\Gamma_{\mathrm{Rb}}}, \tag{4.3}$$

where r_{e} is the classical electron radius, c is the speed of light, and f is the oscillator strength of the D_1 transition, which has been shown to have a value of 0.337 [15].

The spectral profile of the laser has a Gaussian line-shape and varies with frequency according to:

$$I(\nu) = I_0 e^{-(\frac{\nu-\nu_{\mathrm{Las}}}{\Gamma_{\mathrm{Las}}})^2}, \tag{4.4}$$

where ν_{Las} is the centre frequency of the laser, Γ_{Las} is the standard deviation of the Gaussian laser spectrum[1], and I_0 is the beam intensity on the cell front which is given by:

$$I_0 = \frac{P}{Ah\sqrt{\pi}\Gamma_{\mathrm{Las}}\nu_{\mathrm{Las}}}, \tag{4.5}$$

where P is the power incident on the front of the cell which has a cross-sectional area A and h is the Planck constant. The photon flux Φ through the cell can

[1] conversion of the more frequently quoted FWHM to standard deviation was done using: $\Gamma_{\mathrm{Las}} = \frac{Las_{\mathrm{FWHM}}}{(2\sqrt{2\ln(2)})}$

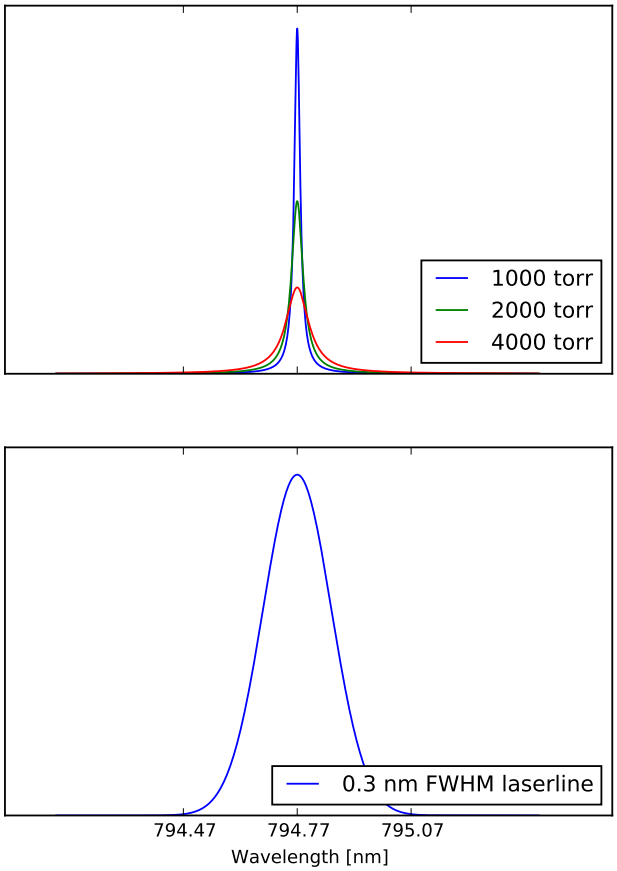

Figure 4.1: Comparison of a 0.3 nm FWHM laser linewidth (bottom) to the pressure broadened Rb D_1 cross-section (top) for pressures of 1000 torr, 2000 torr and 4000 torr. Broadening occurs at a rate of ∼18 GHz per amagat.

be defined as;

$$\Phi(z,\nu) = I(\nu)e^{(-\lambda^{-1}(z,\nu)z)}, \tag{4.6}$$

where λ^{-1} is the position dependent absorption length. For a cell illuminated by a circularly polarised beam of positive helicity σ^+, λ^{-1} is defined as:

$$\lambda^{-1}(z,\nu) = \sigma_s(\nu)[\mathrm{Rb}](1 - P_{\mathrm{Rb}}(z)) \tag{4.7}$$

in which [Rb] is the number density of the Rb vapour in the cell (illustrated

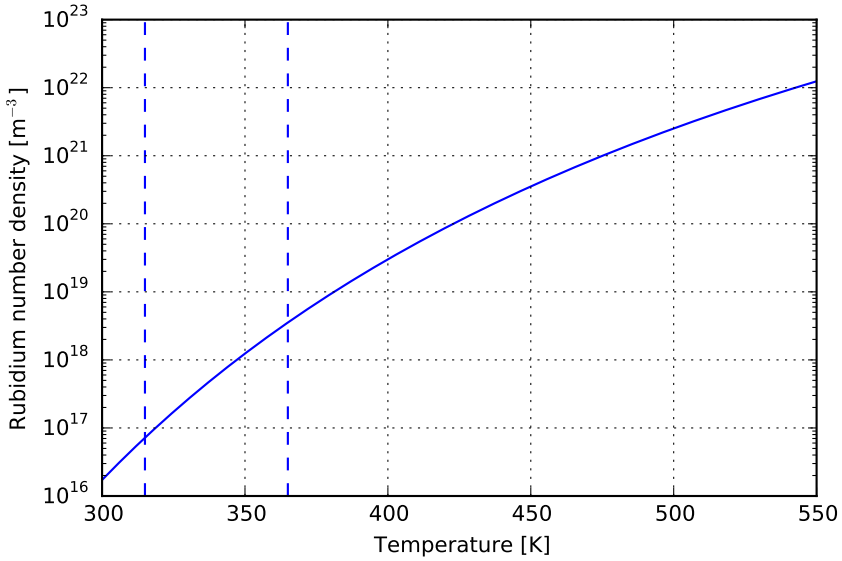

Figure 4.2: Rb number density ([Rb]) against temperature. The dashed lines indicate the temperature range in which the XeUS polariser operates.

in figure 4.2) and $P_{\mathrm{Rb}}(z)$ is the position dependent Rb polarisation. [Rb] in this case has been determined using the Killian formula as quoted by Freeman [17]:

$$[\mathrm{Rb}] = \frac{10^{26.180-(\frac{4040}{T})}}{T}. \tag{4.8}$$

To solve for the optical pumping rate γ_{OP}, equations (4.1), (4.2) and (4.6) can be combined to give the following integral (in accordance with (4.1)) and solved numerically using Simpson's integral method over a given frequency range $[\nu_{\mathrm{min}}, \nu_{\mathrm{max}}]$ for discrete values of z:

$$\gamma_{\mathrm{OP}}(z,\nu) = \int_{\nu_{\mathrm{min}}}^{\nu_{\mathrm{max}}} I_0 e^{-(\frac{\nu-\nu_{\mathrm{Las}}}{\Gamma_{\mathrm{Las}}})^2} e^{(-\lambda^{-1}z)} \sigma_0 \frac{\Gamma_{\mathrm{Rb}}^2}{4(\nu-\nu_{D_1})^2+\Gamma_{\mathrm{Rb}}^2} d\nu \tag{4.9}$$

where $\nu_{\mathrm{min}} = \nu_{\mathrm{Las}} - 5\Gamma_{\mathrm{Las}}$ and $\nu_{\mathrm{max}} = \nu_{\mathrm{Las}} + 5\Gamma_{\mathrm{Las}}$.

In a similar fashion to Norquay *et al.*[15], γ_{OP} is evaluated at 25 discrete points along the optical cell. Figure 4.3 shows the unevaluated function (4.9) for each z value in a cell heated to 82 °C loaded with 2000 torr Xe and 200 torr

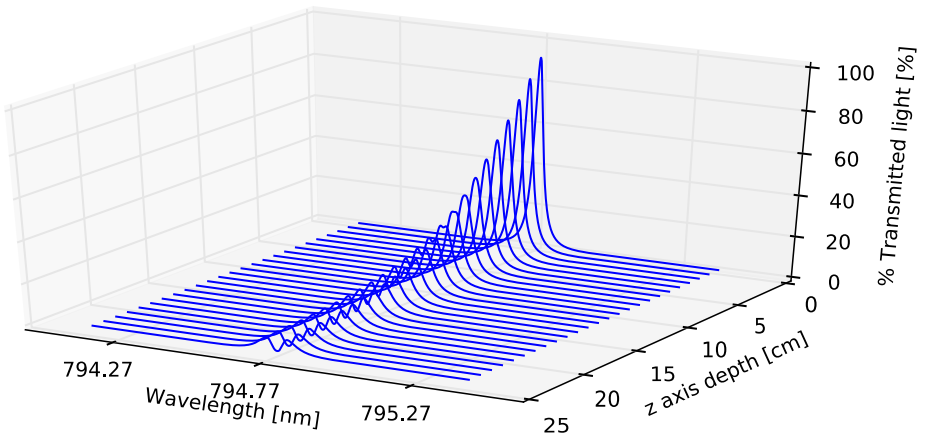

Figure 4.3: Absorption of the incident laser light by the D_1 transition as a function of position within the optical cell at 82 °C in a cell loaded with 2000 torr Xe and 200 torr N_2. P = 170 W at 0.3 nm FWHM. The calculations are evaluated in the frequency domain (equation 4.9) but plotted here in terms of wavelength for ease of reading.

N_2, illuminated by 170 W of laser power with a FWHM of 0.3 nm. Preferential absorption of the light can be observed at the central wavelength by the time the light reaches the back of the optical cell.

4.1.2 Rubidium Polarisation

The rubidium polarisation, P_{Rb}, is a function of the optical pumping rate, $\gamma_{\mathrm{OP}}(z,\nu)$, and the rubidium spin destruction Γ_{SD}:

$$P_{\mathrm{Rb}} = \frac{\gamma_{\mathrm{OP}}}{\gamma_{\mathrm{OP}} + \Gamma_{\mathrm{SD}}}. \tag{4.10}$$

Spin destruction of the rubidium electronic polarisation, Γ_{SD}, can occur by two mechanisms; (1) binary collisions with atoms or (2) via the formation of short-lived Rb-Xe van der Waals molecules (vdW). The binary term is:

$$\Gamma_{\mathrm{SD}}^{\mathrm{BC}} = \sum_{\mathrm{i}} [\mathrm{G_i}] \kappa_{\mathrm{SD}}^{\mathrm{Rb\text{-}i}}, \tag{4.11}$$

Table 4.1: Gas-specific binary spin-destruction rates.

Cross-section	**Value**
Rb-Rb	$\kappa_{\mathrm{SD}}^{\mathrm{Rb\text{-}Rb}} = 4.2 \times 10^{-13}$ cm^{3}s^{-1} [116]
Rb-He	$\kappa_{\mathrm{SD}}^{\mathrm{Rb\text{-}He}} = 3.45 \times 10^{-19}(T/298\ \mathrm{K})^{4.26}$ cm^{3}s^{-1} [117]
Rb-N_2	$\kappa_{\mathrm{SD}}^{\mathrm{Rb\text{-}N_2}} = 3.44 \times 10^{-18}(T/298\ \mathrm{K})^{3}$ cm^{3}s^{-1} [118]
Rb-Xe	$\kappa_{\mathrm{SD}}^{\mathrm{Rb\text{-}Xe}} = 6.02 \times 10^{-15}(T/298\ \mathrm{K})^{1.17}$ cm^{3}s^{-1} [119]

where $\kappa_{\mathrm{SD}}^{\mathrm{Rb\text{-}i}}$ is the Rb spin-destruction cross-section for Rb binary collisions with each of the gas atoms present in the cell, and where $[\mathrm{G_i}]$ is the atomic number density of each gas. Values of the cross-sections can be found in table (4.1).

The Rb spin-destruction rate due to van der Waal's Rb-Xe molecules has been estimated as [120]:

$$\Gamma_{\mathrm{SD}}^{\mathrm{vdW}} = \left(\frac{66183}{1 + 0.92\frac{[\mathrm{N_2}]}{[\mathrm{Xe}]} + 0.31\frac{[\mathrm{He}]}{[\mathrm{Xe}]}}\right)\left(\frac{T}{423}\right)^{-2.5} \tag{4.12}$$

where square brackets indicate gas number density in m^{-3}. Gathering expressions 4.12 and 4.11, the total spin destruction is thus:

$$\Gamma_{\mathrm{SD}} = \Gamma_{\mathrm{SD}}^{\mathrm{BC}} + \Gamma_{\mathrm{SD}}^{\mathrm{vdW}}. \tag{4.13}$$

Due to the fact that the expression for P_{Rb} (equation 4.10) is a function of itself (by equations 4.1, 4.6 and 4.7) it must be solved numerically and in this case it was treated as an equilibrium function. The approach taken was as follows: an initial P_{Rb} value was fed into the calculations (P_{Rb}=0), and an output value of P_{Rb} was calculated. This value was then compared to the intial P_{Rb} value. If the difference was greater than 1×10^{-4} the new value was fed back into the calculation as the initial polarisation and the output polarisation was calculated again. This process continues until the difference is less than 1×10^{-4}, i.e. the two values are the same to an accuracy of

Table 4.2: Gas-specific van der Waal spin-exchange rates.

Atomic species	**vdW rate**
Xenon	$\xi_{Xe} = 5230$ Hz [121]
Nitrogen	$\xi_{N_2} = 5700$ Hz [122]
Helium	$\xi_{He} = 17000$ Hz [12]

99.99%. At which point the value is accepted as the true P_{Rb} value. This procedure is undertaken for each of the 25 discrete spatial points along the length of the cell. The average of the 25 points is then taken to obtain the spatially averaged P_{Rb} value $\langle P_{\mathrm{Rb}} \rangle$ which is used in the calculation of xenon polarisation P_{Xe}. In this way the optical pumping section of the model and the rubidium polarisation section of the model are closely linked in that they must be evaluated simultaneously: each new calculation of P_{Rb} requires evaluation of the γ_{OP} integral, for each discrete z.

4.1.3 Xenon Polarisation

In a continuous-flow system, the nuclear spin polarisation of ^{129}Xe generated through spin-exchange with polarised Rb electrons after a given residence time t_{res} is:

$$P_{\mathrm{Xe}}^{\mathrm{cell}}(t_{res}) = \frac{\gamma_{\mathrm{SE}}}{\gamma_{\mathrm{SE}} + \Gamma} \langle P_{\mathrm{Rb}} \rangle (1 - \exp^{-(\gamma_{\mathrm{SE}} + \Gamma) t_{res}}) \tag{4.14}$$

where t_{res} is the amount of time the xenon spends in the optical pumping cell as it flows on its path from the gas cylinder to the cold finger, Γ is the loss rate of ^{129}Xe nuclear polarisation and $\langle P_{\mathrm{Rb}} \rangle$ is the spatially averaged rubidium polarisation within the optical cell. Γ is thought to be dominated by wall relaxation and is equal to $\frac{1}{\mathrm{T}_1}$, therefore experimentally measured values of T_1 can be used in the simulations to calculate Γ.

Finally, the Rb-Xe spin-exchange rate, γ_{SE}, which is the sum of a binary

and vdW's terms, is given by the following expression:

$$\gamma_{\mathrm{SE}} = \gamma_{\mathrm{SE}}^{\mathrm{vdW}} + \gamma_{\mathrm{SE}}^{\mathrm{BC}} = \left(\frac{1}{\sum_{\mathrm{i}} \left(\frac{[\mathrm{G_i}]}{\xi_{\mathrm{i}}} \right)} + \kappa_{\mathrm{SE}}^{\mathrm{Rb\text{-}Xe}} \right) [\mathrm{Rb}], \tag{4.15}$$

where ξ_{i} is the vdW rate for each gas atom, with number density again given by $[\mathrm{G_i}]$. The vdW rates are given in table (4.2). $\kappa_{\mathrm{SE}}^{\mathrm{BC}}$ is the binary collision spin exchange cross section and has been calculated to be 2.17×10^{-16} $\mathrm{cm^3 s^{-1}}$ [123].

4.1.4 Modifications to the Optical Pumping Model: Retro-Reflection, Stopped-Flow and Rb Clusters

In stopped-flow SEOP, the SEOP gas mixture is held static within the optical cell and therefore t_{res} becomes the total optical pumping time t:

$$P_{\mathrm{Xe}}^{\mathrm{cell}}(t) = \frac{\gamma_{\mathrm{SE}}}{\gamma_{\mathrm{SE}} + \Gamma} \langle P_{\mathrm{Rb}} \rangle (1 - \exp^{-(\gamma_{\mathrm{SE}} + \Gamma)t}). \tag{4.16}$$

In the case that wall relaxation is low (and hence the $\mathrm{T_1}$ is long), the xenon nuclear spin polarisation will accumulate according to equation (4.16) and the polarisation will reach steady state as t tends infinity. Under this condition the terminal polarisation can be calculated as:

$$\lim_{t \to \infty} P_{\mathrm{Xe}} = \frac{\gamma_{\mathrm{SE}}}{\gamma_{\mathrm{SE}} + \Gamma} \langle P_{\mathrm{Rb}}(z, r) \rangle. \tag{4.17}$$

The XeNA, XeUS and N-XeUS polarisers utilise retro-reflectors in order to make use of circularly polarised photons that have passed through the optical cell and would otherwise be wasted, directing them back along the optical axis. To simulate for this, the rubidium polarisation is first calculated in the absence of retro-reflection in the manner described in the previous sections to determine the amount of transmission if there were no retro-reflector present. The rubidium polarisation is then re-calculated but as though a second laser

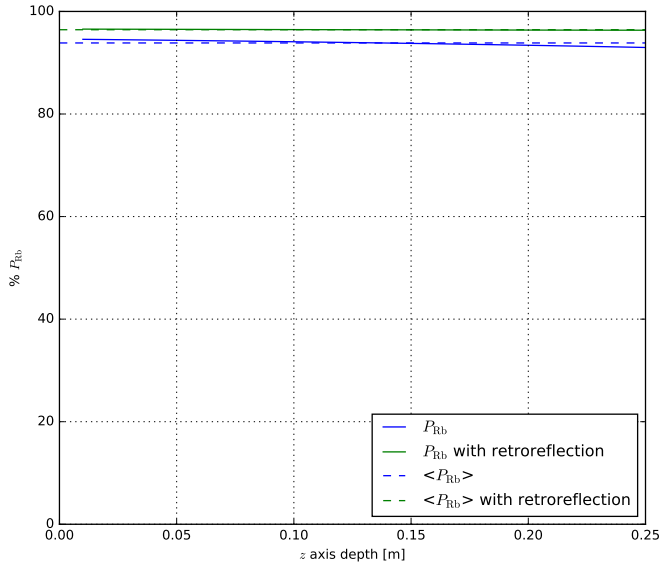

(a)

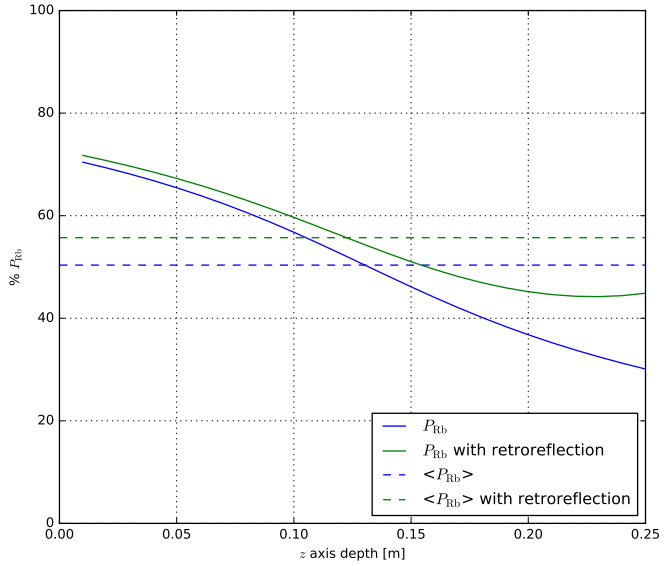

(b)

Figure 4.4: a) P_{Rb} with and without retro-reflection as a function of z for a 275 torr Xe loading at 82 °C. b) P_{Rb} with and without retro-reflection as a function of z for a 2000 torr Xe loading at 82 °C.

is simultaneously incident on the optical cell from the far end with power $P_2 = P_1 \times f_{tr}$, where f_{tr} is the fraction of the light from laser 1 (Las_1) transmitted through the cell. In the retro-reflection case, the expression of $\gamma_{\mathrm{OP}}(z,\nu)$ therefore becomes:

$$\gamma_{\mathrm{OP}}^{\mathrm{Retro}}(z,\nu) = \gamma_{\mathrm{OP}}^{\mathrm{Las_1}}(z,\nu) + \gamma_{\mathrm{OP,}}^{\mathrm{Las_2}}(z,\nu) \tag{4.18}$$

where $\gamma_{\mathrm{OP}}^{\mathrm{Las_1}}$ and $\gamma_{\mathrm{OP}}^{\mathrm{Las_2}}$ must be evaluated simultaneously. The effect of retro-reflection on the rubidium polarisation is illustrated in figures 4.4(a) and 4.4(b).

The final modification, with respect to the model presented by Freeman *et al.*, is that the newly introduced Rb cluster terms have been omitted. Freeman *et al.* state that Rb clusters are paramagnetic, and cause depolarisation of Rb, depolarisation of Xe, and cause undue scattering of the incident laser light. Further, they recount the observations of Atutov *et al.* [124] who observed that the clusters, when irradiated with light resonant at the D_1, become unstable and explode releasing free electrons which would further depolarise Rb and Xe in a SEOP cell.

The Rb cluster formation mechanism is the flow of cold gas over a molten alkali metal [124]. These conditions precisely mirror those of continuous-flow polarisers: cold noble gas flow over molten alkali metal. This mechanism is not present in the stopped-flow polarisers, so these effects were omitted from the model.

Now that such a severe source of relaxation has been identified within the continuous-flow polarisers the polarisation levels achieved in these systems is certain to improve as solutions to mitigate the effect are developed. Freeman *et al.* have already begun to develop and implement such solutions. These include: an optical cell with a rubidium pre-saturator to prevent the formation of Rb clusters; spectrally narrowed lasers that permit operation at a lower

pressure and the use of more efficient optical flats; a new cold finger design with a longer path length that facilitates more complete collection of the xenon while maintaining a uniform temperature across the Xe ice to reduce T_1 relaxation. With these changes implemented they have already seen an increase from 9% to 34% in 300 ml dose production [17] and anticipate further gains.

4.1.5 Implementation

All code was written in the Python programming language, as provided within the freely available Anaconda distribution. Correct execution of the code was confirmed by reproducing values quoted by Norquay *et al.* in [15].

Table 4.3: Physical properties that govern the input parameters for simulations. Columns marked with a * are simulations only.

	JMR	**XeUS mapping data**	**Xeus: Helium***	**XeUS: 3 inch cell***	**XeUS: 3 inch cell, constant V***
Cell radius [cm]	1.27	2.54	2.54	3.81	3.81
Cell cross-sectional area [cm^2]	5.07	20.27	20.27	45.6	45.6
Cell length [cm]	15	25	25	25	11.11
Cell volume [cm^3]	76.01	506.71	506.71	1140.09	506.71
Surface area	129.83	439.52	439.52	689.68	357.17
Surface-area-to-volume ratio	1.71	0.87	0.87	0.61	0.70
In-cell T_1 [hrs]	0.16	2.5	2.5	3.56	3.1
Γ_{SD} [Hz]	0.00166	0.0001111	0.0001111	0.00007803	0.00008961
Laser power [W]	29	100, 125, 140, 170	170	170	170
Laser FWHM [nm]	0.25*, 0.27, 3*, 10*	0.3	0.3	0.3	0.3
Retro-reflection	No	Yes	Yes	Yes	Yes

4.2 Results and Discussion

4.2.1 Comparison to the JMR Data

Figure 4.5 shows the results of the SEOP experiments where the rich-xenon stopped-flow regime was first found (reproduced from [23] with permission). The figure (also shown earlier as part of a composite in figure 3.2 reprinted from [46]) shows the NMR signal intensity as a function of temperature for the gas mixes investigated which in this case were 50, 100, 300, 500, 950, 1400 torr of Xe, each backfilled to 2000 torr with N_2. It can be seen that the maximum signal intensity for each gas mix occurs at a different temperature, and that as the xenon density ([Xe]) increases, its respective peak value occurs at an increasingly lower temperature. This trend can be seen more clearly in the figure inset. These datasets were acquired using *in situ* NMR spectroscopy, a 1 inch optical cell 15 cm in length, and a 29 W pump laser of 0.27 nm FWHM. The T_1 was measured to be 0.16 hours. Details can be reviewed in table 4.3.

Figure 4.6(a) shows a plot of the expected magnetisation, equivalent to the NMR signal intensity shown in figure 4.5, as predicted by the standard model of SEOP for these experimental parameters. It can be seen that many of the characteristics of the data are reproduced. As [Xe] increases, the respective peak in magnetisation occurs at increasing lower temperatures. This can be seen more clearly in figure 4.6(b), which is equivalent to the inset of figure 4.5. It is not possible to establish how well normalised the simulation is to the experimental results as only the signal intensity was quoted (as opposed to the absolute in-cell polarisations), but the overall trends are well reproduced. In terms of the exact temperatures the for the peak magnetisations, the simulations, at their worst, fall to within 12 °C of the experimental values.

When the experimental results in figure 4.5 (from [23]) were first obtained,

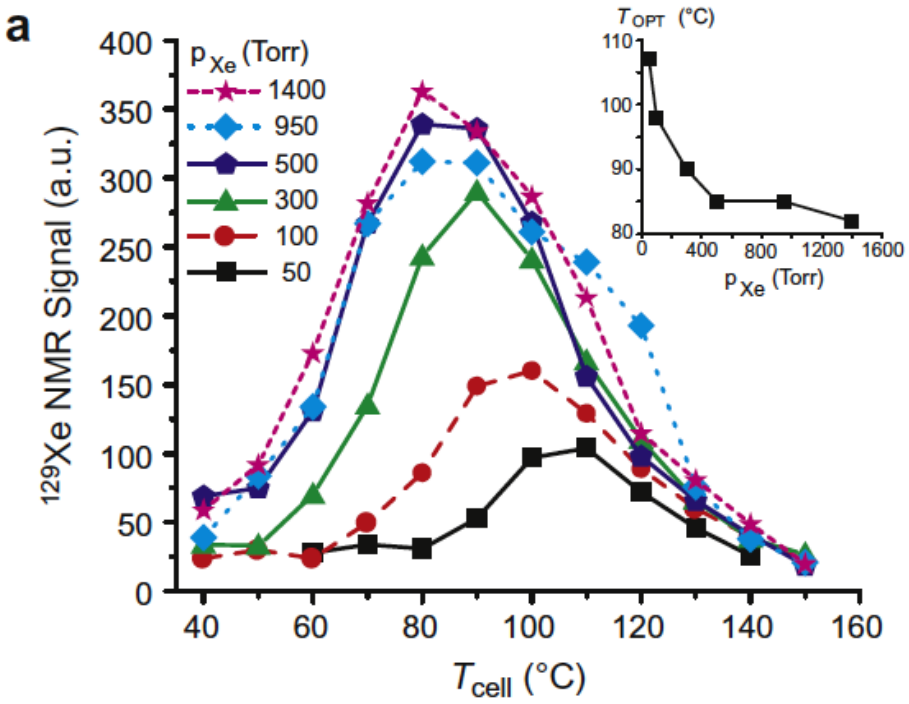

Figure 4.5: NMR signal intensity (or magnetisation) of hyperpolarised ^{129}Xe as a function oven temperature and gas mix [23]. The inset shows the optimal temperature for each gas mix as a function of temperature. Cell geometry and laser parameters are quoted in the first column of table 4.3. Reproduced from [23] with permission. (This data is also displayed in 3.2(a)).

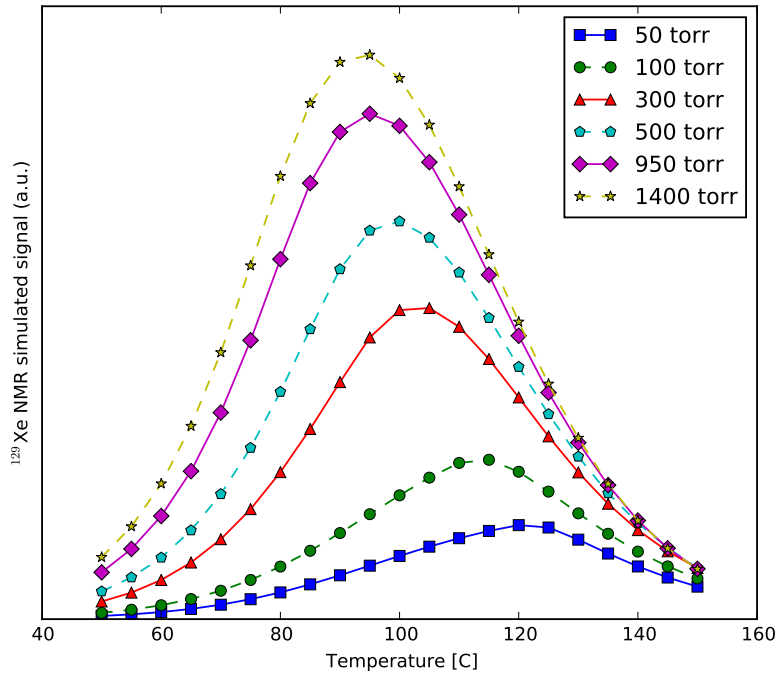

(a)

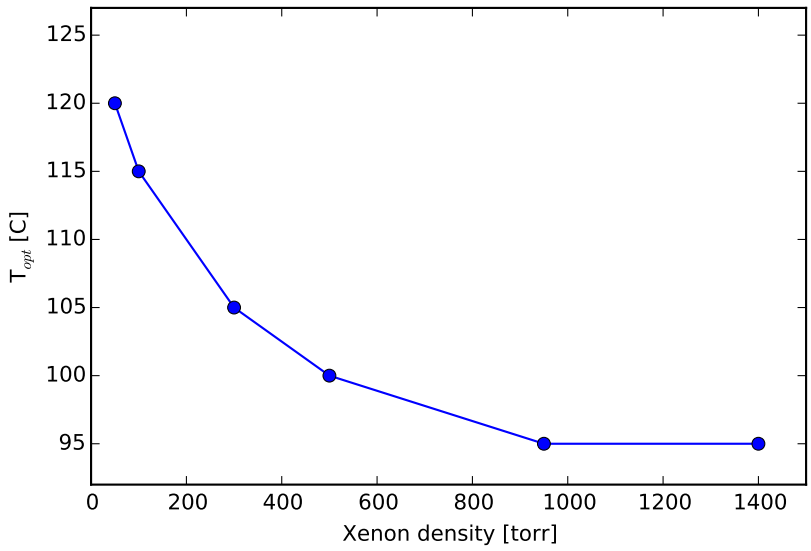

(b)

Figure 4.6: (a) Simulation of the JMR data generated using the standard model of SEOP. (b) T_{opt} trend observed in the JMR data and the original simulations is reproduced by the stand model of SEOP (parameters in table 4.3). Compare a) and b) here to the main body and inset of figure 4.5 respectively.

simulations were performed to understand why the xenon-rich mixes performed so well in-spite of the high [Xe]. It was suspected that it may be related to the use of the VHG narrowed lasers which were being used to pump the system for the first time. The simulations therefore considered the SEOP system as a function of pump laser linewidth [109]. The results of these simulations are shown in figure 4.7, left, along with the equivalent result from the standard model of SEOP, figures 4.7, right. It can be seen that the original simulations indicate that as the linewidth of the laser is increased P_{Xe} and T_{opt} decrease, and that as the laser linewidth is reduced the richer Xe mixes enjoy a differential gain in signal intensity. Further, both formalisms show that P_{Xe} becomes more sensitive to temperature as the linewidth is narrowed. The difference in gain at higher densities is striking: note the 1500 torr polarisation level in the top and bottom right of figure 4.7 which jumps from $\sim$1% to almost 20%.

Figure 4.8 shows more clearly the T_{opt} behaviour across these data sets. It can be seen that though normalised differently, both sets show increased sensitivity to temperature at the narrower linewidth of 0.25 nm. This shows why - before such narrowed lasers were used for pumping - the temperature sensitive nature of the optimal polarisations as a function of [Xe] had not been previously noticed.

It is possible that the inverse temperature dependence is due to the increased rate of spin destruction at higher [Xe] - driven the Rb-Xe spin-rotation interaction - which causes the Rb to be more opaque, reducing P_{Rb} within the cell. By reducing the temperature of the cell as [Xe] increases, [Rb] reduces, increasing transmission of the light and increasing P_{Rb} again - and bringing P_{Xe} with it.

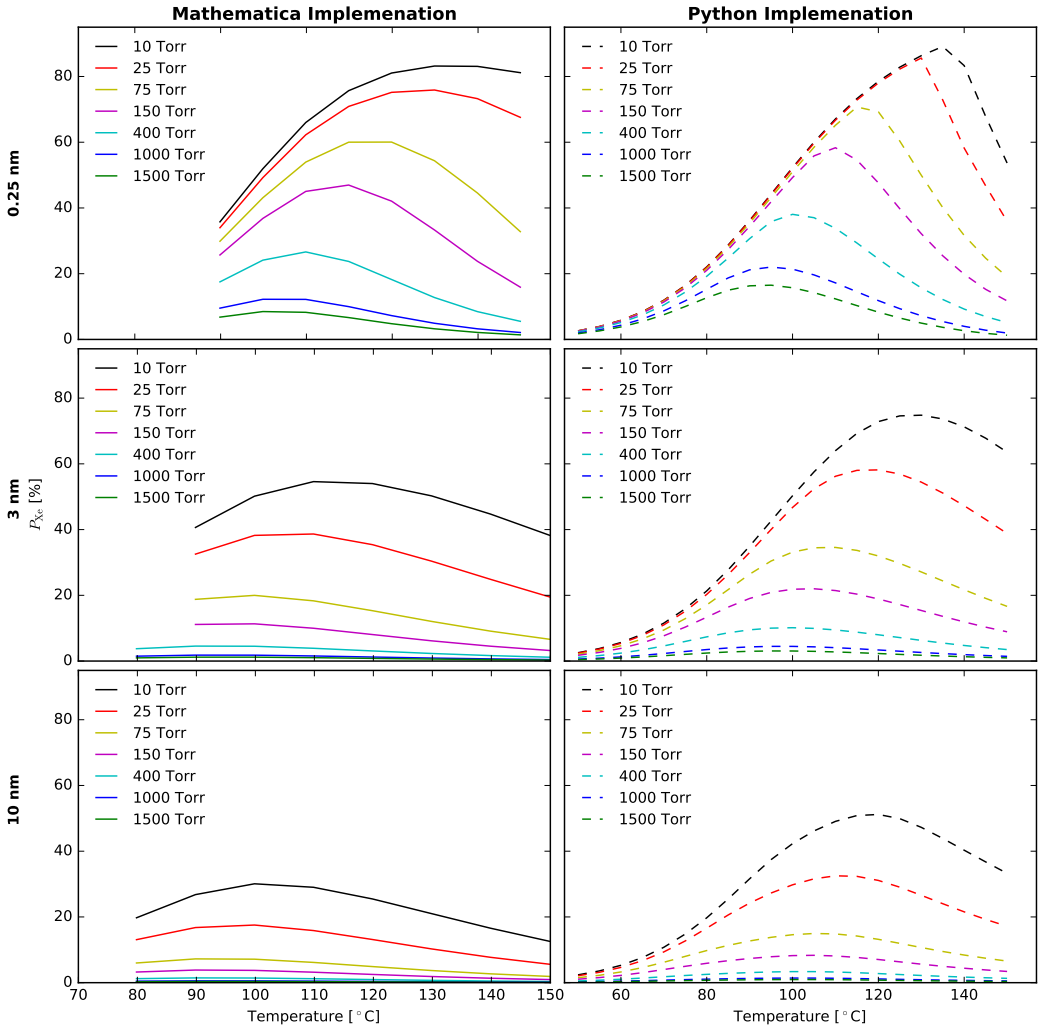

Figure 4.7: Simulations of SEOP as a function of laser linewidth. (a), (c) and (e) (left panels) are the results of the original simulations. It can be seen that as the linewidth increases polarisation for a given gas mix drops and T_{opt} becomes more sensitive to temperature. These trends are borne out by the standard model as shown in (b), (d) and (f) (right panels).

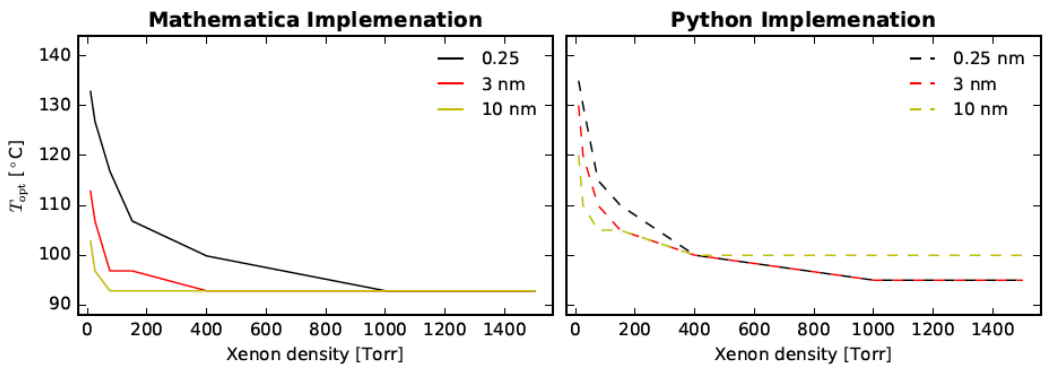

Figure 4.8: a) T_{opt} as a function of laser linewidth according to the 2D model of SEOP. T_{opt} becomes increasingly sensitive as the linewidth is decreased. b) T_{opt} as a function of laser linewidth according to the standard model of SEOP. T_{opt} becomes increasingly sensitive as the linewidth is decreased.

4.2.2 Comparison to the XeUS Mapping Data

After performing qualitatively well against the early xenon-rich data ([23]), the standard model was then compared to a larger dataset collected with the XeUS polariser [20] in which absolute xenon polarisations *were* measured, allowing for a quantitative assessment of the model. It was a multidimensional study in which P_{Xe} was measured as a function of laser power (100, 125, 140, 170 W), temperature (45-95 °C) and xenon density (275, 515, 1000, 1500 and 2000 torr). In these experiments a 2 inch cell of 25 cm length was used. The pump laser had a maximum output of ∼170 W at ∼795 nm and a spectral FWHM of ∼0.3 nm. All cells were prepared according to the protocol described in the methods section of chapter 3 and experimental details can be seen in table 4.3.

Figure 4.9 shows the results of the multidimensional study. P_{Xe} and γ_{SEOP} were measured as a function of oven temperature, incident laser power and xenon density and the maximum values for each gas mix are plotted as maps in panels (c),(e),(g),(i) and (k) for P_{Xe} and panels (d),(f),(h)(j) and (l) for γ_{SEOP}. 4.9(a) shows a cross-section of the P_{Xe} and γ_{SEOP} data for the 1000 torr mix at ∼100 W of lasing power (a cross-section of panel (g)), and panel

(b) shows the optimal values of P_{Xe} and γ_{SEOP} for each gas mix.

As with the previous dataset, it can be seen that as [Xe] is increased the peak polarisation decreases. This is best illustrated in panel (b). All of the P_{Xe} data (panels (c),(e),(g),(i) and (k)) suggest that better results could be obtained with greater incident laser power as they all peak at the highest laser power, 170 W.

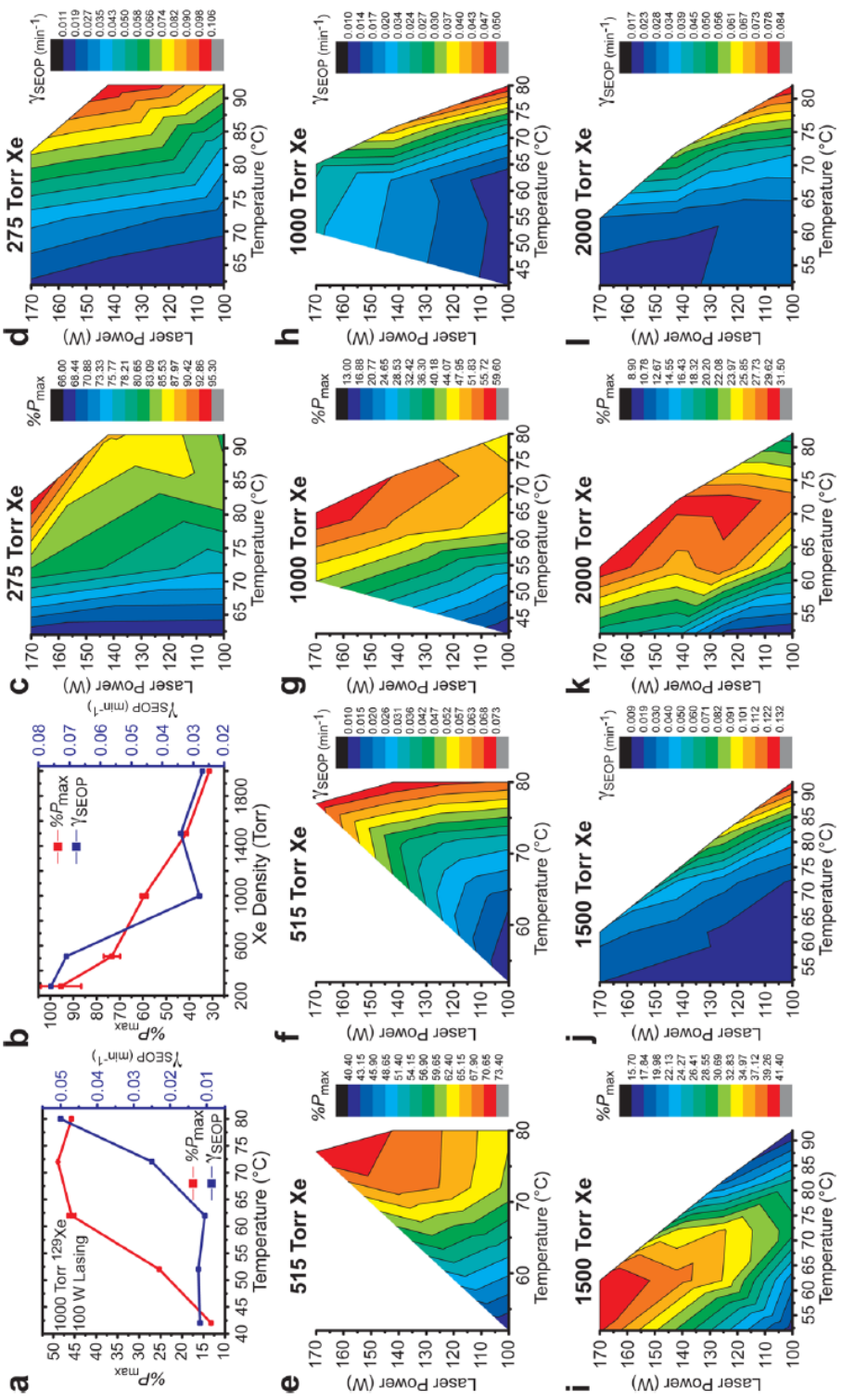

Figure 4.9: Results of the multi-parameter study conducted on the XeUS polariser. P_{Xe} and γ_{SEOP} were measured as a function of oven temperature, incident laser power and xenon density. The maximum values for each gas mix are plotted as maps (c),(e),(g),(i) and (k) for P_{Xe} and (d),(f),(h)(j) and (l) for γ_{SEOP}. (a) shows a cross-section of the P_{Xe} and γ_{SEOP} data for the 1000 torr mix (at 100 W) and panel (b) the optimal values of P_{Xe} and γ_{SEOP} for each gas mix. Reprinted from [20] with permission.

When considering the γ_{SEOP} data (panels (d),(f),(h)(j) and (l)) it can be seen that increasing the cell temperature gives rise to an exponential increase in γ_{SEOP}. This is due do its dependence on [Rb] which increases exponentially with temperature (equation 4.8). Hints of laser induced thermal issues are evident in these panels. A pure dependence on the rubidium density would mean that the colour contours would run purely vertically, but it can be seen that as the laser power is increased γ_{SEOP} begins to elevate at lower oven temperatures due to laser induced heating.

When considering P_{Xe}, it can be seen that at all densities it initially grows with temperature, but peaks at a given temperature (which decreases for increasing [Xe]). This is likely because [Rb] becomes too high, occluding the laser light as it penetrates into the cell which in turn lowers the P_{Rb} at the back of the cell, bringing the average P_{Rb} and thus P_{Xe}.

Figures 4.10 and 4.11 show contour plots of P_{Xe} for stopped-flow SEOP simulations with these experimental parameters. Both can be compared to figure 4.9 (c),(e),(g),(i) and (k). It is useful to see the same data presented on different axes because in the first instance it allows for comparison to the experimental data (which have differing temperature axes), and in the second instance it allows one to compare the broader patterns when the data appear scaled on the same axes. When comparing the model to the data it can be seen that across the entire parameter space the experimental SEOP data is well described by the model. The model also predicts that the highest xenon polarisations occur at the highest laser power.

γ_{SEOP} (figure 4.12) exhibits a laser power independent trend governed only by [Rb]. This is what would be expected in a polariser where full thermal control can be maintained at even the highest laser powers.

Figure 4.13 shows predicted behaviour for P_{Rb}. Considering P_{Rb} at a given

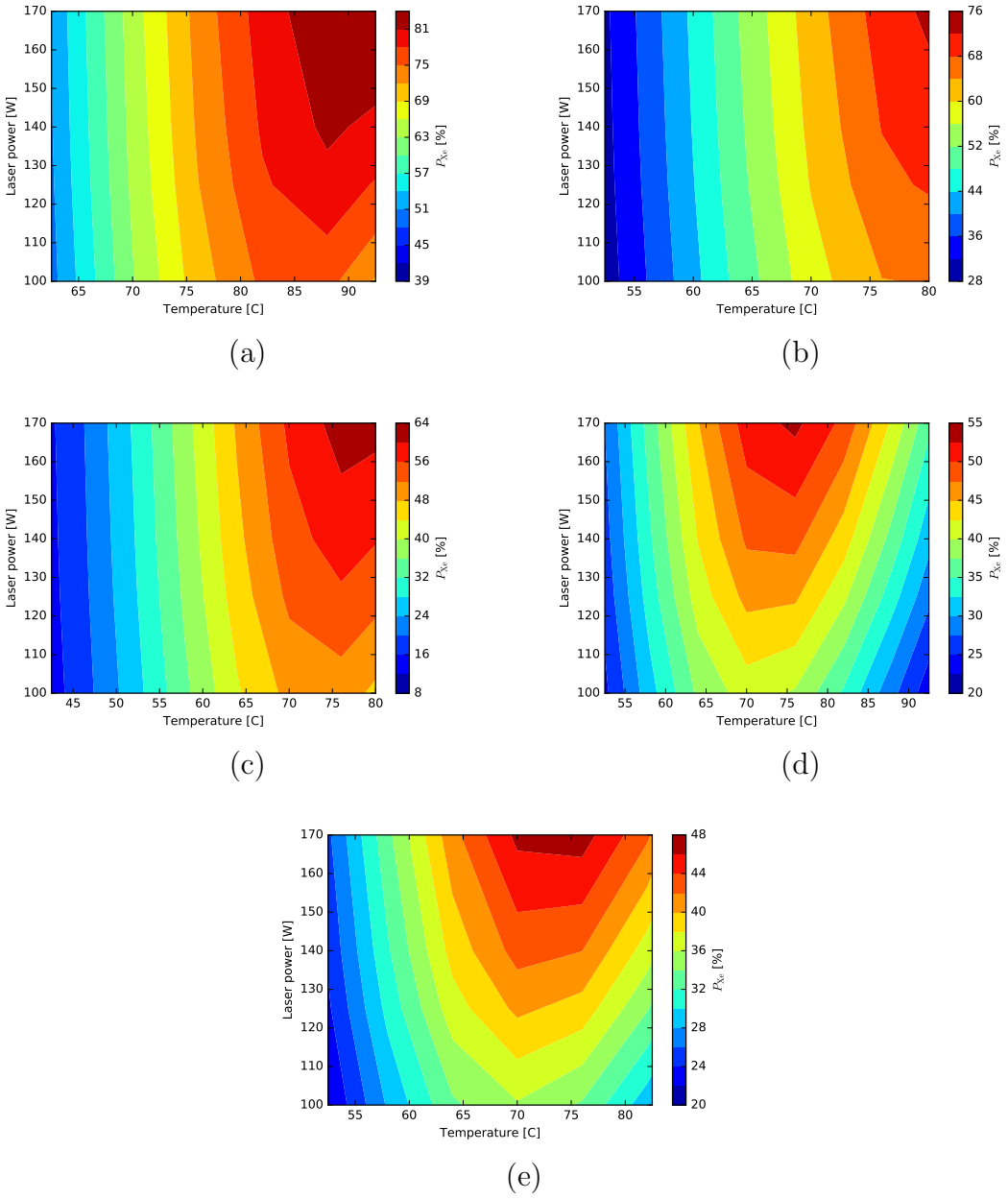

Figure 4.10: Simulations of the maximum P_{Xe} as a function of oven temperature, incident laser power and xenon density with axes adjusted to match the data in figure 4.9. (a) 275 torr xenon. (b) 515 torr xenon. (c) 1000 torr xenon. (d) 1500 torr xenon. (e) 2000 torr xenon. Compare to panels (c),(e),(g),(i) and (k) of figure 4.9.

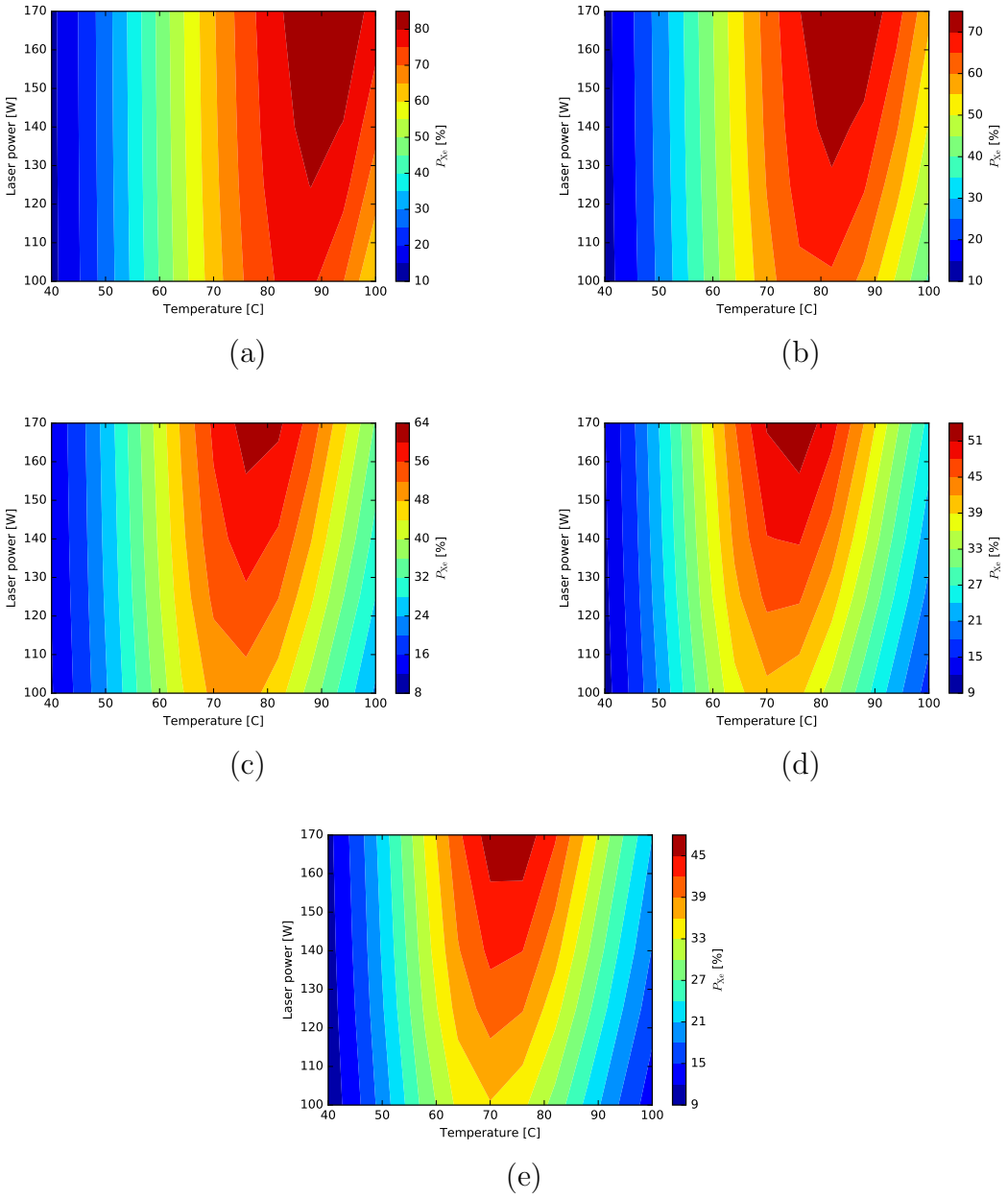

Figure 4.11: Simulations of the maximum P_{Xe} as a function of oven temperature, incident laser power and xenon density with no axes adjustment. (a) 275 torr xenon. (b) 515 torr xenon. (c) 1000 torr xenon. (d) 1500 torr xenon. (e) 2000 torr xenon. Compare to panels (c),(e),(g),(i) and (k) of figure 4.9.

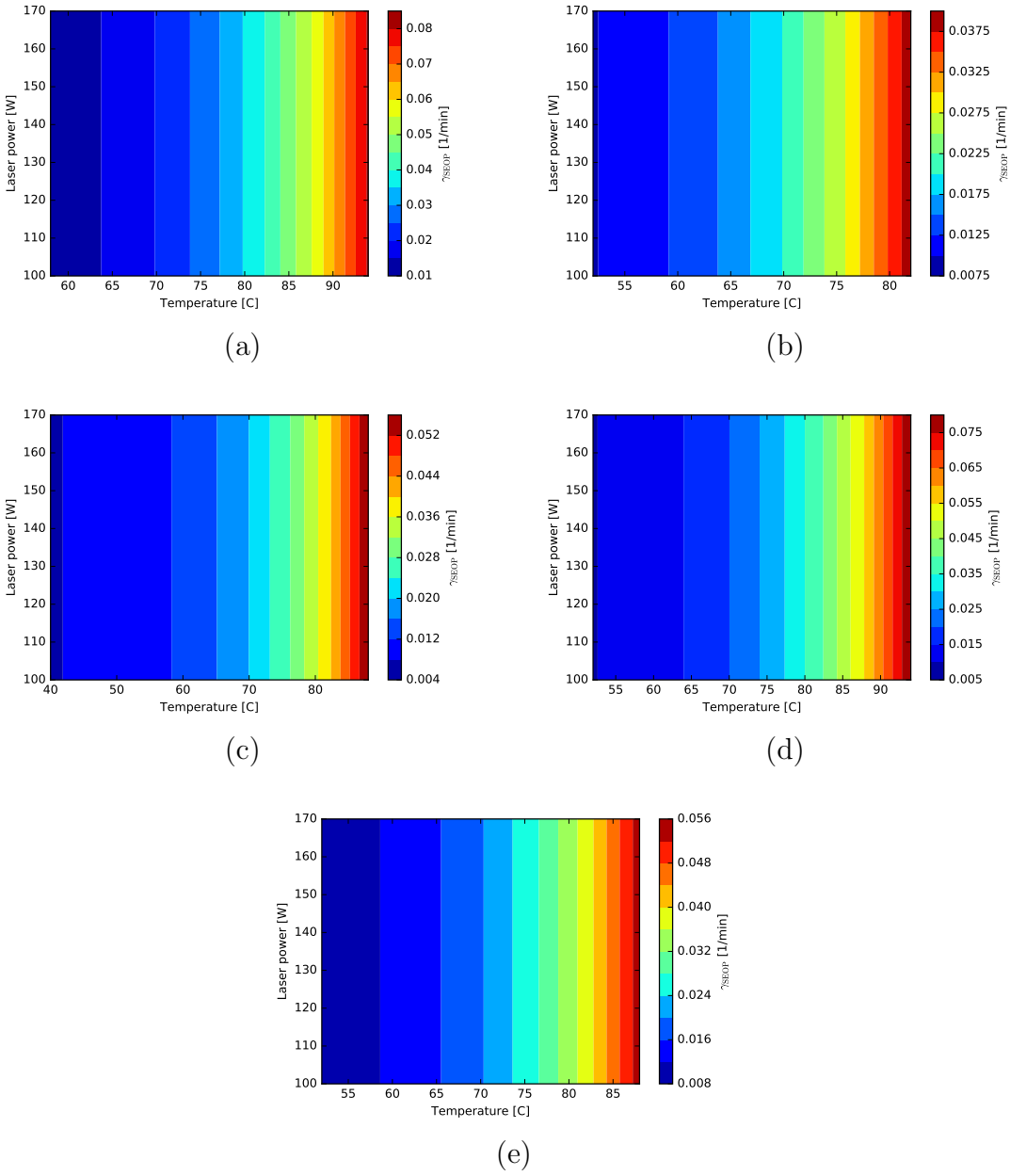

Figure 4.12: Simulations of γ_{SEOP} as a function of oven temperature, incident laser power and xenon density. (a) 275 torr xenon. (b) 515 torr xenon. (c) 1000 torr xenon. (d) 1500 torr xenon. (e) 2000 torr xenon. Compare to panels (d),(f),(h)(j) and (l) of figure 4.9.

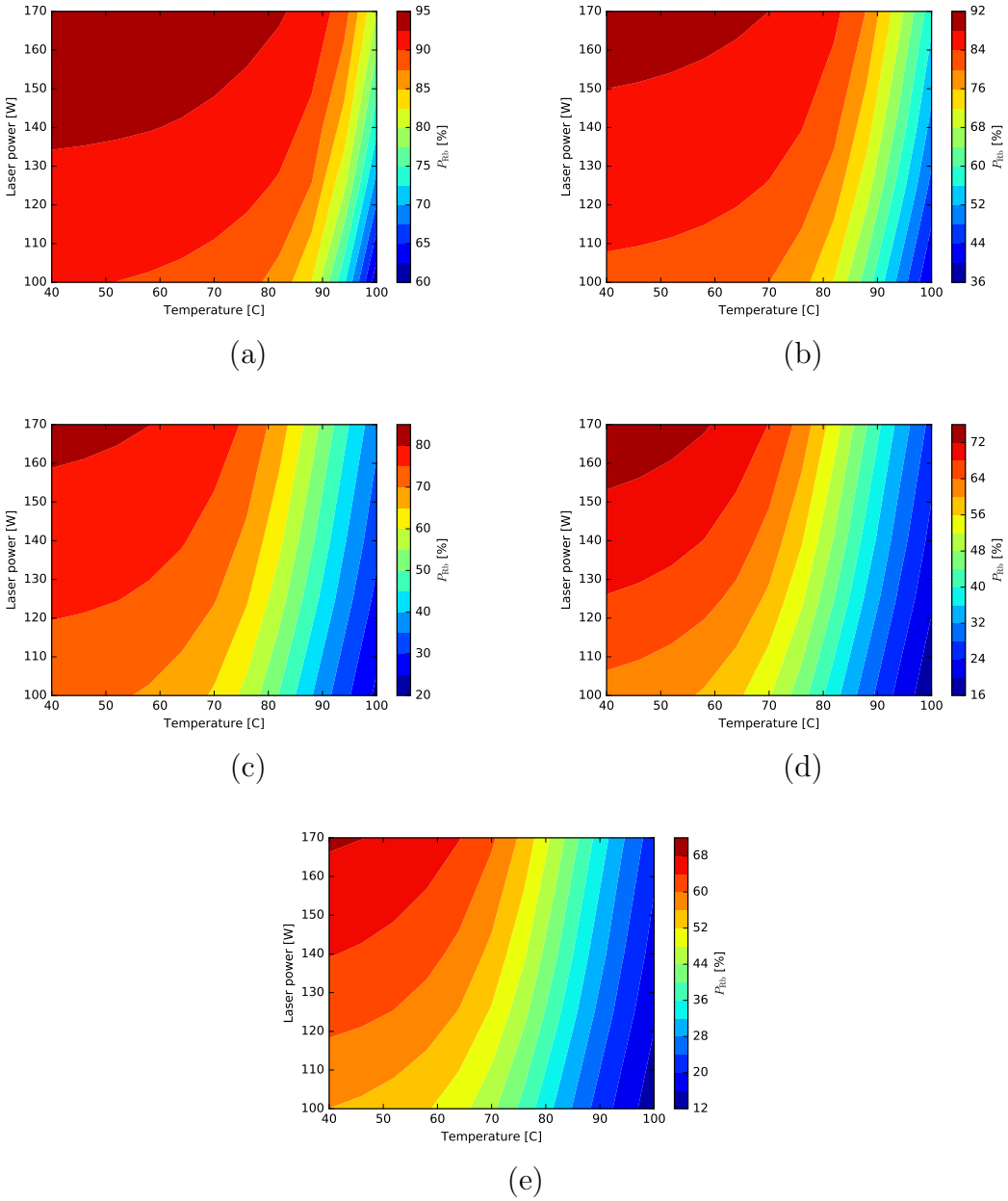

Figure 4.13: Simulations of P_{Rb} as a function of oven temperature, incident laser power and xenon density. (a) 275 torr xenon. (b) 515 torr xenon. (c) 1000 torr xenon. (d) 1500 torr xenon. (e) 2000 torr xenon.

laser power in any of the panels, it can be seen that it decreases with increasing temperature. This is due to the exponentially increasing number of absorbers which quickly inhibit the ability of the polarised photons to reach through the entire cell. Increasing the laser power from 100 to 170 W results in an increase in Rb polarisation across all of the gas mixes due to the increased number of photons to absorbers.

The behaviour of P_{Xe} as a function of temperature can be thought of approaching P_{Rb} all of the time. Before P_{Xe} peaks, P_{Rb} is high but γ_{SEOP} and [Rb], which scale with temperature, are too low for it to reach the same level. After the peak value the xenon polarisation is much closer to P_{Rb} - because the SE rate and [Rb] are high - but P_{Rb} drops because of the presence of too many absorbers (Rb atoms). Consequently P_{Xe} also drops because it cannot exceed P_{Rb}. This can be seen more clearly later in figure 4.20.

Figure 4.14 shows the same data as panel (a) but for all of the gas mixes and allows the model to be compared to the data at 100 W of lasing power. Both retro-reflected and non-retro-reflected cases are shown (green and blue dashed lines respectively) against the experimental data (red solid line). It can be seen here that the 1500 torr xenon data deviates the most of all of the gas mixes in an anomalous fashion. This is may be due to an issue with the surfacil coating which reduced the in-cell T_1 (the same lower P_{Xe} values are evident in the contour lots of figure 4.9).

Figure 4.15 shows the optimal P_{Xe} values from the XeUS multi-parameter study as a function of xenon density plotted for comparison against the standard model simulation with and without retro-reflection. Good qualitative agreement is observed and quantitatively the model closely predicts the 515 torr and 1000 torr mixtures. The steeper gradient in the data may be due to thermal effects that have not been accounted for in the model which worsen

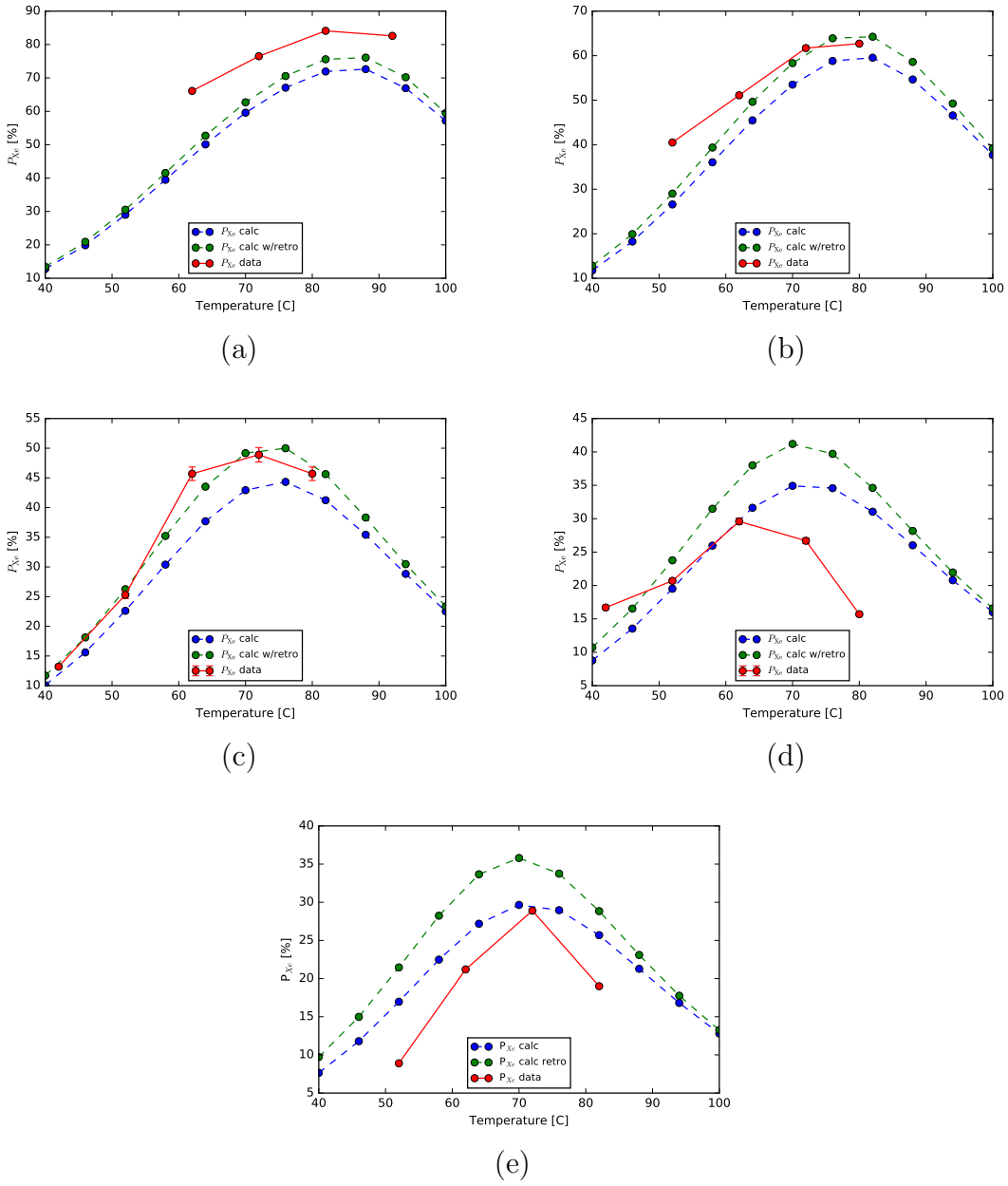

Figure 4.14: Cross-sections of simulations of P_{Xe} as a function of oven temperature and xenon density at 100 W of laser power, with and without retro-reflection. Shown as a comparison to panel (a) in figure 4.2.2. (a) 275 torr xenon. (b) 515 torr xenon. (c) 1000 torr xenon. (d) 1500 torr xenon. (e) 2000 torr xenon.

with xenon density. For instance, the system gets hotter as more xenon is added, due, in part, to the poor thermal conductivity of the xenon, and therefore the experimental values for P_{Xe} are lower because the polariser could not be allowed to run to full steady state under these conditions without encountering a runaway condition. It is for this reason that the optimal xenon polarisations are lower than predicted by the model. These effects were evident in the γ_{SEOP} data in figures 4.9 (d),(f),(h)(j) and (l)).

From this plot it is also evident that retro-reflection provides a greater boost in polarisation at higher [Xe] than at lower [Xe]: at 2000 torr the gain is twice that enjoyed by the 275 torr mix. This is in keeping with the differential gain in polarisation trend explored previously in figure 4.7.

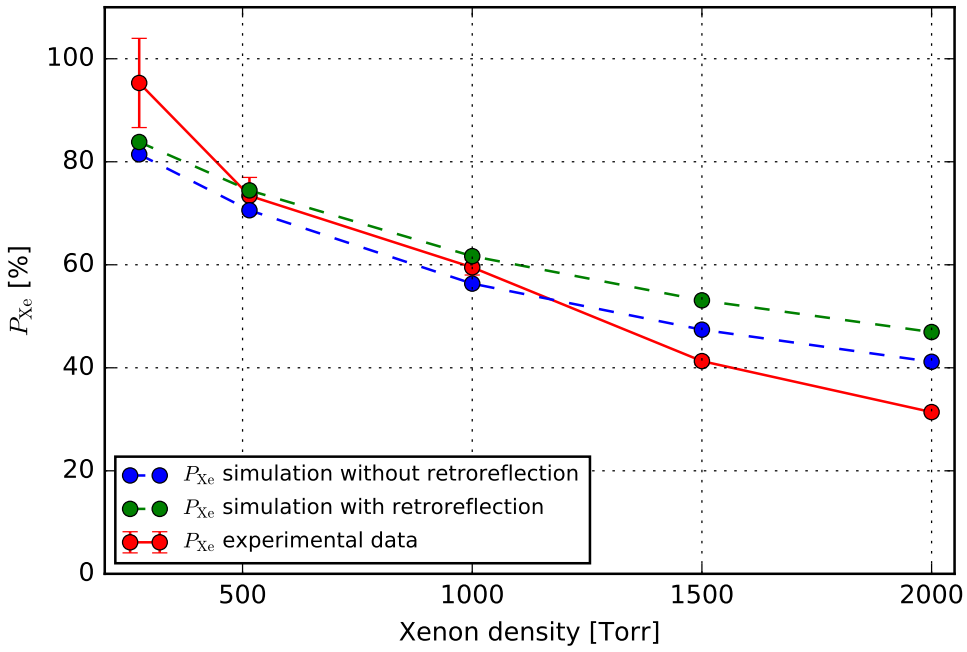

Figure 4.15: Optimal P_{Xe} values from the XeUS multiparameter study as a function of [Xe] plotted for comparison against the standard model simulation with (green dashed line) and without (blue dashed line) retro-reflection. Good qualitative agreement is observed and quantitatively the model closely predicts P_{Xe} for the 515 torr and 1000 torr mixtures. The steeper gradient in the data may be due to thermal effects that have not been accounted for in the model which worsen with xenon density.

4.2.3 Exploratory Simulations for XeUS

After validating the model against the original low power, 1 inch cell data set by Whiting *et al.* [23] and subsequently against the multidimension dataset collected using XeUS by Nikolaou *et al.* [20], the model was used to explore the surrounding parameter space to see how stopped-flow polarisers could be further optimised in terms of output level or production rate. These simulations considered scenarios which could readily be implemented on the XeUS line of polarisers with minimal changes to the overall engineering of the system. These exploratory simulations considered how the xenon polarisation and magnetisation are affected as a function of (1) buffer gas (with the addition of helium as a second buffer gas), (2) cell geometry, (3) total pressure, and (4) laser linewidth. The simulations of the XeUS data that that were presented in the last section are used as a reference dataset in order to make comparisons. The results of these exploratory simulations are discussed below. Retro-reflection was applied throughout.

Cell Geometry and Addition of Helium

Figure 4.16 shows how the system behaves with helium added to a 2 inch cell. From this it can be seen that in a cell of almost 50% helium there has been ostensibly no negative impact on P_{Xe}, and that the optimal temperature T_{opt} in fact drops by a few degrees. The fact that the polarisation has not dropped when considered in this framework is good because it means that helium is not detrimental to the spin-exchange physics of the system. There are other benefits to adding helium to the cell that may occur in practice but which are not evident in the simulation: Helium is 25-fold more thermally conductive than xenon, and it may be that the addition of helium allows for greater dissipation of heat from the system, thus avoiding the onset of rubidium

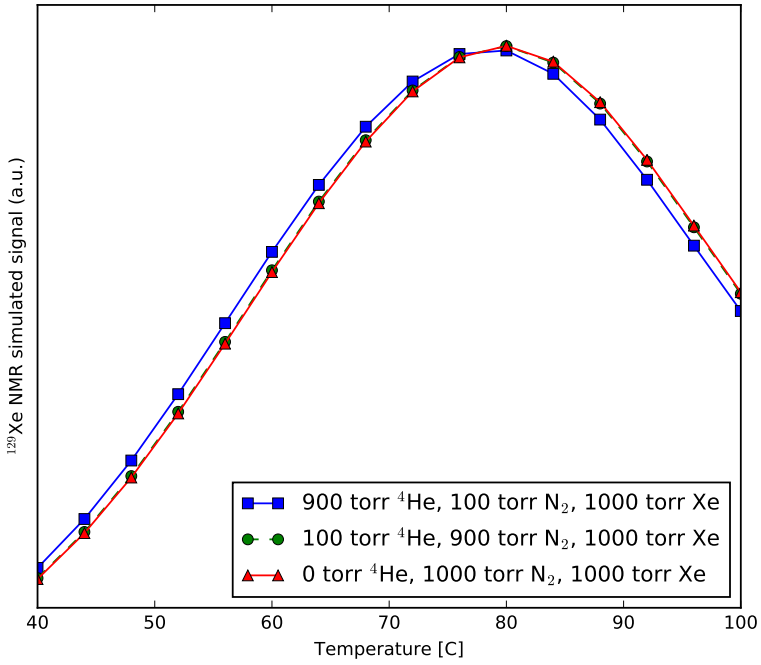

Figure 4.16: Effect of changing the buffer gas composition on P_{Xe} for other normal XeUS operating conditions (i.e. 2 inch cell, 170 W, 0.3 nm FWHM). The gas mixes simulated have the following proportions of a total cell pressure of 2000 torr: 50:50:0, 50:5:45, 50:45:5, where ratios are stated as xenon:nitrogen:helium. The simulation of the largely helium cell shows its T_{opt} occurs at a lower temperature, and at essentially no cost in xenon polarisation. This has added benefit in terms of polariser duty cycle because cool-down will start from a lower temperature. The presence of helium may provide other benefits not simulated for including improved captivity to control or mitigate rubidium runaway within the cell.

runaway, which is particularly important at higher xenon densities due to xenon's attendant rate of spin destruction and poorer thermal conductivity. Another downstream benefit to including helium in the mix is that it may make the inhalation of the gas mixture easier for those with compromised breathing, due to the lower coefficient of viscosity of helium relative to xenon.

Based on this result, helium should be included in XeUS cells because (1) it does not negatively impact P_{Xe}, (2) it is more thermally conductive and therefore it should be possible to maintain greater control over the cells at

higher laser powers and higher temperatures, (3) its thermal conductivity will enable fast heating and cooling of the cells between runs and therefore increase the operational duty cycle of the polariser, (4) the presence of helium in the mix may enable patients to inhale the hyperpolarised gas mixture with greater ease, (5) T_{opt} is slightly lower which again contributes to a faster duty cycle.

Figures 4.17(a) and 4.17(b) show the resulting respective expected polarisations and magnetisations for comparisons of different cell geometries. As a further comparison, helium is also shown as a buffer gas in the case of the 3 inch cell. Three cell geometries were considered here, the parameters of which are displayed in table 4.3; (1) the current XeUS cell (R = 2 inch, L = 25 cm), (2) a wider 3 inch cell with the same length (R = 3 inch, L = 25 cm), and (3) a 3 inch cell in which the internal volume has been kept constant with respect to the R = 2 inch cell (R = 3 inch, L = 11.11 cm). The cell geometry is an important factor to consider because it determines how the laser light is distributed through the cell, the volume of gas to be polarised, and the rate of wall induced relaxation through the surface-to-volume ratio. A large surface-to-volume ratio will result in greater relaxation as the dominant relaxation mechanism in stopped-flow SEOP is wall relaxation. In order to account for the wall relaxation, the T_1 of the XeUS cells from the multi-dimensional data was scaled according to the new surface to volume ratio (table 4.3).

From figure 4.17(a) it can be seen that the existing 2 inch XeUS cell exhibits the highest P_{Xe} followed by the short 3 inch cell (which keeps the volume constant with the original XeUS cell). The long 3 inch cell comes second to last and the 3 inch cell with helium present is lowest, though only marginally with respect to the long 3 inch cell, and particularly at high [Xe]. When considering the results in terms of magnetization (figure 4.17(b)) it can be seen that the 3 inch cell provides almost twice the signal of the 2 inch XeUS

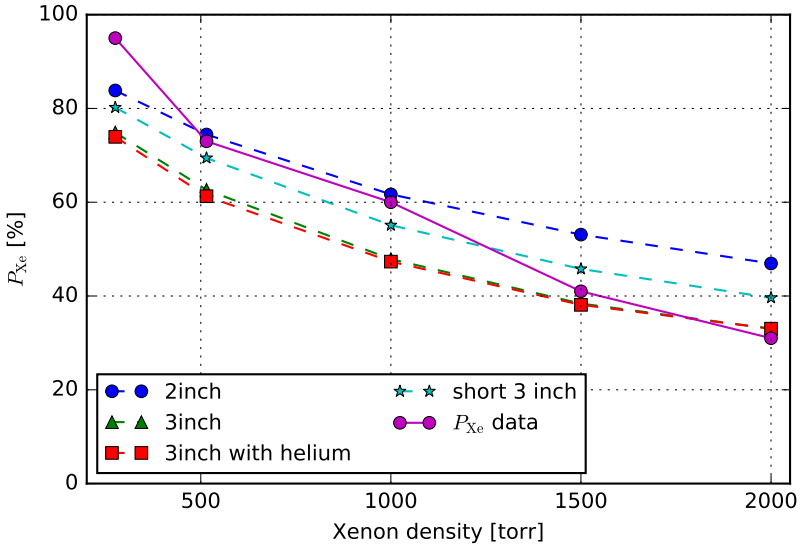

(a)

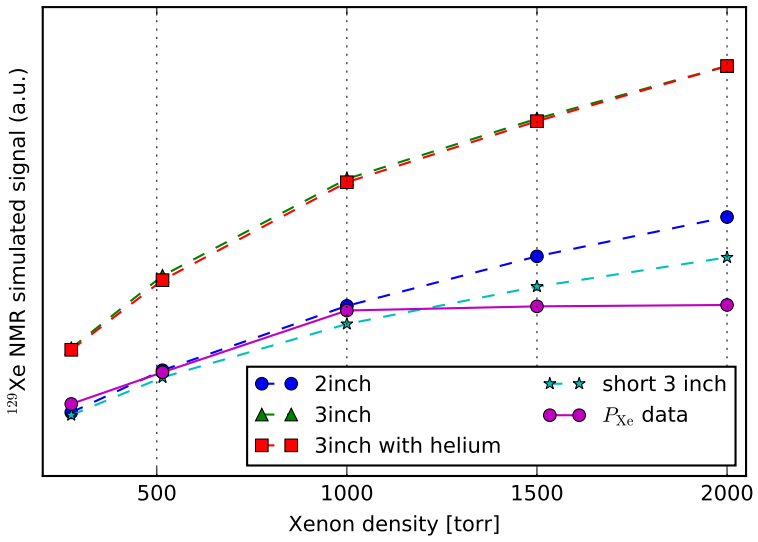

(b)

Figure 4.17: a) Comparison of optimal xenon polarisations for different XeUS cell geometries and gas loadings. Geometries include the current R=2 inch cell (25 cm long), a R=3 inch cell (25 cm long), a R=3 inch cell with helium (25 cm long) and a R=3 inch cell with a constant volume (11.11 cm long). b) Corresponding comparison of optimal xenon magnetisations. Though the polarisation is slightly lower for the R=3 inch (25cm) cell relative to an R=2 inch cell, this magnetisation plot shows that almost double the amount of signal can be obtained by going to a 3 inch cell because the increase in volume more than compensates for the slight drop in polarisation. Further to this, a 3 inch cell with helium provides comparable results. 'P_{Xe} data' are the measured values for the 2 inch cell in the XeUS multiparameter study discussed in the preceding sections.

cell. This can be in part attributed to the fact increasing the diameter by 1 inch from 2 inches to 3 inches while keeping the length constant actually increases the volume within the cell by more than a factor of two while at the same time P_{Xe} has barely decreased. It can also be seen that the presence of helium in the 3 inch cell again does not impact the SEOP physics of the system; the achieved polarisation and magnetisation level are essentially the same. The 3 inch cell may also run hotter than the 2 inch cell due to the reduced S/V ratio, though this effect would also be mitigated with the addition of helium (this assumption is explored and validated in the next chapter using Raman spectroscopy). Investigations with a 3 inch XeUS cell and helium as a buffer gas are highly encouraged based on these simulations.

Total Cell Pressure

The XeUS data above (figure 4.9) explore xenon-rich SEOP as a function of xenon partial pressure at a fixed total pressure of 2000 torr. Here, in figures 4.18(a) and 4.18(b), xenon-rich SEOP is explored as a function of the total pressure, with 5 total pressure considered: 500, 1000, 2000, 4000 and 10000 torr. For each of these total pressures the variance with partial pressure is also presented. Partial pressures correspond to 14%, 25%, 50%, 75% and 90% of the total pressure indicated by the blue, green, red, light blue and purple dashed lines respectively. From figure 4.18(a) it can be seen that polarisation decreases with increasing pressure, but from figure 4.18(b) it can be seen that magnetisation increases, with the lower partial pressure gaining the most. It can also be noted here that in 4.18(a), the gradient of the lines reflects the efficiency with which the polarisation increases with laser power, and there is little difference in efficiency across the total pressures indicating is it not inherently more efficent to conduct SEOP at a higher or lower pressure.

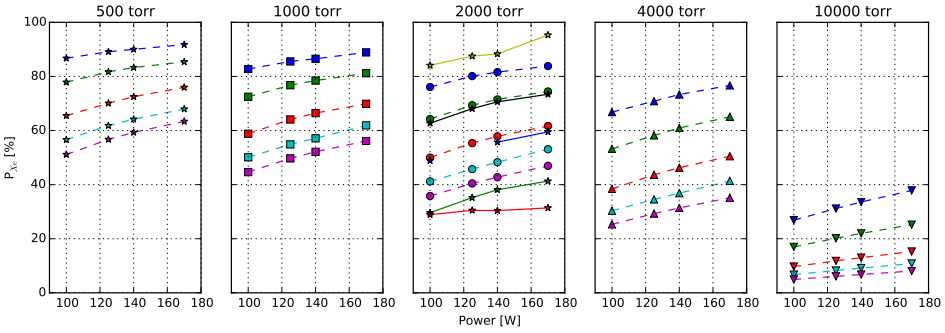

(a)

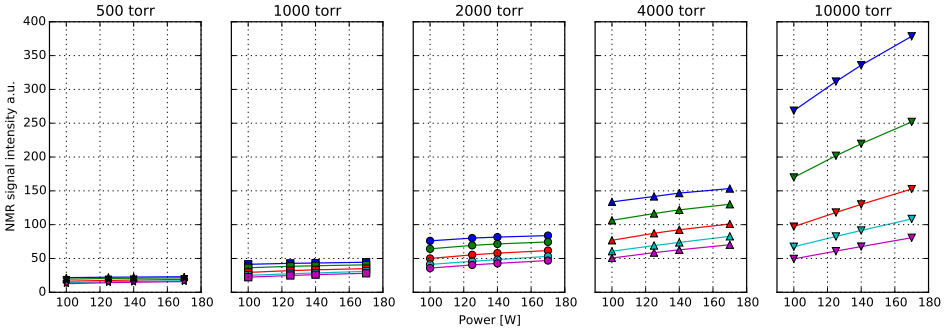

(b)

Figure 4.18: a) Optimal xenon polarisation as a function of laser power for each of the partial pressures of xenon calculated at 5 total pressures increasing from 500 torr to 20000 torr. Partial pressures correspond to 14%, 25%, 50%, 75% and 90% of the total pressure indicated by the blue, green, red, light blue and purple dashed lines respectively. The gradient of the lines reflects the efficiency with which the polarisation increases with laser power. There is little difference in efficiency across the total pressures. Optimal polarisation increases with lower total pressure. b) Corresponding comparison of optimal xenon magnetisations. Despite the decreasing polarisation with increasing pressure the magnetisation increases with greater gains observed in the lowest xenon partial pressures.

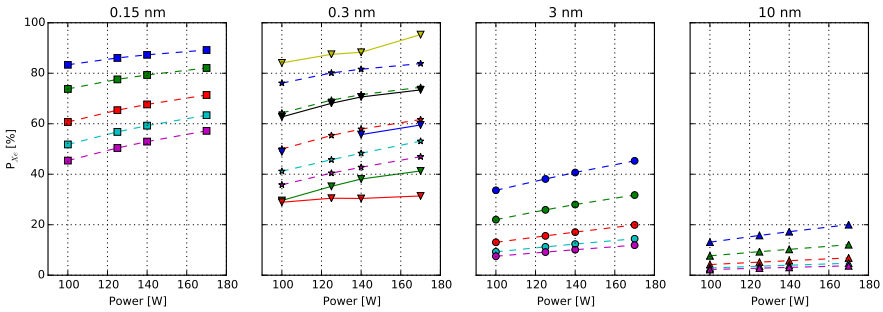

Figure 4.19: Optimal xenon polarisation as a function of laser power for each of the xenon partial pressures at 4 laser linewidths: 0.15 nm (squares), 0.3 nm (stars), 3 nm (circles) and 10 nm (triangles). Partial pressures of xenon of 275 torr, 515 torr, 1000 torr, 1500 torr and 2000 torr are indicated by the blue, green, red, cyan and purple dashed lines respectively. Solid lines show the corresponding data. Polarisation increases with decreasing linewidth. The gradient of the lines reflects the efficiency with which the polarisation increases with laser power. There is little difference in efficiency across the linewidths.

Laser Linewidth

Figure 4.19 shows how the xenon polarisation is expected to behave under the existing XeUS conditions for laser line widths of 0.15, 0.3, 3 and 10 nm. It can be seen that, as shown earlier in figure 4.7, greater polarisations can be expected at narrower linewidths. This is due to improved coupling between the laser line and the Rb D_1 transition.

Summary

Based on the exploratory simulations presented here a number of options exist for increasing the magnetisation output of the XeUS type polarisers. Cheapest and easiest to implement would be the inclusion of helium within the gas mixtures. It is demonstrated here that helium will have ostensibly no impact on P_{Xe} but will have other benefits that can not be demonstrated within the framework of the standard model. A 3 inch cell will double magnetisation output relative to the current cell. This will require modification to a number

of the components of the polariser including the optical train, the AR coated window, retro-reflector, and 3D printed oven. Fortunately, QPC lasers have been able to develop a 3 inch equivalent of the current 2 inch optical train which is compatible with the existing laser systems and the 3D printed oven can be quickly modified in a CAD program and reprinted easily.

Further, higher pressures and narrower linewidths will also bring further gains in output. However, operating at 5 times greater pressure will bring engineering challenges in manufacturing a cell that can tolerate the pressure, particularly under intense SEOP conditions. Nonetheless, it is likely some increase in pressure can likely be achieved. Perhaps most expensive is the further narrowing of the laser.

4.2.4 Constant Laser Absorption at Optimal Polarisations

When examining the polarisations predicted by the model it became apparent that there was a distinct pattern in the amount of power absorption that occurred for a given mix's optimal polarisation. That is, for a given mix's optimal polarisation, the power absorption was constant at approximately $\sim$67%. This can be seen firstly in figure 4.20. Here, four simulations are shown: two at 100 W of lasing power in a 275 torr mix and again in a 1000 torr xenon mix; and two at 170 W of lasing power power in a 275 and also in the 1000 torr xenon mix. The vertical dashed lines on each of the four plots indicate the optimal xenon polarisation for those particular conditions, and the horizontal dashed line indicates the corresponding laser absorption that resulted in that optimal polarisation. From this it can be seen that the laser absorption in every case is $\sim$67% regardless of the laser power or xenon density.

This effect is further explored in the next two figures over a much broader

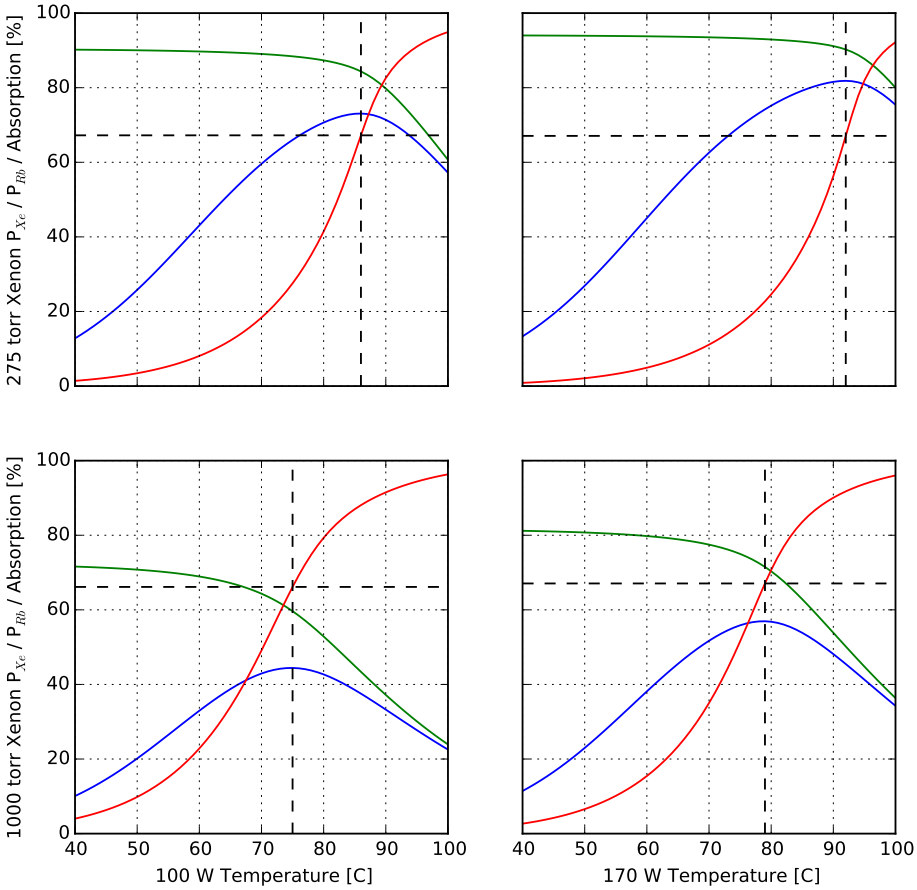

Figure 4.20: Four simulations of stopped-flow SEOP in a 2 inch cell at the same total gas pressure of 2000 torr and laser linewidth of 0.3 nm. Top and bottom rows are 275 torr and 1000 torr of xenon respectively, backfilled with nitrogen. Left and right are 100 W and 170 W of incident power respectively. Green, blue and red lines show % rubidium polarisation, % xenon polarisation and % power absorbed as a function of cell temperature. It can be seen from the plots that at the optimal P_{Xe} for each condition (vertical dashed lines), the % power absorbed is always approximately 67%, i.e. independent of xenon partial pressure and laser power.

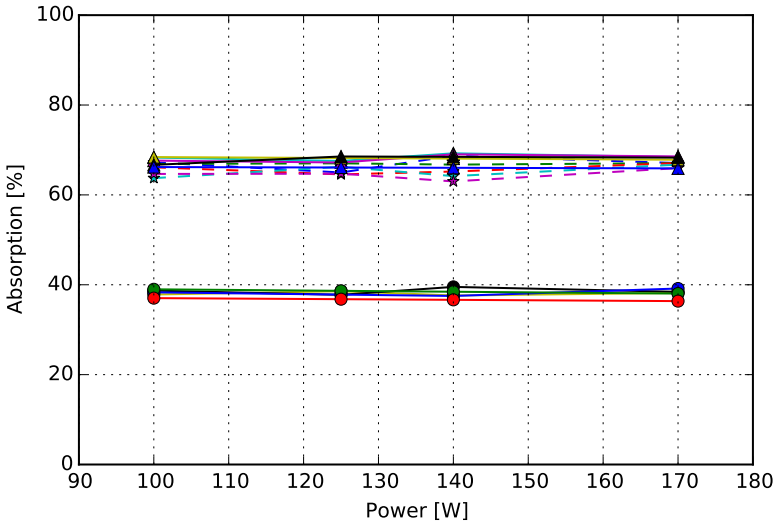

(a)

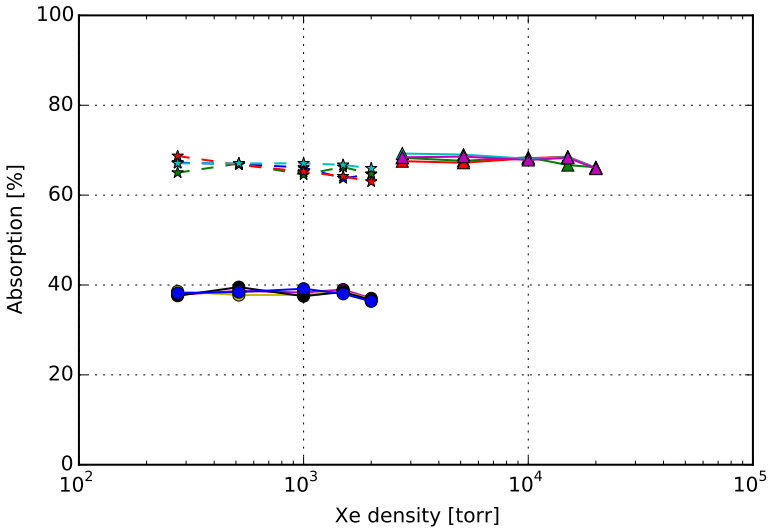

(b)

Figure 4.21: a) % power absorbed as a function of laser power for 3 groups of experimental conditions: stars show the current XeUS conditions (2000 torr, 0.3 nm); triangles show current conditions but with the partial pressures of the constituent gas mixes (and hence total pressure) increased by a factor of 10 (i.e. 2750, 5150, 10000, 15000, 20000 torr xenon); and circles show current XeUS conditions but with a broadband 10 nm laser. Each group contains each of the 5 xenon fractions. b) % power absorbed as a function of xenon density for 3 groups of experimental conditions: stars show the current XeUS conditions (2000 torr, 0.3 nm); triangles show current conditions but with the partial pressures of the constituent gas mixes increased by a factor of 10 (i.e. 2750, 5150, 10000, 15000, 20000 torr xenon); and circles show current XeUS conditions but with a broadband 10 nm laser.

range of conditions. Figure 4.21(a) shows the % power absorbed as a function of laser power for 3 groups of experimental conditions: stars show the current XeUS conditions (2000 torr, 0.3 nm); triangles show current conditions but with the partial pressures of the constituent gases in the respective mixes (and hence total pressure) increased by a factor of 10 (i.e. 2750, 5150, 10000, 15000, 20000 torr xenon); and circles show current XeUS conditions but with a broadband 10 nm laser. Each group contains each of the 5 xenon fractions. The plot indicates that % absorption is independent of incident laser power under all conditions, although at a broader linewidth the constant level of absorption is at a lower value.

Figure 4.21(b) shows the % power absorbed as a function of [Xe] for 3 groups of experimental conditions: stars show the current XeUS conditions (2000 torr, 0.3 nm); triangles show current conditions but with the partial pressures of the constituent gases in the respective mixes (and hence total pressure) increased by a factor of 10 (i.e. 2750, 5150, 10000, 15000, 20000 torr xenon); and circles show current XeUS conditions but with a broadband 10 nm laser. The plot indicates that % absorption is independent of [Xe], but dependent on the laser linewidth. This absorption condition may provide a new means of monitoring optimal conditions on stopped-flow polarisers if thermal runaway issues can be kept in hand.

4.3 Conclusion

The xenon-rich stopped-flow SEOP regime has been simulated for the first time using the standard model of SEOP. The model was validatated against two datasets (in two different cell geometries); the first dataset where regime was first shown [23], and a second much larger dataset that was calibrated for absolute polarisation values and covered a much larger regions of parameter space

[20]. In the first case, the simulation qualitatively matched the un-calibrated data very well. In terms of the exact temperatures for the expected peak values of the simulated magnetisations, the simulations, at their worst, deviated by no more than 12 °C of the experimental values. In the second case, close quantitative agreement was made though a steeper gradient appeared in the optimal P_{Xe} as a function of [Xe] - that is, polarisation fell slightly faster with increasing xenon density in the experimental data - and this is most likely due to thermal effects that could not be accounted for in the simulation (thermal effects that are evident in the XeUS γ_{SEOP} data in figures 4.9 (d),(f),(h)(j) and (l)). Regardless of this discrepancy, the model was considered to provide a good approximation of the regime and exploratory simulations of the surrounding parameter space were performed.

Based on these exploratory simulations, it is expected that output can be increased by 1) using a wider cell of the same length; 2) by introducing helium into the mixture; 3) by increasing the total pressure; and 4) by further decreasing the laser linewidth. Each of these modifications have varying degrees of cost or engineering difficulty associated with them and the best outcome would be a combination of all 4 modifications.

Additionally, retro-reflection was incorporated into the model and was shown to be differentially beneficial at higher xenon densities.

Scrutiny of the laser absorption revealed for the first time that in the stopped-flow regime, optimal polarisation per xenon fraction occurs at the same level of absorption. If a system can be developed where complete thermal control can be maintained, this phenomena will enable rapid optimisation of polarisers.

Chapter 5

Raman Spectroscopic Studies of Rb-Xe SEOP

Xenon-rich stopped-flow SEOP is a regime in which thermal effects can become strongly manifest. The first contributor is the Xe itself which, having a comparatively low thermal conductivity, impedes heat dissipation relative to the buffer gases. Xenon also has a high rate of rubidium spin destruction which leads to greater thermal loads due to an increased rate of quenching collisions. These issues becomes worse with increasing [Xe]. A second factor is that in stopped-flow SEOP there is no flow of gas to remove excess heat in the system, as is the case in continuous-flow SEOP. Thirdly, as evidenced by simulations in the previous chapter, SEOP at high xenon densities gains polarisation differentially at high laser fluxes - that is through power or reduced laser linewidths - and these high laser fluxes drive further heat into the system via the collisions with nitrogen. These thermal issues complicate the optimisation of the SEOP process because of the temperature dependent interplay between many of the variables in SEOP. Due to its ability to probe the temperature of the gas directly, Raman spectroscopy provides a unique insight into these thermal effects. This chapter contains the results of Raman investigations of xenon rich stopped-flow SEOP.

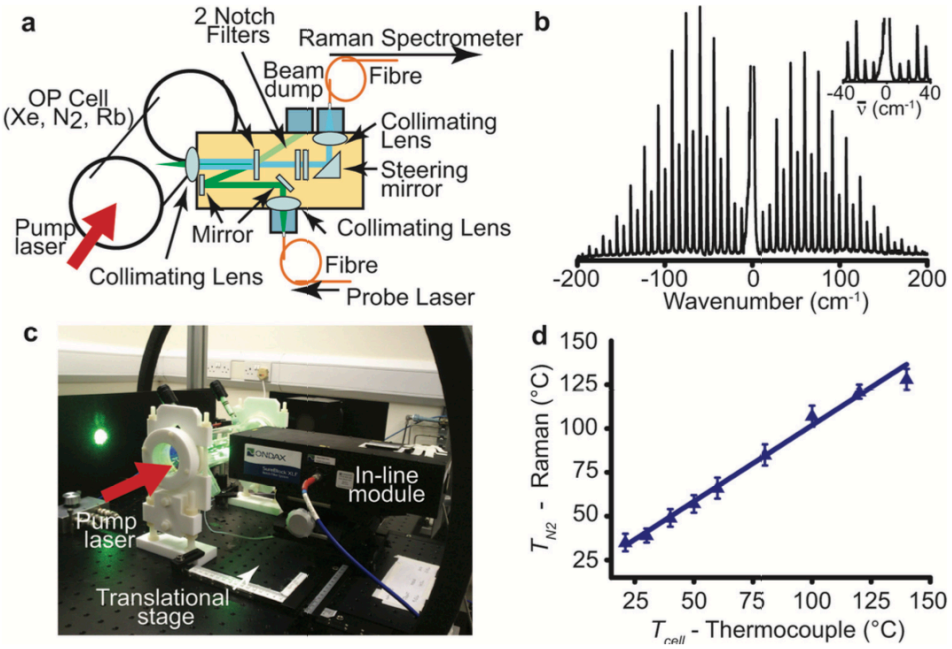

Figure 5.1: The in-line Ondax module (a) schematic representation. (b) Example N_2 rotational Raman spectrum. (c) Photograph of the in-line Raman module which also shows the translational stage. (d) Plot of the Raman temperature N_2 against the oven temperature as measured by the thermocouple in a calibration experiment in the absence of SEOP. Reprinted from [126] with permission.

As stated previously, nitrogen is frequently added to the SEOP mixture in order to collisionally quench destructive rubidium fluorescence. As nitrogen is a diatomic molecule, energy imparted during collisions within the optical cell can be absorbed by the rotational and vibrational phonon modes and subsequently scattered as they relax to the translational modes [125]. By examining the rotational modes, which relax to the translational mode almost immediately, Raman spectroscopy can be used to directly determine the temperature of the SEOP gas mixture.

The method of probing SEOP-like experiments with Raman spectroscopy was demonstrated by Walter *et al.* in 2001 when they examined energy transport during optical pumping [125]. In these experiments the cells were loaded with rubidium, helium and nitrogen and optically pumped using a broadband

2 nm pump laser. Raman excitation was performed with a 514.5 nm 6 W probe laser. They observed conductive heat transfer during optical pumping at low levels of power absorption and convective heat transfer at high levels of absorption: an issue that may be important when a noble gas is present in the cell as this will impact wall residence time - a dominant source of relaxation. Furthermore, Raman temperatures were significantly elevated relative to thermocouple temperatures and the deviation was a function of laser absorption and gas composition. These elevations reached 100 °C to 200 °C above the wall temperatures. These studies utilised low pump laser powers and predominantly helium rich loadings and the authors noted that investigations under conditions of high laser flux and less helium were warranted.

Whiting *et al.* investigated energy thermalisation in xenon-rich stopped-flow SEOP initially using an orthogonal Raman arrangement [127] . These experiments utilised a 70 W frequency-narrowed LDA with a FHWM of ∼0.25 nm. The design of the optical cell was such that the glass cell containing the Rb and noble gas was surrounded by an outer glass cylinder that served as the oven (see figure 5.5). This design ensured full optical access to facilitate Raman measurements. The probe laser was a 5 W 532 nm Verdi laser and the lens for detection was mounted orthogonally to the incident probe beam to spatially filter it from the resulting spectrum. Different partial pressures of xenon were studied to determine how increasing laser power would effect both the Raman temperature, T_{N_2}, and the ^{129}Xe polarisation. The highest xenon signal corresponded with the highest T_{N_2} (greater than 1000 K at times), and the high temperatures were attributed to low concentration of N_2 and the high concentration of xenon. While these experiments effectively showed the interdependence of laser power, cell temperature, gas density and composition, detection sensitivity was an issue.

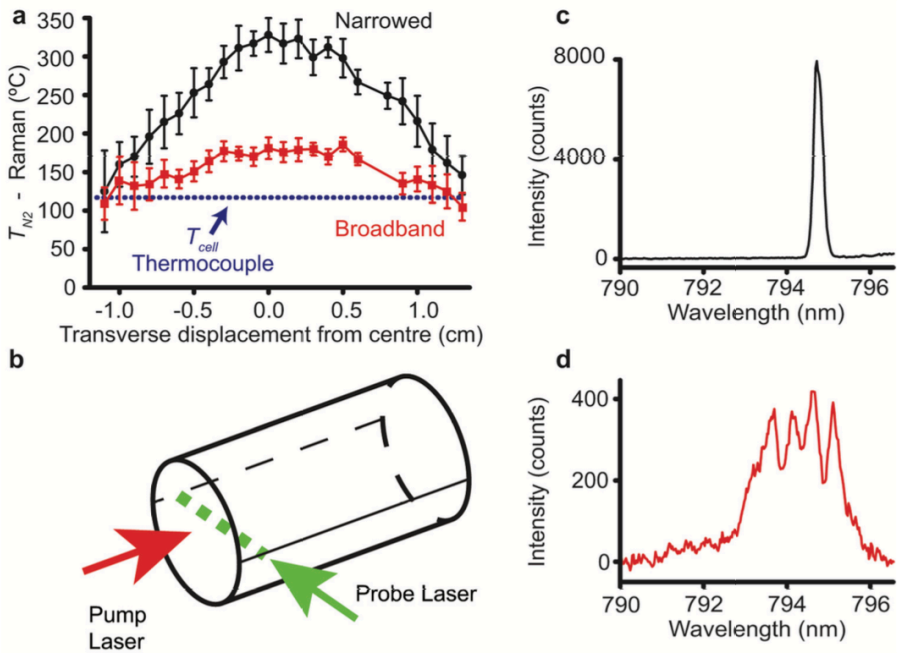

Figure 5.2: (a) Comparison of the spatial variation of the steady-state values of T_{N_2} during SEOP with both broadband and narrowband lasers. (b) Schematic representation of the experiment. (c, d) Spectral profiles of the VHG-narrowed and broadband LDAs, respectively; FWHM = 0.26 and 2.13 nm. Reprinted from [126] with permission.

While the orthogonal method was useful for initial work, the arrangement of the excitation and detection apparatus made the system prone to vibrations and misalignments. These factors would be a barrier to examining the experiment as a function of position. The method was therefore developed further with the in-line module [126]. With this instrumentation, scattered photons were detected in the same plane as the excitation beam. Panels (a) and (c) of figure 5.1 show a schematic and photograph of the in-line module. The module contains two ultra-narrow-band notch filters and an ultra-narrow-band beam splitter that together attenuate the Rayleigh scattered light allowing resolution of the Stokes and anti-Stokes lines as close as 10 cm^{-1} (panel (b)). The compact design allows the system to be easily mounted on a translational stage that facilitates discrete measurements along the length or radius of the optical cell.

As a demonstration of the unit it was used to compare the impact of optically pumping a 'lean' xenon gas mixture of 100 torr Xe and 1900 torr N_2 with both broad- and narrowband lasers (2.13 and 0.26 nm FWHM respectively). The mix was heated to 150 °C using a forced air oven, and T_{N_2} was measured transverse to the pump beam in 1 mm intervals 21 mm behind the front window after 5 minutes of SEOP with each laser. Figure 5.2 shows an overview of the experiment and results. From panel (a) it can be seen that in both cases T_{N_2} was elevated above the thermocouple reading by ∼40 °C for the broadband laser and ∼200 °C for the narrowed laser, likely due to the increased proportion of photons in the narrowband laser that can induce a transition in the Rb, ultimately leading to increased thermalisation as the energy is quenched in collisions with N_2. Direct comparison to the orthogonal arrangment indicated a 23-fold improvement in SNR.

The work presented in this chapter continues the examination of stopped-

flow SEOP with Raman spectroscopy by taking of advantage of the increased SNR provided by the in-line module, and the portability of the system. Experiments presented consider SEOP as a function of [Xe], buffer gas, laser wavelength and position.

5.1 Principles of Temperature Measurement with Raman Spectroscopy

Raman scattering was first postulated by Smekal in 1923 [128] and observed by Raman and Krishnan in 1928 [129]. In Raman spectroscopy, photons of a fixed frequency interact inelastically with electrons acting as molecular phonons, exciting them to a short-lived virtual excited state. This virtual state is a result of the incident light distorting the electron cloud. On relaxing from this state, the electrons return to a different vibrational or rotational state, and emit a photon that is shifted in frequency with respect to the originally incident photon. When collected, the scattered photons form a characteristic Raman spectrum which can be used to determine information on the rotation and vibrational states of the molecule, which in turn can be analysed to yield gas temperature [3].

The frequency shifts described above can both increase and decrease the frequency of the scattered light. If a nitrogen molecule is in the ground state when the photon is incident, it will be excited to the short-lived virtual state before relaxing back to a higher excited vibrational state than it began in. This increases the wavelength of the emitted, now scattered, light and is known as Stokes scattering (figures 5.3). If the nitrogen is in an excited state when the photon is incident it is excited to the short lived virtual state before relaxing down to either its original lower excited state, resulting in elastic Rayleigh scattering, or to a lower excited state, decreasing the wavelength of the emit-

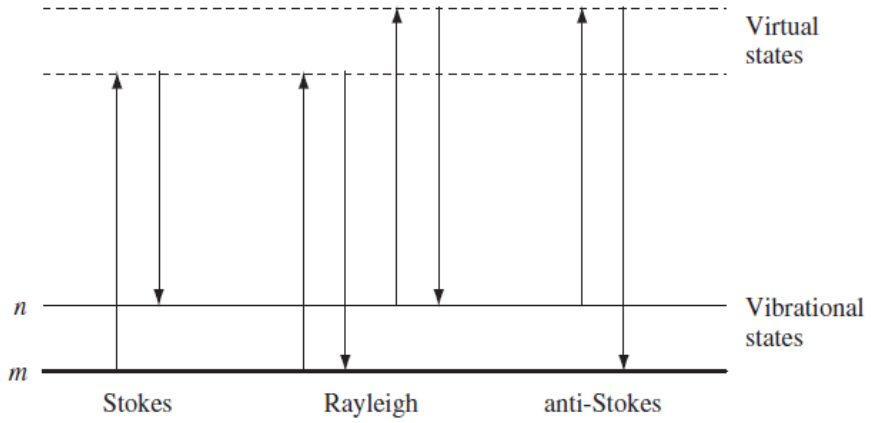

Figure 5.3: Energy transitions in Rayleigh, Stokes and anti-Stokes scattering. Reprinted from [3] with permission.

ted light in what is known as anti-Stokes scattering. If the dominant Rayleigh scattering contribution is removed, the Stokes scattering contribution is always greater than the anti-Stokes contribution because there are no energy levels below the ground state for the excited nitrogen molecules to relax to by anti-Stokes. The transitions can be seen in figure 5.3. If there are no electronic transitions at the energies of the Stokes and anti-Stokes transitions, the efficiency will increase as the fourth power of the frequency of the incident light [3].

A prominent feature of nitrogen Raman spectra is the alternating pattern of full and half height peak intensities (figure 5.1(b)). This is a consequence of the exchange interaction and quantum mechanical selection rules imposed on the molecule's spin quantum number, I, as governed by the Pauli exclusion principle. Fermions, particles with half-integer spins, must have wave-functions which are anti-symmetric with respect to exchange, and Bosons, particles with integer spin, must have symmetric wave-functions under particle exchange.

The molecular wave-function of the nitrogen can be written:

$$\Psi_{tot}(R_1 R_2 r_a r_b I_1 I_2 s_a s_b) = \psi_e(r_a r_b)\chi_e(s_a s_b)\psi_n(R_1 R_2)\chi_n(I_1 I_2) \tag{5.1}$$

where $\psi_e(r_a r_b)$ is the electronic spatial component of the molecular wave-function with electron locations r_a and r_b, $\chi_e(s_a s_b)$ is the electron spin contribution, with electron spins s_a and s_b, $\psi_n(R_1 R_2)$ is the nuclear spatial contribution of the molecular wave-function where R_1 and R_2 are the nuclear co-ordinates, and $\chi_n(I_1 I_2)$ is the nuclear spin contribution with I_1 and I_2 as the two nuclear spins. The spatial component of the nuclear wave-function, $\psi_n(R_1 R_2)$, is the product of rotational ϕ_n^{rot} and vibrational ϕ_n^{vib} terms:

$$\phi_n = \phi_n^{vib} \phi_n^{rot} \tag{5.2}$$

where the vibrational term is always symmetric under exchange, and may be ignored in our case as all spectra are purely rotational. As N_2 is a Boson, the molecular wave-function must be symmetric under particle exchange. The molecular spin multiplicity, I_{tot}, can take three possible values, $I_{tot} = 0, 1, 2$ (where the multiplicity is $2I + 1$ and I=1). With the electronic part of the of the molecular wave-function constrained to be symmetric under exchange, the nuclear part must be even as well. This means that only even J values are permitted when $I_{tot} = 0$ or 2, with a total spin multiplicity of $\Sigma(2I + 1) = 5 + 1 = 6$, and only odd J values are permitted when $I = 1$ with a multiplicity of $\Sigma(2I + 1) = 3$. This gives rise to the 2:1 intensity ratio in even-J and odd-J peaks in the nitrogen spectra [130].

In order to calculate the rotational Raman temperature, the relative line intensity, $I(J)$, of a transition, J, is compared to the signal received by the spectrometer, $S(J)$. A constant of proportionality, G, includes all the experimental constants (as referred to by Walter *et al.* [125]) of a particular set-up, including the volume of the nitrogen gas, cross-section of the transition, photon

scattering cross-section and intensity of probe beam.

$$S(J) = GI(J) \tag{5.3}$$

The following derivation which originates from Hickman *et al.* [131] can be exploited to extract temperature information from the nitrogen Raman spectra. Firstly, we consider the relative line intensity equation for a ro-vibrational spectrum from a J to J' state:

$$I(J) \propto \nu^4 n_J P_{J\rightarrow J'} \tag{5.4}$$

where

$$n_J = g(2J+1)exp\left(\frac{-BJ(J+1)hc}{k_B T}\right) \tag{5.5}$$

and for Stokes scattering where the selection rule for the transition is defined as $\Delta J = +2$

$$P_{J\rightarrow J'} = \frac{3(J+1)(J+2)}{2(2J+1)(2J+3)} \tag{5.6}$$

where J is the rotational quantum number, ν is the frequency of the rotational line (assumed to be constant over the range that we work in), g is the ground state degeneracy due to nuclear spin, B is the rotational constant for N_2 (~ 2 cm^{-1}) [130], c is the speed of light, and k_B is Boltzmann's constant.

Starting from equation 5.4, the proportionality relation can be removed by utilising a constant, for example C [131, 1]:

$$I(J) = C\nu^4 n_J P_{J\rightarrow J'} \tag{5.7}$$

If we make $C = 1/G$ where G contains all experimental optical factors as described above, then we arrive at equation 5.8.

$$S(J) = I(J)G = \nu^4 n_J P_{J\rightarrow J'} \tag{5.8}$$

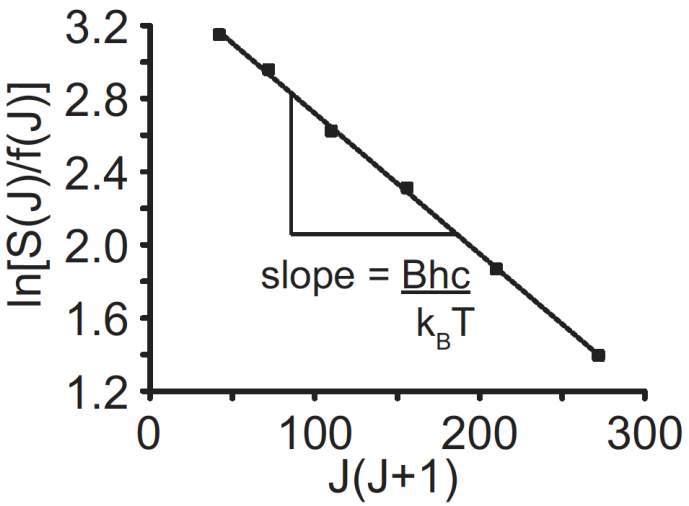

Figure 5.4: Illustration of how the terms in equation 5.17 can be used in the calculation of the Raman temperature T_{N_2}. Reprinted from [1] with permission.

From equation 5.8 we can substitute in equations 5.5 and 5.6.

$$S(J) = g\nu^4(2J+1)exp\left(\frac{-BJ(J+1)hc}{k_BT}\right)\frac{3(J+1)(J+2)}{2(2J+1)(2J+3)} \tag{5.9}$$

Cancelling out the $(2J+1)$ terms,

$$S(J) = g\nu^4 exp\left(\frac{-BJ(J+1)hc}{k_BT}\right)\frac{3(J+1)(J+2)}{2(2J+3)} \tag{5.10}$$

Simplifying equation 5.10 using $f(J)$,

$$f(J) = \frac{3(J+1)(J+2)}{2(2J+3)} \tag{5.11}$$

Following through we arrive at equation 5.16.

$$S(J) = g\nu^4 f(J) exp\left(\frac{-BJ(J+1)hc}{k_BT}\right) \tag{5.12}$$

$$\frac{S(J)}{g\nu^4 f(J)} = exp\left(\frac{-BJ(J+1)hc}{k_BT}\right) \tag{5.13}$$

$$ln\frac{S(J)}{g\nu^4 f(J)} = \frac{-BJ(J+1)hc}{k_BT} \tag{5.14}$$

$$ln\frac{1}{\nu^4} + ln\frac{S(J)}{gf(J)} = \frac{-BJ(J+1)hc}{k_BT} \tag{5.15}$$

$$-J(J+1)\frac{Bhc}{k_BT} = ln\frac{S(J)}{gf(J)} + 4ln\frac{1}{\nu} \tag{5.16}$$

It is possible to translate a spectrum of Raman peaks (Figure 5.1) into a rotational temperature measurement, taking the peak heights, $S(J)$ for six even J Stokes line (J = 6, 8, 10, 12, 14, 16). Taking equation 5.16 with $g = 1$, and comparing to the equation of a straight line, a plot can therefore be created with a linear fit of

$$J(J+1) \text{ versus } ln\frac{S(J)}{f(J)} \tag{5.17}$$

enabling T to be determined as illustrated in Figure 5.4, with the slope equal to Bhc/k_BT.

5.2 Methods

5.2.1 Raman Excitation and Detection

Raman spectra were collected using a Horiba Yvon U1000 Raman spectrometer and excited using a 5 W Coherent Verdi laser at 532 nm. The Raman laser light is directed into the optical cell using the in-line Ondax module described at the start of the chapter (figure 5.1), which contains two ultra-narrow-band notch filters and an ultra-narrow-band beam splitter that together attenuate the Rayleigh scattered light in the obtained spectra that would otherwise saturate the spectrometer, making impossible to detect the Raman scattering signals which are typically 10^6 times weaker in intensity [130]. The scattered light is collected along the same optical path and is directed to the spectrometer using a beam splitter. The entire module is on a mobile platform that allows the user to position the module at any position along the cell. It can

also be moved forward and backwards, allowing the user to selectively sample radial temperatures within the optical cell. Before experiments commenced, the module was aligned so that probe beam was focused at the centre of the optical cell. This inline module was recently developed by the team in collaboration with Ondax, and provides a 23-fold improvement in SNR on the previous 'orthogonal' arrangement [126].

5.2.2 SEOP Experiments

Two kinds of SEOP experiments are described in this section: build up curves and spectral offsets. For both, the basic SEOP experiment was the same. A 60 W 0.26 nm frequency-narrowed QPC Brightlock pump laser was used for optical pumping. The temperature of the optical cell was controlled by passing compressed, heated air over it. A thermocouple placed inside the oven, but just outside the optical cell, provided feedback to the PID temperature controller which also displayed the temperature.

Laser power was monitored with two power meters. One of the power meters was positioned before the optical cell and the SEOP experiments were initiated by removing it from the optical path. The second power meter was placed after the optical cell, so that readings of the two meters can be used to calculate power absorption by the rubidium within the cell. Absorption of the laser light by the D_1 line of the rubidium vapour was monitored using an Ocean Optics spectrometer angled to detect reflected light from the rear power meter. Xenon polarisation was measured using a Kea NMR spectrometer and three surface NMR coils position beneath the optical cell using a simple pulse-acquire sequence. The positions of the three coils allow for the xenon polarisation to be probed at the front, middle and back of the cell. A schematic of the apparatus is shown in figure 5.5a.

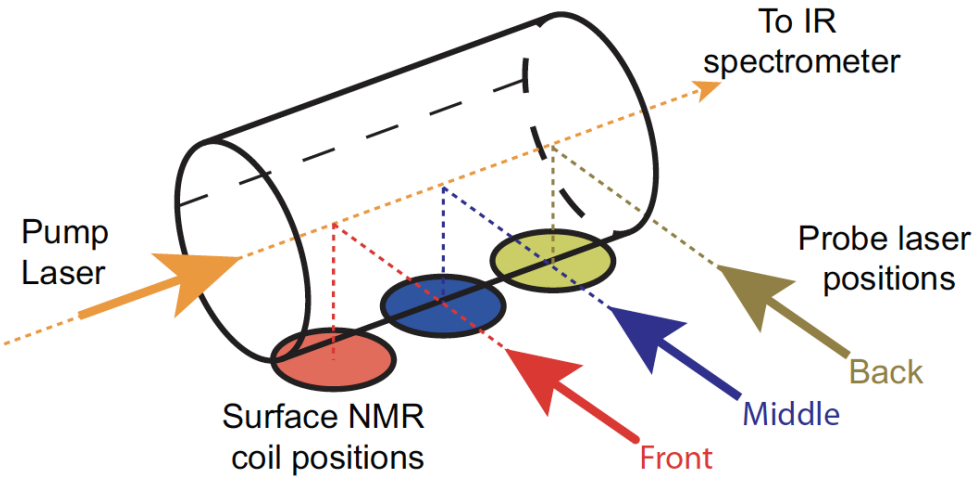

(a)

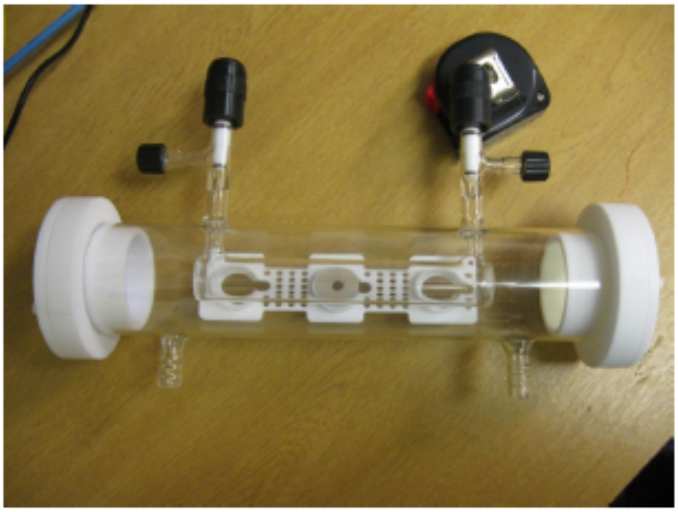

(b)

Figure 5.5: a) Schematic of the co-location of NMR and Raman measurements. b) The optical cell used in Raman SEOP experiments. The smaller central cell contains the gas mixture and a small quantity of rubidium (approximately 0.5 g). This is contained within an outer glass section which acts as the oven. Compressed hot air is forced through the oven using the two inlets at the bottom of the cell. Inside the oven is the white mount for the three NMR coils. Anti-reflective coated windows are used to increase transmission efficiency through the cell and are mounted within two white end pieces. The outer glass section is transparent to enable Raman measurements of the gas during SEOP.

5.2.3 Experimental Protocol

The build up curve experiments allow the study of dynamic behaviour within the cell over a period of 30 minutes. For all build up curves the QPC pump laser was tuned to the D_1 transition at 794.77 nm, with a constant laser current of 40 A. In the initial experiments, at fixed intervals throughout the 30 minutes, measurements of the xenon polarisation and rotational Raman temperature in the middle of the cell, and transmitted power through the whole cell, were recorded while a constant oven temperature was maintained. In later experiments, the Raman and NMR data where recorded as a function of longitudinal position - at the front, middle and back (fig 5.5(a)).

Spectral offset experiments permit the study of SEOP under conditions of varying pump laser frequency. Wavelengths studied include 794.54, 794.64, 794.77, 794.91 and 795.01 nm. These wavelengths can be obtained by setting the QPC Brightlock pump laser's water chiller to 13.5, 15.0, 17.0, 19.0 and 21.0 °C respectively while maintaining a laser current of 40 A. This shifts the centroid wavelength away from the center of the rubidium D_1 transition. In the spectral offset experiments, the Raman rotational temperature and xenon polarisation were recorded in the middle of the cell 10 minutes after the start of the experiment.

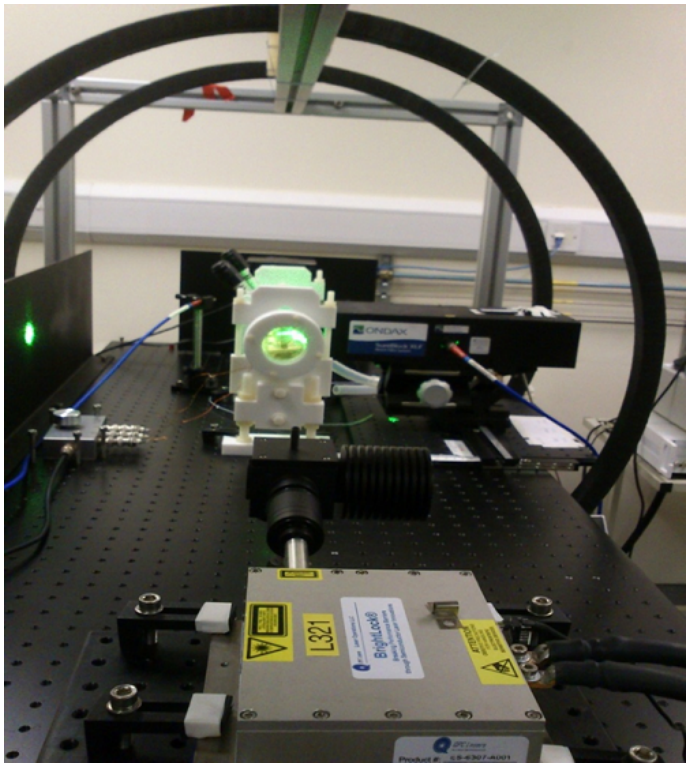

(a)

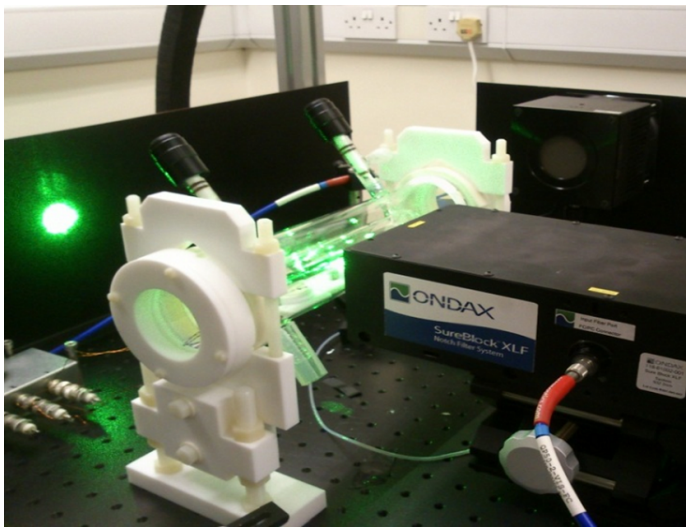

(b)

Figure 5.6: The SEOP experimental apparatus. a) Is is a photograph taken from above the pump laser and shows the co-linear alignment of the centre of the cell, the optical axis, and the z-axis of the magnetic field. b) shows the Raman probe laser and in-line module.

5.2.4 Analysis of Raman Data

This section describes the procedure for the analysis of a Raman spectrum; from the raw text file produced by the spectrometer through to a corrected temperature measurement with its associated error, along with the intermediate steps of background correction and Gaussian fitting of the even J-value Raman spectral peaks. Steps include removal of a scaled, shifted evacuated cell spectrum and adjustment accounting for the transmission efficiency of the filters within the in-line module.

By utilising Matlab, time consuming and error-prone manual processing in BioRad Knowitall (for baseline correction), OriginPro (for Gaussian fit) and Microsoft Excel (for temperature calculations) was replaced by one self contained program. The program can be summarised as follows:

- Firstly the user is asked to select a Raman spectrum (the examples shown are in the absence of spin-exchange optical pumping).

- A correction is applied for the transmission efficiency of the filters supplied from Ondax:

$$\text{corrected intensity} = \left(-4 * 10^{-9}x^2 + 8 * 10^{-5}x - 0.5201\right) * \text{intensity} \tag{5.18}$$

  where x is in wavenumbers relative to 532.21 nm as the central wavelength. See figure 5.11 for implementation of this filter correction.

- Data is baseline corrected. Four noise regions in the spectrum are located and a line is fitted through these regions, this line is subsequently removed from the spectrum, see left part of figure 5.7.

- A Raman spectrum collected from a evacuated cell ($\sim$ 1x10^{-5} torr) is read in and baseline corrected. This spectrum is used for background

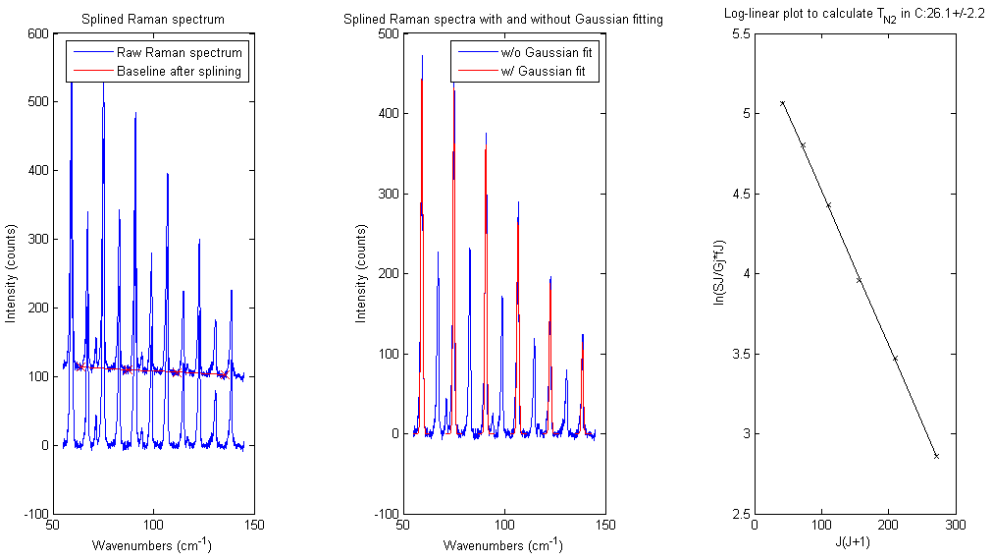

Figure 5.7: Original data which has had a baseline correction and a Gaussian fit programmatically applied, giving a temperature of 26.1 $\pm$ 2.2 °Cfor a measured cell thermocouple temperature of 25 °C. Reprinted from [1] with permission.

subtraction to eliminate atmospheric oxygen and nitrogen contributions from the spectrum that arise from the space between the in-line module and the optical cell.

- Peak locations are found in both the evacuated cell and data spectra.
- A scaled evacuated cell spectrum is produced by taking the ratio of the peak heights of the oxygen peaks present in both datasets.
- The spectra are subsequently aligned by calculating the shift between the nitrogen peaks present in the spectra.
- A difference spectra is then derived from the data spectrum and the shifted, aligned evacuated cell spectrum, removing the contribution of oxygen peaks. See Figure 5.8.
- A Gaussian fit is applied to the difference spectrum using a non-linear least squares fit and the peak heights are recorded.

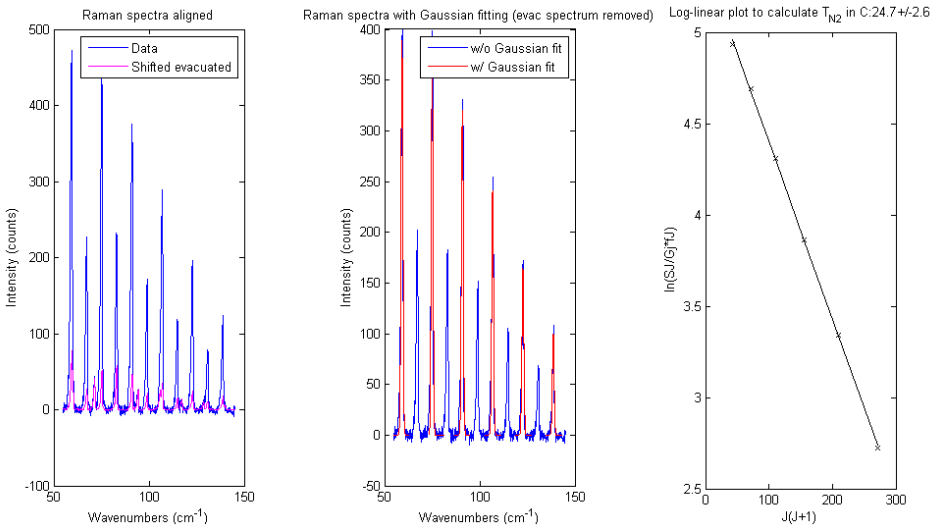

Figure 5.8: This spectrum has been baseline corrected and then an evacuated cell spectrum removed from data spectrum prior to a Gaussian fit being applied. This gives a temperature of 24.7 $\pm$ 2.6 °C for the same spectrum shown in figure 5.7 with a cell thermocouple temperature of 25 °C.

- The rotational temperature is calculated according to the equations in section 5.1.

- The error on the temperature is computed from the reciprocal of the signal to noise of the data spectrum multiplied by the temperature.

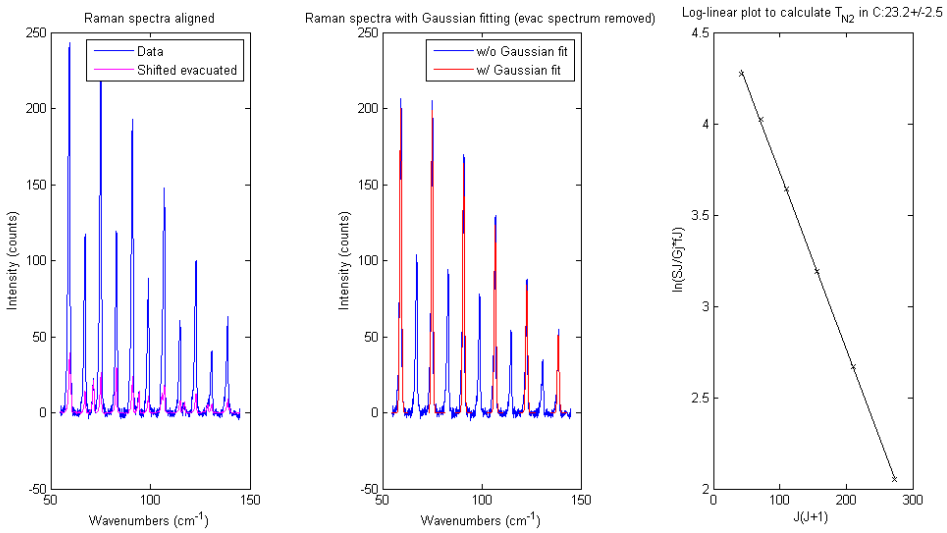

Figure 5.9: Data analysed using all the techniques reported in section 5.2.4: baseline correction, oxygen peak removal by an evacuated cell spectrum removal and consideration of the transmission efficiency for filters in the in-line module. Combined, these methods give a calculated temperature of 23.2 $\pm$ 2.5 °C, for the same spectrum shown in Figure 5.7 with a cell thermocouple temperature of 25 °C. Reprinted from [1] with permission.

Figure 5.10 shows the baselined data prior to background subtraction. It can be seen how the evacuated cell spectrum peaks have been programatically aligned to the position of the peaks from the data spectrum and the heights of the peaks are scaled proportionally. The impact of these methods are illustrated in figure 5.11 where a residual plot is shown for measurements at the front, middle and back of the cell and repeated five times at each position. The dashed line shows the temperature recorded by the thermocouple in the oven inlet and outlet (25 °C). The application of the removal of the evacuated cell spectrum lowers the temperature deviation and this is further lowered by the inclusion of the efficiency of the filters.

During the course of data analysis a trend was noticed in the Raman spectra. It was noted that as the temperature increases, the signal to noise drops because the intensity of the Raman peaks decreases. An example of this can been seen in figure 5.13. It was found to be a well known phenomenon

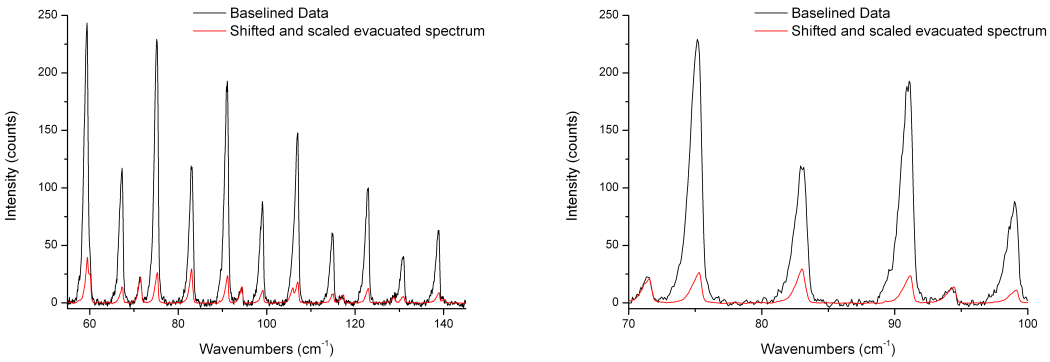

Figure 5.10: a) Spectrally aligned and scaled evacuated spectrum with data spectrum. b) Zoomed in version of (a). Reprinted from [1] with permission.

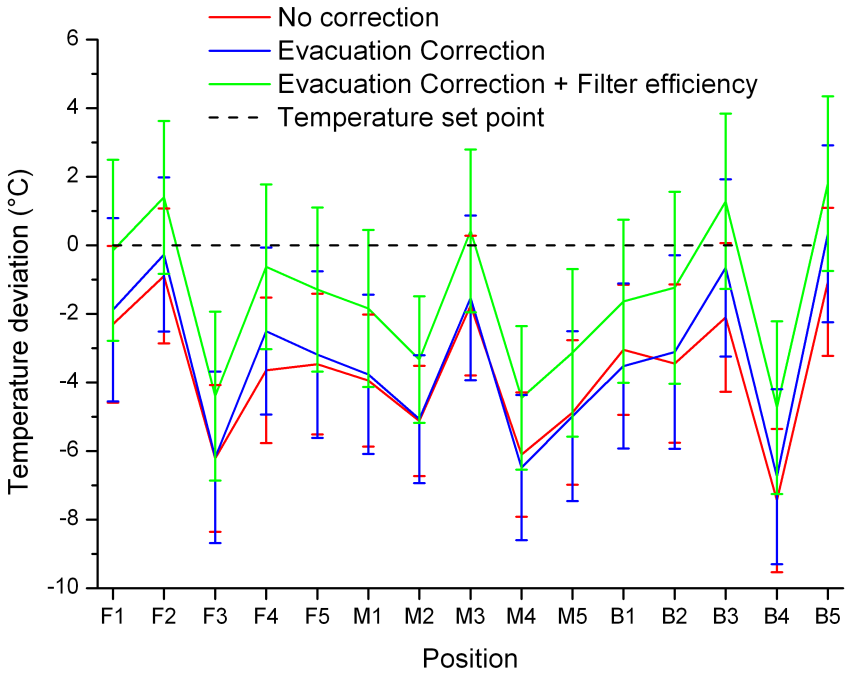

Figure 5.11: Residual plot for 25 °C data spectra at 3 positions in cell front (F), middle (M) and back (B), repeated 5 times at each position. It can be seen that with each subsequent correction applied within the Matlab code the temperature readings move progressively close to the 25 °C line. Reprinted from [1] with permission.

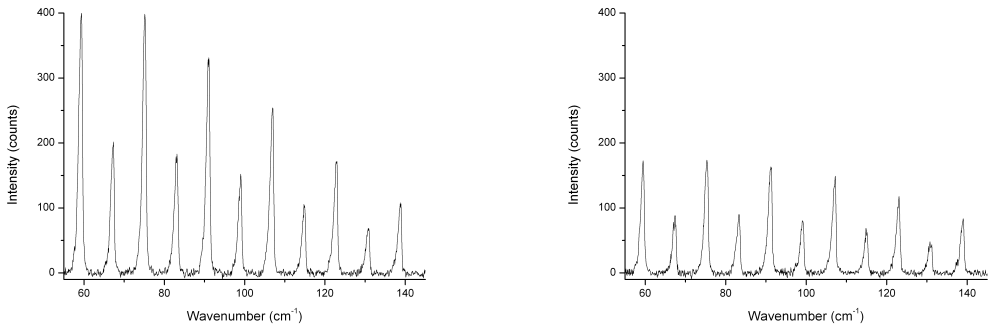

Figure 5.12: Comparison of Raman peak intensities and corresponding absorption coefficient with temperature: a) 25 °C and b) 150 °C Raman data spectrum. These plots have had the Matlab code described above applied. Reprinted from [1] with permission.

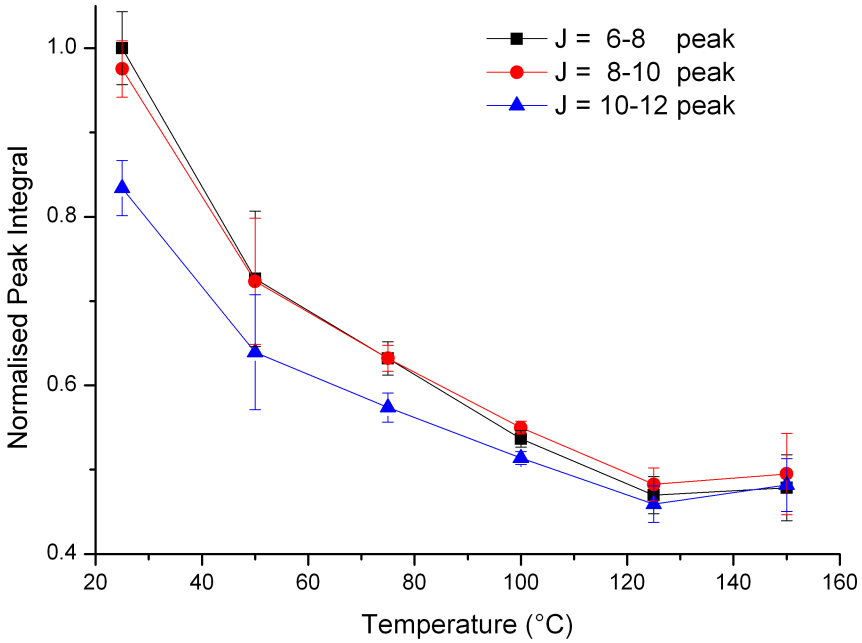

Figure 5.13: Normalised relative absorption coefficient dependence with temperature. Reprinted from [1] with permission.

linked to the Beer-Lambert law which describes the absorbance of a material [132, 133, 134],

$$I = I_0 exp(-k(\nu)l)) \tag{5.19}$$

where radiation of intensity I travels through a sample of length l with an absorption coefficient, k which is a function of the wavenumber, ν. The total strength of a transition is known to be $\int k_\nu \delta\nu$ [132], such that the sum of relative Raman scattering cross-sections can be determined from the integrated peak areas as discussed by Simonelli and Shultz [135]. They showed that as the temperature of a sample increases (in their case an ammonia/water complex), the cross-section of the transition decreases. This can be seen in figure 5.13, experimental data collected in the absence of spin-exchange optical pumping.

5.2.5 Calibration of Raman Temperature Measurements

Raman temperature measurements were validated against thermocouple measurements of a heated optical cell filled with nitrogen heated to 150 °C. The results can be seen in figure 5.1.

5.2.6 Calculating the Polarisation of HP Xenon

Another important aspect of the analysis was the calculation of the percentage polarisation of the HP xenon. This enables polarisation levels as a percentage of the total xenon present to be quoted instead of arbitrary units of NMR intensity. This polarisation calculation is done by comparing the hyperpolarised xenon NMR signal to that of a proton sample at thermal equilibrium, for which the polarisation can be calculated.

The polarisation of a HP xenon sample can be calculated by comparison with a thermal proton sample at the same precession frequency by varying the magnetic field. In our case B_0 for ^{1}H = 8.4 G and B_0 ^{129}Xe = 30.2 G, with a

Table 5.1: Nuclear Spin Properties [136]

Nuclide	Gyromagnetic ratio, γ /MHzT^{-1}	Natural abundance /%
^{1}H	42.5759	99.985
^{129}Xe	11.7769	26.44

precession frequency $\omega = 36.3525$ kHz in both cases (as $\omega = \gamma\ B_0$). A doped proton sample, which acted as the thermal reference sample, was prepared in an optical cell of the same volume as the xenon sample (68±2 cm^3). It was doped with 10 mM of $CuSO_4$, equating to approximately 0.11 g. This resulted in a shortened T_1 of 0.149±0.002 s at Earth's field. When conducting multiple pulse-acquire NMR experiments it is recommended to wait 5 T_1s to allow the sample to relax fully to thermal equillibrium. The purpose of doping the water sample was to reduce the relaxation time and hence reduce the time taken to acquire many NMR spectra. 950,400 acquisitions were required to produce a spectrum of sufficient SNR. The results are shown in figure 5.14.

The details of the polarisation calculation are as follows: The proton molar concentration c_{H} was 111.12 M, and was determined by utilising the molar mass of water (18 g/mol) for 1 litre (1000 g) of water:

$$\text{Water molar concentration} = \frac{1000\ \text{g}}{18\ \text{g/mol}} = 55.56\ \text{M} \tag{5.20}$$

$$c_{\mathrm{H}} = \text{Proton molar concentration} = 2{*}\text{Water molar concentration} = 111.12\ \text{M} \tag{5.21}$$

The molar volume of an ideal gas at 1 atmosphere of pressure at 0 °C is

known to be 22.414 L/mol:

$$V_m = \frac{V}{n} = \frac{RT}{p} = \frac{8.314 \text{ Jmol}^{-1}\text{K}^{-1} \text{ x } 273 \text{ K}}{101.325 \text{ kPa}} = 22.414 \text{ Lmol}^{-1} \tag{5.22}$$

Given the definition of the molar volume, the concentration of xenon, c_{Xe}, is calculated by:

$$c_{\text{Xe}} = \frac{\beta_{\text{Xe}}}{V_m} \frac{p_{\text{Xe}}}{p_{760}} \frac{T_{273}}{T_{\text{Xe}}} \tag{5.23}$$

where β_{Xe} is the natural abundance of ^{129}Xe as shown in table 5.1. p_{Xe} is the pressure of xenon loaded in the optical cell, p_{760} is the pressure of 1 atmosphere (= 760 Torr), T_{273} is 0 °C as defined above and T_{Xe} is the temperature at which the xenon gas is loaded into the cell.

Combining the elements described above, a polarisation enhancement factor, $\epsilon_{enhance}$ can be calculated to determine the enhancement of the hyperpolarised xenon signal compared to the thermally polarised proton signal, this is similar to the equations set out in Ruset's PhD [120]:

$$\epsilon_{enhance} = \frac{c_{\text{H}}}{c_{\text{Xe}}} \frac{sin(\alpha_{\text{H}})}{sin(\alpha_{\text{Xe}})} \frac{\gamma_{\text{H}}}{\gamma_{\text{Xe}}} \frac{S_{\text{Xe}}}{S_{\text{H}}} \tag{5.24}$$

where α_{H} and α_{Xe} are the flip angles for proton and xenon respectively as described in section 5.2.7, S_{Xe} and S_{H} are the signal intensities of the xenon and proton samples respectively. A compensation factor for T_2^*, $C_{T_2}^*$, is introduced to take into account loses in NMR signal due to the acquisition delay, T_{aq}, and T_2^*:

$$C_{T_2}^* = \exp\left(\frac{T_{aq_{\text{Xe}}}}{T_{2_{\text{Xe}}}^*}\right) - \exp\left(\frac{T_{aq_{\text{H}}}}{T_{2_{\text{H}}}^*}\right) \tag{5.25}$$

Combining equations 2.6, 5.24 and 5.25, the xenon polarisation, P_{Xe} can be calculated:

$$P_{\text{Xe}} = \epsilon_{enhance}.C_{T_2}^*.P_{thermal}.100 \tag{5.26}$$

The error on P_{Xe} is calculated from the reciprocal of the signal to noise ratio of the proton spectrum.

5.2.7 Flip Angle Calibration

The flip angle needed for equation 5.24 is determined experimentally by sweeping through incremental rf pulse durations and integrating the area under the resulting fourier transformed FID for each pulse. A sine curve can then be fitted to the resulting data to calibrate the flip angle. For the proton calibration, figure 5.14, 22,464 scans were performed with 100 steps in increments of 4 μs, to determine a 90 ° pulse at 81.2 μs. This was implemented using a Magritek Kea NMR spectrometer with the Pulse Duration Sweep program, the repetition time was 0.5 s. The xenon flip angle calibration was performed manually using a pulse acquire program on the Kea NMR spectrometer.

Acquisition Parameters

The reference proton NMR spectrum was acquired by averaging over 950,400 scans on a 10 mM $CuSO_4$ doped water sample. The pulse duration used was 77 μs equating to $\approx$ 85.6 ° pulse. A 0.5 s repetition time was used at a precession frequency of 36.3525 kHz and a 5 μs acquisition delay. 4096 complex data points were acquired over a spectral width of 50 Hz. This resulted in an acquisition time for each FID of 81.92 μs. The same parameters were used for the single hyperpolarised xenon scan, however the pulse duration was set to 200 μs to maintain a constant flip angle of 90 ° for both species.

5.3 Results and Discussion

Described within this section are the results and interpretation of the various build-up and spectral offset experiments. Before this can be done however, it is

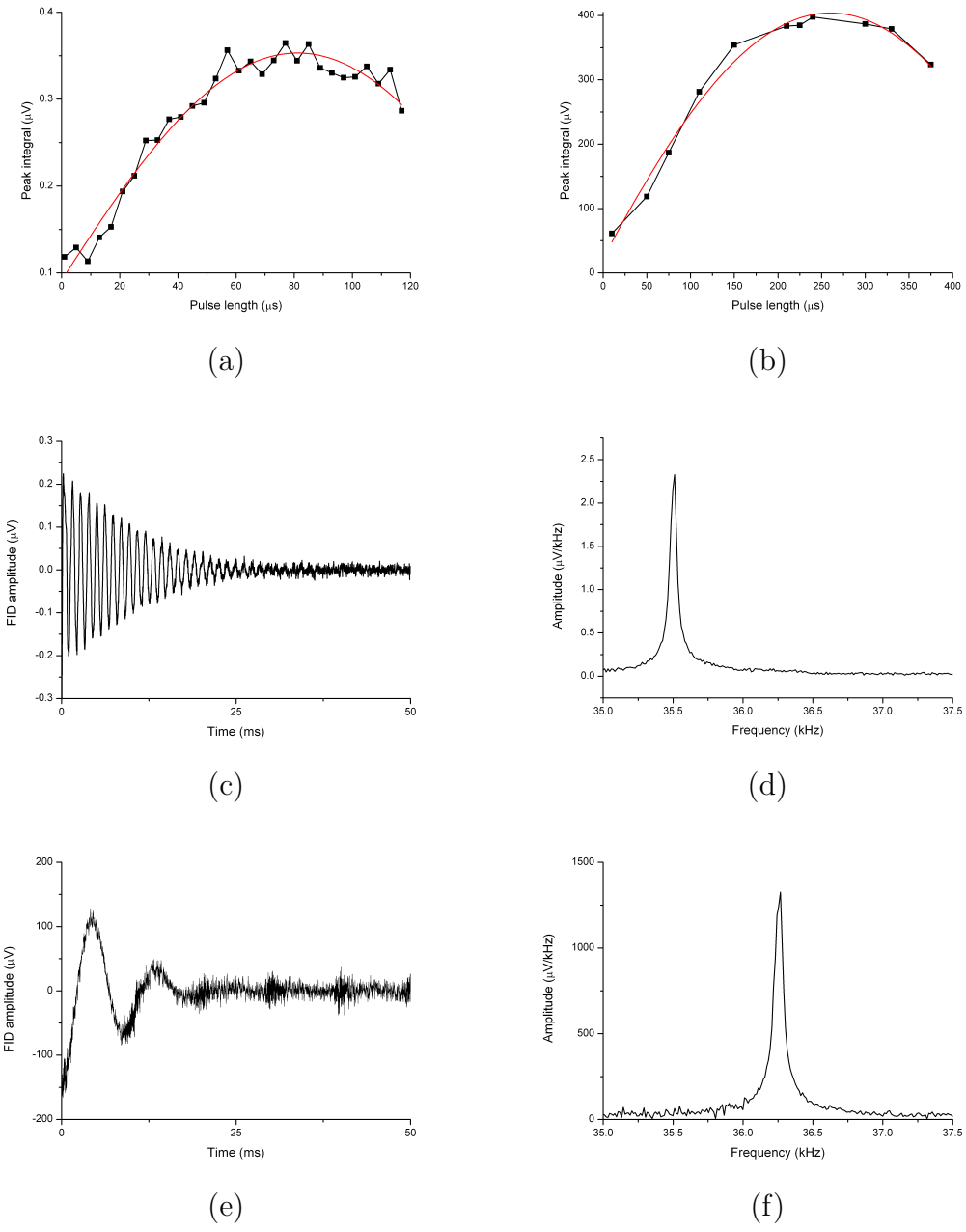

Figure 5.14: Flip angle calibration for proton (a) and xenon (b). A 90 ° pulse is obtained using a 81.2 μs and 260 μs pulse for ^{1}H and ^{129}Xe respectively. (c) Proton reference FID and spectrum (d) acquired from 950,400 scans using a 10 mM $CuSO_4$ doped water sample using $\approx$ 85.6 ° pulse. (e) FID of a single scan of hyperpolarised xenon and (f) the magnitude spectrum, obtained with a 74 °pulse. Reprinted from [1] with permission.

necessary to discuss a recurrent theme - rubidium runaway - a spin destructive phenomenon that occurred in a number of experiments.

Rubidium Runaway

When a SEOP experiment is initiated, the first hallmark of rubidium runaway can be observed as a sharp and simultaneous increase in P_{Xe}, power absorbed and rotational Raman temperature, $T_{\mathrm{N_2}}$. Figure 5.15 provides an example of this. It is thought that spin-exchange occurs initially as normal, with circularly polarised photons optically pumping Rb atoms to the $m_J = +\frac{1}{2}$ sub-level of the $2P_{\frac{1}{2}}$ excited state, evident by the increased power absorption of the laser light. The excited state is quenched through collisions with N_2, thermalising the energy, observed as an increase in $T_{\mathrm{N_2}}$. The quenching collisions cause the excited rubidium atoms to re-populate the ground states with equal probability, and those which relax to the $m_S = +\frac{1}{2}$ state undergo spin-exchange with Xe, evident in the increase in observed P_{Xe}. These processes continue, but as more Rb atoms are quenched by N_2 the temperature increases, which in turn increases the [Rb]. As [Rb] increases more quenching collisions occur and thus a feedback loop occurs with a rapidly increasing temperature. As this process unfolds, the laser light becomes increasingly attenuated and can penetrate less and less into the optical cell because the number of absorbing, unpolarised Rb atoms increases sharply with temperature.

In the presented experiments where rubidium runaway occurs, a sharp drop in P_{Xe} is typically observed after the initial peak described above, while power absorbed remains high. This is because the unpolarised Rb atoms, which are responsible for the power absorption, become localised to the front of the optical cell as [Rb] increases. P_{Xe} therefore drops in the middle of the cell and onwards because no polarised light can get through, and therefore Rb atoms

in the middle of the cell are no longer exposed to circularly polarised light, and hence spin-exchange can no longer occur. This theory is further evidenced by the drop in T_{N_2} in the middle of the cell, another indication that the quenching collisions of the N_2 and polarised Rb atoms have also ceased.

Function of Temperature

The first instance in which rubidium runaway occurs is in figure 5.15. Here, a gas mix containing 100/1100 torr Xe/N_2 with 800 torr of He was studied as a function of temperature - 90, 110 and 140 °C. At 140 °C - the black circles - it can be seen in panel (a) that xenon polarisation peaks at ∼35% within minutes. Panels (b) and (c) show corresponding spikes in T_{N_2} and power absorbed, at ∼300 °C and 35 W respectively. Polarisation then drops to ∼10% within a few minutes and plateaus at this level. At the same time T_{N_2} plateaus at a lower value of ∼200 °C, indicative of reduced SEOP given the measurements were taken at the middle of the cell. Power also plateaus but at an elevated level, corroborating the theory that an optically opaque Rb vapour has blocked laser transmission through the cell.

At 90 °C the temperature is too low and as a consequence [Rb] is suppressed. This results in little power absorption (panel (c), red line) and subsequently little spin-exchange, which is manifest in both low polarisation - with only just reaches 10% by the end of the experiment - and in the low Raman temperature - which remains close to T_{cell} throughout the experiment, never deviating from it by more than ∼10 °C. 110 °C is the closest to optimal temperature in this case (blue lines) with a gradual increase in all parameters throughout. Xenon polarisation builds exponentially and peaks at 35%.

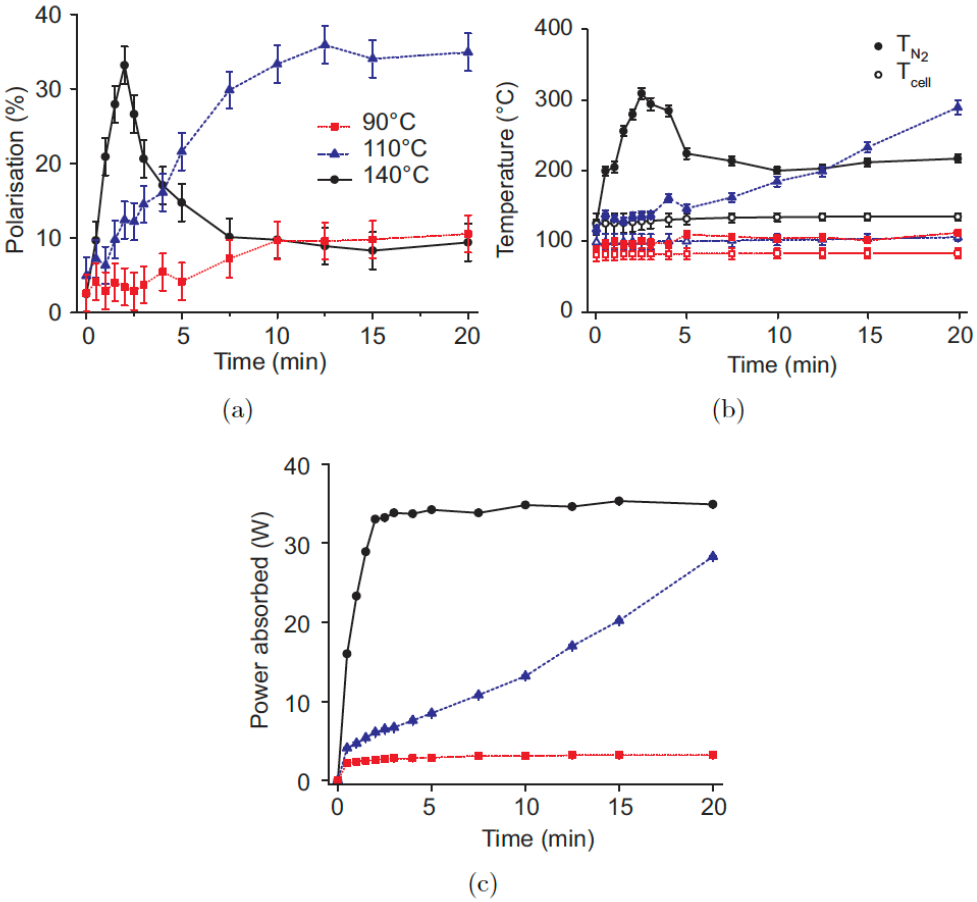

Figure 5.15: Xenon polarisation, Raman temperatures and power absorption as a function of oven temperature and time. Temperatures used were T_{cell} = 90, 110, 140 °C and are denoted by red squares, blue triangles and black circles respectively. In panel (b), the Raman temperatures are denoted by solid coloured shapes, T_{cell} values are hollow. The gas mix was 100/1100 torr Xe/N_2 with 800 torr of helium optically pumped with 60 W of frequency narrowed light. NMR and Raman data (a,b) are taken from the middle of the cell. Reprinted from [1] with permission.

Function of Gas Mix Composition

Fixing the partial pressure of Xe allows investigation of SEOP as a function of buffer gas composition which is interesting as it is likely an interplay that exists. Both gases will pressure broaden the Rb D_1 transition [137], facilitating optical pumping by improving spectral coupling to the pump laser, but only diatomic N_2 can effectively quench the Rb optical de-exciations, generating heat in the process, while facilitating spin-exchange. Therefore it is crucial to have N_2, but He has a greater thermal conductivity, and this may act to control the detrimental thermal effects associated with rubidium runaway by dissipating the thermal energy to the walls of the optical cell more rapidly. Thermal conductivities of the gases are: $17.77^{-2}\mathrm{Wm}^{-1}\mathrm{K}^{-1}$ for helium, $3.091^{-2}\mathrm{Wm}^{-1}\mathrm{K}^{-1}$ for nitrogen, and $0.701^{-2}\mathrm{Wm}^{-1}\mathrm{K}^{-1}$ for xenon (or, as a ratio, $\sim 25:4:1$).

The impact of He on the thermal behaviour within the optical cell can be seen in 5.16. Here, three SEOP experiments are compared in which the partial pressure of Xe and the total cell pressure were held constant at 100 torr and 2000 torr respectively, but increasing amounts of He gas were substituted in place of N_2. As the fraction of He within the cell was increased it can be seen that T_{N_2} is reduced from roughly 200 °C with no He present, to 100 °C with 1400 torr He included in the mixture. The onset of Rb runaway is evident from the sharp spike in P_{Xe} in the first mix, where the polarization initially climbs sharply, peaking abruptly at 6 min before dropping. At this point the high [Rb] creates optical opacity that limits the polarization process. It can be seen that this effect is suppressed as more He is added to the mixture at little cost to the ultimate polarization. Given that existing xenon-rich stopped-flow polarisers operate with substantially higher powered lasers which only further exacerbate these thermal management issues, it may be that He becomes a valuable tool

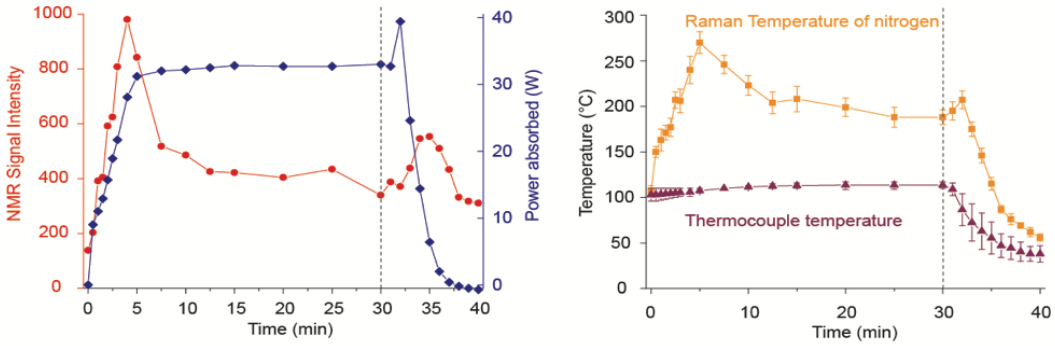

(a)

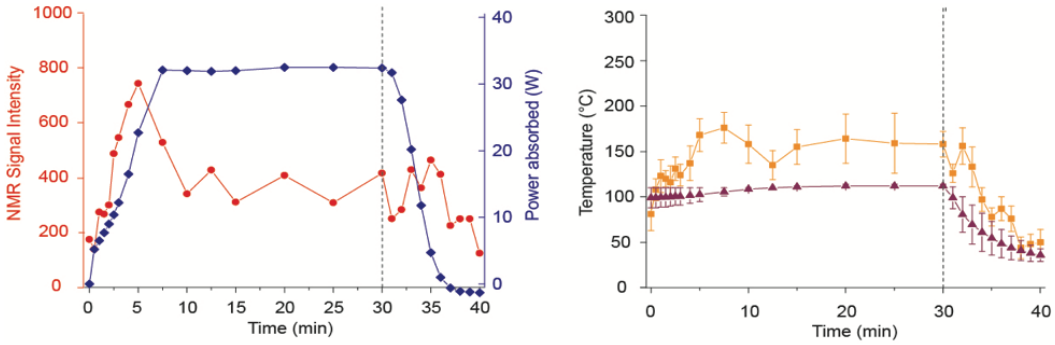

(b)

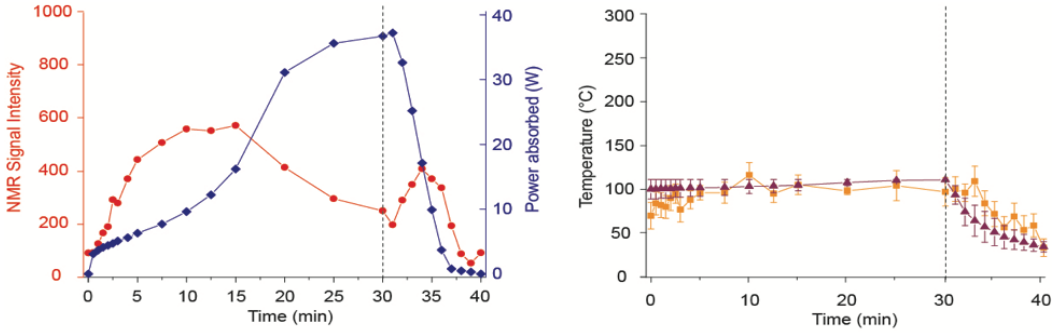

(c)

Figure 5.16: Comparison of SEOP as a function of buffer gas composition. In all panels a), b) and c), red circles denote Xe signal intensity, blue diamonds denote power absorbed, orange squares show Raman temperatures T_{N_2} , and the oven thermocouple temperatures, T_{cell}, are denoted by the green triangles. Gas compositions were 100/1900 torr Xe/N_2 with no He (a), 100/1700 torr Xe/N_2 and 200 torr He (b), and 100/500 Torr Xe/N_2 and 1400 Torr He (c). Reprinted from [138] with permission.

for optimization. Particularly in light of the simulations presented in chapter 4, which indicate He has no impact of the SEOP physics of the system (when used in place of nitrogen).

Function of Position

The experiments that vary buffer gas density and composition indicated that polarization and temperature are likely to vary along the length of the cell, particularly under conditions of Rb runaway. Figure 5.5 illustrates how Raman measurements were taken at coincident locations to NMR measurements at the front, middle, and back of the optical cell using the translational stage (which shown in 5.1 and 5.6(a)). Figure 5.17 shows the results of two experiments where this configuration was used. Both experiments were conducted on a gas mix of 1000/1000 Torr Xe/N2 but at oven temperatures of 120 and 130 °C respectively. At 120 °C, the temperature at the front, middle, and back correspond well to the respective P_{Xe} values, which were both highest at the back of the cell. However, it can be seen that a mere 10 °C increase in oven temperature is enough to induce significant variation in $T_{\mathrm{N_2}}$ along the length of the cell. Indeed, Raman temperatures more than double from ∼240 °C to almost 600 °C. Also, closer examination shows that after 4 min of pump laser illumination during SEOP a switch in the Raman temperatures occurs indicative of a change in the thermal flow patterns within the cell, both likely triggered by Rb runaway. This conclusion is corroborated by the elevated pump laser light absorption, which indicates a spike in absorbers. Again, this disruption temporally coincides with the spike in P_{Xe}, and the onset of rubidium runaway results in a polarisation which is half that in the stable case.

Figure 5.18 is a further example of such behaviour. In this case the gas mix was a 1500/500 torr xenon/N_2 binary mix and the rubidium runaway event at

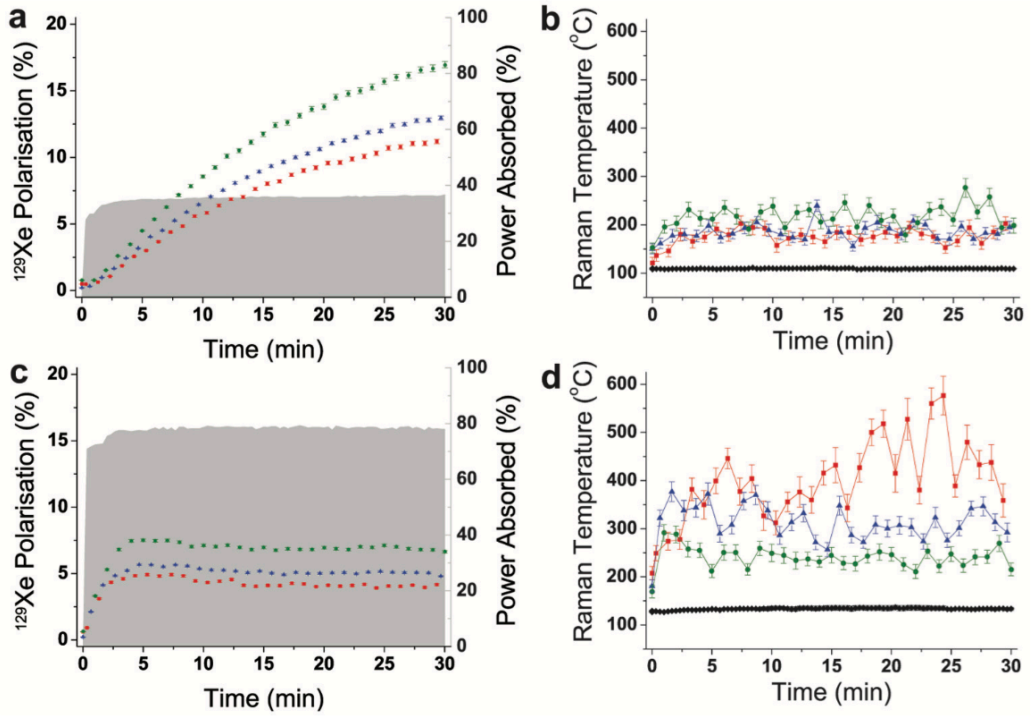

Figure 5.17: Comparison of xenon polarization build-up and T_{N_2} Raman measurements during a 30-min SEOP experiment in an optical pumping cell containing 1000/1000 torr Xe/N_2 at 120 °C (a, b) and 130 °C (c, d). The colours red, blue and green correspond to front, middle and back respectively. The shaded area in figures (a) and (c) represents the percentage of pump laser light absorbed.

130 °C again resulted in a halving of polarisation by the end of the experiment. Thermal behaviour was also significantly impacted with temperatures reaching almost 400 °C and a change in flow patterns can again be inferred from due to the fact that the temperature in the middle of the cell becomes hottest from the time at which P_{Xe} spikes - which is again coincident with a spike in power absorption. It is likely here that overall polarisations are lower and temperatures are higher due to the higher concentration of xenon present in the cell relative to the previous example, figure 5.17.

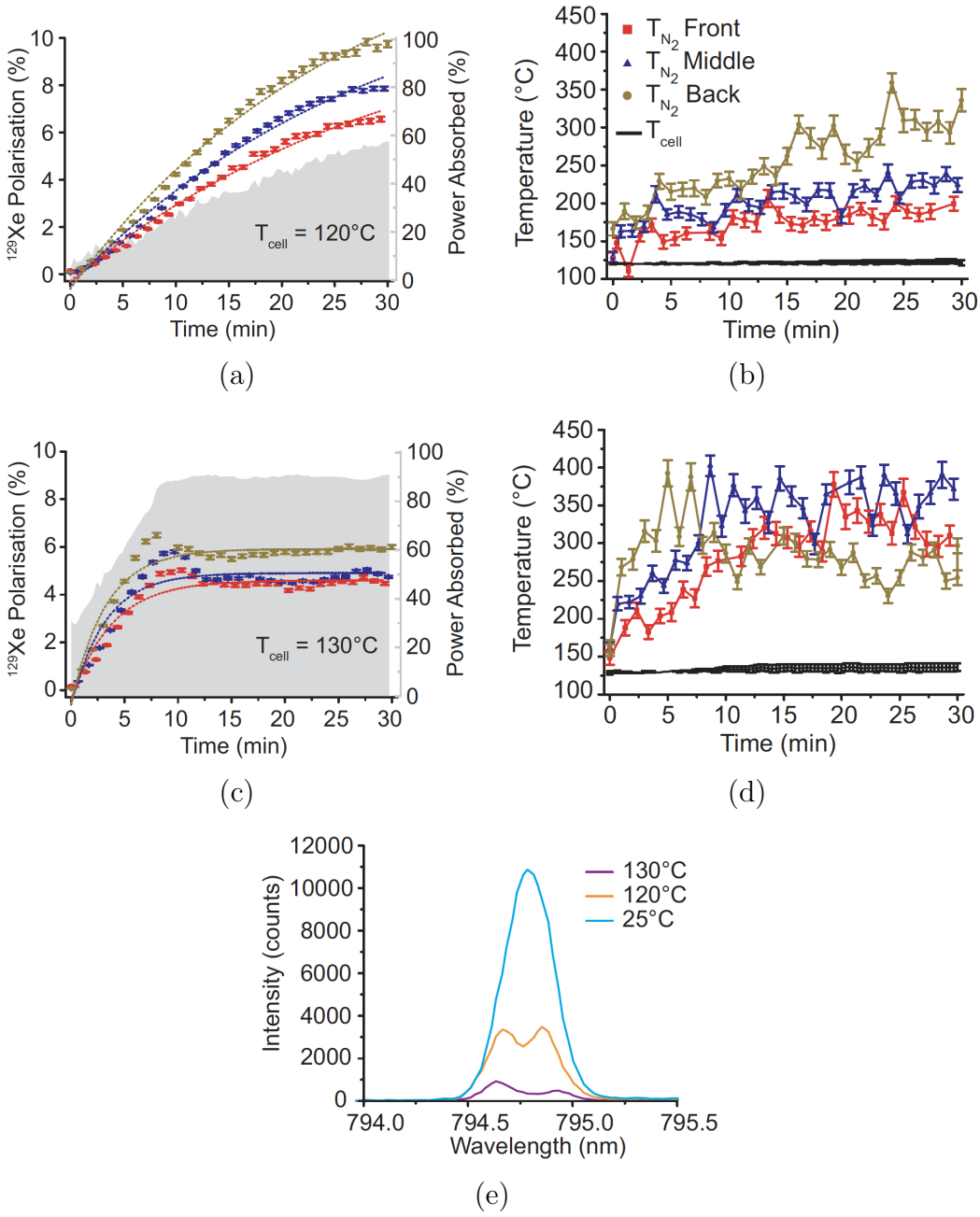

Figure 5.18: Examination of polarisation and internal gas temperatures in steady state and rubidium runaway conditions in a 1500/500 torr Xe/N_2 gas mix. (a) and (b) represent ^{129}Xe and T_{N_2} build up curves at 120 °C under steady state conditions, (c) and (d) are at 130 °C showing rubidium runaway. (e) Transmitted pump laser spectra for a cold cell (cyan), T_{cell}=120 °C (orange) and T_{cell}=130 °C (purple). The grey area in (a) and (c) signifies the percentage power absorbed within the optical pumping cell relative to a room temperature cell. Black error bars in (b) and (d) show the spread of oven temperatures (T_{cell}) recorded by a thermocouple placed in the oven inlet (back) and outlet (front). A large deviation is seen between T_{cell} and T_{N_2} in both experiments. Reprinted from [1] with permission.

Function of Pump Laser Wavelength (Spectral Offsets)

Presented here is a spectral offset experiment on a 100/1100 torr Xe/N_2 with 800 torr He gas mix. Spectral offset experiments permit the study SEOP under conditions of varying pump laser frequency. This was achieved using a QPC Blightlock pump laser that can be thermally tuned by adjusting the temperature of the water cooler and has the result of shifting the laser centroid wavelength away from the center of the rubidium D_1 transition. In this spectral offset experiment the T_{N_2} and P_{Xe} were be recorded 10 minutes after the start of the experiment in the middle of the cell (figure 5.19(a,b)). Also displayed are the corresponding spectral transmission profiles (figure 5.19(c)), recorded using the Ocean Optics HR4000 spectrometer.

On inspection of 5.19, it is evident that for this gas mix the optimal pump laser frequency is that which corresponds most closely with the D_1 transition: 794.77 nm, as the P_{Xe} (b) is at maximum at each of the three positions (front, middle and back) when this wavelength is employed. The central peak at 794.7 nm of the ocean optics spectral data in panel (c) provides an example of good SEOP illumination conditions and this corresponds to the peak in P_{Xe}. Likewise, T_{N_2} (a) at the front, middle and back peak with the laser pumping 794.77 nm.

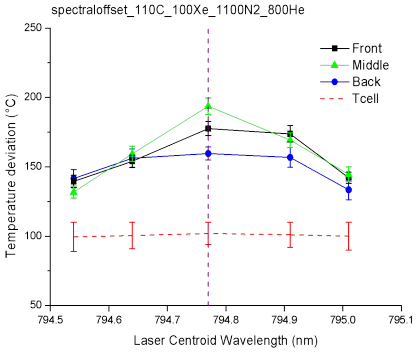

(a)

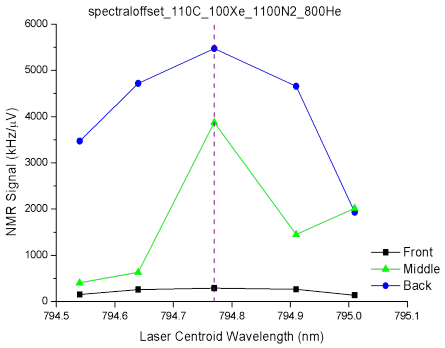

(b)

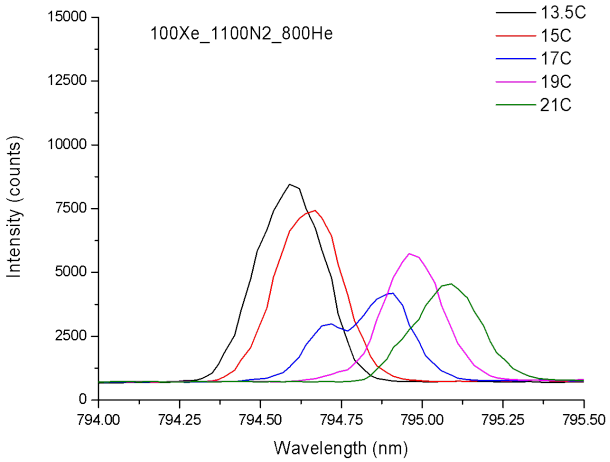

(c) (c)

Figure 5.19: Spectral offset experiment (100Xe 1100N_2 800He). (a) T_{N_2} (b) ^{129}Xe NMR signal intensity and (c) Ocean optics spectral data during a spectral offset experiment. It can be seen that for this gas mix the greatest absorption occurs at the wavelength corresponding closest with the D_1 rubidium transition.

5.4 Conclusion

Xenon-rich stopped-flow SEOP is a regime in which thermal effects can become strongly manifest due to 1) the high concentrations of xenon, which conducts heat poorly relative to commonly used buffer gases and cause increased rates of rubidium SD which further add to the thermal load, 2) because there is no flow of gas to remove excess heat in the system which is the case in continuous-flow SEOP and 3) because high-flux lasers are commonly employed for optical pumping. In this chapter, Raman spectroscopy was used to examine xenon-rich stopped-flow SEOP under steady state and turbulent 'rubidium runaway' conditions because of its ability to probe the temperature of the gas directly.

Using the in-line module mounted on a translational stage and a combination of Raman, NMR and IR spectroscopies, rubidium runuaway was shown to impact heavily on P_{Xe}, $T_{\mathrm{N_2}}$, and laser absorption as a function of z-axis position. Raman measurements under the condition of rubidium runaway revealed a disturbance in the convective flow patterns and temperature elevations as high as 600 °C.

Encouragingly, helium was shown to impair the onset of rubidium runaway, reducing the temperature in one cell by 100 °C. It is evident from the results that an interplay exists between the N_2 and He loading. Both will pressure broaden the Rb D_1 transition [137], facilitating optical pumping by improving spectral coupling to the pump laser, but only N_2 can effectively quench the rubidium optical de-excitations, generating heat in the process, while facilitating spin-exchange. Therefore it is crucial to have nitrogen, but helium has a ∼5-fold greater thermal conductivity, and this may act to control the detrimental thermal effects associated with rubidium runaway by dissipating the thermal energy to the walls of the optical cell more rapidly, permitting the use of more

powerful lasers that will serve to increase P_{Xe}.

As previously observed, it was also clear from the data presented here that the thermocouple temperature readings do not provide an accurate in-cell indication of temperature. Thermocouple readings typically remained within 10 °C of the oven temperature set-point while $T_{\mathrm{N_2}}$ was at times elevated beyond this by a further 500 °C .

Raman spectroscopy of xenon-rich stopped-flow will continue to be an useful tool for optimisation, particularly while further gains in P_{Xe} are sought by increasing the incident laser power. Simulations suggest that increased flux - through power or reduced laser linewidths - will result in greater polarisations, though this will also drive further heat into the system via quenching collisions with N_2.

Even under steady state conditions it was seen that the Raman temperatures exceed oven temperatures, by a significant margin in some cases. It could be that by combining the simulations of stopped-flow SEOP in chapter 4 with precise measurements of gas temperature provided by Raman spectroscopy described in this chapter, a more accurate model of the SEOP phenomenon can be achieved which answers long standing questions in SEOP. For instance, in the simulations, all of the temperature dependent terms were evaluated at the oven temperature. This resulted in a close match to the observed results but they deviated as more thermally insulating, spin destructive xenon was added to the mix - both factors that would increase internal gas temperatures. By using internal gas temperatures obtained from Raman temperature measurements in the simulations, specifically in the temperature dependent *gaseous* terms (such as the spin destruction and spin-exchange rates), and the oven set temperature for the Rb density (which rests directly on the surface of the cell), a closer match of the data and model may be achieved while providing strong

evidence that these terms are in fact governed by separate temperatures - i.e. the internal gas temperature and the wall surface temperature.

Chapter 6

Raman Spectroscopic Studies of Rb-Cs-Xe 'Hybrid' SEOP

Rb has long been the alkali metal of choice for SEOP of Xe, and this is for a variety of reasons. Rb is cheap and relatively easy to work with; it has a melting point higher than room temperature (39.3 °C) so in general it is solid during cell handling and can easily be melted for cell loading. It has a high vapour pressure at relatively low temperatures, i.e. at only 10's of degrees above room temperature (evident in figure 4.2). Most importantly though for its dominance in SEOP is the availability of high-powered, tunable, frequency narrowed lasers at it's D_1 transition ($\sim$794.77 nm).

However, it has been shown by Whiting *et al.* that conducting SEOP with Cs and a Cs D_1 laser (at 894.3 nm) results in higher ^{129}Xe polarisation than for SEOP with Rb and equivalent D_1 laser [139]. Unfortunately laser technology at the D_1 of Cs is significantly less developed and suitable lasers are not available at the high power outputs of Rb lasers. For this reason it is not currently possible to fully exploit the potential of Cs-Xe SEOP directly.

It may be possible, however, to indirectly harness the potential of Cs-Xe SEOP in a 'hybrid' mode using the existing Rb laser technology. That is, to use Cs as an auxiliary SEOP metal which acts as an intermediary between

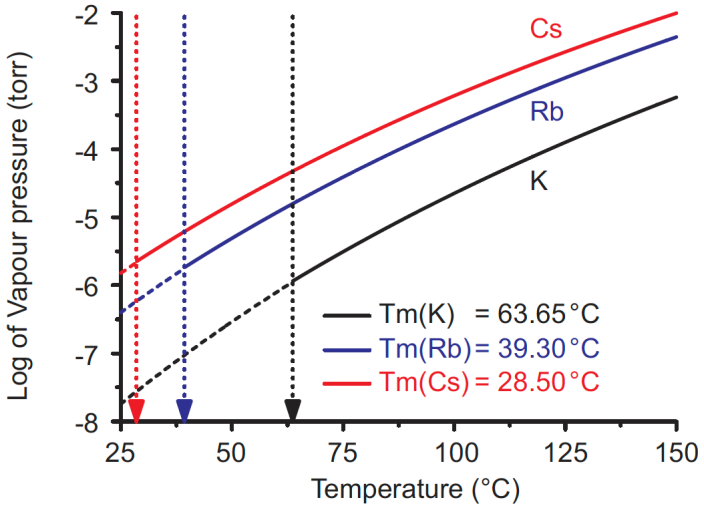

Figure 6.1: Vapour pressure curves of K, Rb, and Cs. Reprinted from [1] with permission.

Rb and Xe. Previous studies have shown that the binary Cs-Xe spin-exchange rate exceeds that of Rb-Xe (2.81 ± 0.2 x $10^{-}16$ cm^3s^{-1} vs 1.75 ± 0.12 x $10^{-}16$ cm^3s^{-1})[140, 141], and that the Rb-Cs binary exchange rate exceeds that of the Rb-Rb rate (2.3 ± 0.2 x $10^{-}14$ cm^2 vs 1.9 ± 0.2 x $10^{-}14$ cm^2) [142]. Therefore P_{Xe} may accumulate faster in the presence of both Cs and Rb than for Rb alone when an Rb laser is used to optically pump the system. Precedent for this so-called 'hybrid' method already exists, as it was first shown by Babcock *et al.* that the build up rate in a Rb-He system could be increased by a factor of 4 with the addition of potassium with no changes to the laser [143]. This followed the original patent application by Happer *et al.* in 2001 [144]. In Rb-K-^{3}He SEOP, the optimal K/Rb ratio was found to be in the range of 2-6 [143, 118]. Success of the Rb-Cs-Xe hybrid method would have major implications; all existing polarisers would be able to increase output by simply adding Cs when preparing the optical cells, ultimately yielding improvements in diagnostic MR examinations. All other existing polariser hardware - such as the expensive laser and optics - would remain the same.

In this thesis, a series of experiments are presented for the analogous Rb-Cs-Xe hybrid system to explore the potential of using Rb laser technology to harness the potential of Cs hyperpolarisation in the absence of a high-powered Cs laser. Initial experiments comprised of hybrid metal loadings in which the two constituent metals were not premixed before loading into the optical cell. In later experiments Rb and Cs were mixed into alloys of differing ratios.

Hybrid Rb-Cs-Xe was investigated as a function of gas mix, temperature (in the same way as the pure-Rb experiments of the previous chapter) and Rb-Cs ratio. The ratio of the metals is a key variable, not only in terms of the ultimate contribution the respective metals make to the SEOP physics of the system, but also because the melting point of the alloy is a function of the ratio of the metals and has practical implications for experimental handling of the cell. Most importantly, if the melting point is too low the alloy will remain liquid. This would result in a high risk that the alloy may coat the end optical windows and risk cell rupture through localised absorption of laser power. Figure 6.3(a) shows the melting point of a Rb-Cs alloy as a function of Rb fraction. It can be seen that the melting point of the alloy is lowest at a 1:1 ratio with a melting point of 9.78 °C. The melting point is highest when the alloy has a dominant fraction of either Cs or Rb (giving a melting point of 28.5 °C or 39.3 °C respectively).

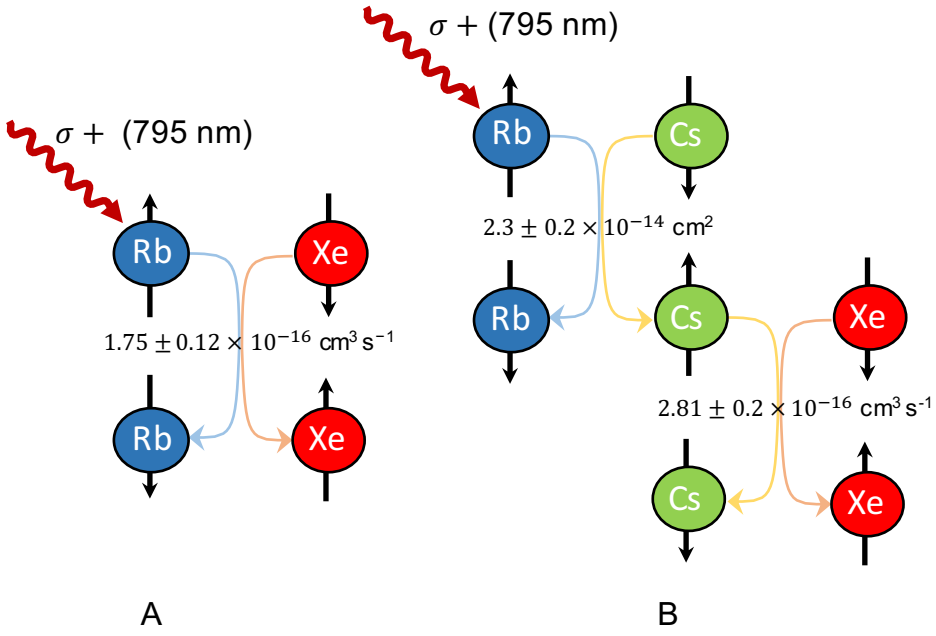

(a)

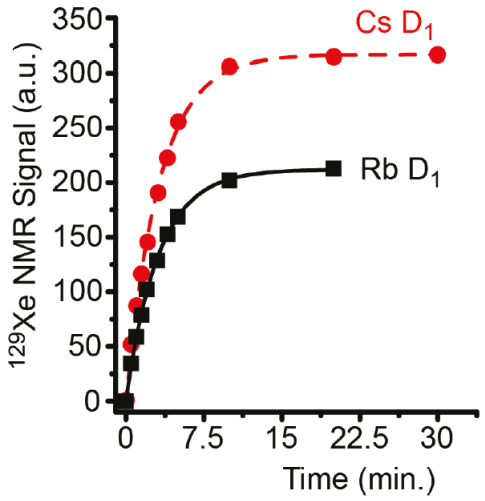

(b)

Figure 6.2: (a) Conceptual representation of Rb-Cs-Xe hybrid SEOP. (A) Rb-Xe spin-exchange (B) Rb-Xe spin-exchange via the axillary metal Cs. Cs-Xe binary spin exchange rate exceeds that Rb-Xe (2.81 $\pm$ 0.2 x 10^{-16} cm^3s^{-1} vs 1.75 $\pm$ 0.12 x 10^{-16} cm^3s^{-1})[140, 141]. The Rb-Cs binary spin-exchange rate also exceeds that of Rb-Rb (2.3 $\pm$ 0.2 x 10^{-14} cm^2 vs 1.9 $\pm$ 0.2 x 10^{-14} cm^2. The later of which is not illustrated in the graphic) [142]. (b) P_{Xe} as a function of time in SEOP using Cs vs. Rb using the respective D_1 lasers. Cs laser power ~46 W. Rb laser power ~53 W. Cell loading: 2000 torr Xe, 600 torr N_2. Reprinted from [139] with permission.

6.1 Methods

The optical cells were cleaned and prepared according to the protocol described in the methods section of chapter 3 up to the point of loading the alkali metal into the optical cell which is now described in the following section.

6.1.1 Measurement and Loading of the Alkali Metal Alloy

As described previously, loading of the alkali metals must take place in an inert environment. For the hybrid experiments this included the weighing and mixing of the alkali metals (AMs). A mass balance was used to determine the ratio of AMs. The metals and apparatus were weighed before and after loading into a glass beaker for mixing, this enabled calculation of the quantity that had been delivered to the optical cell via the pipette.

More specifically, the apparatus were weighed first: an empty mixing Schlenk tube with valve (m), a clean pipette and bulb (n), and an Rb Schlenk tube with valve (o). A fraction of the Rb was then transferred to the mixing Schlenk tube using a pre-heated pipette (heating prevents solidification of the metal in the pipette). The components were then weighed again: mixing Schlenk tube with valve containing Rb (p), used pipette bulb (q) and original Rb Schlenk tube (r). The mass of the Rb in the Schlenk tube therefore equals (p) - (m). This procedure was then repeated for Cs. To ensure no errors occurred a consistency check can be performed: (m)+(n)+(o) = (p)+(q)+(r). Using the measured masses the mass ratio of the two metals can be calculated.

Once the two metals were in the mixing Schlenk tube they were heated and mixed to form an alloy and left to cool to check that the melting point was higher than room temperature. Finally the alloy was loaded into the OP cell via pre-heated pipette. To determine the quantity of AM mix that was

loaded into the cell the mass of the Schlenk tube, valve, pipette and bulb were measured before and after loading.

Where the metals were unmixed, they were weighed individually and pipetted into opposite ends of the optical cell. In cases where an alloy was formed, the mixture was pipetted into the cell in one go.

6.1.2 SEOP Experimental Procedure

SEOP experiments were conducted in the same way as the pure-Rb SEOP experiments of the previous chapter. Optical pumping was conducted with a ∼60 W 0.26 nm FWHM Ultra100 Brightloc laser. The B_0 field was held constant at 30.2 G giving a xenon B_1 frequency of 36.3525 kHz. Measurement modalities included Raman and NMR spectroscopies as a function of position along the optical cell and global near IR spectroscopy positioned after the cell to detect transmitted light. Figure 6.3(b) shows a hybrid loaded cell mounted within the cell holders prior to an experiment. Experiments were initiated by removing the power meter in front of the optical cell and the experiments ran for a duration of 30 minutes.

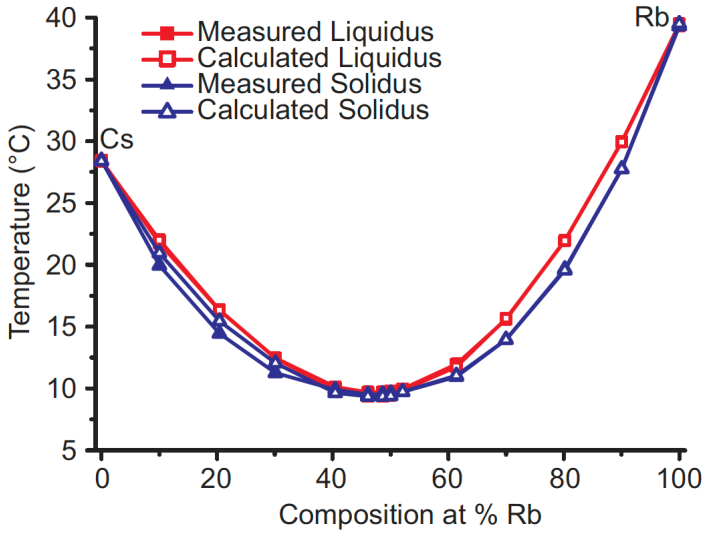

(a)

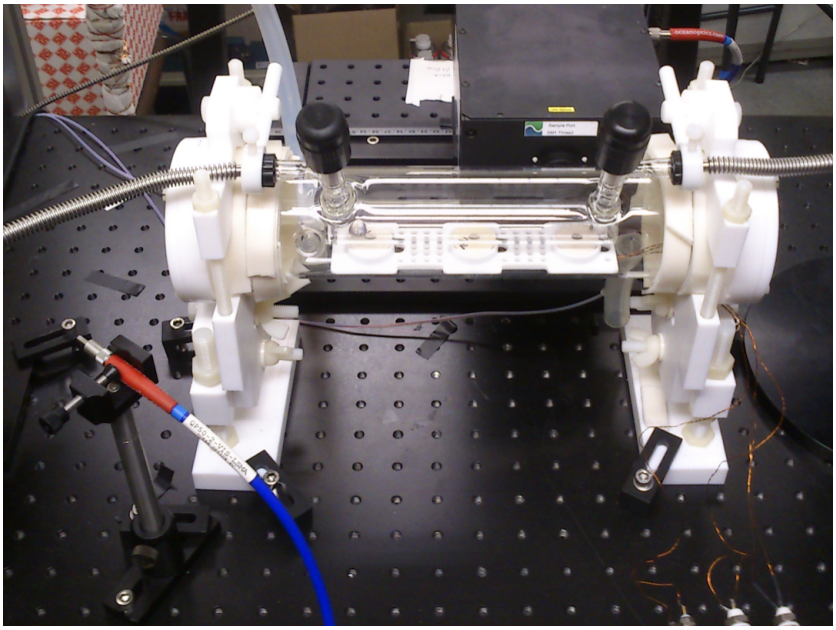

(b)

Figure 6.3: (a) Melting point of a Cs-Rb alloy as a function of % of Rb. Reprinted from [1] with permission. (b) Rb/Cs hybrid SEOP cell prior to experiment.

6.2 Results and Discussion

These experiments showed that Rb-Cs-Xe SEOP is possible and good levels of P_{Xe} were achieved in both 100 torr and 1500 torr xenon gas mixes (both backfilled to 2000 torr with N_2). In figure 6.4 it can be seen that the greatest hybrid result was slightly over 50 % in a 10Rb:1Cs ratio, with 20Rb:1Cs close behind in the 100 torr xenon mix. It can also be seen that both 10Rb:1Cs ratios performed in an almost identical manner where one was an alloy and one had the two metals separate. The lowest performing hybrid ratio was 2Rb:1Cs, with P_{Xe} peaking at 10Rb:1Cs and dropping slightly again at 20Rb:1Cs. The fastest build-up was seen in the 20Rb:1Cs ratio. The peak hybrid P_{Xe} level is almost the level achieved for pure Rb SEOP and clearly demonstrates that Rb-Xe SEOP is possible in the presence of Cs. However, the hybrid result never exceeds that of pure Rb for the conditions that were explored. This is also true for the build-up rate. It is anticipated that the higher vapour pressure of Cs results in a suppression of the Rb vapour hampering the optical pumping process and therefore P_{Xe}.

If the vapour pressure of Cs is too high relative to Rb it will dominate the atmosphere within the cell and suppress the Rb vapour at the optical pumping stage of the SEOP process. In the analogous Rb-K-He hybrid system the vapour pressure relation was reversed, this can be seen in figure 6.1. Evidence of the suppression of the Rb vapour phase in our Rb-Cs-Xe system can be seen in 6.2. P_{Xe} and $T_{\mathrm{N_2}}$ drop as Cs is introduced and the spatial gradients of P_{Xe} and $T_{\mathrm{N_2}}$ also reduce. All may be indicative of a Cs dominated vapour that suppresses the Rb vapour and optical pumping (and thus $T_{\mathrm{N_2}}$).

This suppression of the Rb vapour phase meant that the optimal T_{cell} was not observed for the Rb-Cs hybrid. For instance, from figure 6.2 it can be seen

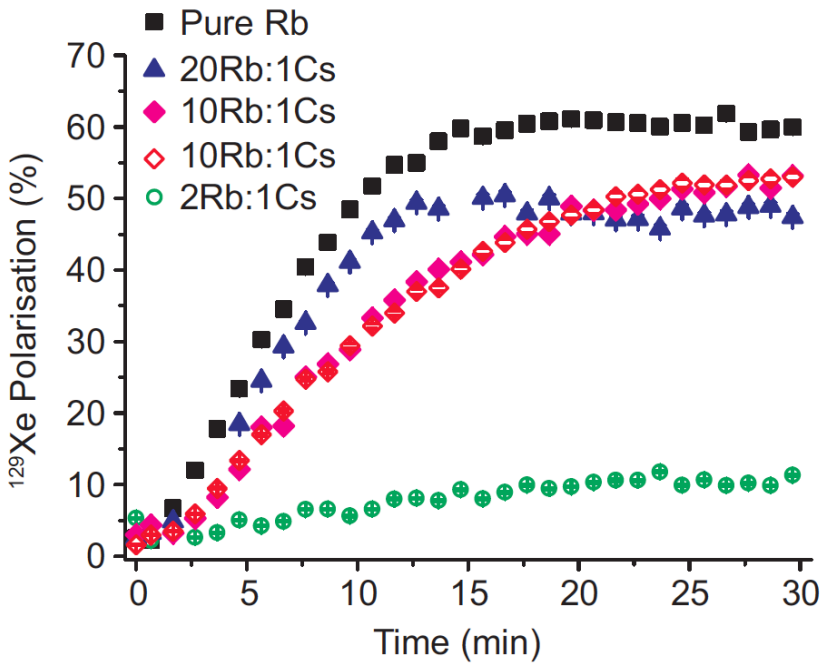

Figure 6.4: Polarisation build-up curves as a function of AM ratio in a gas mix of 100 torr ^{129}Xe and 1900 torr N_2. Measurements are taken from the middle NMR coil (centre of the cell). Open symbols indicate un-mixed AMs, solid symbols indicate AMs mixed as an alloy. P_{Xe} for the hybrid cells never exceeds that of the pure Rb cell. Greatest hybrid P_{Xe} is given by the 10Rb:1Cs ratio, the greatest build-up rate is given by the 20Rb:1Cs ratio. Reprinted from [1] with permission.

in both cases, at 100 torr Xe and 1500 torr Xe, that a fold-over in temperature did not occur, i.e. the optimal T_{cell} was not yet found for the hybrid cell. Therefore it may be the case that Rb-Cs-Xe hybrid can exceed the pure Rb-Xe case. A major factor that prevented the observation of the optimal T_{cell} was a limitation in the forced air oven which could not heat beyond 140 °C. A second factor that may become an issue at higher temperatures is the fragile nature of the Surfacil coating that reduces relaxation of the HP-xenon at the walls. Higher temperatures destroy the coating and P_{Xe} values would quickly reduce as a consequence. This means that an alternative wall coating may be required to conduct hybrid SEOP investigations at higher temperatures.

Measurement of the relative densities of the AMs within the cell would pro-

vide useful information on what is occurring within these hybrid cells, allowing more precise optimisation. One method by which to achieve this would be to monitor the optical absorption of light from a 421.5 nm light source by the $5S_{\frac{1}{2}}$-$6P_{\frac{1}{2}}$ transition [145], although other transitions may also be used [146]. Alternatively, Faraday rotation methods can be employed [147].

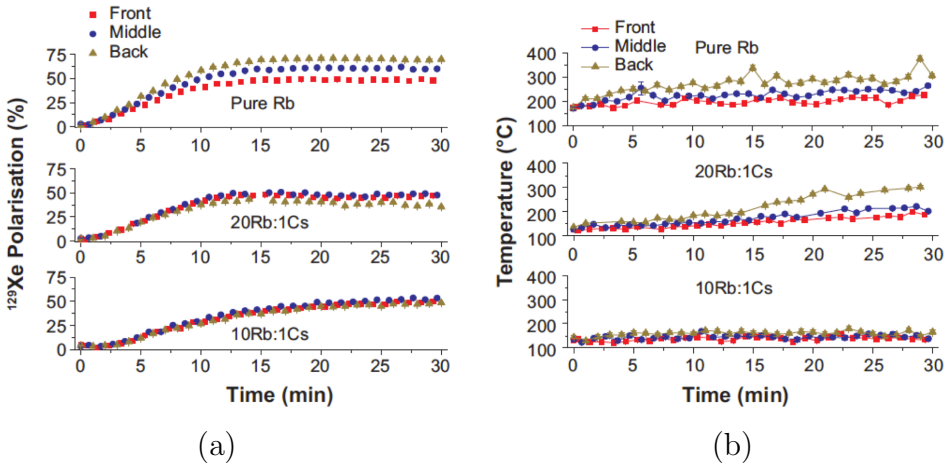

Figure 6.5: (a) P_{Xe} as a function of position (front, middle, back) for pure Rb, 20Rb:1Cs, and 10Rb:1Cs hyrbid mixes. (b) Corresponding Raman temperature. All data presented at a T_{cell} of 140 °C in a 100 torr Xe 1900 torr N_2 gas loading illuminated by ∼60 W of laser power at ∼795 nm with FWHM = 0.26 nm. P_{Xe} and T_{N_2} drop as Cs is introduced and the spatial gradients of P_{Xe} and T_{N_2} also reduce. All may be indicative of a Cs dominated vapour that suppresses the Rb vapour and optical pumping (and thus T_{N_2}). Reprinted from [1] with permission.

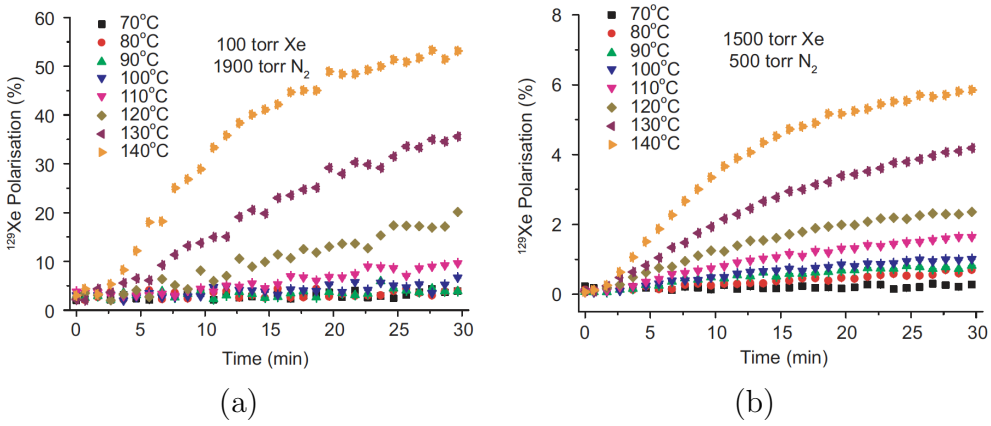

Figure 6.6: P_{Xe} as a function of T_{cell} for the 10Rb:1Cs ratio in (a) a 100 torr Xe 1900 torr N_2 mix, and (b) a 1500 torr Xe 500 torr N_2 mix. In both (a) and (b) P_{Xe} increases with T_{cell}. At 140 °C P_{Xe} is still increasing and so the optical T_{cell} is higher but could not be reached do to limitations of the instrumentation and the surfacil coating which breaks down above 140 °C. Reprinted from [1] with permission.

6.3 Conclusion

The experiments presented here indicate that SEOP is possible in a Rb-Cs-Xe hybrid system. High levels of P_{Xe} were obtained (greater than 50%) but did not exceed the levels attained in a pure Rb system. However, the optimal T_{cell} was not yet found in the hybrid system due to limitations of the equipment: temperatures over 140 °C could not be reached. T_{cell} is above 140 °C and a likely explanation for the higher T_{cell} (relative to the pure Rb experiments) is that the vapour pressure of Cs is too high relative to Rb and dominates the atmosphere within the cell, suppressing the Rb vapour at the optical pumping stage of the process. In the analogous Rb-K-He hybrid system the vapour pressure relation was reversed, this can be seen in figure 6.1. Work will continue on hybrid SEOP, both in seeking the optimal temperature and on implementing methods for the measurement of the relative densities of the AMs within the cell. When higher temperatures can be reached, regular in-cell T_1 measurements are recommended to confirm the condition of the Surfacil coating.

Chapter 7

Hyperpolarised Xenon Lung MRI: Clinical Progress at Nottingham

This chapter provides a brief summary of the clinical HP-xenon work conducted by my group to date and serves to illustrate both progress on the imaging project, and the future impact of a higher polarisation that will come with the deployment of the N-XeUS polariser. Imaging work so far has been part of a pilot study that will precede a much larger phase 2 clinical trial that will focus on the development and validation of new HP-Xe based metrics for COPD and IPF. While no formal studies have yet been conducted, much progress has been made in terms of preparing and refining aspects of the scanner set up, the sequences, and the lung imaging protocol.

The ethics of the study at Nottingham permits the imaging of 150 patients. So far, eight healthy volunteers have been scanned with patients to be imaged in due course after experimental optimisations. Each volunteer and patient can be scanned using HP xenon a maximum of four times over a maximum of four visits. With the eight volunteers, twenty one HP-xenon MR scans have been performed. A key aim of these ongoing scans is to optimise the imaging protocol and determine optimal parameters for later imaging studies.

7.1 Methods

The scanner used throughout was a 1.5 T GE HDxT Signa. The system is equipped with a broadband multi-nuclear amplifier which permits imaging at the xenon frequency (17.663299 MHz). The xenon coil used for lung imaging was an 8 channel birdcage coil (RAPID Biomedical). Proton images were acquired using the scanner's built-in body coil.

Patient monitoring was performed prior to, during and after imaging. Heart rate, blood oxygen and blood pressure were monitored and screening visits were conducted using spirometry based pulmonary function tests.

Prior to human imaging studies it was necessary to measure the specific aborption rate (SAR) of the sequences. SAR can be a factor at high-fields or where many rf pulses are used with a sequence such as echo-planar imaging (EPI). To confirm SAR was not a issue for our imaging protocol water phantoms were scanned for extended durations using a high flip angle. A magnetically compatible thermocouple was used to monitor the temperature within the water phantoms. No appreciable increase in temperature occurred during the course of the experiments and it was therefore concluded that for substantially shorter scans undergone by our volunteers - which would be using lower flip angles and hence less rf - SAR would not be a safety issue.

Flip angle calibrations were performed using HP phantoms. Assuming T_1 is long relative to the measurement, a train of constant rf pulses can be used to determine the flip angle according to the following equation:

$$S(n) = S_0 cos(\alpha)^{n-1} \tag{7.1}$$

in which S_0 is the amplitude of the first signal, S is the signal intensity for a given scan acquisition number n, and α is the flip angle. The flip angle

was determined by fitting the above equation to the resulting signal decays that occur due to the repeated rf excitations. Manual flip angle calibration was necessary because the scanner's auto-prescan function, which is used as a matter of routine in most non-HP experiments, inefficiently consumes HP magnetisation - both temporally and in terms of rf - while calibrating the flip angle.

Polarised xenon was provided by the facility's MHRA approved GE2000 polariser. A mix of 2% xenon, 10% nitrogen and ∼88% helium was used. The polariser is currently equipped with a 60 W Integra laser. 600 ml and 1000 ml doses were used throughout and delivered to the patient via Tedlar bags. Polarisation was measured using the polarisation measurement station, a low-field NMR system that has been pre-calibrated against a known signal standard by the manufacturer.

Two sequences were used during the course of the scans taken so far. Prior to a software upgrade on the scanner bb2dfast was used. After the software upgrade, bbFGRE was used: a broad-banded stock GE sequence (figure 7.1(b)). Both sequences could be used in a number of configurations to enable standard imaging and dynamic imaging. The bbFGRE sequence has the advantage that it can encode centre-out instead of sequentially, enabling a higher flip angle. Switching to this sequence resulted in a 4-fold gain in image SNR. Image reconstruction was performed using software developed by Steven Hardy.

7.2 Results and Discussion

Figure 7.1(a) shows typical HP images acquired using the centric bbFGRE sequence. Panel (A) is an infinite thickness coronal slice image. This type of image is now acquired first during every imaging session to provide a check that all aspects of the experiment are running as expected. Panel (E) shows an

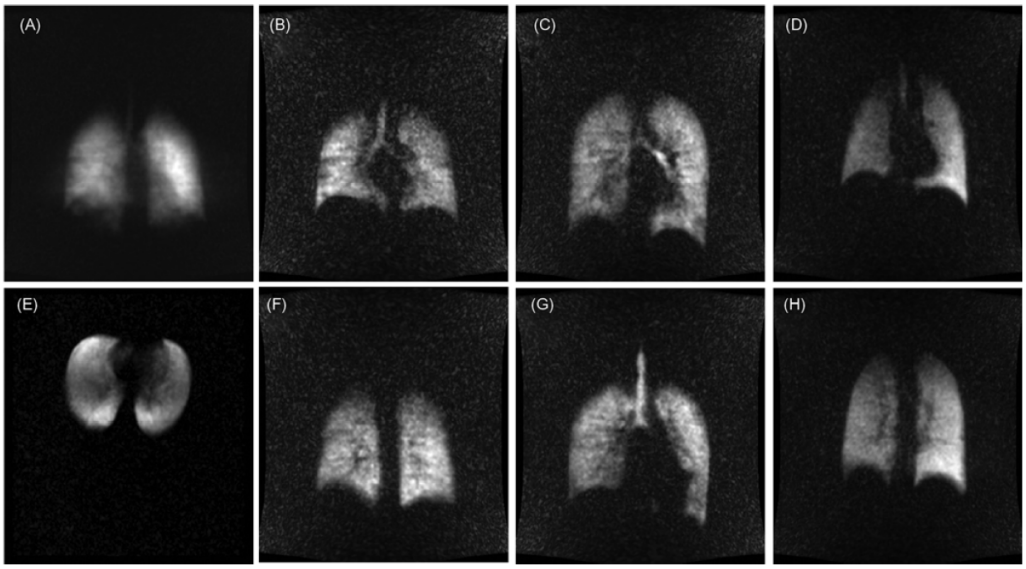

(a)

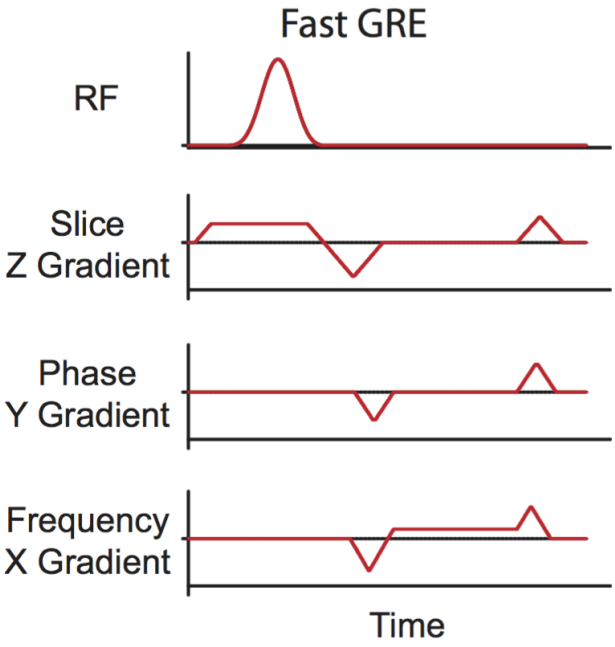

(b)

Figure 7.1: a) Examples of xenon MR images of healthy human lungs. (A) Infinite slice in a 26 YO male. (E) Infinite axial slice in a 23 YO female. (B,F), (C,G), and (D,H), pairs of coronal images from three healthy volunteers: a 26 YO male, a 22 YO male, and a 29 YO male, respectively. HP xenon was produced on a GE2000 polariser using a 2% Xe natural abundance mix. Polarisation values were ∼9%. bbFGRE sequence used throughout. $\alpha = 5.5\,^{\circ}$, FOV = 48 × 48 cm, TE = 4.2 ms, TR = 9 ms. Slice thickness = 25 mm for all panels bar (A) and (E) which are infinite thickness. Reprinted from [30] with permission. b) bbFGRE sequence timing diagram.

infinite slice axial image. Panels (B,F), (C,G), and (D,H) show pairs of coronal images - different slices from the same respective scans - in three healthy volunteers: a 26 YO male, a 22 YO male, and a 29 YO male, respectively.

Figure 7.2 shows a series of acquisitions from the second of two dynamic scans that were performed. Dynamic scans show the movement and distribution of the gas as a function of time and are recorded during the course of a HP xenon inhalation. In the first image the upper airways are exclusively visible and the airspaces within the lungs become increasingly visible as the HP gas is more deeply inhaled, with SNR and inhaled volume peaking at image number 5. From that point the signal decreases due to continued rf depletion of the HP magnetisation and the higher in vivo relaxation rate.

Functional HP xenon MRI methods rely on the capacity to detect the dissolved phase signals [9, 8], and this can be challenging due to the fact that only 2% of the inhaled gas diffuses through the septal tissue into the blood stream [8, 149]. Experiments were therefore conducted to see if this was possible with the current experimental configuration. Figure 7.3(a) shows an NMR spectrum acquired during a breath hold. Three peaks can be resolved within the plot. The large peak at 200 ppm originates from the gas phase [8]. The two smaller peaks close to 0 ppm originate from the blood plasma and the septal lung tissue [8]. The spectrum required 25 signal averages to reach this level of SNR. While it is encouraging that detection of the dissolved phase was possible with the current experimental setup, more signal will be required to improve the resolution and conduct dissolved phased imaging studies.

Figure 7.3(b) summarises the polarisation performance of the GE2000 polariser which provided HP gas throughout the experiments. It can be seen from the figure that initially 0.6 litre doses were used more commonly. Best results were obtained using 1 litre doses and this became the dominant mix

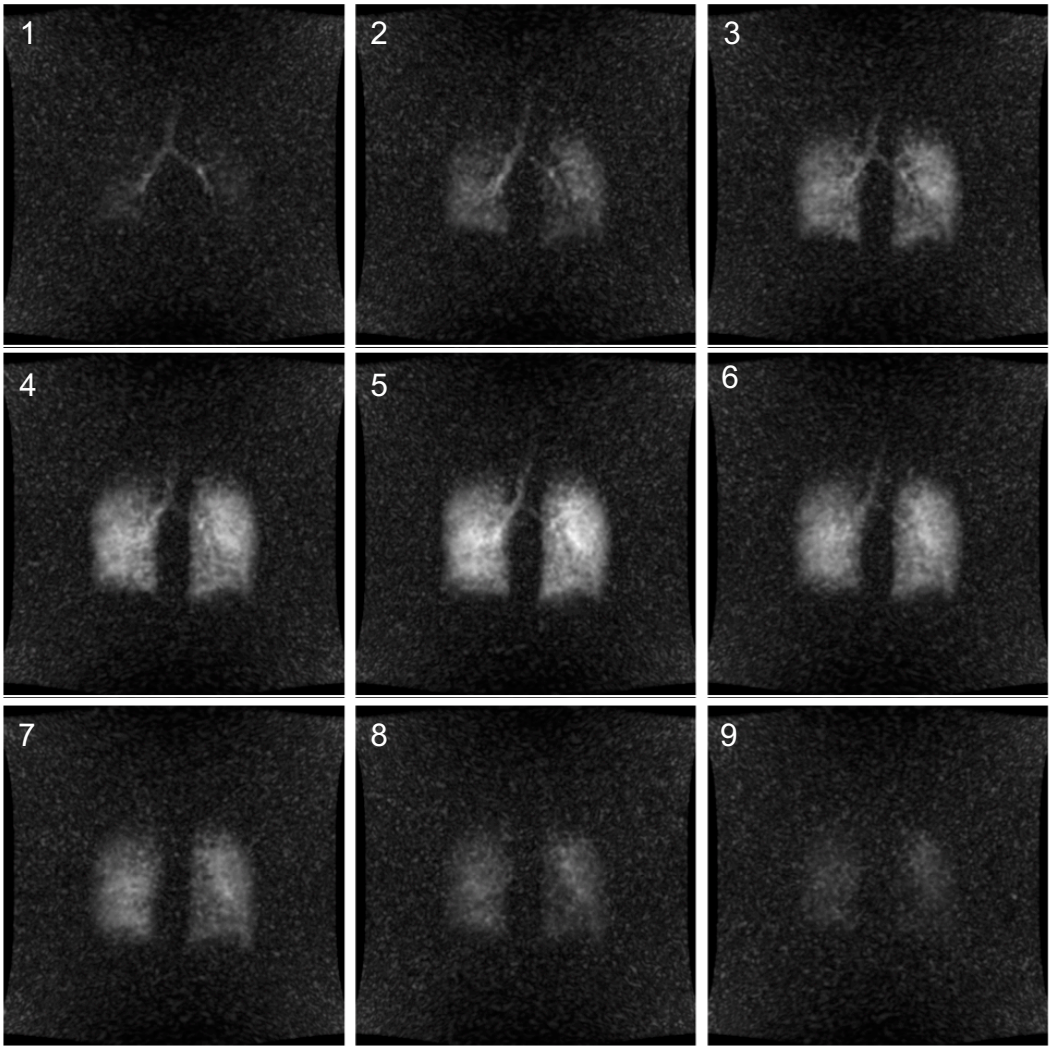

Figure 7.2: Dynamic coronal lung images acquired using the bb2dfast sequence during the inhalation of 1 litre of 8.2% polarised HP-Xe. The images were acquired 1.2 s apart for an acquisition period of 10.8 s for the 9 images. $\alpha = 5.5\,^{\circ}$, FOV = 48 $\times$ 48 cm, TE = 4.2 ms, TR = 9 ms. Reprinted from [148] with permission.

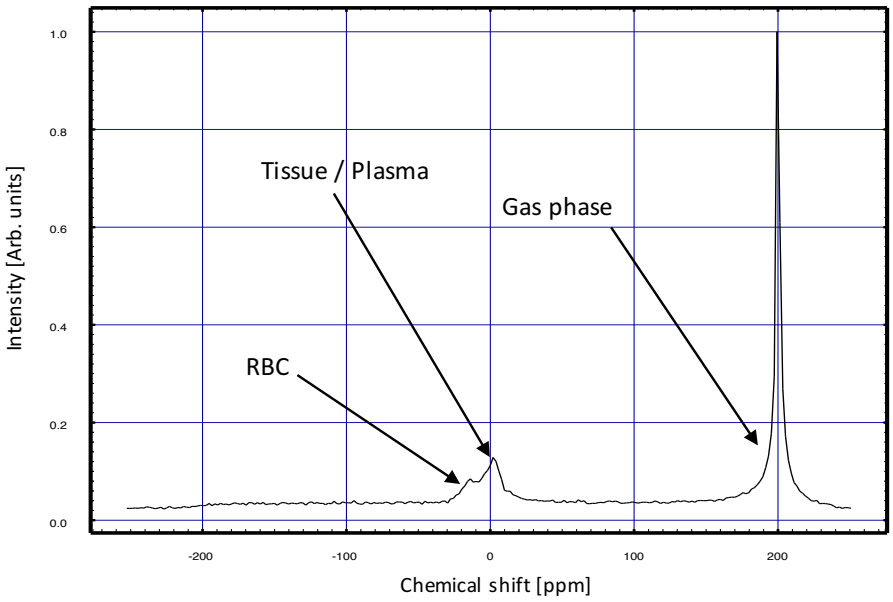

(a)

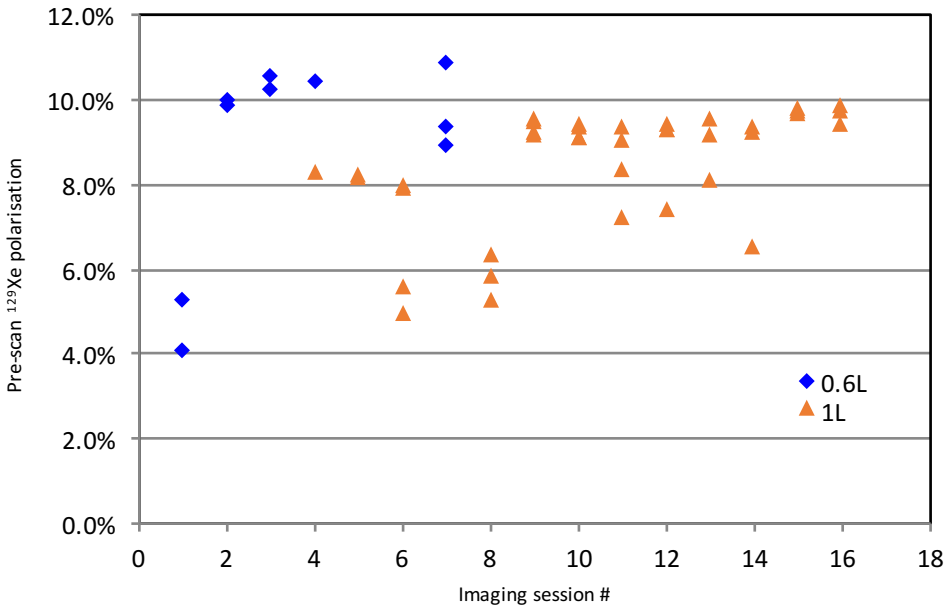

(b)

Figure 7.3: a) Dissolved phase NMR spectrum of HP-Xe. Gas phase, tissue phase and dissolved phase peaks can be resolved. Acquisition parameters were TR = 360 ms, bandwidth = 7042 Hz, N.Samples = 4096, No. of Acquisitions = 25. Reprinted from [148] with permission. b) in-bag xenon polarisations produced by the GE2000 polariser as a function of imaging session.

after the first few sessions. More importantly, it can be seen that the typical performance of the GE polariser falls in the region of 10%. In the 1 litre bags, the polarisation level has not yet exceeded 10%.

To date, in the sample of healthy volunteers imaged, there have been no xenon-induced adverse affects. The next stage of the project will be to image patients with compromised lung function. These patients will need to be monitored closely for hypoxia, for not only will the air in their lungs be displaced by xenon, xenon is also a known anaesthetic [150], and these effects will be more pronounced in those with compromised lung function.

7.3 Conclusion

A summary of the imaging work conducted to date has been presented. Coronal plane ventilation images, time-course dynamic images and a dissolved phase spectrum have been successfully acquired. Overall image SNR was initially enhanced by changing from sequential to centric phase encoding. There may be scope for further improvements in image SNR as the flip angle has not yet be fully optimised.

The greatest potential for improved image quality however, currently lies with the N-XeUS polariser. Once operational, the imaging performance will see a significant enhancement. Even in a compromised state - a laser operating at only 33% percent of its capacity (50 W of a possible 150 W), and with relatively low in-cell T_1 values - the N-XeUS polariser was able to produce HP xenon doses that were comparable to the current output of the GE2000 polariser. In due course, the laser on the N-XeUS will be replaced with a 180 W, 0.15 nm laser (a factor of 2 narrower than the Ultra 500 employed by XeUS and N-XeUS with 30 W more output), and if the cell preparation procedures can be brought in line with those of our collaborators (bringing in-

cell T_1 values up from 0.6 hrs to over 3 hrs [22]) polarisations will likely exceed those documented in the current XeUS literature - which stands at almost 80 % in 1000 torr cells [21]. This is already an apparent polarisation of 40% and a factor of 4 in SNR over the GE polariser. As discussed in the simulations chapter, this performance could be further enhanced with modifications the cell geometry and the gas mix.

Chapter 8

Conclusions

The N-XeUS polariser

In chapter 3 the construction and demonstration of a clinical scale hyperpolariser was described. Although performance of the polariser was compromised due to a faulty laser, the achieved polarisation levels (16.65±0.27% for the 50:50 mix and 11.64±0.23% for the 80% mix, corresponding to apparent polarisations of 8.33±0.14% and 9.312±0.18% respectively) were still comparable to that of the existing continuous-flow system installed at the MIU (the performance of which has not exceeded 10% polarisation in 1 litre bags during the course of the study (see 7.3(b))). In the coming months, the laser of the N-XeUS polariser will be replaced with an improved model that has a 2-fold narrower linewidth with a further 30 W of output power. The gain in SNR of the MR images when the N-XeUS polariser is ultimately operational in the clinic should therefore improve firstly by approximately the factor the current laser fell short (a factor of more than 2), plus a substantial additional factor, due to both the narrower linewidth and increased power of the new laser. As demonstrated in the simulations chapter, xenon-rich SEOP gains differentially at narrower linewidths. For instance, the simulation in figure 4.19 shows that P_{Xe} of a 2000 torr Xe mix increases from 46.9% to 57.1% when the linewidth of the pump laser is halved from 0.3 nm to 0.15 nm at 170 W - a gain of

over 10% polarisation - and that is without a boost in additional power (note how close this example is to the current and incoming lasers). Once the new laser is installed and optical cell preparation is brought in line with that of our collaborators (who have obtained longer than 3 hr T_1's [22]) the polarisation performance of the N-XeUS polariser stands a very strong chance of setting new records, particularly if further modifications laid out in the simulations chapter are implemented.

The N-XeUS polariser is now installed at the Medical Imaging Unit (MIU) at the Queens Medical Centre and, pending MHRA approval and installation of the new laser, will provide HP-xenon in the ongoing Xe lung imaging study. The N-XeUS polariser introduced new clinically-oriented features to the XeUS line of polarisers, including modifications to the gas manifold enabling a nitrogen fill/purge capability, and permitting the removal of the costly turbo-molecular vacuum pump system.

Additionally, a low-cost low-field prototype NMR spectrometer was developed and demonstrated, which will further reduce the capital cost of such a polariser and further facilitate automation of the system. The prototype reached a high level of maturity, achieving an SNR of 125 at a cost of ∼$300. This is 66 times cheaper than the commercial alternative currently in use on N-XeUS (costing ∼$20000) while only being outperformed by a factor of 5. Encouragingly, there is still room to affordably improve the design by 1) including a mixer to reduce the bandwidth (and increase acquisition periods), and 2) further increasing the amplification of the FID.

At such a low cost and with such potential for customisation and integration (in terms of both hardware and software), the prototype NMR spectrometer is well placed to be incorporated into the N-XeUS polariser and has the potential to be an attractive prospect to any hyperpolarisation lab engaged in the

development of HP methods or instrumentation.

Simulations of xenon-rich stopped-flow SEOP

In chapter 4, the xenon-rich stopped-flow SEOP regime was been simulated for the first time using the standard model of SEOP. The model was validatated against two datasets (in two different cell geometries); the first dataset where the xenon-rich stopped-flow regime was first shown [23], and a second much larger dataset that was calibrated for absolute polarisation values and covered a much larger region of parameter space [20]. In the first case, the simulation qualitatively matched the un-calibrated data very well. In terms of the exact temperatures for the expected peak values of the simulated magnetisations, the simulations, at their worst, deviated by no more than 12 °C of the experimental values. In the second case, close quantitative agreement was made though a steeper gradient appeared in the experimental results - that is, polarisation fell slightly faster with increasing xenon density - and this is most likely due to thermal effects that could not be accounted for in the simulation (thermal effects that are evident in the XeUS γ_{SEOP} data in figures 4.9 (d),(f),(h)(j) and (l)). Regardless of this discrepancy, the model was considered to provide a good approximation of the regime and exploratory simulations of the surrounding parameter space were performed.

Based on these exploratory simulations, it is expected that output of the polariser can be increased by 1) using a wider cell of the same length; 2) by introducing helium into the mixture; 3) by increasing the total pressure; and 4) by further decreasing the laser linewidth. Each of these modifications have varying degrees of cost or engineering difficulty associated with them and the best outcome would be a combination of all 4 modifications.

Additionally, retro-reflection was incorporated into the model and was

shown to be differentially beneficial at higher xenon densities.

Scrutiny of the laser absorption revealed for the first time that in the stopped-flow regime, optimal polarisation per xenon fraction occurs at the same level of absorption. If a system can be developed where complete thermal control can be maintained this phenomenon will enable rapid optimisation of polarisers.

Raman spectroscopic studies of Rb-Xe SEOP

As established, xenon-rich stopped-flow SEOP is a regime in which thermal effects can become strongly manifest due to 1) the high concentrations of xenon, which conducts heat poorly relative to commonly used buffer gases and causes high rates of Rb spin destruction which further drive higher temperatures, 2) because there is no flow of gas to remove excess heat in the system which is the case in continuous-flow SEOP and 3) because high-flux lasers are commonly employed for optical pumping. In chapter 5, Raman spectroscopy was used to examine xenon-rich stopped-flow SEOP under steady state and turbulent 'rubidium runaway' conditions because of its ability to probe the temperature of the gas directly.

Using the in-line module mounted on a translational stage and a combination of Raman, NMR and IR spectroscopies, rubidium runaway was shown to impact heavily on P_{Xe}, $T_{\mathrm{N_2}}$, and laser absorption as a function of z-axis position. Raman measurements under the condition of rubidium runaway revealed a disturbance in the convective flow patterns and temperature elevations as high as 600 °C.

Encouragingly, He was shown to impair the onset of rubidium runaway, reducing the temperature in one cell by 100 °C. It is evident from the results that an interplay exists between the N_2 and He loading fraction. Both gases

will pressure broaden the Rb D_1 transition [137], facilitating optical pumping by improving spectral coupling to the pump laser, but only N_2 can effectively quench the Rb optical de-excitations, generating heat in the process, while facilitating spin-exchange. Therefore it is crucial to have N_2, but He has a greater thermal conductivity, and this may act to control the detrimental thermal effects associated with rubidium runaway by dissipating the thermal energy to the walls of the optical cell more rapidly, permitting the use of more powerful lasers that will serve to increase P_{Xe}.

Raman spectroscopy of xenon-rich stopped-flow will continue to be an useful tool for optimisation, particularly while further gains in P_{Xe} are sought by increasing the incident laser power. Simulations suggest that increased flux - through power or reduced laser linewidths - will result in greater polarisations, though this will also drive further heat into the system via quenching collisions with N_2.

Even under steady state conditions it was seen that the Raman temperatures exceed oven temperatures, by a significant margin in some cases. It could be that by combining the simulations of stopped-flow SEOP in chapter 4 with precise measurements of gas temperature provided by Raman spectroscopy described in chapter 5, a more accurate model of the SEOP phenomenon can be achieved which answers long standing questions in SEOP. For instance, in the simulations, all of the temperature dependent terms were evaluated at the oven temperature. This resulted in a close match to the observed results but they deviated as more thermally insulating, spin destructive xenon was added to the mix - both factors that would increase internal gas temperatures. By using internal gas temperatures obtained from Raman temperature measurements in the simulations, specifically in the temperature dependent *gaseous* terms (such as the spin destruction and spin-exchange rates), and the oven set

temperature for the Rb density (which rests directly on the surface of the cell), a closer match of the data and model may be achieved while providing strong evidence that these terms are in fact governed by separate temperatures - i.e. the internal gas temperature and the wall surface temperature.

Raman spectroscopic studies of Rb-Cs-Xe 'hybrid' SEOP

In chapter 6, it was shown that SEOP is possible in a Rb-Cs-Xe hybrid system. High levels of P_{Xe} were obtained (greater than 50%) but did not exceed the levels attained in a pure Rb system. However, the optimal temperature, T_{opt}, was not yet found in the hybrid system due to limitations of the equipment: temperatures over 140 °C could not be reached. T_{opt} is above 140 °C and a likely explanation for the higher T_{opt} (relative to the pure Rb experiments) is that the vapour pressure of Cs is too high relative to Rb and dominates the atmosphere within the cell, suppressing the Rb vapour at the optical pumping stage of the process. In the analogous Rb-K-He hybrid system the vapour pressure relation was reversed. Work will continue on hybrid SEOP, both in seeking the optimal temperature and on implementing methods for the measurement of the relative densities of the AMs within the cell. When higher temperatures can be reached, regular in-cell T_1 measurements are recommended to confirm the condition of the Surfacil coating.

HP-xenon lung MRI at Nottingham

Chapter 7 presented a summary of the imaging work conducted to date. Coronal plane ventilation images, time-course dynamic images and a dissolved phase spectrum have been successfully acquired. Overall image SNR was initially enhanced by changing from sequential to centric phase encoding. There may be scope for further improvements in image SNR as the flip angle has not yet be

fully optimised.

The greatest potential for improved image quality currently lies with the N-XeUS polariser. Once operational, the imaging performance will see a significant enhancement. As discuss above, even in a compromised state - a laser operating at only 33% percent of its capacity (50 W of a possible 150 W), and with relatively low in-cell T_1 values - the N-XeUS polariser was able to produce HP xenon doses that were comparable to the current output of the GE2000 polariser. In due course, the laser on the N-XeUS will be replaced with a 180 W, 0.15 nm laser (a factor of 2 narrower than the Ultra 500 employed by XeUS and N-XeUS with 30 W more output), and if the cell preparation procedures can be brought in line with those of our collaborators (bringing in-cell T_1 values up from 0.6 hrs to over 3 hrs [22]) polarisations will likely exceed those documented in the current XeUS literature - which stands at almost 80 % in 1000 torr cells [21]. This is already an apparent polarisation of 40% and a factor of 4 in SNR over the GE polariser. As discussed in the simulations chapter, this performance could be further enhanced with modifications to the cell geometry and the gas mix.

Bibliography

[1] H. L. Newton, *Hyperpolarised xenon production via Rb and Cs optical pumping applied to functional lung MRI.* PhD thesis, University of Nottingham, 2014.

[2] M. Albert, G. Cates, B. Driehuys, W. Happer, B. Saam, C.S. Springer Jr, and A. Wishnia, "Biological magnetic resonance using laser-polarized ^{129}Xe," *Nature*, vol. 370, p. 199, 1994.

[3] E. Smith, *Modern Raman Spectscopy: A Practical Approach.* John Wiley & Sons, Inc, 2005.

[4] National Institute for Health and Clinical Excellence *Chronic obstructive pulmonary disease: Costing report*, p. NICE clinical guideline 101, February 2011.

[5] American Thoracic Society *Standards for the Diagnosis and Management of Patients with COPD*, 2004.

[6] National Institute for Health and Clinical Excellence *Idiopathic pulmonary fibrosis: The diagnosis and management of suspect Idiopathic Pulmonary Fibrosis*, p. NICE clinical guideline 163, 2013.

[7] P. Lebedev and V. Pryanichnikov, "Present and future production of xenon and krypton in the former ussr region and some physical properties of these gases," *Nuclear Instruments and Methods in Physics Research Section A: Accelerators, Spectrometers, Detectors and Associated Equipment*, vol. 327, no. 1, pp. 222–226, 1993.

[8] J. Wolber, A. Cherubini, A. S. K. Dzik-Jurasz, M. O. Leach, and A. Bifone, "Spin-lattice relaxation of laser-polarized xenon in human blood," *Proc Natl Acad Sci U S A.*, vol. 96 (7), p. 36643669, 1999.

[9] I. Muradyan, J. P. Butler, M. Dabaghyan, M. Hrovat, I. Dregely, I. Ruset, G. P. Topulos, E. Frederick, H. Hatabu, W. F. Hersman, and S. Patz, "Single-breath xenon polarization transfer contrast (SB-XTC): Implementation and initial results in healthy humans," *Journal of Magnetic Resonance Imaging*, vol. 37, no. 2, pp. 457–470, 2013.

[10] B. M. Goodson, "Nuclear magnetic resonance of laser-polarized noble gases in molecules, materials, and organisms," *Journal of Magnetic Resonance*, vol. 155, p. 157, 2002.

[11] B. Driehuys, G. D. Cates, and W. Happer, "Surface relaxation mechanisms of laser-polarized ^{129}Xe," *Phys. Rev. Lett.*, vol. 74, pp. 4943–4946, Jun 1995.

[12] B. Driehuys, G. D. Cates, E. Miron, K. Sauer, D. K. Walter, and W. Happer, "High-volume production of laser-polarized ^{129}Xe," *Applied Physics Letters*, vol. 96, no. 12, pp. 1668 –1670, 1996.

[13] I. C. Ruset, S. Ketel, and F. Hersman, "Optical pumping system design for large production of hyperpolarized ^{129}Xe," *Physical Review Letters*, vol. 96, p. 053002, 2006.

[14] G. Schrank, Z. Ma, A. Schoeck, and B. Saam, "Characterization of a low-pressure high-capacity Xe-129 flow-through polarizer," *Physical Review A*, vol. 80, p. 063424, DEC 2009.

[15] G. Norquay, S. R. Parnell, X. Xu, J. Parra-Robles, and J. M. Wild, "Optimized production of hyperpolarized ^{129}Xe at 2 bars for in vivo lung magnetic resonance imaging," *Journal of Applied Physics*, vol. 113, no. 4, p. 044908, 2013.

[16] M. Freeman, K. Emami, and B. Driehuys, "Characterizing and modeling the efficiency limits in large-scale production of hyperpolarized ^{129}Xe," *Physical Review A*, vol. 90, no. 2, p. 023406, 2014.

[17] M. S. Freeman, *The Efficiency Limits of Spin Exchange Optical Pumping Methods of* ^{129}Xe *Hyperpolarization: Implications for in vivo MRI Applications*. PhD thesis, Duke University, 2015.

[18] P. Nikolaou, A. M. Coffey, L. L. Walkup, B. M. Gust, N. Whiting, H. Newton, S. Barcus, I. Muradyan, M. Dabaghyan, G. D. Moroz, M. S. Rosen, S. Patz, M. J. Barlow, E. Y. Chekmenev, and B. M. Goodson, "Near-unity nuclear polarization with an open-source ^{129}Xe hyperpolarizer for NMR and MRI," *Proceedings of the National Academy of Sciences*, 2013.

[19] P. Nikolaou, A. M. Coffey, L. L. Walkup, B. M. Gust, N. Whiting, H. Newton, I. Muradyan, M. Dabaghyan, K. Ranta, G. D. Moroz, *et al.*, "Xena: An automated open-source ^{129}Xe hyperpolarizer for clinical use," *Magnetic Resonance Imaging*, vol. 32, no. 5, pp. 541–550, 2014.

[20] P. Nikolaou, A. M. Coffey, K. Ranta, L. L. Walkup, B. M. Gust, M. J. Barlow, M. S. Rosen, B. M. Goodson, and E. Y. Chekmenev, "Multi-dimensional mapping of spin-exchange optical pumping in clinical-scale

batch-mode ^{129}Xe hyperpolarizers," *The Journal of Physical Chemistry B*, vol. 118, no. 18, pp. 4809–4816, 2014.

[21] P. Nikolaou, A. M. Coffey, L. L. Walkup, B. M. Gust, C. D. LaPierre, E. Koehnemann, M. J. Barlow, M. S. Rosen, B. M. Goodson, and E. Y. Chekmenev, "A 3D-printed high power nuclear spin polarizer," *Journal of the American Chemical Society*, vol. 136, no. 4, pp. 1636–1642, 2014.

[22] P. Nikolaou, A. M. Coffey, M. J. Barlow, M. S. Rosen, B. M. Goodson, and E. Y. Chekmenev, "Temperature-ramped ^{129}Xe spin-exchange optical pumping," *Analytical Chemistry*, vol. 86, no. 16, pp. 8206–8212, 2014.

[23] N. Whiting, P. Nikolaou, N. A. Eschmann, B. M. Goodson, and M. J. Barlow, "Interdependence of in-cell xenon density and temperature during Rb/Xe-129 spin-exchange optical pumping using VHG-narrowed laser diode arrays," *Journal of Magnetic Resonance*, vol. 208, pp. 298–304, FEB 2011.

[24] P. Nikolaou, N. Whiting, N. A. Eschmann, K. E. Chaffee, B. M. Goodson, and M. J. Barlow, "Generation of laser-polarized xenon using fiber-coupled laser-diode arrays narrowed with integrated volume holographic gratings," *Journal of Magnetic Resonance*, vol. 197, no. 2, pp. 249–254, 2009.

[25] N. Whiting, P. Nikolaou, N. Eschmann, M. Barlow, R. Lammert, J. Ungar, W. Hu, L. Vaissie, and B. Goodson, "Using frequency-narrowed, tunable laser diode arrays with integrated volume holographic gratings for spin-exchange optical pumping at high resonant fluxes and xenon densities," *Applied Physics B*, vol. 106, no. 4, pp. 775–788, 2012.

[26] M. L. Hirsch, B. A. Smith, M. Mattingly, A. G. Goloshevsky, M. Rosay, and J. G. Kempf, "Transport and imaging of brute-force ^{13}C hyperpolarization," *Journal of Magnetic Resonance*, vol. 261, pp. 87–94, 2015.

[27] S. J. Nelson, J. Kurhanewicz, D. B. Vigneron, P. E. Larson, A. L. Harzstark, M. Ferrone, M. van Criekinge, J. W. Chang, R. Bok, I. Park, *et al.*, "Metabolic imaging of patients with prostate cancer using hyperpolarized [1-^{13}C] pyruvate," *Science Translational Medicine*, vol. 5, no. 198, pp. 198ra108–198ra108, 2013.

[28] S. E. Day, M. I. Kettunen, F. A. Gallagher, D.-E. Hu, M. Lerche, J. Wolber, K. Golman, J. H. Ardenkjaer-Larsen, and K. M. Brindle, "Detecting tumor response to treatment using hyperpolarized ^{13}C magnetic resonance imaging and spectroscopy," *Nature Medicine*, vol. 13, no. 11, pp. 1382–1387, 2007.

[29] B. M. Goodson, N. Whiting, A. M. Coffey, P. Nikolaou, F. Shi, B. M. Gust, M. E. Gemeinhardt, R. V. Shchepin, J. G. Skinner, J. R. Birchall, *et al.*, "Hyperpolarization methods for MRS," in *Handbook of in vivo Magnetic Resonance Spectroscopy* (P. Bottomley and G. J.R., eds.), pp. 557–574, John Wiley & Sons, 2016.

[30] B. Goodson, K. Ranta, J. Skinner, A. Coffee, P. Nikolaou, M. Gemeinhardt, D. Anthony, S. Stephenson, S. Hardy, O. B. J, M. Barlow, and E. Chekmenev, "The physics of hyperpolarized gas MRI," in *Hyperpolarized and Inert Gas MRI* (F. Hane and M. Albert, eds.), pp. 23–46, Elsevier, 2017.

[31] P. Nikolaou, B. M. Goodson, and E. Y. Chekmenev, "NMR hyperpolarization techniques for biomedicine," *Chemistry–A European Journal*, vol. 21, no. 8, pp. 3156–3166, 2015.

[32] J. H. Ardenkjær-Larsen, B. Fridlund, A. Gram, G. Hansson, L. Hansson, M. H. Lerche, R. Servin, M. Thaning, and K. Golman, "Increase in signal-to-noise ratio of [greater than] 10,000 times in liquid-state nmr," *Proceedings of the National Academy of Sciences*, vol. 100, no. 18, pp. 10158–10163, 2003.

[33] C. R. Bowers and D. P. Weitekamp, "Parahydrogen and synthesis allow dramatically enhanced nuclear alignment," *Journal of the American Chemical Society*, vol. 109, no. 18, pp. 5541–5542, 1987.

[34] R. W. Adams, J. A. Aguilar, K. D. Atkinson, M. J. Cowley, P. I. Elliott, S. B. Duckett, G. G. Green, I. G. Khazal, J. López-Serrano, and D. C. Williamson, "Reversible interactions with para-hydrogen enhance nmr sensitivity by polarization transfer," *Science*, vol. 323, no. 5922, pp. 1708–1711, 2009.

[35] P. Rovedo, S. Knecht, T. Bäumlisberger, A. L. Cremer, S. B. Duckett, R. E. Mewis, G. G. Green, M. J. Burns, P. J. Rayner, D. Leibfritz, *et al.*, "Molecular MRI in the earth's magnetic field using continuous hyperpolarization of a biomolecule in water," *The Journal of Physical Chemistry B*, 2016.

[36] L. S. Lloyd, A. Asghar, M. J. Burns, A. Charlton, S. Coombes, M. J. Cowley, G. J. Dear, S. B. Duckett, G. R. Genov, G. G. Green, *et al.*, "Hyperpolarisation through reversible interactions with para hydrogen," *Catalysis Science & Technology*, vol. 4, no. 10, pp. 3544–3554, 2014.

[37] H. Zeng, J. Xu, J. Gillen, M. T. McMahon, D. Artemov, J.-M. Tyburn, J. A. Lohman, R. E. Mewis, K. D. Atkinson, G. G. Green, *et al.*, "Optimization of SABRE for polarization of the tuberculosis drugs pyrazi-

namide and isoniazid," *Journal of Magnetic Resonance*, vol. 237, pp. 73–78, 2013.

[38] L. Schearer, "Optical pumping of neon p 2 3 metastable atoms," *Physical Review*, vol. 180, no. 1, p. 83, 1969.

[39] L. Young, D. Yang, and R. Dunford, "Optical production of metastable krypton," *Journal of Physics B: Atomic, Molecular and Optical Physics*, vol. 35, no. 13, p. 2985, 2002.

[40] T. Hadeishi and C.-H. Liu, "Nuclear alignment of the s 0 1 ground state of xe 131 by electron pumping and metastability-exchange collisions," *Physical Review Letters*, vol. 19, no. 5, p. 211, 1967.

[41] J. Becker, W. Heil, B. Krug, M. Leduc, M. Meyerhoff, P. Nacher, E. Otten, T. Prokscha, L. Schearer, and R. Surkau, "Study of mechanical compression of spin-polarized ^{3}He gas," *Nuclear Instruments and Methods in Physics Research Section A: Accelerators, Spectrometers, Detectors and Associated Equipment*, vol. 346, no. 1-2, pp. 45–51, 1994.

[42] A. Kastler, "Optical methods of atomic orientation and of magnetic resonance," *J. Opt. Soc. Am.*, vol. 47, pp. 460–465, Jun 1957.

[43] M. Bouchiat, T. Carver, and C. Varnum, "Nuclear polarization in He-3 gas induced by optical pumping and dipolar exchange," *Physical Review Letters*, vol. 5, no. 8, pp. 373–375, 1960.

[44] B. Grover, "Nobel gas NMR detection through noble-gas-rubidum hyperfine contact interactions," *Physical Review Letters*, vol. 40, no. 6, pp. 391–392, 1978.

[45] T. G. Walker and W. Happer, "Spin-exchange optical pumping of noble-gas nuclei," *Reviews of Modern Physics*, vol. 69, no. 2, p. 629, 1997.

[46] B. Goodson, N. Whiting, H. Newton, J. Skinner, K. Ranta, P. Nikolaou, M. Barlow, and E. Chekmenev, "Spin-exchange optical pumping at high xenon densities and laser fluxes: Principles and practice," in *Hyperpolarized Xenon-129 Magnetic Resonance* (T. Meersmann and E. Brunner, eds.), pp. 96–121, Royal Society of Chemisty, 2015.

[47] E. Brunner, "Enhancement of surface and biological magnetic resonance using laser-polarized noble gases," *Concepts in Magnetic Resonance*, vol. 11, no. 5, pp. 313 – 335, 1999.

[48] I. Saha, P. Nikolaou, N. Whiting, and G. B.M, "Characterization of violet emission from Rb optical pumping cells used in laser-polarized xenon NMR experiments," *Chemical Physics Letters*, vol. 428, pp. 268 – 276, 2006.

[49] N. Whiting, P. Nikolaou, N. A. Eschmann, M. J. Barlow, R. Lammert, J. Ungar, W. Hu, L. Vaissie, and B. M. Goodson, "Using frequency-narrowed, tunable laser diode arrays with integrated volume holographic gratings for spin-exchange optical pumping at high resonant fluxes and xenon densities," *Applied Physics B: Lasers and Optics*, vol. 106, pp. 775–788, Mar. 2012.

[50] A. Thompson, A. Bernstein, T. Chupp, D. DeAngelis, G. Dodge, G. Dodson, K. Dow, M. Farkhondeh, W. Fong, J. Kim, *et al.*, "Quasielastic scattering of polarized electrons from polarized 3-He and measurement of the neutron's form factors," *Physical Review Letters*, vol. 68, no. 19, p. 2901, 1992.

[51] J. T. Singh, P. A. Dolph, W. A. Tobias, T. D. Averett, A. Kelleher, K. Mooney, V. V. Nelyubin, Y. Wang, Y. Zheng, and G. D. Cates, "Development of high-performance alkali-hybrid polarized 3-He targets for electron scattering," *Physical Review C*, vol. 91, no. 5, p. 055205, 2015.

[52] E. Lelievre-Berna, "Mid-term report of the NMI3 neutron spin filter project," *Physica B: Condensed Matter*, vol. 397, no. 1, pp. 162–167, 2007.

[53] T. R. Gentile and W. Chen, "Polarized 3-He spin filters for neutron science," in *Proceedings of the XVth International Workshop on Polarized Sources, Targets, and Polarimetry (PSTP2013). 9-13 September, 2013. Charlottesville, Virginia, USA. Online at http://pos. sissa. it/cgi-bin/reader/conf. cgi? confid= 182, id. 22*, vol. 1, p. 22, 2013.

[54] S. Karpuk, F. Allmendinger, M. Burghoff, C. Gemmel, M. Güldner, W. Heil, W. Kilian, S. Knappe-Grüneberg, C. Mrozik, W. Müller, *et al.*, "Spin polarized 3-He: from basic research to medical applications," *Physics of Particles and Nuclei*, vol. 44, no. 6, pp. 904–908, 2013.

[55] T. Chupp, R. Hoare, R. Walsworth, and B. Wu, "Spin-exchange-pumped 3-He and 129-Xe zeeman masers," *Physical Review Letters*, vol. 72, no. 15, p. 2363, 1994.

[56] N. R. Newbury, A. Barton, P. Bogorad, G. Cates, M. Gatzke, B. Saam, L. Han, R. Holmes, P. Souder, J. Xu, *et al.*, "Laser polarized muonic helium," *Physical Review Letters*, vol. 69, no. 2, p. 391, 1992.

[57] M. Ebert, T. Grossmann, W. Heil, E. Otten, R. Surkau, M. Thelen, M. Leduc, P. Bachert, M. Knopp, and L. Schad, "Nuclear magnetic resonance imaging with hyperpolarised helium-3," *The Lancet*, vol. 347, no. 9011, pp. 1297–1299, 1996.

[58] J. C. Leawoods, D. A. Yablonskiy, B. Saam, D. S. Gierada, and M. S. Conradi, "Hyperpolarized 3-He gas production and MR imaging of the lung," *Concepts in Magnetic Resonance*, vol. 13, no. 5, pp. 277–293, 2001.

[59] H. Moller, X. Chen, B. Saam, K. Hagspiel, G. Johnson, T. Altes, E. de Lange, and H. Kauczor, "MRI of the lungs using hyperpolarized noble gases," *Magnetic Resonance in Medicine*, vol. 47, pp. 1029–1051, JUN 2002.

[60] J. M. Wild, H. Marshall, X. Xu, G. Norquay, S. R. Parnell, M. Clemence, P. D. Griffiths, and J. Parra-Robles, "Simultaneous Imaging of Lung Structure and Function with Triple-Nuclear Hybrid MR Imaging," *Radiology*, vol. 267, pp. 251–255, APR 2013.

[61] B. T. Saam, D. A. Yablonskiy, V. D. Kodibagkar, J. C. Leawoods, D. S. Gierada, J. D. Cooper, S. S. Lefrak, and M. S. Conradi, "MR imaging of diffusion of ^{3}He gas in healthy and diseased lungs," *Magnetic Resonance in Medicine*, vol. 44, no. 2, pp. 174–179, 2000.

[62] M. Salerno, E. E. de Lange, T. A. Altes, J. D. Truwit, J. R. Brookeman, and J. P. Mugler, "Emphysema: hyperpolarized helium-3 diffusion MR imaging of the lungs compared with spirometric indexesinitial experience 1," *Radiology*, vol. 222, no. 1, pp. 252–260, 2002.

[63] J. Woods, "Congressional hearing: caught by surprise: Causes and consequences of the helium-3 supply crisis," *Testimony before the House Committee on Science and Technology, Subcommittee on Investigations and Oversight*, 2010.

[64] V. V. Terskikh, I. L. Moudrakovski, S. R. Breeze, S. Lang, C. I. Ratcliffe, J. A. Ripmeester, and A. Sayari, "A general correlation for the ^{129}Xe NMR chemical shift-pore size relationship in porous silica-based materials," *Langmuir*, vol. 18, no. 15, pp. 5653–5656, 2002.

[65] D. Raftery, H. Long, T. Meersmann, P. Grandinetti, L. Reven, and A. Pines, "High-field NMR of adsorbed xenon polarized by laser pumping," *Physical Review Letters*, vol. 66, no. 5, p. 584, 1991.

[66] A. Cherubini and A. Bifone, "Hyperpolarised xenon in biology," *Progress in Nuclear Magnetic Resonance Spectroscopy*, vol. 42, no. 1, pp. 1–30, 2003.

[67] D. M. Lilburn, G. E. Pavlovskaya, and T. Meersmann, "Perspectives of hyperpolarized noble gas MRI beyond ^{3}He," *Journal of Magnetic Resonance*, vol. 229, pp. 173–186, 2013.

[68] O. Taratula and I. J. Dmochowski, "Functionalized ^{129}Xe contrast agents for magnetic resonance imaging," *Current opinion in chemical biology*, vol. 14, no. 1, pp. 97–104, 2010.

[69] P. Berthault, G. Huber, and H. Desvaux, "Biosensing using laser-polarized xenon NMR/MRI," *Progress in Nuclear Magnetic Resonance Spectroscopy*, vol. 55, pp. 35 – 60, 2009.

[70] L. Schroeder, "Xenon for NMR biosensing: Inert but alert," *Physica Medica*, vol. 29, no. 1, pp. 3 – 16, 2013.

[71] G. Duhamel, P. Choquet, E. Grillon, L. Lamalle, J.-L. Leviel, A. Ziegler, and A. Constantinesco, "Xenon-129 MR imaging and spectroscopy of rat brain using arterial delivery of hyperpolarized xenon in a lipid emulsion," *Magnetic Resonance in Medicine*, vol. 46, no. 2, pp. 208–212, 2001.

[72] M. L. Mazzanti, R. P. Walvick, X. Zhou, Y. Sun, N. Shah, J. Mansour, J. Gereige, and M. S. Albert, "Distribution of hyperpolarized xenon in the brain following sensory stimulation: preliminary MRI findings," *PLoS One*, vol. 6, no. 7, p. e21607, 2011.

[73] G. Norquay, G. Leung, N. J. Stewart, G. M. Tozer, J. Wolber, and J. M. Wild, "Relaxation and exchange dynamics of hyperpolarized ^{129}Xe in human blood," *Magnetic Resonance in Medicine*, vol. 74, no. 2, pp. 303–311, 2015.

[74] R. K. Ghosh, *Spin exchange optical pumping of neon and its applications*. 2009.

[75] R. Stoner, "Testing local lorentz invariance with zeeman masers," *in" CPT and Lorentz Symmetry", edited by VA Kostelecky (World Scientific, Singapore, 1999), p. 201.*, vol. 1, p. 201, 1999.

[76] Z. Wu, W. Happer, M. Kitano, and J. Daniels, "Experimental studies of wall interactions of adsorbed spin-polarized Xe-131 nuclei," *Physical Review A*, vol. 42, no. 5, p. 2774, 1990.

[77] I. L. Moudrakovski, C. I. Ratcliffe, and J. A. Ripmeester, "^{131}Xe, a new NMR probe of void space in solids," *Journal of the American Chemical Society*, vol. 123, no. 9, pp. 2066–2067, 2001.

[78] T. Meersmann, S. A. Smith, and G. Bodenhausen, "Multiple-quantum filtered xenon-131 NMR as a surface probe," *Physical Review Letters*, vol. 80, no. 7, p. 1398, 1998.

[79] Y. Millot, P. P. Man, M.-A. Springuel-Huet, and J. Fraissard, "Quantification of electric-field gradient in the supercage of Y zeolites with ^{131}Xe

(I= 3/2) NMR," *Comptes Rendus de l'Académie des Sciences-Series IIC-Chemistry*, vol. 4, no. 11, pp. 815–818, 2001.

[80] C. F. Horton-Garcia, G. E. Pavlovskaya, and T. Meersmann, "Introducing krypton NMR spectroscopy as a probe of void space in solids," *Journal of the American Chemical Society*, vol. 127, no. 6, pp. 1958–1962, 2005.

[81] G. E. Pavlovskaya, Z. I. Cleveland, K. F. Stupic, R. J. Basaraba, and T. Meersmann, "Hyperpolarized krypton-83 as a contrast agent for magnetic resonance imaging," *Proceedings of the National academy of Sciences of the United States of America*, vol. 102, no. 51, pp. 18275–18279, 2005.

[82] J. S. Six, T. Hughes-Riley, D. M. Lilburn, A. C. Dorkes, K. F. Stupic, D. E. Shaw, P. G. Morris, I. P. Hall, G. E. Pavlovskaya, and T. Meersmann, "Pulmonary MRI contrast using surface quadrupolar relaxation (square) of hyperpolarized ^{83}Kr," *Magnetic Resonance Imaging*, vol. 32, no. 1, pp. 48–53, 2014.

[83] B. Saam, "T_1 relaxation of ^{129}Xe and how to keep it long," in *Hyperpolarized Xenon-129 Magnetic Resonance*, pp. 122–141, 2015.

[84] B. Anger, G. Schrank, A. Schoeck, K. Butler, M. Solum, R. Pugmire, and B. Saam, "Gas-phase spin relaxation of Xe-129," *Physical Review A*, vol. 78, no. 4, p. 043406, 2008.

[85] X. Zeng, E. Miron, W. V. Wijngaarden, D. Schreiber, and W. Happer, "Wall relaxation of spin polarized ^{129}Xe nuclei," *Physics Letters A*, vol. 96, no. 4, pp. 191 – 194, 1983.

[86] U. Ruth, T. Hof, J. Schmidt, D. Fick, and H. Jänsch, "Production of nitrogen-free, hyperpolarized ^{129}Xe gas," *Applied Physics B*, vol. 68, no. 1, pp. 93–97, 1999.

[87] H. Middleton, R. D. Black, B. Saam, G. D. Cates, G. P. Cofer, R. Guenther, W. Happer, L. W. Hedlund, G. Alan Johnson, K. Juvan, *et al.*, "MR imaging with hyperpolarized ^{3}He gas," *Magnetic Resonance in Medicine*, vol. 33, no. 2, pp. 271–275, 1995.

[88] J. R. MacFall, H. C. Charles, R. D. Black, H. Middleton, J. C. Swartz, B. Saam, B. Driehuys, C. Erickson, W. Happer, G. D. Cates, *et al.*, "Human lung air spaces: potential for MR imaging with hyperpolarized ^{3}He.," *Radiology*, vol. 200, no. 2, pp. 553–558, 1996.

[89] P. Bachert, L. R. Schad, M. Bock, M. V. Knopp, M. Ebert, T. Grobmann, W. Heil, D. Hofmann, R. Surkau, and E. W. Otten, "Nuclear magnetic

resonance imaging of airways in humans with use of hyperpolarized ^{3}He," *Magnetic Resonance in Medicine*, vol. 36, no. 2, pp. 192–196, 1996.

[90] J. P. Mugler, B. Driehuys, J. R. Brookeman, G. D. Cates, S. S. Berr, R. G. Bryant, T. M. Daniel, E. E. De Lange, J. H. Downs, C. J. Erickson, W. Happer, D. P. Hinton, N. F. Kassel, T. Maier, C. D. Phillips, B. T. Saam, K. L. Sauer, and M. E. Wagshul, "MR imaging and spectroscopy using hyperpolarized ^{129}Xe gas: Preliminary human results," *Magnetic Resonance in Medicine*, vol. 37, no. 6, pp. 809–815, 1997.

[91] H.-U. Kauczor, D. Hofmann, K.-F. Kreitner, H. Nilgens, R. Surkau, W. Heil, A. Potthast, M. V. Knopp, E. W. Otten, and M. Thelen, "Normal and abnormal pulmonary ventilation: visualization at hyperpolarized He-3 MR imaging.," *Radiology*, vol. 201, no. 2, pp. 564–568, 1996.

[92] H. Kauczor, M. Ebert, K. Kreitner, T. Grossmann, H. Nilgens, D. Hofmann, R. Surkau, T. Roberts, W. Heil, E. Otten, *et al.*, "Helium-3 MRT of pulmonary ventilation: the initial clinical applications," *RoFo: Fortschritte auf dem Gebiete der Rontgenstrahlen und der Nuklearmedizin*, vol. 166, no. 3, pp. 192–198, 1997.

[93] M. Kirby, S. Svenningsen, N. Kanhere, A. Owrangi, A. Wheatley, H. O. Coxson, G. E. Santyr, N. A. Paterson, D. G. McCormack, and G. Parraga, "Pulmonary ventilation visualized using hyperpolarized helium-3 and xenon-129 magnetic resonance imaging: differences in COPD and relationship to emphysema," *Journal of Applied Physiology*, vol. 114, no. 6, pp. 707–715, 2013.

[94] J. C. Woods, C. K. Choong, D. A. Yablonskiy, J. Bentley, J. Wong, J. A. Pierce, J. D. Cooper, P. T. Macklem, M. S. Conradi, and J. C. Hogg, "Hyperpolarized ^{3}He diffusion MRI and histology in pulmonary emphysema," *Magnetic Resonance in Medicine*, vol. 56, no. 6, pp. 1293–1300, 2006.

[95] A. Ouriadov, A. Farag, M. Kirby, D. G. McCormack, G. Parraga, and G. E. Santyr, "Lung morphometry using hyperpolarized ^{129}Xe apparent diffusion coefficient anisotropy in chronic obstructive pulmonary disease," *Magnetic Resonance in Medicine*, vol. 70, no. 6, pp. 1699–1706, 2013.

[96] J. Butler, R. Mair, D. Hoffmann, M. Hrovat, R. Rogers, G. Topulos, R. Walsworth, and S. Patz, "Measuring surface-area-to-volume ratios in soft porous materials using laser-polarized xenon interphase exchange nuclear magnetic resonance," *Journal of Physics: Condensed Matter*, vol. 14, no. 13, p. L297, 2002.

[97] K. Ruppert, J. R. Brookeman, K. D. Hagspiel, and J. P. Mugler, "Probing lung physiology with xenon polarization transfer contrast (XTC)," *Magnetic Resonance in Medicine*, vol. 44, no. 3, pp. 349–357, 2000.

[98] K. Ruppert, J. F. Mata, J. R. Brookeman, K. D. Hagspiel, and J. P. Mugler, "Exploring lung function with hyperpolarized ^{129}Xe nuclear magnetic resonance," *Magnetic Resonance in Medicine*, vol. 51, no. 4, pp. 676–687, 2004.

[99] S. Mansson, J. Wolber, B. Driehuys, P. Wollmer, and K. Golman, "Characterization of diffusing capacity and perfusion of the rat lung in a lipopolysaccaride disease model using hyperpolarized ^{129}Xe," *Magnetic Resonance in Medicine*, vol. 50, no. 6, pp. 1170–1179, 2003.

[100] B. Driehuys, G. P. Cofer, J. Pollaro, J. B. Mackel, L. W. Hedlund, and G. A. Johnson, "Imaging alveolar–capillary gas transfer using hyperpolarized ^{129}Xe MRI," *Proceedings of the National Academy of Sciences*, vol. 103, no. 48, pp. 18278–18283, 2006.

[101] I. Muradyan, J. P. Butler, M. Dabaghyan, M. Hrovat, I. Dregely, I. Ruset, G. P. Topulos, E. Frederick, H. Hatabu, W. F. Hersman, *et al.*, "Single-breath xenon polarization transfer contrast (SB-XTC): Implementation and initial results in healthy humans," *Journal of Magnetic Resonance Imaging*, vol. 37, no. 2, pp. 457–470, 2013.

[102] B. Driehuys, H. E. Möller, Z. I. Cleveland, J. Pollaro, and L. W. Hedlund, "Pulmonary perfusion and xenon gas exchange in rats: MR imaging with intravenous injection of hyperpolarized ^{129}Xe," *Radiology*, vol. 252, no. 2, p. 386, 2009.

[103] Z. I. Cleveland, H. E. Möller, L. W. Hedlund, J. C. Nouls, M. S. Freeman, Y. Qi, and B. Driehuys, "In vivo MR imaging of pulmonary perfusion and gas exchange in rats via continuous extracorporeal infusion of hyperpolarized ^{129}Xe," *PLoS ONE*, vol. 7, p. e31306, 02 2012.

[104] J. P. Mugler, T. A. Altes, I. C. Ruset, I. M. Dregely, J. F. Mata, G. W. Miller, S. Ketel, J. Ketel, F. W. Hersman, and K. Ruppert, "Simultaneous magnetic resonance imaging of ventilation distribution and gas uptake in the human lung using hyperpolarized xenon-129," *Proceedings of the National Academy of Sciences*, vol. 107, no. 50, pp. 21707–21712, 2010.

[105] S. Patz, I. Muradyan, M. I. Hrovat, M. Dabaghyan, G. R. Washko, H. Hatabu, and J. P. Butler, "Diffusion of hyperpolarized ^{129}Xe in the lung: a simplified model of ^{129}Xe septal uptake and experimental results," *New Journal of Physics*, vol. 13, no. 1, p. 015009, 2011.

[106] Y. V. Chang, "MOXE: A model of gas exchange for hyperpolarized ^{129}Xe magnetic resonance of the lung," *Magnetic Resonance in Medicine*, vol. 69, no. 3, pp. 884–890, 2013.

[107] Y. V. Chang, J. D. Quirk, I. C. Ruset, J. J. Atkinson, F. W. Hersman, and J. C. Woods, "Quantification of human lung structure and physiology using hyperpolarized ^{129}Xe," *Magnetic Resonance in Medicine*, vol. 71, no. 1, pp. 339–344, 2014.

[108] Polarean, "The 9820 continuous-flow polariser," *http://www.polarean.com/*, 2016.

[109] K. Ranta, L. Walkup, N. Whiting, P. Nikolaou, M. Barlow, and B. Goodson, "Interplay of temperature, Xe density, and laser linewidth during Rb-Xe spin-exchange optical pumping: Simulation vs. experiment," in *52nd Experimental Nuclear Magnetic Resonance Conference 2011, Boston, USA*, 2011.

[110] M. Gatzke, G. Cates, B. Driehuys, D. Fox, W. Happer, and B. Saam, "Extraordinarily slow nuclear spin relaxation in frozen laser-polarized Xe-129," *Physical Review Letters*, vol. 70, no. 5, p. 690, 1993.

[111] N. Kuzma, B. Patton, K. Raman, and W. Happer, "Fast nuclear spin relaxation in hyperpolarized solid ^{129}Xe," *Physical Review Letters*, vol. 88, no. 14, p. 147602, 2002.

[112] S. Parnell, M. Deppe, J. Parra-Robles, and J. Wild, "Enhancement of ^{129}Xe polarization by off-resonant spin exchange optical pumping," *Journal of Applied Physics*, vol. 108, no. 6, pp. Art–no, 2010.

[113] Digilent, *Analog Discovery Pin-Out*. Digilent, 1300 Henley Court, Pullman, WA, 99163, Oct. 2012.

[114] M. S. Conradi, "FET Q switch for pulsed NMR," *Review of Scientific Instruments*, vol. 48, no. 3, pp. 359–361, 1977.

[115] M. E. Wagshul and T. Chupp, "Laser optical pumping of high-density Rb in polarized ^{3}He targets," *Physical Review A*, vol. 49, no. 5, p. 3854, 1994.

[116] A. B.-A. Baranga, S. Appelt, M. Romalis, C. Erickson, A. Young, G. Cates, and W. Happer, "Polarization of ^{3}He by spin exchange with optically pumped Rb and K vapors," *Physical Review Letters*, vol. 80, no. 13, p. 2801, 1998.

[117] R. S. Virgincar, Z. I. Cleveland, S. Sivaram Kaushik, M. S. Freeman, J. Nouls, G. P. Cofer, S. Martinez-Jimenez, M. He, M. Kraft, J. Wolber, *et al.*, "Quantitative analysis of hyperpolarized ^{129}Xe ventilation imaging

in healthy volunteers and subjects with chronic obstructive pulmonary disease," *NMR in Biomedicine*, vol. 26, no. 4, pp. 424–435, 2013.

[118] W. Chen, T. Gentile, T. Walker, and E. Babcock, "Spin-exchange optical pumping of He-3 with Rb-K mixtures and pure K," *Physical Review A*, vol. 75, no. 1, p. 013416, 2007.

[119] I. Nelson and T. Walker, "Rb-Xe spin relaxation in dilute Xe mixtures," *Physical Review A*, vol. 65, no. 1, p. 012712, 2001.

[120] I. C. Ruset, *Hyperpolarized 129Xe Production and Applications*. PhD thesis, University of New Hampshire, 1999.

[121] G. Cates, R. Fitzgerald, A. Barton, P. Bogorad, M. Gatzke, N. Newbury, and B. Saam, "Rb-^{129}Xe spin-exchange rates due to binary and three-body collisions at high Xe pressures," *Physical Review A*, vol. 45, no. 7, p. 4631, 1992.

[122] C. V. Rice and D. Raftery, "Rubidium - xenon spin exchange and relaxation rates measured at high pressure and high magnetic field," *Journal of Chemical Physics*, vol. 117 (12), p. 5632, 2002.

[123] Y.-Y. Jau, N. N. Kuzma, and W. Happer, "Magnetic decoupling of 129-Xe-Rb and 129-Xe-Cs binary spin exchange," *Physical Review A*, vol. 67, no. 2, p. 022720, 2003.

[124] S. Atutov, A. Plekhanov, A. Shalagin, R. Calabrese, L. Tomassetti, and V. Guidi, "Explosive evaporation of Rb or K fractal clusters by low power CW radiation in the presence of excited atoms," *The European Physical Journal D*, vol. 66, no. 5, pp. 1–6, 2012.

[125] D. K. Walter, W. Griffith, and W. Happer, "Energy transport in high-density spin-exchange optical pumping cells," *Physical Review Letters*, vol. 86 (15), pp. 3264 – 3267, 2001.

[126] H. Newton, L. L. Walkup, N. Whiting, L. West, J. Carriere, F. Havermeyer, L. Ho, P. Morris, B. M. Goodson, and M. J. Barlow, "Comparative study of in situ N_2 rotational Raman spectroscopy methods for probing energy thermalisation processes during spin-exchange optical pumping," *Applied Physics B: Lasers and Optics*, Aug. 2013.

[127] N. Whiting, H. Newton, P. Morris, M. J. Barlow, and B. M. Goodson, "Observation of energy thermalization and $\sim$ 1000 K gas temperatures during spin-exchange optical pumping at high xenon densities," *manuscript in preparation*, 2014.

[128] A. Smekal, "Zur quantentheorie der dispersion," *Naturwissenschaften*, vol. 11, no. 43, pp. 873–875, 1923.

[129] K. Raman, "A new class of spectra due to secondary radiation," *Indian Journal of Physics*, vol. 2, pp. 399–419, 1928.

[130] A. Compaan, A. Wagoner, and A. Aydinli, "Rotational raman scattering in the instructional laboratory," *American Journal of Physics*, vol. 62 (7), pp. 639 – 645, 1994.

[131] R. S. Hickman and L. H. Liang, "Rotational temperature measurement in nitrogen using raman spectroscopy," *Review of Scientific Instruments*, vol. 43, pp. 796 – 799, 1972.

[132] R. S. Mulliken, "Intensities of electronic transitions in molecular spectra i. introduction," *Journal of Chemical Physics*, vol. 7, pp. 14 – 20, 1939.

[133] G. Herzberg, *Molecular Spectra and Molecular Structure Vol II, Infrared and Raman Spectra of Polyatomic Molecules*. D. Van Nostrand Company, Inc, 13th ed., 1968.

[134] J. M. Hollas, *Modern Spectroscopy*. John Wiley, 3rd ed., 1998.

[135] D. Simonelli and M. J. Shultz, "Temperature dependence for the relative raman cross section of the ammonia/water complex," *Journal of Molecular Spectroscopy*, vol. 205, pp. 221 – 226, 2001.

[136] *Tables of Physical & Chemical Constants*. 3.8.1 Nuclear moments and magnetic resonance: Kaye & Laby Online. Version 1.0 (2005) www.kayelaby.npl.co.uk, 16th ed., 1995.

[137] M. V. Romalis, E. Miron, and G. D. Cates, "Pressure broadening of Rb D_1 and D_2 lines by ^{3}He, ^{4}He, N_2, and Xe. line cores and near wings," *PRA*, vol. 56, pp. 4569–4578, Dec. 1997.

[138] J. Birchall, N. Whiting, J. Skinner, M. Barlow, and B. Goodson, "Using raman spectroscopy to improve hyperpolarized noble gas production for clinical lung imaging techniques," in *Hyperpolarized and Inert Gas MRI*, pp. 23–46, 2017.

[139] N. Whiting, N. A. Eschmann, B. M. Goodson, and M. J. Barlow, "^{129}Xe-Cs (D_1,D_2) versus ^{129}Xe-Rb (D_1) spin-exchange optical pumping at high xenon densities using high-power laser diode arrays," *Physical Review A*, vol. 83, p. 053428, 2011.

[140] Y.-Y. Jau, N. N. Kuzma, and W. Happer, "Measurement of ^{129}Xe- Cs binary spin-exchange rate coefficient," *Physical Review A*, vol. 69, no. 6, p. 061401, 2004.

[141] Y.-Y. Jau, N. N. Kuzma, and W. Happer, "High-field measurement of the ^{129}Xe-Rb spin-exchange rate due to binary collisions," *Physical Review A*, vol. 66, no. 5, p. 052710, 2002.

[142] H. M. Gibbs and R. J. Hull, "Spin-exchange cross sections for ^{87}Rb-^{87}Rb and ^{87}Rb-^{133}Cs collisions," *Physical Review*, vol. 153, no. 1, p. 132, 1967.

[143] E. Babcock, I. Nelson, S. Kadlecek, B. Driehuys, L. Anderson, F. Hersman, and T. G. Walker, "Hybrid spin-exchange optical pumping of ^{3}He," *Physical Review Letters*, vol. 91, no. 12, p. 123003, 2003.

[144] W. Happer, G. D. Cates Jr, M. V. Romalis, and C. J. Erickson, "Alkali metal hybrid spin-exchange optical pumping," Nov. 20 2001. US Patent 6,318,092.

[145] I. Dregely, I. Ruset, E. Kotkowski, and F. Hersman, "Scaling up 129xe hyperpolarization-a diagnostic tools system," in *ISMRM*, vol. 15, (Berlin), 2007.

[146] A. Gallagher and E. Lewis, "Determination of the vapor pressure of rubidium by optical absorption," *JOSA*, vol. 63, no. 7, pp. 864–869, 1973.

[147] J. Stenger, M. Beckmann, W. Nagengast, and K. Rith, "A compact Faraday rotation monitor for density and polarization of optically pumped alkali atoms," *Nuclear Instruments and Methods in Physics Research Section A: Accelerators, Spectrometers, Detectors and Associated Equipment*, vol. 384, no. 2, pp. 333–336, 1997.

[148] S. M. Hardy, *Study of hyperpolarised 3-He MRI diffusion on asthma and cystic fibrosis, and development of hyperpolarised 129-Xe MRI lung imaging.* PhD thesis, University of Nottingham, 2016.

[149] I. Dregely, I. C. Ruset, J. F. Mata, J. Ketel, S. Ketel, J. Distelbrink, T. A. Altes, J. P. Mugler, G. Wilson Miller, F. William Hersman, and K. Ruppert, "Multiple-exchange-time xenon polarization transfer contrast (MXTC) MRI: Initial results in animals and healthy volunteers," *Magnetic Resonance in Medicine*, vol. 67, no. 4, pp. 943–953, 2012.

[150] A. Oros and N. Shah, "Hyperpolarized xenon in NMR and MRI," *Physics in Medicine and Biology*, vol. 49, pp. R105–R153, OCT 21 2004.